



The
University
Of
Sheffield.

Locally Refined POD-Galerkin Based Reduced Order Modelling for Fluid-Structure Interaction Problems of Wind Turbines

Jiaxin Dong

A thesis submitted in partial fulfilment of the requirements for the degree of
Doctor of Philosophy

The University of Sheffield
Faculty of Engineering
Department of mechanical engineering

Submission Date

Autumn 2022

For my mom who gave me moral lessons on discipline from an earlier age
and helped pay for my studies

Acknowledgements

I would like to like to gratefully thank to my supervisors, Prof. Lin Ma, Prof. Derek Ingham and Prof. Mohamed Pourkashanian, for their continuous support through my Ph.D. studies. They revealed me the fascination of science, encouraged me throughout the tough times in the Ph.D. pursuit, mentored me in both academic and personal development. Their enthusiasm and insight in research are contagious and motivational, making every discussion an enjoyable moment for me. His guidance and support are far beyond scientific research but also in my life and future career. It has been an honour for me to be his Ph.D. student and I could not have imagined having a better Supervisor.

I also want to express my appreciation to my labmates and friends in Energy Institute. I will particularly mention Fanting Hu, she helped me to start my new life and research when I first arrived, and helped me a lot during my whole Ph.D study.

Lastly, I would like to thank my mom for her love and encouragement.

Abstract

Fluid-structure interactions, especially full rotor simulations for wind turbines, are still computationally inefficient. Although the Proper Orthogonal Decomposition (POD) with Galerkin based Reduced Order Modelling (ROM) has become a popular tool to solve many fluid dynamics problems, most studies are limited to fluid flows in a fixed or infinite domain. The ROM, with either spatially or temporally adaptive snapshots, are still lacking in research, and in this paper, a POD– Galerkin based ROM for a Fluid-Structure Interaction (FSI) problem is proposed. The aim is to reduce the complexity of the costly solution techniques for solving the governing non-linear unsteady partial differential equations that govern the aerodynamic flows over fluid-solid systems with moving interfaces. This novel POD-based ROM is applied to several cases of plunging-pitching aerofoils as well as fluid-structure interaction simulations of a 3D vertical axis wind turbine full rotor simulation. For both applications, this model is shown to be very effective when performed with the proposed snapshot grids, thus reducing the computational cost while maintaining the same level of accuracy.

The goal of this PhD project is to develop a new ROM approach to the FSI problem applicable to moving and/or deforming solid boundary and then applied it to the Vertical Axis Wind Turbine (VAWT) structure analysis in order to improve the wind turbine fluid-structure interaction analysis method regarding both the simulation efficiency and accuracy. A new and novel local refinement strategy on the ROM method is proposed in order to balance the increase in time cost and accuracy. Moreover, this strategy includes elastic behaviour of solid domains, thus increases the capability of the approach to solve FSI problems with large moving interfaces between the rigid body and the fluid.

A literature review on fluid-structure interaction methods and VAWT aeroelastic behaviour is presented in order to identify the gap of this project. In

addition, a comprehensive review of POD method, especially focused on adaptive snapshot methods, is conducted.

A novel adaptive grid discretisation, based on a two-dimensional refinement strategy in which an internal node has exactly four children, has been proposed and developed. The strategy is implemented using a quad-tree data structure which can be implemented automatically and/or manually. The Stuart vortices, a special flow field with an analytical solution, is selected as the validation of the approaches.

Then a novel adaptive POD-Galerkin Based approach is proposed for FSI problems with moving and deforming fluid-structure interface. This approach is straight-forward, easy to apply, and can predict any kind of moving boundaries, no matter whether it is rigid or flexible or flow-induced or prescribed, as long as the solid body information is known. This approach has been applied on various cases, including both two-dimensional and three-dimensional and/or both translational and rotational rigid cases, e.g., an oscillating aerofoil.

As a validation of the proposed novel ROM approaches, the methods have also been employed to the dynamic behaviours of a Horizontal Axis Wind Turbine (HAWT) and a VAWT for the cases of the conceptual National Renewable Energy Laboratory's (NREL's) 5-MW reference offshore wind turbine and the 1.2kW Windspire VAWT, respectively for both vibration and deformation analysis.

The proposed novel adaptive POD-Galerkin Based ROM shows a good agreement in FSI simulations with flexible solid domain boundaries which the traditional ROM cannot predict accurately. Compared to the full-order CFD solution, the proposed ROM method is more computationally efficient, as only the pivotal parameters are included and calculated during simulations. In addition, by introducing the self-adaptive strategy, this proposed ROM method shows a better performance than the traditional ROM method in terms of time cost and accuracy.

Contents

1	Introduction	1
1.1	Aims and Objectives	3
2	Literature Review on Reduced Order Modelling and Wind Turbine Aeroelasticity	6
2.1	Fluid-Structure Interaction Modelling of Wind Turbines	7
2.1.1	Aerodynamic Modelling	7
2.1.1.1	Blade Element Momentum method	8
2.1.1.2	Vortex method	9
2.1.1.3	Actuator methods	11
2.1.1.4	CFD (computational fluid dynamics) modelling	13
2.1.2	Structural Modelling	15
2.1.2.1	Beam Model	16
2.1.2.2	3D FEM Model	18
2.2	Fluid-Structure Interaction Modelling Methods	20
2.2.1	Mesh movement	21
2.2.2	Time advancement schemes	26
2.2.3	Fluid-Structure Interface strategies	31
2.3	Reduced Order Modelling	34
2.3.1	Proper Orthogonal Decomposition	35
2.3.1.1	Stability	36
2.3.1.2	Non-linearity	37
2.4	Current Applications of ROM for Wind Turbine Aeroelasticity Modelling . .	40
2.4.1	Aeroelastic ROMs for wind turbines	45
2.5	Summary	49
2.5.1	Knowledge Gaps	49
2.5.2	Novelty	51

3	Methodology	52
3.1	Introduction	52
3.2	Governing Equations	53
3.3	Modelling Reduction via Proper Orthogonal Decomposition	53
3.3.1	Proper Orthogonal Decomposition	53
3.3.1.1	Singular Value Decomposition	54
3.3.1.2	The Proper Orthogonal Decompositon	55
3.3.1.3	Temporal discretisation of the POD method (Method of Snapshots)	57
3.3.2	Galerkin method	58
3.4	Implementation of a POD-Galerkin based ROM for fluid mechanics	58
3.5	Evaluation of POD-Galerkin Applications	60
3.5.1	Error Estimation	60
3.5.2	Computation of the POD basis	61
3.6	Numerical examples of the POD-Galerkin ROM	63
3.7	Conclusion	74
4	Locally Refined POD-Galerkin Based ROM	75
4.1	Introduction	75
4.2	Methodology	75
4.2.1	Adaptive Snapshot Subspaces	75
4.2.1.1	Preparation for the POD method	79
4.2.1.2	POD basis functions and approximation	80
4.2.1.3	Uniform discretisation	81
4.2.1.4	Adaptive discretisation	82
4.3	Applications	84
4.3.1	Adaptive ROM simulation for Stuart Vortices	84
4.3.2	Adaptive ROM simulation for flow around an oscillating aerofoil	91
4.4	Conclusion	96
5	Locally Refined POD-Galerkin Based ROM with Moving Fluid-Solid Interface	97
5.1	Introduction	97
5.2	Methodology	97
5.2.1	POD-Galerkin based ROM for fluid-structure interactions	99
5.2.1.1	The governing equations	99
5.2.1.2	Mesh motion description	103
5.2.1.3	Fluid-rigid body interaction algorithm	103

5.3	Applications of the proposed model on FSI of moving interface	103
5.3.1	ROM simulation for flow around an oscillating circular cylinder . .	104
5.3.1.1	Simulation modelling	104
5.3.1.2	POD construction	106
5.3.1.3	ROM simulation results	109
5.3.2	ROM simulation for flow around an oscillating aerofoil	113
5.3.2.1	Flow-induced vibration of a NACA 0015 aerofoil at Reynolds number $Re = 173,000$	116
5.3.2.2	Flow-induced vibration of a NACA 0015 aerofoil at $Re =$ 570000	126
5.3.2.3	Forced Vibration of an Oscillating Aerofoil	134
5.4	Conclusion	145
6	Locally Refined POD-Galerkin Based ROM with Deforming Fluid-Solid Inter- face	147
6.1	Introduction	147
6.2	Modelling of a slender body using the finite segment method	148
6.2.1	Coordinates	149
6.2.2	Equations of motion	154
6.2.2.1	Kinetic energy	154
6.2.2.2	Potential energy	157
6.2.2.3	Dissipation of energy	160
6.2.3	The fluid-structure interface	161
6.3	Applications of the Proposed Model on the FSI Simulation of the Fluid Solid interface	162
6.3.1	Adaptive ROM simulation for teardrop/flat design oscillation . . .	162
6.3.1.1	Simulation Modelling	162
6.3.1.2	Reduced Order Modelling	167
6.3.1.3	ROM simulation results	169
6.4	Conclusions	176
6.5	Nomenclature	177
7	ROM FSI Simulation of the NREL 5-MW HAWT	180
7.1	Introduction	180
7.2	Full Order Modelling on FSI of HAWT	180
7.2.1	Simulation of the HAWT	180
7.2.2	Computation Settings	182

7.3	Reduced Order Modelling	188
7.4	Results	190
7.4.1	Convergence analysis	191
7.4.2	Stability analysis	193
7.4.3	Deformation analysis	198
7.4.4	Computational time	205
7.5	Conclusion	207
8	3D ROM FSI Simulation of the 1.2kW Windspire VAWT	209
8.1	Introduction	209
8.2	Fluid-Structure Interaction of the VAWT	209
8.2.1	The Vertical Axis Wind Turbine employed	209
8.2.2	Computational Settings	211
8.3	Reduced Order Modelling	218
8.4	Results	223
8.4.1	Convergence analysis	223
8.4.2	Deformations	225
8.4.3	Aerodynamic Simulations	225
8.4.4	Self-starting behaviour simulation	229
8.5	Conclusion	231
9	Conclusions and Future Work	233
9.1	Conclusions	233
9.2	Future Work	236
	Bibliography	238

List of Figures

2.1	Wake modelling of one blade of a two-bladed rotor using the vortex model, reproduced from [40].	10
2.2	Wake modelling of a 3-bladed NREL 5MW Horizontal Axis Wind Turbine based on an modified acuator line model, reproduced from [48].	12
2.3	Illustrative Vorticity magnitude of a 2D Vertical Axis Wind Turbine.	13
2.4	An examples of a beam model of Horizontal Axis wind turbine blades, different segments indicate different beam elements.	16
2.5	An example of a 3D FEM model of a wind turbine composite blade.	19
2.6	An example of the flow-induced vibration modelling using tension (blue) and torsion (red) springs.	22
2.7	Illustration of the proposed two methods to represent a computational domain. (left) The computational domain using a static mesh with updated grid cells; (right) the computational domain using the deforming mesh approach.	25
2.8	Schematic demonstration of the monolithic FSI approach.	27
2.9	Schematic demonstration of the conventional serial staggered (CSS) scheme.	28
2.10	Schematic of the conventional Parallel staggered (CPS) scheme.	29
2.11	Schematic demonstration of the conventional Improved Serial Staggered (ISS) scheme.	29
2.12	Schematic demonstration of the conventional Improved Parallel Staggered (IPS) scheme.	30
2.13	Comparison of the pressure coefficient on DU96-W180 wind turbine aerofoil between CFD solution and POD solution using different number of POD modes, reproduced from [75].	42
2.14	Comparison between the pitch and plunge solution of beam model obtained from the Reduced Order Modelling and the CFD solution.	48
3.1	A comparison of the decay of the singular values and eigenvalues.	62
3.2	A comparison of the decay of the approximation errors.	63

3.3	Schematic description of the flow induced vibration of an oscillating circular cylinder.	64
3.4	Comparison between the CFD solution and the proposed ROM solution using 12 POD modes for the flow past a oscillating cylinder at $Re = 1690$ and time instances 5.0s and 10.0s.	66
3.5	Errors in the flow past an oscillating cylinder problem at $Re = 1690$ predicted by the proposed ROM using 12 and 24 POD modes.	67
3.6	Singular eigenvalues in order of decreasing magnitude of the ROM for the Flow past a cylinder at $Re = 5000$	68
3.7	Comparison of the solutions of the flow past an oscillating cylinder problem at $Re = 35000$ and time instances 10.0 and 20.0 between CFD solution and the proposed ROM using 12 basis functions.	69
3.8	Comparison of the solutions of the flow past a oscillating cylinder problem at $Re = 35000$ and time instances 10.0 (1) and 20.0 (2) between CFD solution (a) and the proposed ROM using 12 (b), 24 (c) and 36 (d) basis functions.	70
3.9	The error for the flow past a oscillating cylinder problem at $Re = 35000$ predicted by the proposed ROM using 12 (a) and 36 (b) basis.	71
3.10	Schematic presentation of the grid dimension used in different levels of uniformly refined ROMs.	72
3.11	Comparison of the solutions of the flow past an oscillating cylinder problem at $Re = 35000$ between the CFD solution and the proposed ROM obtained from different refinement levels at $t=10s$	72
3.12	Comparison of the online CPU time history on the flow past an oscillating cylinder problem at $Re= 5000$ between the full-order CFD solution and ROMs.	73
3.13	Offline CPU time history for the ROM on the flow past an oscillating cylinder at $Re= 5000$ (up to 200 snapshots).	74
4.1	Flowchart of the proposed self-adaptive POD-Galerkin ROM	76
4.2	Illustration of meshes resulting from refinement by newest vertex refinement based on a common initial grid corresponding to a finite element space V_0	78
4.3	A typical example of an adaptive discretisation at different time steps	79
4.4	Velocity field snapshot of the Stuart vortices at $t = 10\pi$ second.	85

4.5	Rebuilt velocity flow field and the velocity difference at $t = 10\pi$ second to the analytical solution obtained from different uniform grids. (1). 30×15 grids, (2). 60×30 grids, (3). 120×60 grids, (4). 240×120 grids and (5). 480×240 grids; (a). the rebuilt velocity flow field and (b). the velocity difference to the analytical solution.	87
4.6	Adaptive discretisation for the Stuart vortices reduced order modelling. .	88
4.7	Illustrative example of the adaptive mesh refinement for the Stuart vortices solution.	88
4.8	Rebuilt velocity flow field and the velocity difference at $t = 10\pi$ second to the analytical solution obtained from different adaptively refined grids. (1). 30×15 – adaptive grids, (2). 60×30 – adaptive grids, (3). 120×60 – adaptive grids, and (4). 240×120 – adaptive grids; (a). the rebuilt velocity flow field and (b). the velocity difference to the analytical solution.	89
4.9	Velocity differences for different numerical discretisations at $t = 10\pi$ second.	90
4.10	The energy spectrum of the POD modes in the case of the limit cycle oscillation at the Reynolds number $Re = 173,000$	92
4.11	Vorticity contours of the first 6 POD modes and the mean flow for a two-dimensional pitching and plunging aerofoil in the case of the limit cycle oscillation ($Re=173,000$) (a) – (f): first six POD modes, (g): Vorticity contours of the mean flow.	93
4.12	Self-adaptive solution for a two-dimensional pitching and plunging aerofoil in the case of the limit cycle oscillation ($Re=173,000$) at different snapshots. Left: numerical solution; Middle: reconstructed flow field using self-adaptive ROM; Right: grid refinements.	94
4.13	A comparison of the POD-Galerkin results using the adaptive and uniform grid discretisation for the flow passing a pitching and plunging aerofoil in the case of a limit damping oscillation at a Reynolds numbers $Re = 173,000$	95
5.1	Schematic description of problem domain and the notation of FSI problems	99
5.2	Mesh convergence study of the flow-induced vibration of an oscillating circular cylinder.	104
5.3	Time step convergence study of the flow-induced vibration of an oscillating circular cylinder.	105

5.4	Schematic diagram of the meshes of interest of the flow-induced vibration of an oscillating circular cylinder.	106
5.5	Overset mesh combination of domain of interest of the flow-induced vibration of an oscillating circular cylinder.	106
5.6	Schematic diagram of the normalised POD modes and the mean flow of the velocity field of the cylinder oscillating at $Re = 1690$	108
5.7	ROM accuracy regarding the energy coverage with different number of POD modes.	109
5.8	The reconstructed displacement of the centre of gravity of the circular cylinder in the first six seconds of one oscillation period using POD modes of different size.	110
5.9	Comparison between the computational x -axis velocity field (left, reproduced from [112, 151]) and the result obtained using the snapshot ROM method (right).	110
5.10	Comparison between the computational y -axis velocity field (left, reproduced from [112, 151]) and the result obtained using the snapshot ROM method (right).	110
5.11	Comparison of the solutions of the flow past a oscillating cylinder problem at $Re = 1690$ and time instances 10.0 and 30.0 between full order solution and the proposed ROM using 12 basis functions.	111
5.12	Displacement of the position of the centre of gravity of the circular cylinder within the first seven seconds of one oscillation period.	112
5.13	The error of velocity profile obtained via different numbers of POD modes in the case of the flow induced vibration of a cylinder oscillating at $Re = 1690$	113
5.14	Schematic of the domain of the flow-induced vibration of the NACA 0015 aerofoil.	114
5.15	Schematic of the mesh used in the case of the flow-induced vibration of the NACA 0015 aerofoil.	115
5.16	Structural model of the flow-induced vibration of the NACA 0015 aerofoil.	115
5.17	Schematic illustration of a 2-D pitching and plunging aerofoil.	116
5.18	Schematic of the domain settings of the flow-induced vibration of the NACA 0015 aerofoil at Reynolds number $Re = 173,000$	117
5.19	Comparison of the phase between the pitch angle and plunge of the NACA 0015 aerofoil limit cycle oscillation at $Re = 173,000$	118

5.20	Time history of the pitch and plunge of the NACA 0015 aerofoil limit cycle oscillation over normalised periods at $Re = 173,000$	119
5.21	The energy spectrum of the POD modes in the case of the limit cycle oscillation at $Re = 173,000$	120
5.22	Vorticity contours of the first 6 POD modes and the mean flow for a two-dimensional pitching and plunging aerofoil in the case of the limit cycle oscillation ($Re = 173,000$) (a) - (f): first six POD modes, (g): vorticity contours of the mean flow.	121
5.23	Proposed solution for a two-dimensional pitching and plunging aerofoil in the case of the LCO at $Re = 173,000$ at different snapshots. Left: numerical solution; Right: reconstructed flowfield using the new proposed ROM.	122
5.24	A comparison of the POD-Galerkin results using the adaptive and uniform grid discretisation for the flow passing a pitching and plunging aerofoil in the case of a limit damping oscillation at $Re = 173,000$	123
5.25	Decay of the normalized error for the POD basis using the adaptive and uniform grid discretisation for the flow passing a pitching and plunging aerofoil at the Reynolds number $Re=173,000$	124
5.26	Comparison of the online CPU time history on the the two-dimensional pitching and plunging aerofoil in the case of the limit cycle oscillation at the Reynolds number $Re=173,000$ between the full-order CFD solution and the ROMs.	125
5.27	CPU time history for the ROMs on a two-dimensional pitching and plunging aerofoil in the case of the limit cycle oscillation at the Reynolds number $Re=173,000$	125
5.28	Schematic of the domain settings of the flow-induced vibration of the NACA 0015 aerofoil at $Re = 570000$	126
5.29	Time history of the pitch (a) and plunge (b) of the NACA 0015 aerofoil limit cycle oscillation over normalised periods $Re = 570000$	127
5.30	The normalised POD modes of the POD modes in the case of the limit cycle oscillation of the NACA 0015 aerofoil at $Re = 570000$	128
5.31	Vorticity contours of the first 6 POD modes and the mean flow for a two-dimensional pitching and plunging aerofoil in the case of the limit cycle oscillation at $Re = 570000$ (a) - (f): first six POD modes, (g): Vorticity contours of the mean flow.	129

5.32	Proposed solution for a two-dimensional pitching and plunging aerofoil in the case of the limit cycle oscillation at $Re = 570000$ at different snapshots. Left: numerical solution; Right: reconstructed flowfield using the new proposed ROM.	130
5.33	A comparison of the POD-Galerkin results using the adaptive and uniform grid discretisation for the flow passing a pitching and plunging aerofoil in the case of a limit damping oscillation at the Reynolds number $Re=570,000$.	131
5.34	Decay of the normalized error for the POD basis using the adaptive and uniform grid discretisation for the flow passing a pitching and plunging aerofoil at the Reynolds number $Re=5700,000$	132
5.35	Comparison of the online CPU time history on the the two-dimensional pitching and plunging aerofoil in the case of the limit cycle oscillation at the Reynolds number $Re=570,000$ between the full-order CFD solution and the ROMs.	133
5.36	CPU time history for the ROMs on a two-dimensional pitching and plunging aerofoil in the case of the limit cycle oscillation at the Reynolds number $Re=570,000$ between the proposed ROM and the uniform ROMs solution.	133
5.37	Normalised pitch and plunge profiles of the NACA 0015 aerofoil.	134
5.38	Schematic diagram of the domain of the NACA 0015 aerofoil forced vibrating at $Re = 570000$	135
5.39	The normalised POD modes in the case of the forced oscillation at the Reynolds number $Re = 570,000$	136
5.40	ROM accuracy regarding the energy with different number of POD modes in the case of the forced oscillation at $Re = 570000$	137
5.41	Comparison between the adaptive ROM solution and the corresponding uniform ROM solution in the case of the forced oscillation at $Re = 570000$.	138
5.42	Comparison between the proposed adaptive solution and the uniform ROM for a two-dimensional forced vibration aerofoil at $Re = 570000$ at timesteps $t/T=0.25$ (1) and 0.45 (2).	139
5.43	Error $err(N)$ of velocity profile obtained via different numbers of POD modes in the case of the flow induced vibration of the oscillating aerofoil NACA 0015 at $Re = 570000$	140
5.44	Comparison of CPU time history between the proposed ROM and the uniform ROM on the prescribed of the NACA 0015 aerofoil at $Re = 570000$	141

5.45	Illustrative demonstration of the adaptive ROM solution and the corresponding uniform ROM solutions.	142
5.46	Comparison of the proposed adaptive solutions for a two-dimensional forced vibration aerofoil at $Re = 570000$ at timesteps $t/T = 0.25$ (1) and 0.45 (2).	143
5.47	Error $err(N)$ of velocity profile obtained via different numbers of POD modes using adaptive ROM models in the case of the flow induced vibration of an oscillating aerofoil NACA at $Re = 570000$	144
5.48	CPU time history for the proposed adaptive ROMs on the prescribed of the NACA 0015 aerofoil at $Re = 570000$	145
6.1	Flexible link before and after solid body deformation and its discretisation.	149
6.2	Illustrative demonstration of the Euler angles used for solid body rotation.	150
6.3	Illustrative demonstration of the notation used for the i -th segment . . .	152
6.4	Illustrative demonstration of the additional notation used for the i -th segment	153
6.5	Illustrative demonstration of the twisting and bending spring modelling .	157
6.6	Stiffness coefficients of the combined spring	159
6.7	Schematic demonstration of the flexible aerofoil heaving periodically. . .	162
6.8	Schematic demonstration of the domain of the vibration of the Teardrop/flat design FSI simulation.	163
6.9	Schematic demonstration of the domain of the vibration investigation of the teardrop/flat design FSI simulation.	165
6.10	Mesh convergence study of the vibration investigation of the teardrop/flat design FSI simulation at Reynolds number $Re=9,000$	166
6.11	Time step convergence study of the teardrop/flat design FSI simulation at Reynolds number $Re=9,000$	166
6.12	Computational domain of flexible flapping teardrop/plate shape oscillation simulation.	168
6.13	Normalised POD modes of the proposed adaptive POD-Galerkin ROM model for the teardrop/plate oscillation simulation.	169
6.14	Proposed solution for the three-dimensional teardrop/flat design oscillation at Reynolds number $Re=9000$	170
6.15	A comparison of the POD-Galerkin results using the adaptive (b) and the uniform (a) grid discretisation for the teardrop/flat design oscillation at the Reynolds number $Re=9,000$	171

6.16	Proposed solution for the three-dimensional teardrop/flat design oscillation at Reynolds number $Re=27000$	171
6.17	Different number of finite element segments used in the teardrop/flat design vibration simulation.	172
6.18	Displacement of trailing edge of teardrop/flat aerofoil vibration simulation at Reynolds number 9,000.	173
6.19	Decay of the normalised error for the POD basis using the adaptive and uniform grid discretisation for the teardrop/flat design oscillation at the Reynolds number $Re=9,000$	174
6.20	Comparison of the CPU time history on the three-dimensional teardrop/flat design oscillation at the Reynolds number $Re=9,000$ between the full-order CFD solution and the ROMs.	175
6.21	Comparison of the offline CPU time history on the three-dimensional teardrop/flat design oscillation at the Reynolds number $Re=9,000$ of different ROMs. . .	176
7.1	Illustrative modelling of the NREL 5-MW offshore wind turbine.	181
7.2	Computational domain of NREL 5-MW reference wind turbine for 3D FSI simulation.	183
7.3	Mesh hierarchy of NREL 5-MW reference wind turbine for 3D FSI simulation.	184
7.4	Illustrative demonstration of the NREL 5-MW offshore wind turbine blade.	186
7.5	Cross sectional aerofoil profile of the NREL 5-MW wind turbine blade. . .	186
7.6	Distributed blade structural properties of the NREL 5-MW wind turbine blade.	187
7.7	Initial uniform ROM mesh of 3D computational domain for NREL 5-MW reference wind turbine FSI simulation. Each grid represents a $5 \times 5 \times 5$ mesh grids in ROM calculation.	188
7.8	Illustrative demonstration of the ROM refined mesh of 3D computational domain for the NREL 5-MW reference wind turbine FSI simulation after one iteration.	189
7.9	An illustration of segment representation of HAWT blade, 16 segments are used in this example.	189
7.10	Energy spectrum of the POD modes for the NREL 5MW HAWT.	190
7.11	Initial wind turbine setting for the HAWT FSI simulation.	191

7.12	The error of the NREL 5MW wind turbine blade projection residuals with respect to the number of modes. The blade deflections are compared to the full-order CFD at 12 m/s steady wind speed and the projection basis is composed of undeflected blade mode shapes.	192
7.13	First 6 mode shapes of the NREL 5-MW wind turbine blade.	194
7.14	Finite element segment modelling of the NREL 5-MW wind turbine. red and black bodies represent they are modelled as flexible and rigid body respectively.	195
7.15	Rated rotational speed with respect to the wind speed of the NREL 5-MW wind turbine.	197
7.16	Total deformation of the NREL 5MW wind turbine blade at wind speed 8 <i>m/s</i> and rotor speed 9 RPM.	198
7.17	Illustrative representation of the HAWT deformation working at wind speed 8 <i>m/s</i> and rotor speed 9 RPM.	199
7.18	Comparison of out-of-plane deflections for blade 1 tip between rebuilt ROM solution and the baseline OC3 code for wind speed 8 m/s.	202
7.19	Comparison of in-plane deflections for blade 1 tip between rebuilt ROM solution and the baseline OC3 code for wind speed 8 m/s.	203
7.20	Comparison of AOA for NREL 5-MW wind turbine working at wind speed 8 m/s, $r/R=0.93$	204
7.21	The total normalised CPU time cost of the proposed uniform and adaptive ROM.	207
8.1	Geometry description of the 1.2 kW Windspire VAWT.	210
8.2	Computational domain of the Windspire 1.2kW VAWT for the 3D FSI simulations.	211
8.3	2D cross section of the blade profile and boundary layer overset mesh.	212
8.4	Mesh region hierarchy of the Windspire 1.2kW VAWT for the 3D FSI simulations.	213
8.5	2D cross section of the computational mesh along the rotor axis and 4 overset mesh regions have been applied on the background mesh.	213
8.6	Structural modelling of the 1.2 kW Windspire VAWT.	215
8.7	Cross sectional aerofoil profile of the 1.2kW Windspire VAWT DU06W200 blade profile.	216
8.8	Mesh convergence study of the flow-induced vibration of an oscillating cylinder.	216

8.9	Time step convergence study of the flow-induced vibration of an oscillating cylinder.	217
8.10	Initial uniform ROM mesh of the 3D computational domain for Windspire VAWT FSI simulation. Each grid represents a $5 \times 5 \times 5$ mesh grids in ROM calculation.	218
8.11	Illustrative demonstration of the ROM refined mesh of the 3D computational domain for the VAWT FSI simulation.	219
8.12	ROM grids of the initial reduced order modelling grid.	219
8.13	Lagrangian multiplier of two refined ROM mesh iterations on XY-plane around the rotor: (a) initial meshes, (b) refined after 1 iteration, (c) refined after 2 iterations.	220
8.14	Finite element segment modelling of the WindSpire VAWT. blue and black bodies represent that they are modelled as flexible and rigid bodies, respectively.	221
8.15	Energy spectrum of the POD modes for the Windspire VAWT working at a speed 8m/s.	222
8.16	First six POD modes of the Windspire VAWT FSI Simulation at 6.0 m/s and rotor speed of 20.6 rad/s (X-Y view).	223
8.17	The error of the Windsprrie VAWT blade projection residuals with respect to the number of modes. The blade deflections are compared to the full-order CFD at 8 m/s steady wind speed and the projection basis is composed of undeflected blade mode shapes.	224
8.18	Time history of the blade bending displacement on one VAWT blade at different time snapshots during one operating period, inlet velocity 8.0 m/s (blue) and 6.0 m/s (red).	225
8.19	Error between the referenced CFD solution and the proposed ROM solution.	226
8.20	Rebuilt velocity flow field from the intitial ROM mesh (a) and the mesh after two iterations (b).	227
8.21	Velocity difference between the rebuilt ROM solution and FSI (a) initial ROM, (b) ROM after refined two iterations.	227
8.22	Time history of the aerodynamic torque for the aerodynamic simulations (a) 8.0 m/s; (b) 6.0 m/s.	228
8.23	Time history of the aerodynamic torque of the Windspire VAWT working at 6.0 m/s via different reduced order modelling approaches.	229
8.24	Time history of the rotor speed (a) starting from 0 rad/s; (b) starting from 4 rad/s.	230

8.25 Time history of the blade maximum displacement on one VAWT blade at different time snapshots during self-starting stage at 0 m/s via FSI Simulation (blue) and ROM modelling (red). 231

List of Tables

3.1	Basic parameters of the structural dynamics and aerodynamics for flow around an oscillating circular cylinder, reproduced from [112].	64
4.1	Time costs and velocity differences for the uniform discretisation.	86
4.2	Time costs and velocity differences for the adaptively refined discretisation.	90
4.3	Time costs and velocity differences for the uniform adaptively refined discretisation.	96
5.1	Properties employed in the aerofoil model for the flow-induced vibration of the NACA 0015 aerofoil.	114
6.1	Properties employed in the numerical model for the vibration investigation of the teardrop/flat design.	163
7.1	Basic properties of the NREL 5-MW offshore wind turbine. Baseline turbine properties	182
7.2	Structural properties of the NREL 5-MW reference wind turbine.	185
7.3	187
7.4	First 6 mode shapes of the NREL 5-MW wind turbine blade.	195
7.5	Number of rigid segments used in the wind turbine model.	196
7.6	First 10 natural frequencies of the NREL 5-MW wind turbine model.	197
7.7	Comparison between rebuilt ROM simulation with different numbers of segments on the HAWT aerodynamic parameters and OC3 codes at wind speed 8 m/s and rotor speed 9 RPM.	200
7.8	Comparison between rebuilt ROM simulation with different numbers of segments on the Blade 1 tip deflections at wind speed 8 m/s and rotor speed 9 RPM.	201
7.9	Comparison between rebuilt ROM simulation with different numbers of segments on the turbine blade and OC3 codes regarding torque and computational efficiency at wind speed 11.4 m/s and rotor speed 12.1 RPM.	205

7.10	Comparison between rebuilt ROM simulation with different numbers of segments on the turbine blade and OC3 codes regarding blade 1 tip deflections at wind speed 11.4 m/s and rotor speed 12.1 RPM.	205
8.1	Geometric and material properties of the 1.2kW Windspire VAWT	210
8.2	Structural properties of the 1.2kW Windspire VAWT.	215
8.3	Comparison between the Windspire VAWT FSI simulation and the referenced codes at various speeds.	218
8.4	Number of rigid segments used in the wind turbine model.	221

Chapter 1

Introduction

Wind turbines, in particular vertical axis wind turbines (VAWT) experience large unsteady pressure loads when exposed to the flow field because of its unique design leading to significantly high deflection and fatigue problems. Therefore, special care must be taken to design these components such that they are capable of withstanding loads of this magnitude.

The complexity of the Fluid-Structure Interaction (FSI) Analysis of the VAWT is much more challenging than those in the Horizontal Axis Wind Turbine (HAWT). Different from the HAWT, the rotation axis of a VAWT is orthogonal to the upcoming wind direction, the angle of attack of the wind turbine blades changes rapidly during one revolution, resulting in the airflow swapping between fully attached and fully separated. These large and rapid changes make an impact on the variations in many terms, and in particular the aerodynamic torque and the forces on the VAWT blades. The process of an FSI of VAWTs needs to undergo a mesh refinement and have smaller time-steps when performing the transient simulations in order to achieve accurate results [105]. In addition, as the size of the wind turbine increases, it can no longer be considered rigid, and the aeroelastic behaviour in the VAWTs needs to be considered.

There are several key aspects of the VAWT aeroelastic behaviour that needs to be considered in the FSI analysis, e.g., the elastic behaviour often comes from the blade, the tower and its connection. As there is an increasing scale up in the modern wind turbines, then the traditionally implementations on the HAWT approaches, such as the rigid blade modelling or single blade modelling, is no longer accurate enough to provide reasonable results. This hinders the efficiency of the FSI study on VAWTs. In addition, the computational analysis of nonlinear aeroelastic systems, such as the VAWT is still an expensive proposition.

The cost and complexity of Fluid-Structure Interaction on wind turbines are still the main obstacles when conducting numerical investigations into wind turbine fluid-structure

interactions. Various researches have been conducted to reduce time cost, for example, the Reduced Order Modelling (ROM) approach. By analysing the contribution of the most relevant modes of the fluid system and/or the coupled system, the ROM aims to reduce the complexity of the problem. That's why it's common for simulations to ignore all the other modes in favour of concentrating on the crucial ones. By drastically reducing the number of degrees of freedom, the computational cost is decreased [18].

The idea behind the Reduced Order Modelling is to build a computationally less expensive model of the aeroelastic system from a very small set of solutions produced by a high-fidelity model, frequently from CFD simulations. By defining the crucial modes of the coupled system and the fluid system based on their contributions, the ROM aims to simplify the issue [118].

One of the examples of ROM is the Proper Orthogonal Decomposition (POD) - Galerkin projection approach. Although it is a well-developed tool for model reduction, it is highly sensitive to small changes in the state due to its inherent limitations. In addition, the implementation of this approach is limited, although it is capable of solving nonlinear systems, and often requires very careful tuning in order to produce satisfactory results. The POD method forms a reduced basis by linearly combining the snapshots corresponding to all the training parameter values [70]. This linear combination minimises the root-mean-average (RMS) error over the training process by sacrificing the computational cost on the training spaces. Both methods lose their computational efficiency when the dimension of the snapshot spaces increases, and eventually becoming the same as the span of the snapshots [75]. The model order reduction with spatial adaptivity has been studied in various researches [7, 8] for snapshot computations with adaptive wavelets and in Yano's paper [185] for snapshot computations with adaptive mixed finite elements. The main issue that has been addressed in these publications is the assessment of the error between the reduced-order solution and the experimental data and/or theoretical solutions. When performing static computations, the error between the ROM and numerical solution can be estimated by assuming that there is a relatively good enough snapshot base. For the case of adaptive snapshot computations, Ali et al. [8] use the wavelet techniques to estimate the required dual norm of the continuous residual. In contrast, Yano [185] proposed a solution to the continuous domain using a reduced formulation coupled approach for specified finite elements. Since its introduction into the fluid mechanics community [82, 27], the POD - Galerkin projection has quickly become a popular tool for Model Order Reduction. It has been successfully applied to solve many fluid dynamics problems, for instance, an F-16 aircraft [113]. However, most studies are limited to fluid flows in a fixed or an infinite domain. The implementation of the

POD-Galerkin projection is not straightforward when there are moving solid boundaries or structures in the fluid flow, which is the case for wind turbines and in many other applications. Actuation modes, Eulerian-Lagrangian dynamic mesh adaptation methods have been proposed to allow the transition between the moving/deforming near field to the stationary far field. There is also a different route taken by Liberge and Hamdouni [112], in which they consider a fictitious stationary domain, including both fluid and solid and apply the POD-Galerkin projection on a modified equation for both the fluid and solid. However, these methods assume that all solid bodies are rigid, which undermines the accuracy of the POD method. On the other hand, various POD with time-adaptive snapshot methods have been studied in [9]. Several approaches were suggested in order to treat the non-linearities in various ways. One illustrative example of these techniques is the coupling of the POD method with the Hamilton-Jacobi equations for the order reduced system. A temporal refinement strategy is implemented based on the given threshold to update the POD basis for more reasonable results. In addition, the POD with one-dimensional space-adaptive snapshots has already been addressed in [108], where the POD computation relies on a polynomial approximation of the snapshots. However, in the case of 2D or 3D problems, the POD with either spatially or temporally adaptive snapshots are still lacking in research [79]. The traditional ROM treats the solid domain as a fluid using penalty methods. **The structure domain is considered a special fluid whose moduli and density are relatively large by adding a penalty term** [153]. Although this method is capable of dealing with moving FSI problems, POD modes have to be calculated at every time step which undermines its efficiency over the full-order solutions. Several modifications have been introduced by various authors to fix this issue but the capability for the FSI problem with a deforming solid body is still lacking research. Another point of interest lies in the accuracy of the ROM model, which highly relies on the grid that is used during the POD approach. A proper local refined method would only apply on the necessary domain based on a threshold strategy. The increase in the number of grid points produces more accurate results but it increases the time cost which undermines the benefit of the ROM method.

1.1 Aims and Objectives

The goal of this PhD project is to develop a new ROM approach to the FSI problem that is applicable to moving and/or deforming solid boundaries and then apply it to the VAWT structure analysis in order to improve the wind turbine fluid-structure interaction analysis method regarding both the simulation efficiency and accuracy. A new and novel local

refinement strategy on the ROM method is proposed in order to balance the increase in time cost and accuracy. Moreover, this strategy includes the elastic behaviour of solid domains, thus increasing the capability of the approach to solve FSI problems with large moving interfaces between the rigid body and the fluid.

The rest of this thesis is arranged in the following manner:

In Chapter 2, a literature review on fluid-structure interaction methods and VAWT aeroelastic behaviour is presented. Various methods are listed and analysed to identify the research gaps in this project. In addition, a comprehensive review of the POD method, especially focused on adaptive snapshot methods, is included in Chapter 2.

A brief overview of the Proper Orthogonal Decomposition (POD) - Galerkin method is presented in Chapter 3.

In Chapter 4, an adaptive grid discretisation, based on a two-dimensional refinement strategy in which an internal node has exactly four children, has been proposed and developed. The strategy is implemented using a quad-tree data structure which can be implemented automatically and/or manually. To stress the necessity and importance of the adaptive grid refinement, the Stuart vortices, a special flow field with an analytical solution, is selected as the application of the approaches.

In Chapter 5, a POD-Galerkin based ROM approach is proposed, which defines the moving solid boundaries/bodies as a continuous time-varying domain. This approach is straight-forward, easy to apply, and can predict any kind of moving boundaries, no matter whether it is rigid or flexible or flow-induced or prescribed, as long as the solid body information is known. A series of flows with moving boundaries have been predicted by this method, including both two-dimensional and three-dimensional and/or both translational and rotational rigid cases, e.g., an oscillating aerofoil.

In Chapter 6, a new and novel POD-Galerkin ROM approach for flexible cases is proposed. By defining the moving solid boundaries/bodies as a characteristic function on the same combined fluid-solid domain, the POD-Galerkin projection method has also been applied on the moving solid boundaries/bodies. The concept of flexible bodies within a MBS is depicted, including beam elements and modal bodies on the basis of order-reduced bodies. The interface between the mechanical and fluid solver is proposed which allows the exchange of forces and body kinematics. This approach has been applied on both two-dimensional and three-dimensional with deforming boundaries, e.g., a teardrop/flat plate design is flexible in the chordwise direction only.

As a validation of the proposed novel ROM approaches, the proposed adaptive POD methods have also been employed to multiple problems. In order to improve the accu-

racy of the proposed model, the dynamic behaviours of a HAWT and VAWT working at various situations were examined in Chapter 7 and 8, respectively.

In Chapter 7, the novel ROM method is validated in the case of 3D FSI simulations for the conceptual NREL 5-MW reference offshore wind turbine. The proposed method solves the case of a deforming solid body by considering the deformation as a cumulation of a series of rigid segments. During the validation simulation, the turbine blades are assumed to be flexible. Various numbers of segmentations on each blade are investigated prior to the simulation. The reconstructed ROM solutions are compared to numerical results as well as experimental data when it is approachable. In addition, error estimations and time analyses are compared to the corresponding full-order numerical solution.

Finally, in Chapter 8, the aeroelastics, including vibration and deformation analyses of a typical VAWT has been conducted. The turbine was loaded with a varying inflow and the resulting self-starting behaviour and fluctuations in the rotational velocity were observed. The deflections of the blades were analysed and compared to the solution obtained when using the traditional POD methods, based on the penalty methods. It is assumed that the structure of interest is a special kind of fluid whose density and moduli are relatively large. In addition, the capability of the proposed ROM method combining with the refinement approach is presented, investigated and compared to traditional ROM methods.

Chapter 2

Literature Review on Reduced Order Modelling and Wind Turbine Aeroelasticity

The aeroelasticity behaviour of wind turbine aerodynamics, for example, relies on the aerodynamic loading of flexible structures. Thanks to increasing computing power and improvements in computational mechanics techniques, high-fidelity computer simulations of coupled fluid-structure issues are becoming more practical for investigation. In the field of computational sciences, fluid-structure interaction simulations have emerged as a hot issue. However, there are significant challenges associated with the creation of the computational building pieces required to carry out these simulations and the way in which they are sewn together to permit a linked physics simulation. The aeroelastic problems of wind turbines are getting worse as their blades get larger and more flexible. In addition, because of the growth in size and flexibility of large turbine blades, the wind turbines are becoming more susceptible to aeroelastic issues. The aeroelasticity of wind turbines, also known as the fluid-structure interaction, can lead to a severe impact on both the wind turbine blades and tower. Therefore, accurate FSI modelling of wind turbines is crucial in the development of large wind turbines. This PhD project focuses on the technology of coupling fully nonlinear models for the fluid flow with a structural model for the wind turbines using a novel reduced order modelling approach. Further, the nonlinear behaviour of the fluid motion is an essential aspect of many aeroelastic phenomena of interest.

2.1 Fluid-Structure Interaction Modelling of Wind Turbines

Instability issues, such as edgewise instability and flutter, caused by aeroelastic processes can be disastrous for the blades and the wind turbine as a whole. Moreover, new aeroelastic instabilities may emerge from the alterations in blade design necessitated by the increased size of wind turbines. Most current aeroelastic models of wind turbines assume very modest blade deflections and are thus linear in nature. However, this assumption breaks down when wind turbines get bigger, since the blades experience larger and larger deflections, introducing considerable geometric nonlinearities. Furthermore, the aerodynamic and structural design differences in VAWTs cause them to face unique aerodynamic and aeroelastic issues compared to HAWTs. Since the axis of rotation is perpendicular to the direction of the wind, the blades of a wind turbine encounter enormous and frequent changes in the angle of attack, causing the airflow to alternate between being totally connected and entirely detached. This causes the aerodynamic torque operating on the rotor to fluctuate with high frequency and amplitude, necessitating a finer mesh resolution and a lower time-step size for realistic simulations [105]. Therefore, investigating the aeroelasticity characterisation of large wind turbine blades is playing an essential role in the development of large wind turbines [77].

The aerodynamic component of an aeroelastic model calculates aerodynamic loads, while the structural component determines the structural dynamic reactions, and the fluid-structure interaction techniques connect these two parts. One common simplification of the wind turbine blade structure in low-fidelity models is to represent them as 1D beam components defined by their cross-sectional geometry. The aerofoil aerodynamics is often modelled by employing the Blade Element Momentum (BEM) theory and CFD approaches are often applied in high-fidelity models. Due to the intrinsic complexity of wind turbine fluid-structure interactions, such as the complexity of the blade structural layout, obtaining accurate results is challenging and time-consuming and requires much work. Therefore, some model reduction approaches are proposed to increase the efficiency and accuracy of wind turbine FSI problems.

2.1.1 Aerodynamic Modelling

Friedmann is credited with having performed some of the early work on the dynamic modelling of wind turbine blades [63, 134]. In his work, the equations of motion of a single turbine blade were modelled. The blade was supposed to be an elastic beam that had a stiff root section and a free moving tip. In spite of this, the capacity of classical beam theory to predict the structural dynamics of turbine blades is no longer adequate

due to the increase in length and flexibility of the blades [6]. When the beam is loaded in the lateral direction, classical beam theory implies that there would be only tiny deflections in the blades. However, this is not the case with the blades of wind turbines, since they are susceptible to blade deflections in both the flap-wise and edge-wise directions. In addition, the assumption of modest blade deflections is no longer valid since turbine blades are highly flexible, particularly when it comes to large-scale turbine facilities. This is because large-scale turbines are more likely to experience larger deflections. As a result, the discussion around the structural modelling of wind turbine blades has shifted toward the necessity of developing non-linear beam theory-based models that require a smaller number of assumptions [6]. It is essential to perform aeroelastic modelling of wind turbine blades by using a proper aerodynamic method. There are several types of aerodynamic methods that have been implemented in the aeroelastic modelling of wind turbine blades, for example, the Blade Element Momentum method, vortex method, generalised actuator type method and CFD (computational fluid dynamics) method, etc.

2.1.1.1 Blade Element Momentum method

In 1935, Glauert [68] originally proposed the BEM (Blade Element Momentum) method by combining blade element theory and blade momentum theory. Ageze et al. [6] and Buhl et al. [33] provide a comprehensive list of aeroelastic codes. According to the findings of the review carried out by Ageze and colleagues [6], all aeroelastic algorithms make use of the BEM model in order to compute the aerodynamic loads. By breaking a wind turbine blade up into its component parts, the BEM model is able to calculate the aerodynamic loads that are placed on the blade. Data from a 2D aerofoil is utilised in the calculation of the aerodynamic load that each element experiences independently. The total load that the blade is subjected to is calculated by adding up the loads that are placed on its constituent segments. However, because of the model's heavy reliance on 2D aerofoil data, it is unable to produce reliable 3D results without the incorporation of empirical adjustments for the effects of 3D aerodynamics. This limitation prevents the model from being used in practise [78]. A number of adjustments, including ones provided by Du and Selig [53]; Chaviaropoulos and Hansen [42] and Snel [156], have been put forward in order to take rotational effects into account up until stall. Viterna and Corrigan [171] proposed correction formulae of the BEM method following the occurrence of stall.

Blade Element Momentum theory is limited in wind turbine problems due to it being based on steady flow. Therefore, it is incapable of providing promising results in transient simulations. For every time step, the structural solver requires the aerodynamic loads to be computed at each segmented position on the blade. These calculations are then utilised as input. Despite this, the BEM model is frequently utilised in low-fidelity models because to its low cost in terms of computational resources and its high speed. In addition, it assumes that each annular ring is independent of every other annular ring, and does not account for wake expansion, tip losses or yaw. However, several limitations have been overcome, and this has been by introducing empirical correction factors from applications, or based on wind turbine experience. For instance, Chattot [40] has established the validity of the BEM based on experimental data.

Compared to other aerodynamic models, especially the CFD approach, the BEM method is efficient and capable of providing accurate results when reliable aerofoil aerodynamic data are available. The BEM theory, however, becomes less accurate and, as a result, less applicable as the geometry of wind turbine blades continues to evolve and as the operating circumstances become more challenging. By developing correction models and applying them to certain tip geometries, one may gain a greater agreement with the experimental results. This can be done in a number of ways. However, it is difficult to generalise these correction models for the tip loss and the rotational effects to a broad variety of blade geometries and operating situations. This is due to the fact that the tip loss is a function of rotation. In spite of these restrictions on their application, BEM methods are extensively utilised for modelling blade aerodynamics with the CFD approach. This is particularly the case in low-fidelity computations, as BEM methods may be implemented as a computationally economical steady-state model.

2.1.1.2 Vortex method

The vortex model has also been employed in the wind turbine aeroelastic applications to improve the quality of the wake dynamics models of wind turbine rotors. In this model, lifting lines or surfaces represent both the trailing and shed vorticity in the wake. Figure 2.1 presents an example of the wake modelling of a two-bladed wind turbine rotor using the vortex model. The vortex model considered here is the Goldstein model, which allows for the interaction between the blade elements to take place as with the Prandtl Lifting Line theory.

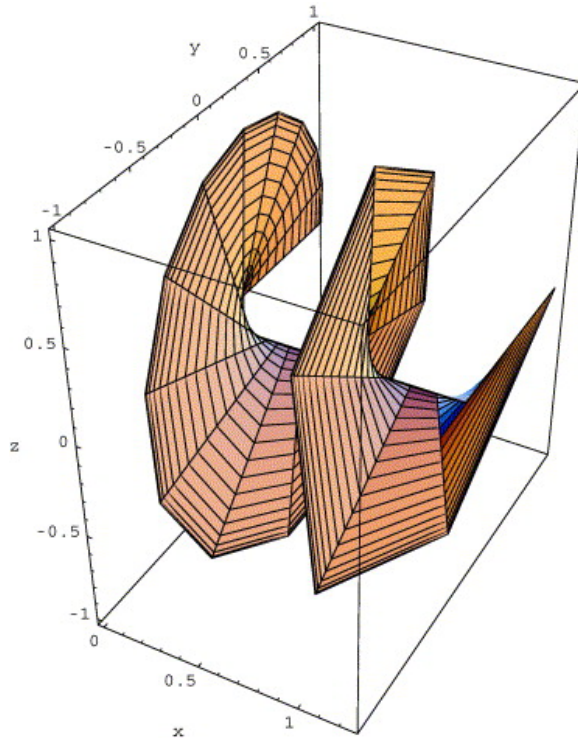


Figure 2.1: Wake modelling of one blade of a two-bladed rotor using the vortex model, reproduced from [40].

The wake in the vortex models can be calculated using either the prescribed wake method or free-wake method. In a prescribed wake method, the semi-empirical formulas make the assumption that the wake shedding from the blade may be represented as stiff. This is an important assumption to make. The prescribed-wake feature included in these models reduces the amount of time spent on computing but restricts their use to situations with consistent incoming flows.

Free-wake vortex models have also been employed to wind turbine blades to study the unsteady wakes of the blades [46] as well as the aeroelasticity of the wind turbine blades [64]. Compared to the prescribed wake model, it employs the free-wake method, and therefore it is capable of solving unsteady flow problems with much more computational time.

Compared to the BEM approach, the vortex model is much more computationally expensive. Also due to the singularities of the vortex panels when developing the wake, the vortex model tends to diverge. Finally, it assumes that there are no viscous effects in the model, and this limits its application.

2.1.1.3 Actuator methods

Another attempt on the aerodynamic model of a wind turbine blade is the actuator approach. The principle of the actuator methods is defining a specific wind turbine blade as a disc, line or a surface, concerning the equivalent loads on the disc, line or surface, respectively. It can be categorised into several classes based on the representation of the wind turbine blade, i.e., actuator disc model [159], actuator line model [161] and actuator surface model [102].

The actuator disc model, which was developed from the 1D momentum theory, was the very first actuator model that was utilised for the purpose of researching the blade aerodynamics. In addition to this, the equations of Euler and Navier-Stokes may be numerically coupled with the actuator disc. The force distribution on the flow is used to simulate both the geometry of the blade and the flow that is occurring around it in the numerical practise. This allows for accurate representation of both aspects.

The force that is exerted on an actuator disc in a straightforward scenario with a disc that is loaded evenly is determined by the thrust coefficient and the reference wind speed. The force that is applied on the disc changes as it travels in the radial direction but stays the same throughout the annulus. The force distribution on the blades may be estimated in a manner analogous to that of the BEM by making use of the lift and drag coefficients of the same aerofoil profile. The calculation of the local angle of attack and the lift and drag coefficients is one of the challenges presented by this method. Shen et al. provided a method employing the information on the upstream blade plane in their 2009 publication [150]. They used the non-uniformly loaded actuator disc technique and expanded it to the actuator line approach. In this way, the forces exerted by the blades are modelled by making use of a line that has loads scattered along it. Figure 2.2 presents a visual representation of the wake modelling of a three-blade wind turbine rotor that is based on the actuator line model.

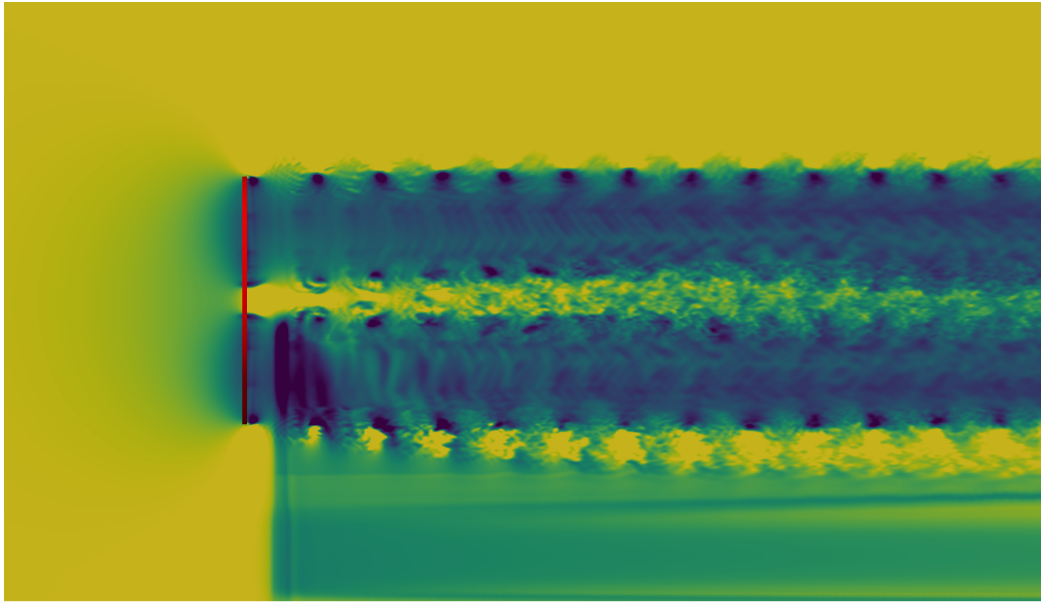


Figure 2.2: Wake modelling of a 3-bladed NREL 5MW Horizontal Axis Wind Turbine based on an modified actuator line model, reproduced from [48].

Figure 2.2 Wake modelling of a three-bladed wind turbine rotor based on the actuator line model, reproduced from [150]. This approach can be extended to the actuator surface method, in which a planar surface represents the wind turbine blade. As a result of Kim's improvements to the actuator surface model for wind turbine evaluations [102], the necessity for a tip loss correction has been avoided. The applicability of the actuator surface approach is restricted since it requires knowledge of the lift and drag coefficients of aerofoils, in addition to the skin friction and pressure distribution on the aerofoil surface. However, Dobrev et al. [50] proposed a simplification in which the pressure distribution in the model can be replaced by a set of linear functions, determined for the local lift and drag coefficients.

The actuator type models that were mentioned before should be given credit for offering a greater insight into the evolution of the 3D flow, as well as credit for contributing to a better understanding of the dynamics of the wake. However, because the Navier-Stokes equations need to be solved in these methods, working with actuator models takes significantly more time. In addition, actuator type models, in which the loads on the blade are still calculated based on the blade element theory and tabulated aerofoil data, do not accurately predict the aerodynamic loads when compared to the CFD approach. This is because the actuator type models still use tabulated aerofoil data [174].

2.1.1.4 CFD (computational fluid dynamics) modelling

In recent years, computational fluid dynamics (CFD) has garnered a significant amount of attention due to the development of more powerful computing resources. The computational fluid dynamics (CFD) approach solves the governing equations of fluid flow, such as Navier-Stokes equations, in an iterative process at thousands of places on and around the blade. This method does not require any preset aerofoil aerodynamic data in order to do the calculation. In addition to aerodynamic load calculations, CFD is also a useful technique for visualising the flow field around the blade, as shown in Figure 2.3.

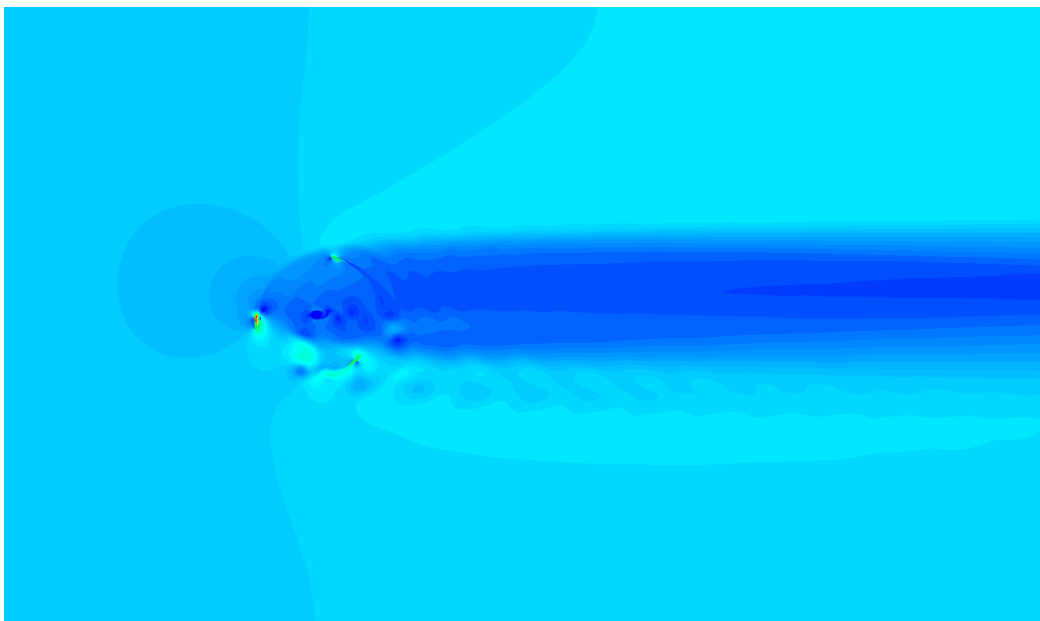


Figure 2.3: Illustrative Vorticity magnitude of a 2D Vertical Axis Wind Turbine.

When performing a 3D CFD simulation, the 3D blade geometry needs to be described accurately in a digitised format to perform the CFD modelling of the wind turbine blades. Blades for wind turbines frequently have a complicated geometric design that includes a variety of span-wise cross-sectional information, such as the shape of an aerofoil, the chord distribution, and the twist angle distribution. CAD software allows the modelling of the blade geometry in its many forms.

The Navier-Stokes equations, which are the governing equations of fluid flow and are derived from momentum, energy, and continuity conservations, serve as the mathematical basis for the computational fluid dynamics (CFD) approach known as computational fluid dynamics (CFD). Because the relative wind speed at wind turbine blades is far lower than the speed of sound, the flow may be regarded to be an incompressible flow. This is because the flow is not subject to pressure changes.

Directly solving the Navier–Stokes equations, also known as DNS (direct numerical simulation), demands a significant amount of computational resources. These resources are so extensive that they exceed the capabilities of the computers that are now available. Moreover, some turbulence modelling is required to apply the NS equations to solve practical engineering problems on the motion of wind turbine blades. Currently, turbulence models are mainly derived based on the RANS (Reynolds Averaged Navier-Stokes) equation, which is capable of providing approximate time-averaged solutions. Various RANS-based turbulence models have been used for wind turbine applications, such as the SST model, $k - \epsilon$ model and Spalart-Allmaras model, etc [98]. In this doctoral project, the $k - \omega$ SST model is found to be most successful for both 2D aerofoil and 3D blade CFD modelling and therefore selected as the turbulence model.

The CFD modelling of both horizontal axis and vertical axis wind turbines has been the subject of a few research, and those studies have shown that all RANS-based turbulence models are unable to effectively describe the stopped flow at a high angle of attack. Use of more complicated turbulence modelling approaches, such as (i) LES (large eddy simulations), which retains large eddies and ignores small eddies in the process of solving Navier-Sokes equations; and (ii) DES (detached eddy simulations), a hybrid method combining the Reynolds Averaged Navier-Stokes) (RANS) and the Large Eddy Simulations (LES), are both potential solutions to this problem. These approaches retain large eddies and ignore small eddies in the process However, both LES and DES are significantly more difficult to compute than the RANS is because they call for far finer computational meshes and the computations need to be carried out with transient analysis. This results in a significantly higher computational cost.

Because of the great accuracy it offers, CFD has seen widespread use in the field of wind turbine wake modelling. Using CFD methods coupled with the RANS turbulence model, certain wind turbine aerodynamics and aeroelasticity have been examined, and the results have shown a good agreement with experimental data. AbdelSalam and Ramalingam [1] used the CFD approach to study the wake characteristics in the near and distant wake areas of the wind turbine blades. They compared the findings of their study to both actual data and an actuator disc model. When compared to the results from the actuator disc model, the CFD model's results demonstrated a higher level of agreement with the experimental data.

Studies have been done to construct hybrid models by combining computational fluid dynamics (CFD) with more straightforward aerodynamic models. Esfahanian et al. [54] came up with a hybrid computational fluid dynamics (CFD) and boundary element modelling (BEM) model to forecast the aerodynamic performance of wind turbine

blades. In their hybrid model, 2D aerodynamic coefficients of a series of span-wise sections of the blades are calculated by the CFD approach while the BEM approach was used to simulate the 3D flow field through the wind turbine blade using potential flow. The hybrid model was able to accurately predict the wind turbine blade's performance. It was proved that the hybrid model could maintain the desired level of accuracy while being significantly quicker than the standard CFD model. By combining an unstable CFD model with a prescribed wake model, Suzuki et al. [160] were able to construct a hybrid CFD/vortex model that could replicate the aerodynamics of wind turbines when seen from yaw angles. When the findings were compared to experimental data as well as a free wake model, it became clear that the hybrid CFD/vortex model offered more accurate predictions than the free wake model did, particularly at low yaw angles. For the purpose of wake modelling of a wind turbine, Sturge et al. [159] introduced a hybrid method that combines the actuator disc and whole rotor CFD. The hybrid method demonstrated more speedy and accurate computations than using either method on its own.

The computational fluid dynamics (CFD) modelling of the aeroelastic behaviour of wind turbine blades as well as the complete turbine has been performed, with encouraging findings and a better knowledge of the flow field around the deformed blades and the turbine as a consequence. Because of its effectiveness, carrying out a full-scale computational fluid dynamics simulation remains the primary barrier to its practical uses in aeroelastic modelling.

2.1.2 Structural Modelling

In previous section, aerodynamic modelling approaches of wind turbines have been carefully reviewed, here the other part of Fluid-Structure Interaction, the structural modelling is presented. In order to carry out aeroelastic modelling of wind turbine blades, it is necessary to incorporate a structural model, the purpose of which is to calculate the dynamic structural response of the blades. The three-dimensional Finite Element Method (FEM) model and the one-dimensional equivalent beam model are the two types of structural models that may be utilised in aeroelastic modelling of wind turbine blades. Wind turbine composite blades are discretised in the 3D FEM model by either employing 2D shell elements or 3D beam elements, both of which are able to describe composite layer properties across the shell thickness. In the aeroelastic modelling of wind turbine blades, there are typically three types of discretisation methods that are used. These methods are the modal approach, the MBD (multi-body dynamics), and the 1D

FEM method. Each of these methods is used to discretise the blade into a series of 1D beam elements for the 1D equivalent beam model.

2.1.2.1 Beam Model

Wind turbine blades are elongated constructions that are only a few hundred millimetres thick and have one of their dimensions that is much greater than the other two dimensions. Beam models allow for an effective modelling of the aforementioned types of structures. The axis of the beam is supposed to be along the biggest dimension, and in order to achieve a higher level of precision in the simulation, a cross-section that is perpendicular to the beam's axis can be assumed to fluctuate over the length of the beam. An example of a beam model of wind turbine blades is presented in Figure 2.4, whereas a HAWT blade is modelled as seven elements with individual cross-section properties.

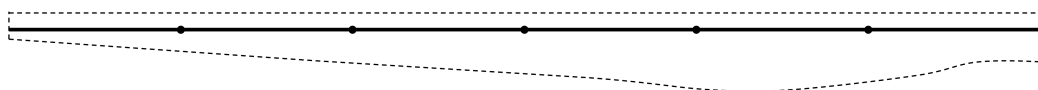


Figure 2.4: An examples of a beam model of Horizontal Axis wind turbine blades, different segments indicate different beam elements.

Both the Euler-Bernoulli beam model and the Timoshenko beam model are examples of linear beam models that are utilised often. Slender beams that are exposed to extensional, torsional, and bending stresses are what the Euler-Bernoulli beam model is concerned with. This model is also known as the classical beam model. The shear deformation effects, on the other hand, are not accounted for in the model. During the early part of the 20th century, Timoshenko [168] devised an alternate model of a beam. Because it takes into account shear deformation as well as rotational bending effects, this model is more suited than the Euler-Bernoulli beam model to describe the behaviour of thick and short beams. There is not much of a difference between the Euler-Bernoulli beam model and the Timoshenko beam model in terms of the fundamental geometry of the wind turbine blades, which have a construction that is long and narrow but not very thick. The Euler-Bernoulli beam model has been utilised in the majority of structural models for the purpose of aeroelastic modelling of wind turbine blades due to the ease with which it can be implemented. These beam models contain the assumption of modest deflections, which is incorrect for a particularly flexible blade design because such blades frequently suffer substantial deflections. These beam models contain the assumption that minimal deflections will occur. A nonlinear beam model that takes into consideration the geometric nonlinearities generated by big deflections is required in

order to handle handling huge deflections. The geometrically exact beam theory (also known as GEBT) is a good illustration of this concept. In this theory, the deformed beam geometry (that is, the displacements and rotations of the beam reference line) is represented in an accurate manner.

Compared to the 3D FEM, the 1D beam model is much computationally efficient, saving much computation time but with sacrificing of providing satisfactory accurate results without corrections. Therefore, the discretisation methods of the 1D beam model are essential. Three different types of methods are often implemented in the wind turbine blade aeroelastic modelling, i.e. the modal approach in which the deflection shape is described as a linear combination of a set of mode shapes, and the multi-body dynamics approach in which the blade is modelled into some bodies, which is connected flexibly or rigidly.

The Finite Element method involves breaking up the structure of interest, which in this example is a wind turbine blade, into a number of smaller components that are also called finite elements. As a result of this, the issue is handled on a more local level (at each finite element), which allows for the determination of engineering parameters like stress and displacement. In order to conduct an analysis of the complete structure, the equations that are used to regulate the finite elements that make up the structure are included into a more extensive system of equations. The approach has the benefit of less limits for the type of configuration to analyse, such as geometrical and material non-linearity, making the Finite Element method being popularly utilised in structural modelling [6]. This makes it possible to build a turbine blade that has undergone a more complicated deformation [77]. The huge number of degrees of freedom associated with this model, however, results in heavy demands on computer resources. The Finite Element approach has been frequently employed since it just requires a limited amount of data, such as the mass and stiffness distribution of the blades, and yet it may still provide a relatively realistic model. In order to correctly set up the models using the modal approach and the Multi-Body Dynamics (MBD) methodologies, precise data and an in-depth familiarity with the structure of the blade are required, as will be demonstrated in the following paragraphs.

The dynamic qualities of a structure can be described using the modal method, which involves developing a model using the structure's presumed mode shapes, often calculated prior to the actual Fluid-Structure Interaction simulation [6]. The number of assumed mode forms, as well as the accuracy of those shapes, are directly related to the precision of this technique. When doing an analysis of wind turbines, it is common practise to make use of the modes with the lowest eigenvalues, such as the first and second

flap-wise modes and the edgewise mode. The model offers a method of modelling that is both efficient and reliable [77]. The model is restricted to a certain amount of degrees of freedom and operates on the assumption that it is linear. It is possible to represent known blades using this model since the structural characteristics of such blades are already obtained before the actual simulation. When there is a lack of experimental data, it is difficult to collect precise modal data, which makes this model inappropriate for modelling structures when the composition of the structure is unknown. This makes it difficult to obtain reliable modal data. When examining the structure from a flap-wise and edgewise perspective, concentrating on the first and second modes ignores the torsional modes that are present in the structure. Because the oscillating angle of attack values of the blade during operation modify the pressure field surrounding the blade, the torsional stiffness of a blade construction is critical. This, in turn, has an effect on the way the blade deflects.

The Multi-Body Dynamics method, on the other hand, reduces the complexity of a structure by breaking it down into discrete pieces that may either be stiff or flexible [44]. The many kinematic restrictions that are used to integrate the various components into the overall configuration are what allow the bodies to be attached to one another. The model is, in fact, a blend of the best qualities associated with both the FE technique and the model approach. The model needs fewer sets of equations of motion, and it takes into account the effects of nonlinearity [124]. However, the setup of the model is difficult since each subassembly of the model needs to be described by an appropriate MBD representation. This makes the configuration of the model a laborious process. In order to assist in solving this problem, Hansen et al. suggested using software that deals with symbolic mathematics.

2.1.2.2 3D FEM Model

Wind turbine composite blades can be produced in the 3D FEM model by making use of either 3D beam elements or 2D shell elements with corrections. These components are able to describe composite layer properties across the shell thickness. In addition, the blades of wind turbines are constructed up of many plies, each of which is a composite mat that is arranged at a different angle. This results in a construction that is extremely complex. It is difficult to get a desirable outcome when working with composite materials because of their inherent nature and the complexity of blade topologies; as a consequence, this factor is typically overlooked in favour of employing features that are equal in nature. Some analysis models have been implemented, such as the Classical Lamination Theory, 2D/3D FEM model to get the ply-wise properties of the wind turbine blades.

An example of a 3D FEM model of wind turbine composite blades is illustrated in Figure 2.5.

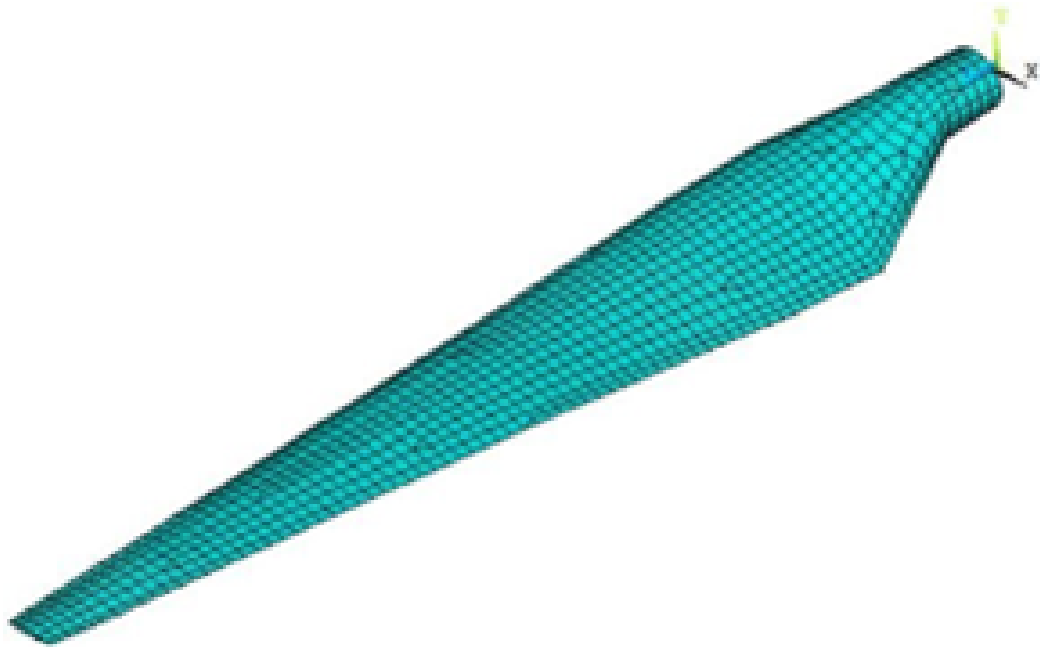


Figure 2.5: An example of a 3D FEM model of a wind turbine composite blade.

Due to the complex aerodynamic shape and structural layout of a wind turbine composite blade, generating a 3D FEM model of the blade using general-purpose commercial finite-element packages, such as ANSYS, is tedious and time-consuming. By connecting it with an aerodynamic model, it has been used in the aeroelastic modelling of wind turbine blades. It is an outstanding tool for evaluating the precise stress distributions within a blade, and it has been used to the modelling of wind turbine blades. In order to do aeroelastic modelling of wind turbine blades, 3D FEM is combined with CFD. For each time step, the aerodynamic loads need to be computed at each segmented position on the blade so that they may be utilised as input to the structural solver [99]. The aeroelastic modelling based on coupled 3D FEM and CFD can provide accurate results, but it is computationally expensive. Several attempts have been proposed to increase the efficiency of the simulation while maintaining the accuracy. One way to save computational cost is to construct a reduced order model (ROM) of the aeroelastic system either using CFD solution snapshots or eigenvalues. The ROM makes an effort to make the problem more manageable by isolating the fundamental modes of the fluid system and/or the coupled system. This is done on the basis of an examination of the contribution that these significant modes make to the problem. The number of degrees of

freedom that must be kept has been drastically cut, which has resulted in a decrease in the computational cost.

Whether taking the aforementioned methods into consideration, it might be difficult to identify when it is more appropriate to employ a complex FE model for wind turbine blade analysis as opposed to a straightforward one-dimensional beam model. There are no clear advantages or disadvantages of these methodologies on the others. A variety of considerations should be taken into account before settling on whether or not to employ a simplified beam model or a full shell model. Hansen et al. [77], Sørensen et al. [162], Glaubert [68] and Hansen et al. [78] have proposed some discussion regarding model definitions and implementations of both the structural theories and the BEM theory for simplified cases. For instance, in many different FEA/CFD-related fields, the determining factors are frequently the available computer capacity and the estimated time required to complete the issue. Massive distributed memory devices may be available to academic researchers, but they are probably definitely not available to practitioners working in industry. Regarding the amount of processing power required and the length of time required to find a solution, beam models are quite efficient. This allows for the analysis of a large number of completely dynamic models in a short period of time. This is especially important for estimating the effects of turbulence on power output and determining the fatigue stress that will be applied to wind turbine blades. When it comes to the resources needed and the complexity of the modelling, shell models are sometimes 10-100 times more demanding than other forms. For instance, generating accurate pressure distributions along a blade at various separations from the root requires the use of a shell element model, which is a highly time-consuming procedure. These models are more suited for determining how the average wind speed affects blade deflection and for providing typical stress and strain distributions that help identify areas that are under extreme stress. These models also include common stress and strain distributions. Geometrical properties, which are necessary for dynamic models, may also be derived from shell models. The second application of shell models is here.

2.2 Fluid-Structure Interaction Modelling Methods

The majority of the aeroelastic methodologies are based on the Arbitrary Lagrangian – Eulerian (ALE) formulation of the equations for the motion of the fluid and a description of the motion of the structure when dealing with the transient aeroelastic problem [51, 164]. This formulation includes the equations for the motion of the fluid. Reconstructing the governing equations in a reference frame that is related to the motion of

the mesh is how the ALE theory achieves its goal of providing a solution to a fluid issue that occurs on a moving mesh. Because of the mesh motion, research on the movement of the mesh that takes into consideration the changing cell elements and flux is required. The ALE method can be replaced with one in which the grid is maintained in its original position within an Eulerian reference frame and the fluid-structure interface is the sole variable that is moved. This necessitates the use of a method, such as the immersed boundary approach, that can apply the interface boundary conditions to arbitrary interface locations.

There have been many different types of structural models developed and implemented. These models range in degree of complexity from straightforward model descriptions to intricate finite element models. The degree of faithfulness that may be achieved is proportional to the geometric complexity as well as the degree of linear structural response [5]. In the case of compressible flow, the aerodynamic loads can be classified using either a linear model or a nonlinear model. The Euler equations require the use of the nonlinear model. This portion of the study is devoted to discussing the most important technical components of the fluid-structure simulations. Specifically, this section discusses mesh movement techniques, time advancement schemes, and fluid-structure interface procedures.

2.2.1 Mesh movement

In the fluid-structure interaction problem, the equations for the fluid motion requires a scheme for the moving fluid mesh nodes in fluid-structure interaction problems as the domain boundaries deform as well as translate and rotate. Currently, most of the well-accepted approaches of mesh movement are categorised into three groups: (i) the spring approach, (ii) the elastic mesh approach, and (iii) re-meshing [25].

The spring analogy technique involves modelling the mesh as a structural system that is represented by some combination of linear and/or torsional springs. This may be done in a number of different ways. In order to find a solution to the Euler equations describing a stiff pitching aerofoil, Batina used a method called the linear spring method [22]. The linear spring approach treats the element or control volume edges as springs with a stiffness that is inversely proportional to the edge length. This ensures that the method produces accurate results. Whenever there is a requirement to relocate the mesh, the equation for static equilibrium provides a solution for the grid point displacements. Figure 2.5 illustrates the cantilevered, rectangular, flexible hydrofoil that was modelled in the research carried out by Caverly et al [37]. They assumed that the

hydrofoil would have a chordwise stiff behaviour while allowing for spanwise bending and torsional flexibilities. The linear spring analogy stops the edges from collapsing, but it doesn't stop the collapse of elements or the crossing of grid lines. In order to address this condition, Farhat et al. [10] inserted torsional springs (in addition to the linear springs) to the grid nodes. This demonstrated enhanced resilience in comparison to the linear spring approach on numerous different two-dimensional model problems. In order to improve the computing efficiency of their work, Murayama et al. widened the application of the torsional spring technique to all three dimensions and updated the implementation. Murayama and colleagues [130] incorporated heuristic near-surface functions that boost the spring stiffness to infinity near a solid surface. This was done so that the robustness of the model could be preserved. Bartels [21] offered a modification to the linear spring analogy in order to avoid the scenario in which the grid would collapse over convex surfaces. He demonstrated the enhanced technique by running a simulation of the actuation of a spoiler in two dimensions. As the first phase in the process of initialising the algebraic mesh, it employs a transfinite interpolation, and then proceeds to the spring-based smoothing operation. However, it is unable to utilise structured meshes in any of its designs. The spring analogy was made more accurate by Lohner and Yang [120], thanks to the utilisation of Laplacian smoothing, which included varying diffusivity dependent on the distance from the surface.

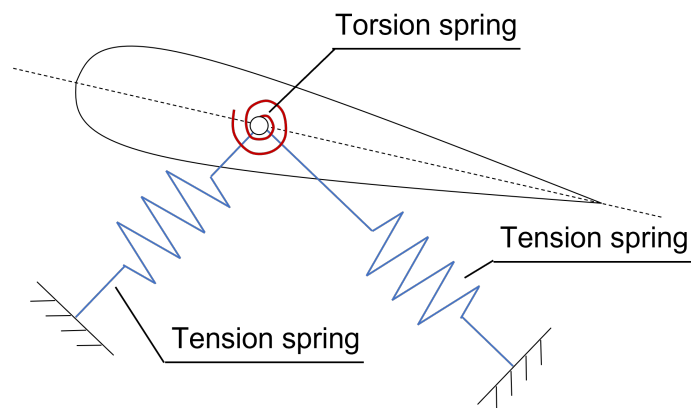


Figure 2.6: An example of the flow-induced vibration modelling using tension (blue) and torsion (red) springs.

A more developed version of the spring approach is represented by the elastic mesh analogy, which is believed that the grid is contained within a single continuous elastostatic body [19]. In order to define the grid deformation scheme, the compressive and shear moduli of the element, as well as the numerical approach that was used to solve

the elastostatic equilibrium equations, are required. In order to solve the linear elastic equilibrium equations, Johnson and Tezduyar [89] utilised a method known as the finite element approach. By scaling the permitted mesh deformation based on the element volume, the deformation of tiny mesh elements that are close to the body may be maintained to a minimum. This strategy is frequently utilised in a number of different examples of stiff, two-dimensional aerofoil oscillation. In aeroelastic simulations, a Reynolds number of 1000 for the chord is considered to be rather low. When dealing with issues involving significant mesh movements and the grid quality is insufficient to allow further calculation, it is unavoidable to resort to remeshing, which reduces the effectiveness of the application of this comparison. The majority of the dynamic mesh procedure has been applied to much more complicated cases of fluid-structure interaction, such as the simulation of flow past an NREL 34m HAWT and the simulation of a large number of spheres falling through a viscous medium. Both of these examples are examples of problems that have been solved by applying the dynamic mesh procedure. In order to prevent the need for additional re-meshing, it is vital to first produce a mesh that is at least somewhat adequate for the complicated challenges at hand.

Esfahanian and colleagues [54] come to the conclusion that when dealing with linear elastic static equilibrium equations, a linear boundary element approach may be able to provide a solution that is more time and effort efficient. The boundary element approach not only allows for the movement of the mesh for global grid types, but it also offers the interpolation matrix for the interface between the fluid and the structure. An NREL wing that has been deformed serves as a demonstration platform for the mesh movement capabilities.

In the area of aerodynamic form optimization, Nielsen and Anderson [132] used the linear elastic analogue in their analysis. Their research shows that the stiffness of the mesh material is dependent on the cell aspect ratio; however, the near-body mesh does not alter nearly as much as the cells that are further away from the object of interest. The numerical approach for solving the pseudo-structural grid system is not, however, one of the provided components. The quality of the mesh has been enhanced for a number of situations involving two-dimensional aerofoils. The deformation of a wing is given as a problem in three dimensions; the mesh motion needed to be accomplished in this case required 10 separate stages of incremental progress.

When the mesh deformations are too big, the linear elastic pseudo-structural analogy is unable to give satisfiable meshes since it is based on linear elasticity. The researchers Bar-Yoseph and colleagues [17] present a solution to this problem by taking into consideration the nonlinearities of the material characteristics and making use of

a nonlinear stress-strain relation. The local element quality is a scalar quantity that gives a measure of the mesh distortion, and the attributes of the grid are dependent on this quality in order to function properly. A finite element approach is used to solve the pseudo-structural equations that were generated as a consequence. There are several examples showing the movement of the mesh, but the grids look too coarse, and the presentation isn't very convincing. Gao et al. In addition, Gao [65] applies a nonlinear structural media analogy, but she the author uses a nonlinear boundary element approach to solve the equations that are generated as a consequence. By working through an optimization issue, one may discover the nonlinear stress-strain relation's parameters and how they work. Robustness and grid quality are proven for an aerofoil pitch issue that was solved progressively in five-degree intervals. The problem has a pitch angle of twenty degrees. The authors' remarks and the lack of measures of the computing cost both hint that the approach may be costly for dynamic mesh applications. The solution to the linear BEM issue looks to be substantially simpler than the solution to the nonlinear BEM problem, which appears to be significantly more difficult [43].

To remesh the volume mesh is an option that may be used in place of the spring approach. Instead of relying on any kind of structural analogy, it updates the mesh whenever the boundary moves depending on the required boundary motion and the geometry of the issue, as illustrated in Figure 2.7. This is done in order to ensure that the mesh is accurate. An algebraic re-meshing approach was used by Morton et al. for structured, overset meshes [129]. This scheme preserves grid line orthogonality near a surface and also maintains the grid point position in the grid overlap areas. One example that demonstrates this method is an issue with a circular cylinder that is elastically attached and freely vibrates. Melville [127] created a method for moving the mesh that was dependent on the closeness of a grid point to other surfaces in the immediate area. Without making any reference to the underlying grid structure or connection, the movement of the surface point has an immediate and direct impact on the inner grid point. The approach makes use of a few different heuristics in order to determine the impact that the surface motions have on the movement of the internal mesh points. On Euler [127] and Navier-Stokes [126] aeroelastic Fluid-Structure Interaction simulations of a fighter plane, it was effectively shown. Baker [15] moved the mesh with the use of a linear elastic structural analogy, and then he employed a technique that involved coarsening and enriching the mesh in order to keep the grid quality stable. Martineau and Georgala [123] have devised a two-step approach for moving mesh that first initialises the mesh based on a rigid-body motion procedure and then conducts a smoothing operation. This algorithm was created by Martineau and Georgala. This process appears to be laborious since it

requires keeping tabs on the distance between each mesh point and element and the two surfaces that are physically closest to them. Complex geometries and substantial deformations frequently necessitate at least periodic remeshing.

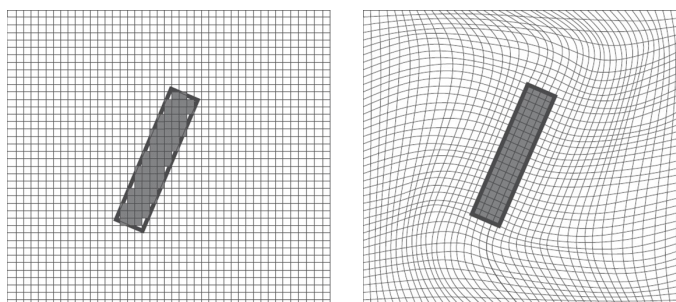


Figure 2.7: Illustration of the proposed two methods to represent a computational domain. (left) The computational domain using a static mesh with updated grid cells; (right) the computational domain using the deforming mesh approach.

There have been some published studies of the resilience of different mesh movement techniques, but these comparisons are in no way complete [57]. It is commonly accepted that the linear spring analogy cannot be used to any issue type other than inviscid situations with very tiny mesh motions. Even while the torsion spring enhancement results in increased resilience, it will still only produce meshes of a low quality for deflections that are sufficiently significant. When compared to linear spring analogies, the linear elastic mesh technique often demonstrates a significant improvement. When compared to the torsional/linear spring method, however, this methodology demonstrates a less apparent but still detectable gain. The resilience for large rigid body movements is further improved by the incorporation of varied linear elastic material characteristics. Nonlinear modelling of the grid pseudo-structure has the potential to enable bigger mesh deflections; however, the increase in computing cost that results from this potential benefit is not indicated.

The majority of the many ways for moving the mesh can be used on either structured or unstructured element types. Two approaches that were suggested by Bartels [21] and Morton [129] are an exception to this rule since they can only be used to structured grids. It is challenging to evaluate how easy it would be to parallelize the procedures. The spring techniques call for the solution of a big matrix system; parallel strategies are easily accessible for such a system. In order to solve elastostatic equilibrium equations or equations very comparable to them, one requires either a parallel finite element algorithm or something very similar to it. In principle, the BEM approaches may be simply parallelized by several users. The fact that grid displacements are dependent

on nothing more than a surface integral assessment is the primary reason why grid point connection information is not required. Extremely difficult algorithmic issues are presented by global parallel re-meshing, which focuses mostly on techniques that call for the monitoring of one's proximity to surrounding surfaces.

2.2.2 Time advancement schemes

Both one-way and two-way coupling are examples of coupling methods that are used for FSI modelling. These coupling approaches can be loosely divided into two distinct classes, one-way and two-way coupling methods. The aerodynamic loads are translated to the structural model as boundary conditions in a model with one-way coupling, and these conditions are employed to determine the model structural solutions. These deflections aren't consistent with the aerodynamic model at all. The load data are gathered independently by the aerodynamic model when a two-way coupling technique is taken. In the same manner that one-way coupling is mapped to the structural model's deflection, these loads are also mapped to it. After then, the deflection is transferred back to the aerodynamic model, and the coupling iteration is carried out one again and again until the desired result convergence is reached. The two-way coupling model generated the most accurate findings thanks to good model synchronisation, in contrast to the one-way coupling model, which produced only approximate results. The two-way coupling strategy was chosen as the coupling method of FSI modelling for this project because it provides the highest level of both computational accuracy and stability.

The two-way coupling FSI codes may be further categorised roughly based on the manner in which the data is exchanged between the disciplines that are involved as well as the frequency of the transfers. The monolithic approach, the fully coupled approach, and the loosely coupled approach are the three categories of methodologies that may be used to advance an accurate fluid-structure simulation ahead in time [136].

The fluid and structural equations of motion are treated as a single equation set and solved using a unified solver in the monolithic technique for aeroelasticity problems [26, 129, 128, 16], as depicted in Figure 2.8. The only thing that differentiates a structural element from a fluid element or control volume is the difference in the variables and the spatial representation scheme for each type of element when it comes to coding. This is how the structural element is distinguished from the other two types of elements. When carrying out a computation using a monolithic technique, the system maintains totally consistent coupling. This means that the fluid and the structure are properly synchronised even if only one time step is being taken. In most cases, this results in increased

resilience and stability as well as more considerable time steps [66].

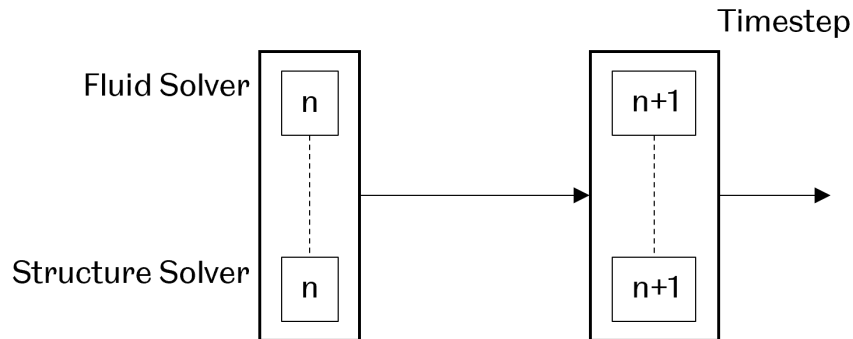


Figure 2.8: Schematic demonstration of the monolithic FSI approach.

The fully coupled strategy synchronises the fluid and structural systems at each time step like the partially coupled approach does, but it utilises a partitioned scheme. The fluid and structure code modules are kept distinct in a partitioned coupled method. However, fluid loads and structural displacements are exchanged back and forth inside the same time step. Both the fluid and the structural systems have their own unique solvers, which means that each solution may be optimised for its particular application. Sub-iterations continue to iterate within the framework of the fully linked method until the entire FSI system has fully converged. The fully connected technique keeps the synchronisation quality of the monolithic scheme while also providing the benefits of a partitioned scheme, which include being simple to code and adaptable to a variety of system configurations.

Due to the fact that it is a partitioned method, the loosely coupled approach is somewhat comparable to the fully coupled approach. On the other hand, the fluid-structure system is not iterated to full convergence at each and every time step that is taken. Instead, the fluid system and the structural system only communicate their data once, or maybe twice, throughout a time step. The updates to the fluid and structural solutions are delayed, also known as staggered, which results in a lower computing cost per time step in comparison to a method that is fully linked. Because the two systems never fully converge, there is an extra error that is introduced on top of the truncation error that is caused by the fluid and structure integration procedures. When building a system that is loosely connected, accuracy and stability are both important factors that need to be addressed [19].

The study carried out by Yu and Kwon[186], in which they coupled a three-dimensional Navier-Stokes codeFSI simulation with a flap-lag-torsion beam model of a wind turbine blade, is an illustration of a complete coupled technique. The approach was applied to

the rotor of the NREL 5MW reference wind turbine while it was operating in steady axial flow circumstances. The findings of this comparison included the mean rotor loads as well as the static blade deformation. After that, the effects of the gravitational pull as well as the unstable aerodynamic loads and dynamic responses of the blades brought on by rotor shaft tilt and interference with the tower are looked at. The Navier-Stokes equations were solved using an implicit temporal approach of the second order with multigrid acceleration. A separate solver was utilised in order to advance the equations. At the conclusion of each cycle of pseudo-time, information was transferred between the two domains, and at each step of physical time, the system as a whole reached a point of full convergence. Weeratunga and Pramono [176] utilised an approach that was quite similar to it, but they employed the 3D Euler equations and a beam/shell finite element model to represent the structure. Instead of mandating complete convergence, several sub-iterations were used for each physical time step that was taken. It was demonstrated that using a fully coupled approach can result in savings in computational cost that are more than three times greater than those seen when using a standard loosely coupled approach. This is primarily due to the fact that the fully coupled approach allows for a larger allowable time step. Cebal and Lohner [38] examined an under relaxed predictor/corrector system that iterates on fluid-structure solutions, passing under relaxed fluid loads and structure displacements and velocities between the solvers.

Farhat et al. have analysed the accuracy of loosely coupled approaches [141, 110, 104, 58, 140, 10]. As can be seen in Figure 2.92.9, the first step of the Conventional Serial Staggered (CSS) scheme is a structural predictor step. This is then followed by a fluid mesh movement and fluid solve, and finally by a structural update.

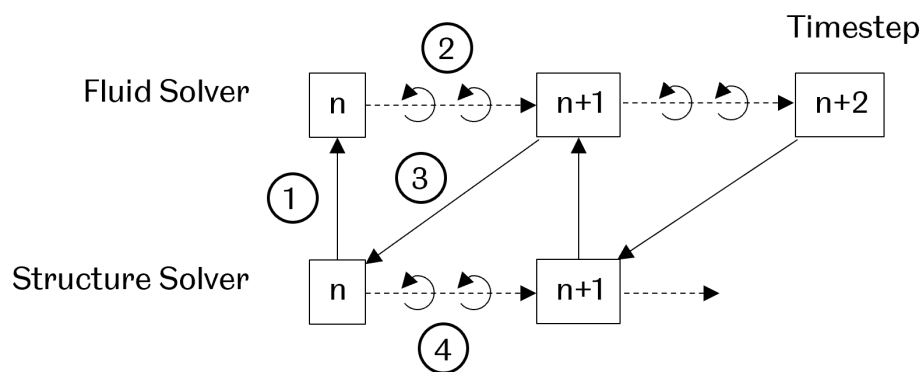


Figure 2.9: Schematic demonstration of the conventional serial staggered (CSS) scheme.

The Conventional Parallel Staggered (CPS) technique does not include any stages that act as predictors or correctors, which means that the fluid and structural solvers are

executed simultaneously, as seen in Figure 2.10. The CPS method offers the benefit of making coupling on parallel computers easier, but this comes at the sacrifice of accuracy and numerical stability. It is also noted by Piperno and coworkers [141] that the time step required for accurate resolution of fluid phenomena is often lower than what is required for the structure in circumstances involving aeroelasticity. The study authors highlight this fact. This is because the structural frequency of flutter and other dynamic aeroelastic modes is often low. It's feasible that a cheaper answer can be found by sub-cycling the fluid solver inside a single structural time step. It is crucial to ensure that the average fluid loads are appropriately computed when transferring the loads from the sub-cycle solutions to the structure in a way that maintains numerical stability.

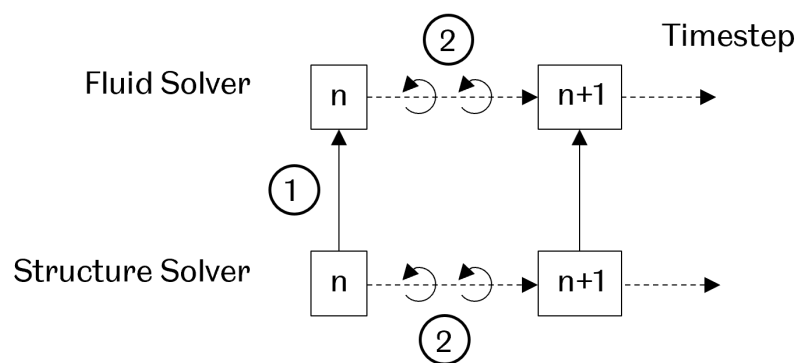


Figure 2.10: Schematic of the conventional Parallel staggered (CPS) scheme.

Figures 2.11 [110] and 2.12 [58] exhibit two updated versions of the loose coupling process: the Improved Serial Staggered (ISS) approach and the Improved Parallel Staggered (IPS) approach. The ISS method includes the addition of a non-trivial structural displacement predictor step. This step is built in such a way that the fluid state and the structure state are one-half time step out of phase with each other.

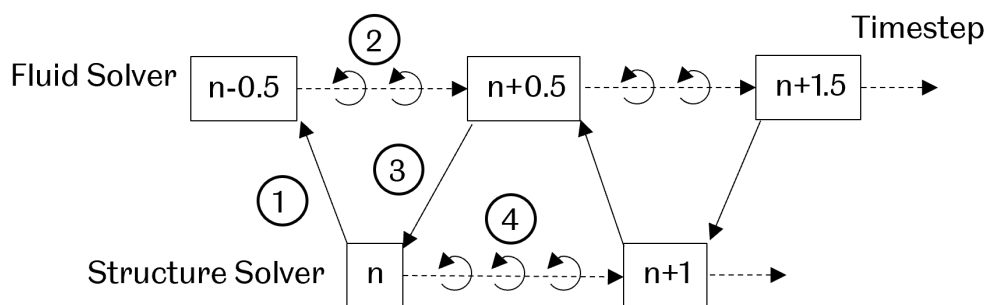


Figure 2.11: Schematic demonstration of the conventional Improved Serial Staggered (ISS) scheme.

Following the transmission of the fluid loads to the structural solver at the one-half time step, the IPS method makes use of the revised structural displacements to pass to the fluid solver to the next full-time step (this is done in parallel with a new structural update). For the purpose of a wing flutter prediction validation scenario, the performance of the upgraded techniques is evaluated and compared to that of the CSS and CPS approaches [58]. Because of the new processes, it is now possible to couple data at a time step that is 20–46 times bigger than the time steps that were previously employed without experiencing any loss of accuracy. For some issues, the ISS algorithm is able to make use of a longer time step that is many times greater than what is possible with the IPS approach.

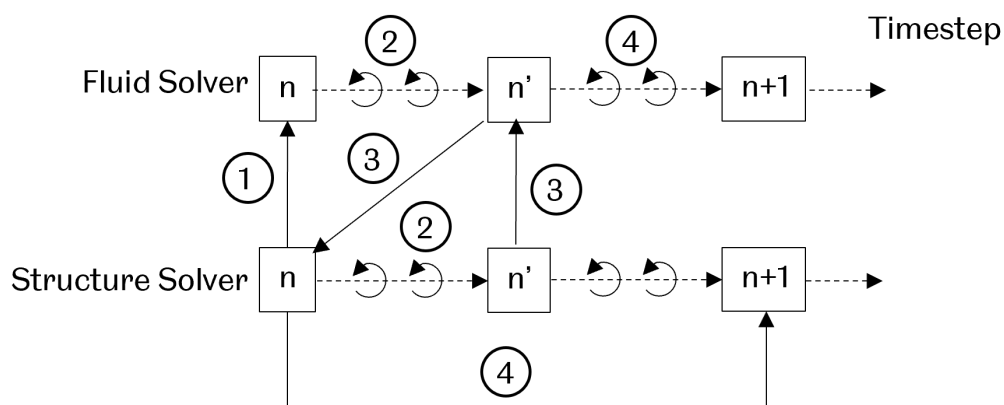


Figure 2.12: Schematic demonstration of the conventional Improved Parallel Staggered (IPS) scheme.

Koobus [104] reviewed on how important it is to respect the discrete form of the geometric conservation rule in order to keep temporal precision and stability. In order to demonstrate compliance with the discrete geometric conservation law, an evaluation of the fluxes at certain intermediate mesh configurations must be performed between time level n and time level $n+1$. In general, a scheme that complies with the geometric conservation law is superior than one that does not in terms of its accuracy and stability. Piperno [140] carried out an energy analysis on the fully coupled fluid-structure/moving mesh transient issue. The results of this research revealed the correctness of several staggered partitioned schemes in terms of the order of the inaccuracy in the energy conservation. While it is feasible to create CSS with a second and third order, the basic CSS scheme already achieves energy conservation at the first order. It has been demonstrated that the ISS method is third order energy saving. Because phenomena like flutter depend on their being a perfect balance in the energy transfer between the fluid and

the structure, energy conservation is an important aspect to consider when conducting aeroelastic stability assessments.

The harmonic balancing method is an entirely distinct strategy for computer modelling of dynamic aeroelastic events [166]. Using temporal Fourier transforms in conjunction with a steady state CFD solver, the fluid dynamic equations that control the system are solved by the harmonic balancing approach. A finite number of temporal frequencies, typically consisting of a fundamental frequency and multiple harmonics, are taken into consideration. When the driving frequency is unknown before beginning a flutter study, there are methods available for solving for the relevant frequency in order to determine it. Each frequency that is taken into consideration virtually necessitates the solution to a steady-state CFD problem, and the solution modes are connected in a non-linear way so that the entire solution may be constructed. To this point, the harmonic balancing fluid solver has only been connected to a basic pitch/plunge structural model of a two-dimensional aerofoil that consists of rigid bodies. It is difficult to imagine how this method could be extended to transient aeroelastic phenomena because the modal signature of the fluid response is broadband in nature. However, the method could be extended to three-dimensional problems if more detailed descriptions of the structural modes were used. The reaction of the control surface upon being actuated would be an illustration of this type of difficulty. However, the harmonic balance approach has the distinct advantage of not requiring the resolution of a transient solution before a periodic or quasi-periodic state is reached. This is in contrast to the time domain simulations, which require the resolution of a transient solution before a periodic or quasi-periodic state can be reached. This has the potential to result in huge savings when computing. Converting a CFD code that operates in the time domain into a solution that operates in the frequency domain will result in hefty code development expenditures.

2.2.3 Fluid-Structure Interface strategies

The most difficult aspect of the code-coupling problem for fluid and structural analysis programmes is the proper management of the interface region. The interface boundary conditions state that the surface stress must be in equilibrium between the fluid and the structure, and that the local displacement of the surface will result in a corresponding local displacement of the fluid. In addition, the interface boundary conditions require that the surface stress be in equilibrium between the fluid and the structure. In order to satisfy further continuity constraints, the fluid surface grid needs to adhere to the fluid-structure interface, and the velocity of the fluid mesh at a location on the interface needs

to be equivalent to the velocity of the interface itself. Before attempting to execute a structural solution, the fluid stresses need to be transferred to the structural grid nodes in order to satisfy the requirements of the stress boundary condition. In order to satisfy the displacement boundary requirement, the ensuing structural displacements must be accompanied by a movement of the fluid mesh boundary at the interface.

There is a lack of cohesion in the literature about fluid-structure interface methods. On the one hand, there is a body of work that focuses on efficient and generic interpolation algorithms for the transfer of data between two surfaces that have different degrees of discretization. The focus of this discussion is on the resilience, precision, and efficiency of the interpolations in the presence of complex geometry and widely varying grids for fluids and structures. Then there is a more focused body of work that focuses on correctly and conservatively managing the interface between finite volume/finite element fluid codes and finite element structural codes. The third category of study focuses on the specifics of incorporating the methodologies into a computer program's source code. Since there is very little cross-referencing in this area of study, even in review papers, it is challenging to evaluate the relative merits of the various approaches. This is due in part to the fact that the application and the level of realism of the structural model are likely two factors that influence the interface technique that is most chosen. When compared to a comprehensive FE model with shell parts, a wing-box model could call for a quite different approach to the interface treatment. This review's objectives are to first identify some of the interface techniques that have been shown on issues in computational aeroelasticity to date and then to highlight some of the driving variables that go into the selection of an interface approach.

Almost all of the approaches used to analyse the interaction between fluid and structure employ interpolation. The fluid grid is then distorted to account for the displacements after the displacements are interpolated from the information of the structural grid to the fluid grid. From the fluid grid points to the structural grid points, fluid loads are interpolated. The performance of such a system will depend on a number of factors, including the interpolation technique's accuracy and durability as well as the grid densities close to the interface. There is a wide variety of potential interpolation methods, some of which are examined and evaluated in Smith et al. [155]. Using the underlying finite element representation of the displacements as a basis for interpolation is a method that is both straightforward and reliable, as demonstrated by research published by Cebra [39] and Farhat [57] and Farhat1998. In a similar manner, the representation of the fluid loads known as finite volume (or fluid discretisation) is utilised in order to interpolate the forces.

The necessity of energy and momentum conservation in the simulation has been reviewed by various researchers, for instance [11, 31]. The displacement of mesh points within fluid and structural solver can be calculated yields the following way,

$$\mathbf{u}_f = \mathbf{T}\mathbf{u}_s \quad (2.1)$$

where \mathbf{T} is the displacement transformation matrix obtained from the flexibility matrix of the structure and its interpolation onto the fluid mesh, \mathbf{u}_f and \mathbf{u}_s are fluid and structure mesh displacement, respectively. Let \mathbf{f}_f and \mathbf{f}_s be the loads from the structural and fluid solver respectively. The load transfer strategy that provides a conservative energy transfer between the two systems from the fluid mesh to the structural meshes must therefore take the following shape.:

$$\mathbf{f}_s = \mathbf{T}^T \mathbf{f}_f \quad (2.2)$$

A comprehensive derivation of comparable expressions is provided by Farhat et al. [57], which also contains a general discussion of the interpolation functions that are utilised. To achieve an accurate and conservative interpolation of loads and displacements, Guruswamy and Byun [73] make use of a technique known as virtual surface interpolation. Chen and Hill [43] provide an original method for defining conservative interpolation matrices using boundary element method. In their paper, the boundary element problem indicates the mesh misalignment of grid points in the CFD domain. The displacement of the grid points inside the CFD domain are recalculated by using the derived transformation matrix between the interface grid and inner grids.

The problem that has to be solved will determine how important it is to save energy at the interface between the fluid and the structure. For the best possible outcomes, a cautious approach is almost always necessary when dealing with issues that include a coarse fluid and/or structural grid. Additionally, the prediction of complicated dynamic aeroelastic phenomena like as flutter and limit cycle oscillations (LCO) could be sensitive to the conservation features of the numerical framework. It is important to prevent this situation because it might potentially generate false instabilities caused by an imbalance in the energy transfer that occurs between the fluid and the structure. Note, however, that effective solutions to issues in aeroelasticity have been found using non-conservative interpolation techniques [72] and systems aimed to conserve momentum, but not necessarily energy [39, 186].

The level of complexity in the structural model is connected to the selection of the appropriate mechanism for data transfer at the interface. Data transmission strategies for

aeroelastic issues are categorised by Guruswamy's review article according to the type of structural model that is used. These include beam elements, multi-body dynamics, plate and shell elements, and comprehensive finite element models of the complete structure. The fluid grid at the near-interface will still be fine enough to capture the intricacies of the flow field in that location, even if the structure is represented with a coarse enough resolution to cause issues. It is necessary to provide a method that is reliable for transferring displacements from the structural representation to the fluid grid. An illustration of this would be the modelling of a three-dimensional wing using two-dimensional plate parts aligned along the mean chord line. This problem is investigated in Brown's study [31], and examples of how interpolation methods perform in real-world scenarios are provided in Smith's article [155].

The implementation of data transfer mechanisms in a practical setting for broad geometric configurations is not an easy task. In Maman and Farhat, the authors provide information on the specifics of a parallel pre-processing software that anchors the fluid grid to the finite element structural grid [122]. Some algorithmic details for a similar methodology are given in Cebal and Lohner [39].

2.3 Reduced Order Modelling

Reduced order modelling are widespread and are of interest in a variety of contexts, such as the design of integrated circuits, electro-mechanical systems, chemical engineering, fluid dynamics, and aerodynamics, to name a few. Numerous investigations, both theoretical and practical in nature, have been carried out. It is possible to argue that the projection-based model reduction approach is the most current debate in the realm of theoretical research. It includes, the proper orthogonal decomposition (POD) method [27], reduced basis method [139, 86, 74], empirical methods such as Gramian method [23, 81], approximate balancing method [45], Volterra series [172], Harmonic balance method [14], and the balanced truncation method [71, 125]. In this review, Volterra Series and Harmonic Balance approaches is selected and compared to the proper orthogonal decomposition method, which is the point of interest of this project.

The basic premise of Volterra series is that a large class of nonlinear systems can be modelled as a sum of multidimensional convolution integrals of increasing order [172]. The Volterra theory was first proposed and applied in electrical engineering and was then utilised to model non-Gaussian fluid loadings and mechanical nonlinearities as well as fluid-structure interactions [148]. Wu and Kareem [179] have studied the prospect of Volterra approach in modelling the Vortex-Induced Vibration problem. Recently, Liu, Li

and Xiang [115] have studied the unsteady aerodynamic behaviour of a flapping wing applying the Volterra theory. The Volterra-based ROM provides the possibility to catch the inherent nature of the nonlinearities and memory effects in fluid-structure interactions.

The introduction of the Harmonic Balance (HB) method into CFD was spurred on by the need to do design analysis for nonlinear, internal flow issues. In the most conventional sense, HB does not qualify as a reduced-order modelling approach. For nonlinear, time-periodic, and unstable situations, the computational savings, while not always large, can be significant. In addition, the reliability of the outcomes contributes to the method's allure as a very desirable choice. For a good number of years, the Harmonic Balance approach has been utilised as a technique for analysing the performance of harmonic ODEs. The method involves assuming a solution in the form of a truncated Fourier series with a preset number of harmonics, substituting the assumed solution into the ODE, and algebraically manipulating the results in order to gather terms with a similar frequency. Any terms that were generated and had a frequency that did not appear in the Fourier series were removed. After that, each harmonic is brought into harmony by imposing the condition that the frequency terms on both sides of the equation must independently meet the equality condition. After balancing, you will have a set of linked algebraic equations that need to be solved so that you may determine the Fourier coefficients of the assumed solution.

This approach created has been employed by Baker et al. [14] to create reduced-order aerodynamic models. Rule et al. [146] have also looked into this approach. The core idea is that for a certain family of inputs or structural movements and the relevant aerodynamic outputs, balanced modes are in some ways an ideal descriptor within the context of POD modes.

2.3.1 Proper Orthogonal Decomposition

Given the difficulty of extracting eigenmodes for very high-dimensional systems, it is of great interest to note that a simpler modal approach is available, as developed by Romanowski [145]. Ballarin and Rozza [16] proposed a POD-Galerkin monolithic ROM for parametrised FSI problems. This approach adopts a methodology from the fields of nonlinear dynamics and signal processing.

In terms of their dependence on the governing equations, the reduced order models may be split into two categories: intrusive Reduced Order Modelling and non-intrusive Reduced Order Modelling. [62]. The non-intrusive ROM is independent to the original

physical system, Xiao, et al.[182] proposed a non-intrusive ROM for fluid-structure interactions by combining the ROM to the interpolation method, namely the radial basis function method. Because of its high level of computational precision and the direction provided by governing equations, the Intrusive ROM serves as the primary subject of this thesis. POD and Galerkin projection are two methods that are often used to produce intrusive ROM. Intrusive ROM is reliant on governing equations and source code. As a result of its invasive nature, it manages to preserve many of the physical qualities that were present in the original system. Two key issues in POD-Galerkin based ROM are stability [189, 149] and non-linearity efficiency [131].

2.3.1.1 Stability

One of the drawback of the Reduced Order Modelling, for instance, the POD-Galerkin ROM, is Stability. The ROM methods cannot predict stable and accurate solutions in cases of flows with high Reynolds numbers [61]. The application of a conventional Bubnov-Galerkin projection of equations onto the reduced order space is the root cause of the instabilities that are frequently seen when using the POD technique. These oscillations are what cause the solutions to become unstable. This phenomenon is very comparable to the Gibbs oscillations that emerge in FEM solutions when the conventional Bubnov-Galerkin approach is used. These oscillations are what cause the simulations to be unstable since they feed into the non-linear factors.

A number of other strategies have been discussed as potential solutions to the POD-Galerkin ROM method's inherent stability. A Petrov-Galerkin technique was given by Xiao and colleagues for the purpose of lower order modelling of the Navier-Stokes equations [181]. The proposed ROM approach enhanced the stability of ROM findings without requiring the tweaking of any parameters. The idea of the proposed model is adopted from the relationship between advection direction and the partial derivative of the solution, which is cosine rule in this case. A Petrov-Galerkin technique was given by Fang et al. for the solution of nonlinear hyperbolic issues as well as discontinuous Galerkin (DG) ROMs [56].

In order to remedy the instability that was present in the POD-Galerkin ROM modelling of strongly stiff systems, Feriedoun and Alireza [147] came up with a method of regularisation. Carlberg et al. [35] and Chu et al. [47] stabilised the solutions of the POD model by introducing a diffusion term into ROMs. This did not need any tuning or optimising on the part of the researchers. By making use of numerical dissipation, Aubry et al. [13] were able to achieve their goal of stabilising the POD-Galerkin ROM approximation to the Navier-Stokes equations. In a later study, Sirisup and Karniadakis [152]

developed a spectral viscosity diffusion convolution operator-based dissipative model in order to manage the stability of the POD solutions' behaviour over the long run. In order to stabilise the reduced order model for unstable fluid flows, Sirisup and Karniadakis [153] offered a POD-penalty technique as a potential solution. An technique known as shift-mode correction was presented by Noack et al [133].

The selection of the inner product that will be utilised to define the Galerkin projection is also connected to the numerical stability of the problem. Iollo and Kalashinkova [85, 96] came up with the idea of a stable, symmetrical inner product that provides specific stability constraints for the linearized compressible Euler equations. They proposed two methods for stabilising POD ROM: the first method relies on the explicit addition of an added dissipation term adopted from the Lax-Wendroff scheme, and the second method consists of constructing the POD for both the function values and the gradient values. Both of these methods are described in further detail below. Both of these methods have been shown to be effective (POD in H1). In order to increase the stability of the POD-Galerkin ROM models of strongly-stiff systems, Feriedoun and Alireza [147] discovered an additional sort of regularisation approach. In this technique, the Helmholtz filtered equivalents of the POD eigenmodes of the non-linear components are used in place of the POD eigenmodes. In order to ensure that the ROM would remain stable, Bond and Daniel [29] made use of a number of linear restrictions for the projection matrix.

2.3.1.2 Non-linearity

When using reduced order modelling, another problem that occurs is the inefficiency of the non-linearity reduction. The POD approach and the Galerkin method are typically utilised in order to determine the ROM. Due to the fact that the original Galerkin approach is restricted to linear variables, it cannot be used to solve issues involving fluid-structure interaction. The nonlinear term still depends on the entire system in its original form after projection onto the smaller region. In this case, the large dimensionality of the whole physical systems governed by partial differential equations continues to determine the processing complexity of the simplified model (PDEs). This is due to the large dimensionality of the complete physical system regulated by PDEs. To address this issue, a variety of non-linear reduction techniques have been suggested [131, 182].

The discrete empirical interpolation technique (DEIM) is one of the strategies that may be used to address the reduction of the nonlinear components and to decrease the computational complexity of the POD method. Another approach that can be utilised is the discrete empirical interpolation technique (DEIT). This may be accomplished in

a variety of different ways. The empirical interpolation technique (EIM), which was introduced by Barrault et al., has a discrete offshoot known as the discrete empirical interpolation method (DEIM)[20]. in the context of reduced-basis model order reduction discretisation of nonlinear partial differential equations. DEIM is an example of reduced-basis model order reduction discretisation of nonlinear partial differential equations. It has been established that DEIM approaches may achieve a factor increase in CPU time that is between 10 and 100 times faster than the time required by the original non-reduced model. The amount of time that may be saved by using a reduced order model is related to the size of the model, and as a result, the number of DEIM points [190].

Barrault et al. [19] developed a technique for finding the ideal collection of sample points at the discrete level in relation to the employment of DEIM kinds of approaches. The initial stage in the approach is to choose the sampling components that minimise the difference between the reconstructed ROM coefficients and the corresponding coefficients (which are obtained by projecting the snapshots onto the reduced order subspace). The primary benefit of this method is that all the necessary information are directly obtained from mesh grids of the Finite Element solver. This results in a method that is highly useful for reconstructing non-smooth functions, such as the right-hand side of the system of equations that results from the formulation used in this article for the reduced order method for the incompressible Navier-Stokes equations.

Regarding the use of DEIM-style methods, Barrault et al. offered a method for selecting the most appropriate group of discrete-level sample sites to employ in their study. The algorithm consists of selecting the sampling components that provide the smallest gap between the recovered reduced basis coefficients and the optimum coefficients (which are obtained by projecting the snapshots onto the reduced order subspace). The fact that just the values at the nodes of the finite element mesh are needed for the DEIM method is the primary benefit of using it. This leads to a strategy that is very convenient for the reconstruction of non-smooth functions, such as the right-hand side of the system of equations that arises from the reduced order strategy for the incompressible Navier-Stokes equations with the formulation that is used in this article. The result of this is that the reduced order strategy for the incompressible Navier-Stokes equations is reduced to a form that is used herein.

The residual DEIM technique was published by Xiao et al. [180], and it is a hybrid approach that brings together the quadratic expansion method and the DEIM. It accomplishes this by first applying the quadratic expansion method on the non-linear terms and then using the DEIM methodology to resolve the residual that exists between the reduced order model and the complete model. This is how it works. That is to say, the

DEIM is what is utilised to absorb any faults that are still there after the quadratic expansion method has been used. Because of this approach, the technique can still accurately describe discrete quadratic non-linearities, in contrast to the DEIM, but it can also be used for extremely non-linear discrete systems, in contrast to the quadratic expansion approach. Moreover, the DEIM cannot do either of these things. When dealing with potentially extremely non-linearities that come from a ROM that uses a non-linear Petrov-Galerkin discretization, the residual DEIM approach is an excellent choice because of how well it fits the bill [55, 181].

Du et al. [52] suggested using quadratic expansion as a method for treating non-linear terms in PDEs. Due to the fact that this technique represents the non-linear term by expansions of precomputed matrices, it is well suited for the handling of discretized quadratic nonlinear operators. Importantly, given that these matrices have already been computed, it is possible to quickly translate them into sets of simplified equations.

The determination of POD modes is computationally very inexpensive, particularly in comparison to the determination of the eigenmodes of the original fluid dynamics model. This is due to the fact that the number of time steps and, consequently, the order of matrix required to compute a reasonable and useful set of POD modes is typically quite large. In the next part, it will be demonstrated that the outcomes achieved using POD modes are in very good agreement with the outcomes obtained using the full-order model as well as the ROM that is founded on eigenmodes. It is also important to note that in order to lower the order of the initial model, one can make use of the POD decomposition and then proceed to do an additional eigenmode analysis of the ROM. This is a method that may be helpful for specific applications and should be considered.

It is crucial to note that a comparable computation may be done in the frequency simulation. The methods assume simple harmonic solutions and calculate data at frequencies spanning the frequency range of interest for data at different time steps. Kim [101] has used the POD frequency domain method for a vortex lattice fluid model, and Hall et al. [76] and Thomas et al. [167] have done so for a Euler fluid model, including shock waves at transonic conditions. Recently, Halawa et al., [75] have applied this method to the surface pressure distribution of a wind turbine aerofoil with emphasis using three POD modes. However, the application in geometric compliant aeroelastic problems is still lacking further investigation.

Handling the non-linearities of the model's governing equations is one of the most challenging aspects of developing effective POD-based ROMs since it is one of the most important factors involved. Calculations of the non-linear components and an estimation of the Jacobian are necessary in iterative algorithms like the Newton method, which

are often utilised in the process of solving non-linear systems of equations. In order to do this, it is often necessary to project the estimated solution back to the initial domain and compute the nonlinear functional in the full-scale domain for each iteration of the algorithm. This is done to ensure that the solution is accurate. The expense of such full-scale non-linear functional computation as well as the forward-and-backward projections may significantly counterbalance the advantage that was realised as a result of the model reduction.

Several approaches have been suggested in order to treat non-linearities in an efficient way. Chaturantabut and Sorensen [41] introduced the Discrete Empirical Interpolation Method in order to treat non-linearities in POD-based ROMs governed by systems of time-dependent partial differential equations (PDE). Carlberg et al. [35] developed the Gauss-Newton with the Approximated Tensors (GNAT) method which also uses the POD in order to reduce the vector of unknowns. However, it operates in a fully discrete domain compared to the previous approach. Jiang and Durlofsky successfully applied the GNAT approach to complex simulations [88]. Rewienski and White developed a method called trajectory piecewise linearization (TPWL) [143] In this method, a number of the system's states and Jacobians are first calculated and saved, then new simulations are obtained as a result of linear expansions around previously saved states. This approach can also be applied in a reduced subspace such as the one obtained through POD. A combination of POD and TPWL (POD-TPWL) is now widely used in order to model sub-surface flows [100]. Trehan and Durlofsky [169] developed an extension of TPWL called trajectory piece-wise quadratic extension procedure (TPWQ) and combined it with POD (POD-TPWQ). For the detailed methodology, please refer to Chapters 3 and 4.

2.4 Current Applications of ROM for Wind Turbine Aeroelasticity Modelling

In this section, the ROM for the fluid-solid interaction problem is summarised and reviewed. Fluid-structure interaction is an interaction phenomenon between deformable or movable solid structures with a surrounding or internal fluid flow [34]. The FSI problem is significant in many fields of science and engineering., such as aerospace wing design [99], biology [28], turbomachinery [36], medicine [183] and especially, wind turbine. However, the computational cost for simulating FSI problems is intensive.

Reduced-order models, also known as ROMs, are primarily intended to do one thing: capture in a straightforward, dependable, and practical manner the in-depth knowledge of the physical behaviour of the flow field. Because of the characteristics of aerodynamic

flows, non-linear unstable partial differential equations are produced. In order to compute these equations, numerical techniques must be constructed on massively parallel supercomputers, which is a highly challenging endeavour. Therefore, there is a critical need for alternative useful tools that can compress the complex system of equations that was originally used into a simple model with fewer dimensions that can characterise the physical process and capture its behaviour with a reduced amount of computing effort. The calculation of a ROM might be accomplished via the use of either numerical simulations or experimental data that has been measured. These models have been utilised well in a variety of contexts, including the stable analysis and design of inviscid aerofoils, thermal chemical processing, and dynamical modelling, to name a few. Unsteady aerodynamics is now receiving the majority of attention in reduced-order modeling's most important contributions.

In 1967, Lumley [119] was the one who came up with the idea of using the Proper Orthogonal Decomposition (POD) method for aerodynamics. This method is used for the investigation of coherent structures seen in turbulent flows. The POD technique is appealing due to the fact that it is a linear approach that is effective in the construction of strong feedback controllers, which ultimately results in airflow that is better regulated over aerofoils. This is the primary reason for the method's popularity. Following then, a significant amount of computational and experimental work has been done by utilising this approach in order to prove its efficacy. [64, 8, 75].

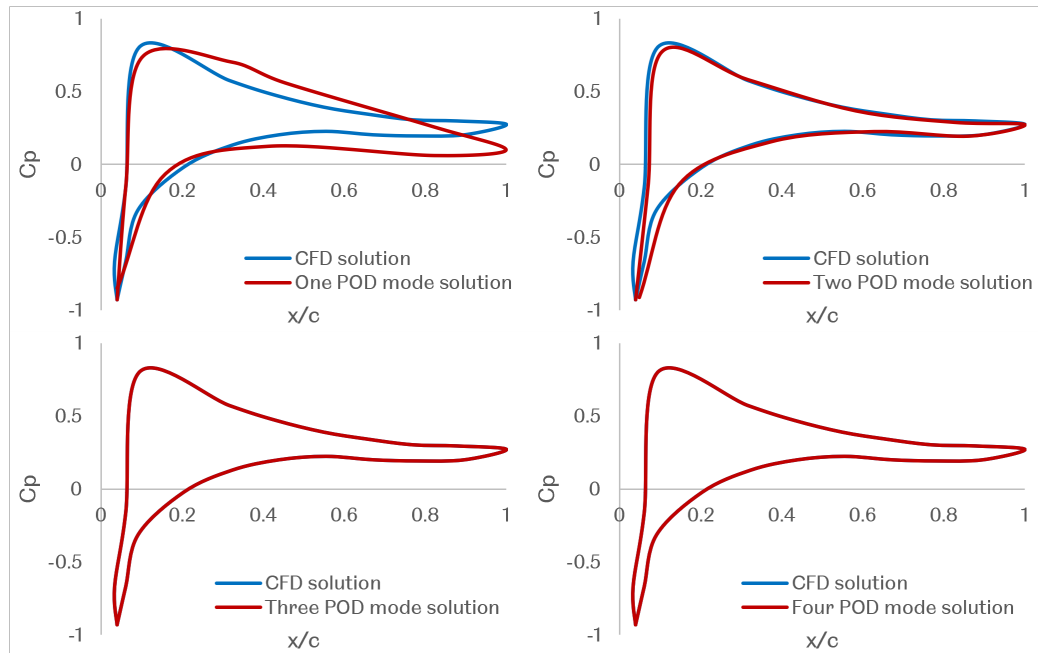


Figure 2.13: Comparison of the pressure coefficient on DU96-W180 wind turbine aerofoil between CFD solution and POD solution using different number of POD modes, reproduced from [75].

Problems involving fluid-structure interaction have been solved by employing the reduced order modelling approach. With the use of POD and Galerkin projection, Barone et al. [18] developed a ROM that can solve coupled fluid and structural issues. When the ROM is applied to issues involving flows that are supersonic and inviscid, as well as flows through square, elastic, and thin rectangular plates, the ROM is verified. Tchieu [165] derived a ROM for three fluid and structure interaction problems: a thin aerofoil undergoing small scale unsteady motions with a freestream flow; vortex-induced vibrations of an arbitrary bluff body with vortices; and two bodies in an inviscid fluid. The first problem involves a thin aerofoil undertaking small scale unsteady motions with a freestream flow [182]. POD and polynomial chaos expansion were utilised by Acar and Nikbay in the construction of computationally efficient ROMs for use in aeroelastic simulations [3]. They devised a stable ROM for a linear fluid and structure interaction issue, which involves a linearized inviscid compressible flow across a flat linear von-Krmn plate. This problem was tackled by Kalashnikova et al [97]. POD-based ROM was utilised by Lieu et al for the purpose of aeroelastic modelling of a whole F-16 jet fighter aircraft configuration [114]. A ROM addressing issues of fluids interacting with stiff bodies was developed by Liberge et al [112]. Forti and Rozza [60] conducted an examination of the shape parametrisation for the using the POD approach as well as the radial basis function method. On the

other hand, the procedures are invasive. POD and radial basis function interpolation approaches were used by Xiao et al. to offer a non-intrusive way for constructing a ROM that can be used to solve issues involving fluid and solid interaction [182]. This approach is confirmed by employing three different fluid-solid coupling test cases. These test cases are as follows: a one-way coupling case (flow past a cylinder), a two-way coupling case (a free-falling cylinder in water), and a vortex-induced vibrations of an elastic beam test case.

In general, the more advanced CFD algorithms generate answers in the time domain. Many excitation periods are needed in order to obtain a harmonic response, and many harmonic responses are needed in order to obtain results in a frequency range that is sufficient for generating a frequency domain aerodynamic forces response using an inverse Fourier transform. Both of these requirements must be met in order to obtain a harmonic response. In addition, impulsive responses or step responses generate a lot of information across a wide range of frequency spectrums. After that, it is feasible to generate the system's reaction by employing Reduced Order Models (ROM) such as, for example, a shortened Volterra series, correct orthogonal decomposition, and the harmonic balancing approach. These are just some examples. Because the response of the system is determined in the time-domain, in order to calculate the flutter speed, it is necessary to first determine a speed at which the oscillations are stable, as well as a speed at which the oscillations are unstable, and then either interpolate or extrapolate the damping with speed. This is because the response of the system is determined in the time-domain.

It is still difficult to describe the aeroelastic behaviour of the construction of a wind turbine. Both the difficulty of the computational modelling and the lack of facilities with which to carry out full-scale testing are major impediments to progress in this field. Consequently, nothing has been accomplished in this domain. Performing full-scale static testing on wind turbine blades is a task that can only be accomplished in a select few labs [116]. At this time, testing on a large scale is only possible in a few number of nations. In addition, Zhou et al. [188] argued that full-scale testing is the primary way available for determining how well wind turbine blades fulfil their function. Simply put, this is due to the fact that smaller turbine blades (those measuring 10 metres or less) have far bigger fatigue margins than the larger flexible blades that are often employed in the field. The only purpose of the aforementioned tests is to characterise the actual blade (structural integrity, fatigue life and vibration characteristics). These studies don't look at the effects of the tower shadow or centrifugal stiffening (when a blade spins at a high angular

velocity, the effects of inertia, centrifugal forces, and Coriolis forces become more pronounced). It's possible that the centrifugal forces will make the bending stiffness greater.

Unfortunately, a large number of Fluid-Structure Interaction (FSI) investigations are solely numerical, and only a small number of the model findings are compared to the actual data. One example of this would be the NREL wind turbines [50, 109, 54]. This is owing to the high costs connected with doing full-scale laboratory testing, as well as the difficulty in gaining access to field data. To this day, there has been no research conducted in which an aeroelastic model has been validated by comparison to data collected in the field. In the studies of Fluid-Structure Interaction on wind turbine blade and tower, the majority of them merely simulate the displacement of the blade and how it affects productivity. Very few people bother to explore the vibrational response of the blade, and out of the few who do, the results are typically oversimplified. In addition, no research has been conducted to evaluate the effect that the tower shadow has on the pitch of a turbine blade or the effect that a vibrating blade has on the structure of the near wake. According to Veers et al. [170], when the pitch changes on the blades are quick enough, it can impact not only the aerodynamic loads that are placed on the blade, but it can also further stimulate vibratory loads, which can have a detrimental effect on the fatigue life of the system.

The structural model of the wind turbine blades is another another obstacle to overcome. Due to the fact that the material characteristics of full-scale turbine blades are not revealed, it is often necessary to calibrate a large number of FE models. For the model to produce correct predictions of the deformation, deflection, and stresses, the calibration of the model needs to be extremely precise. Different features, such as the box spar corners and adhesive joints, each have their own unique set of qualities (the manufacturer's standards for these physical attributes could be somewhat different) [87]. In addition, geometric defects might cause the blade to behave in an unanticipated manner. It is imperative that the calibration procedure that is applied to each and every FE model be made public in order for the validity of the model to be assessed. By carrying out the aforementioned steps, it will be possible to develop an exhaustive calibration procedure for FE models of wind turbine blades.

In addition, the aerodynamics and aeroelastic problems that are presented by VAWTs are distinct from those that are presented by HAWTs as a result of the changes in the structural and aerodynamic design. Wind turbine blades undergo a quick shift in the angle of attack as a direct consequence of the rotating axis being perpendicular to the direction in which the wind is blowing. This causes the airflow to transition from being completely connected to being completely detached. Because of this, the aerodynamic

torque that is operating on the rotor will vary at high frequencies and large amplitudes. In order to get a realistic simulation, the mesh resolution will need to be enhanced, and the time step size will need to be reduced [105]. When the FSI analysis of VAWTs is carried out, the level of complexity of the simulation rises to a new high. The flexibility of VAWTs comes not only from the blades but also from the tower and the way in which it is connected to the rotor and the ground. As a direct consequence of this, the investigation into the fluid-structure interaction of VAWT is still far behind schedule.

2.4.1 Aeroelastic ROMs for wind turbines

Cost and complexity are still the main obstacles when conducting numerical wind turbine fluid-structure interaction research. One alternative to reduce the computational cost is to construct a reduced order model (ROM) of the aeroelastic system. Contributing even more to the computational time required is the fact that, to solve the complicated aerodynamic equations and perform a calculation by solving the eigenproblem, it is necessary to produce aerodynamic solutions for harmonic solicitations

For the determination of the structural modes, one normally neglects dissipation or damping and thus only modelling kinetic energy (or inertia) and potential strain energy (or stiffness) of the structure. The eigenvalues are real (the natural frequencies squared) as are the corresponding eigenmodes. Physically, if one excites the structure with a simple harmonic oscillation at a frequency near that of an eigenvalue, the structure will perform a simple harmonic oscillation at that same frequency, whose spatial distribution is given by the corresponding eigenvector.

The physical interpretation of the aerodynamic modes (as well as the aeroelastic modes), as well as the mathematical derivation of the eigenvalues and eigenvectors or eigenmodes, is nuanced and more challenging, but it is still satisfying. To begin, the eigenvalues are complex quantities; the real and imaginary components of the eigenvalue determine the eigenmode's oscillation frequency as well as its rate of increase or decay (damping). In the case of a structural model, if one is astute enough to stimulate only a single aerodynamic eigenmode, then an oscillation will take place, and the spatial distribution of this oscillation will be represented by the eigenvector that corresponds to it. On the other hand, the eigenvalues of an aerodynamic flow are often considerably closer together than the eigenvalues of structural modes because of the close proximity of these two types of flows. If the computational domain of aerodynamics were extended to infinity, then the eigenvalues for the majority of aerodynamic flows would not be discrete but rather would form a continuous distribution. This would be

the case since infinity is not a finite number. Therefore, experimentally excitation of just one aerodynamic mode at a time is a challenging task. It is conceivable for some flows in turbomachinery to have discrete well-spaced eigenvalues that have a resonant quality [76]. These flows involve limited flows that occur between blades in a cascade. This is also the case for certain of the aerodynamic eigenmodes that may be detected in a wind tunnel, and these can be confirmed by experimentation.

When the structural modes and the aerodynamic modes are fully coupled, a new set of modes known as the aeroelastic modes emerges. This indicates that oscillations of a fluid mode stimulate all of the structural modes, and that the stimulation works in the other direction as well. In general, the eigenvalues and eigenvectors associated with these aeroelastic modes have a character that may be described as being complex. Because the structural and aerodynamic interaction is weak at low speeds (far below the flutter speed, for example), it is typically possible to determine the structural and aerodynamic eigenvalues individually. The reason for this is that the flutter speed. However, if the speed of flutter is approached, there is a possibility that the eigenvalues and eigenvectors may undergo significant changes, and the fluid and structural modes will become more tightly connected. Although it is more common for one or more of the structural modes to become unstable when the flow of velocity gets closer to the flutter speed, it is conceivable for a mode that is aerodynamic in origin at low speeds to become the crucial flutter mode at higher speeds.

In order to cut down on the overall number of modes that need to be employed in a simulation of the overall motion of the aircraft, Winther et al [178] . have proposed making use of aeroelastic modes. Although the aeroelastic modes change with the flow circumstances, that is, the dynamic pressure and Mach number, and as a result, the aeroelastic modes at one condition will not be the same as the aeroelastic modes at another condition, the aeroelastic modes are still referred to as "aeroelastic modes." If a significant number of aeroelastic modes are used, one will be able to adequately characterise the dynamics of the system under every flying situation. However, doing so tends to negate the aim of decreasing the number of modes in the representation. It is also important to point out that the implementation of aeroelastic modes described in Winther et al. [178] does not take into account aerodynamic states or modes in and of themselves. This is a limitation of that particular approach in situations in which the aerodynamic modes themselves are active and strongly couple with the structural modes. This is perhaps the most extreme example possible, but it is still a possibility.

Most aeroelasticity studies on wind turbine blades focus on blade deformation and vibration responses. Both are essential and challenging for the development of wind tur-

bines. Classical beam theory is the foundation for the majority of structural modelling software used for wind turbine blades, particularly for HAWTs. However, increased turbine size has further complicated both the structural and aerodynamic features of the turbine blades, and this has led to the requirement for transient as well as thorough FSI models [121]. In the classic beam theory, the blade deflections are assumed to be small, and this is not more reliable as the increased blade size has resulted in the turbine blades becoming more flexible. As the blade sizes increase, large deformations are possible. Nevertheless, beam-based FSI models are useful for fundamental information over a blade but are not sufficient to provide the distribution of 3D aerodynamic loads on large wind turbines.

When the scale of current vertical axis wind turbine installations is taken into consideration, models consisting of a single blade or those that depict an incomplete turbine construction are no longer adequate. This is due to the fact that big composite turbine blades display a great amount of flexibility when subjected to loading conditions. Since the loading situation varies over the course of a single rotation, it is unreasonable to assume that any two of the blades would behave in the same way when they are in operation. Because there is no tower structure present, it is possible to disregard the transient effects that would normally occur between the tower and the turbine blades. When blades go in front of the tower, there is a reduction in the amount of pressure that is distributed across each blade. This, in conjunction with the rotation of the blade, has the potential to bring about a cyclical drop in pressure as well as bring about vibrations in the blade. As a consequence of this, the requirement for FSI modelling of the complete wind turbine structure is becoming increasingly obvious as wind turbines continue their evolution toward massive flexible structures. Rasmussen et al. [142] and Hansen et al. [77] provide a detailed evaluation of the present state of aeroelastic modelling in their respective works.

Several studies have been carried out using Reduced Order Models (ROM) [145, 18, 184]. One such example is the research done by Rezaei and his colleagues. Within the scope of this investigation, a Reduced Order Model (ROM) for the nonlinear dynamics of an operationally loaded wind turbine blade was developed and presented [144]. ROM models are frequently favoured over typical commercial FE models due to the fact that they need significantly less effort to compute. An investigation of the static as well as the dynamic reactions of the 5MW NREL wind turbines was carried out in order to validate the model's correctness. In order to assess the ROM model's dependability, the findings of the ROM model are also compared to those of complete FE simulations (which are modelled with the ANSYS programme utilising 50 elements of type Beam 188 for each

blade). As noted by Rezaei et al. [144], many previous beam formulations often neglect the torsional degrees of freedom (DOF) associated with large blades. In addition, most current beam formulations have not been assessed regarding accuracy and reliability, which consider a turbine blade under large deflections.

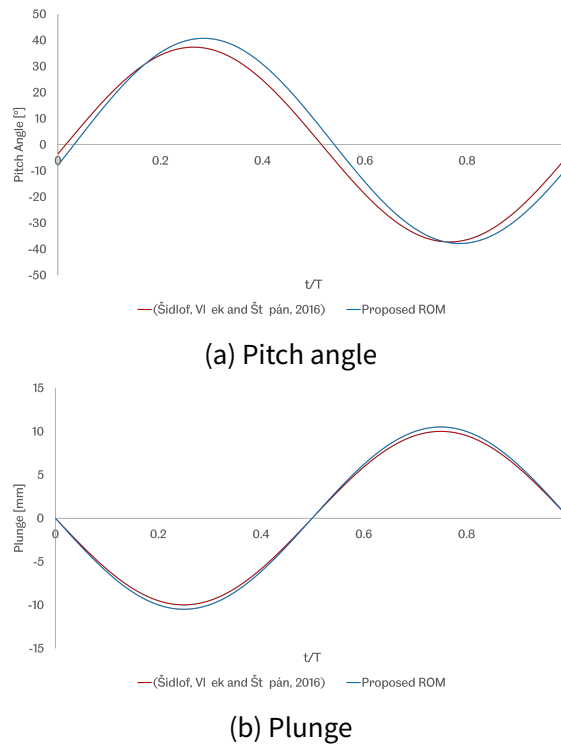


Figure 2.14: Comparison between the pitch and plunge solution of beam model obtained from the Reduced Order Modelling and the CFD solution.

As a result of the research that was done on the FSI modelling, it is now abundantly evident that further work has to be done on this subject in order for there to be any advance made in the field of wind turbine technology. In addition, the wide variety of modelling methodologies and distinct shell pieces that were utilised is evidence that a substantial amount of effort is still required to establish an all-encompassing FSI modelling strategy. The FSI modelling of the whole turbine facility has to be the primary focus of work that will be done in the future because of the ongoing development of HPC technology. It is only through doing this that it will be possible to get a greater knowledge of the dynamic phenomena connected with wind turbine designs and how these phenomena affect the structural properties of a wind turbine.

2.5 Summary

This section presents a review on the wind turbine fluid-structure interaction modelling, covering the aerodynamic and structural models, FSI strategies and model order reduction. The advantages and disadvantages are analysed, and the state-of-the-art implementations are presented. Research in the area of wind turbine aeroelasticity have been ongoing for decades, however, advanced 3D numerical solution work is still in its infancy with many simulations simplified by both the complexity and cost.

2.5.1 Knowledge Gaps

To begin, the beam models such as blade element momentum (BEM) method have been utilised in the majority of the wind turbine fluid-structure interaction models due to the fact that they have a reasonably high efficiency and tolerable accuracy in the calculations. This was noted before. However, this model is not able to provide a complete solution for the aerodynamics and the structure of the problem. In spite of the fact that computational fluid dynamics (CFD) and fully modelled three-dimensional finite element models are far more precise than these basic models, the amount of computing time required to run them is significantly more. One of the trends for fluid-structure interaction of wind turbines is to couple CFD and 3D FEM in order to produce more precise findings and detailed structural solutions, however research on this approach is still scarce. In addition to this, the majority of the research do not focus on the structure of the blade and instead only analyse a single blade (due to the computational time and expense). Last but not least, in contrast to a HAWT, a VAWT has a waking state that is more complex. This is not the only difference, though. As large, flexible wind turbine blades go through a variety of deformations at various phases of the rotation cycle, it is becoming more and more apparent that an entire rotor of a VAWT needs to be modelled. This is because of the complex interactions that occur between the various phases of the rotation cycle. The FSI modelling of the whole structure of the vertical axis wind turbine would offer a more comprehensive understanding of the losses that are transported from the rotor to the tower. This material may give information that is helpful regarding the specifications for the foundation and the structural damping.

In addition, the vast majority of the currently available aeroelastic models for wind turbines are linear models that are predicated on the idea that tiny blade deflections would occur. However, because the blades of the wind turbine frequently experience enormous deflections, which create considerable geometric nonlinearities, this assumption can no longer be considered true as the size of the wind turbine rises. In addition, the

aerodynamics and aeroelastic problems that are presented by VAWTs are distinct from those that are presented by HAWTs as a result of the changes in the structural and aerodynamic design. Wind turbine blades encounter frequent and substantial fluctuations in the angle of attack as a result of the rotating axis being orthogonal to the direction that the wind is blowing. This results in an airflow that is continually alternating between being entirely connected and being fully detached. This, in turn, causes high-frequency and high-amplitude changes in the aerodynamic torque operating on the rotor, which, for correct modelling, requires a finer mesh resolution and a lower time-step size [105]. When the FSI analysis of VAWTs is carried out, the level of complexity of the simulation rises to a new high. The flexibility of VAWTs comes not only from the blades but also from the tower and the way in which it is connected to the rotor and the ground. As a direct consequence of this, research into fluid-structure interactions on VAWTs are still far behind schedule.

Finally, the cost and complexity are still noted as being the main obstacles when conducting numerical investigations into wind turbine fluid-structure interaction research. Computational analysis of nonlinear aeroelastic systems is still an expensive proposition. One example of performing fluid-structure problem is reported by Bazilevs et al. [24] for the aeroelastic analysis of a 5MW Wind Turbine Rotor. The computation was carried out on a 240 core Sun Constellation Linux Cluster with 62,976 processing cores. Because wind turbines are subjected to significant unsteady pressure pressures whenever they are in the flow field, particular caution is required while designing the components that make up these turbines to ensure that they are strong enough to handle loads of this size. Even when executed in parallel on the most cutting-edge supercomputers, the simulations can take a significant amount of time to finish (on the scale of weeks). One way to cut down on the amount of time and effort spent computing is to build a reduced order model (ROM) of the aeroelastic system. This model will attempt to simplify the issue at hand by singling out significant modes of the fluid system and/or the coupled system. The analysis will then be based on the contribution made by these significant modes. The number of degrees of freedom that must be kept has been drastically cut, which has resulted in a decrease in the computational burden. The harmonic balancing technique, the Volterra approach, and the POD approach are three of the many ways that CFD may be used to apply ROMs in various configurations.

Lastly, the POD-Galerkin ROM approach is highly sensitive to small changes in the state of its base modes and this is due to its inherent limitations [61]. The oscillations that emerge in the solutions as a result of applying a conventional POD-Galerkin projection of equations onto the reduced order space are the root cause of the instabilities that

are frequently seen when using the POD technique. This phenomenon is very comparable to the Gibbs oscillations that emerge in the FEM solutions when the conventional Bubnov-Galerkin approach is used. These oscillations are what cause the simulations to be unstable since they feed into the non-linear factors.

In addition, the implementation of the original POD-Galerkin approach is limited, another issue arises in the reduced order modelling is the non-linearity reduction in the efficiency. The original Galerkin method is limited to the linear terms and therefore it is not capable for solving Fluid-Structure Interaction problems. After projecting onto the reduced space, the nonlinear term still depends on the original full system. The error can be quantified and minimised, and this can be done by including the transient portion of the simulation in the ensemble used to construct the POD basis, as well as the use of high-order numerical integration techniques and using carefully chosen time step convergence studies. Therefore, a stability-preserving method for coupling the nonlinear fluid ROM with structural dynamics model for the elastic body is needed to be constructed and tested.

2.5.2 Novelty

This PhD project develops a new and novel local refinement strategy on the ROM method in order to balance the increase in time cost and accuracy, refer to Chapter 3 and Chapter 4. In addition, a new ROM approach to the FSI problem applicable to solve moving (refer to Chapter 4) and/or deforming (refer to Chapter 6) solid boundary is proposed and coupled with the locally refined strategy. This strategy includes the elastic behaviour of solid domains, thus increasing the capability of the approach to solve FSI problems with large moving interfaces between the rigid body and the fluid. The proposed model is then applied and investigated on various testing cases, especially on HAWTs (refer to Chapter 7) and VAWTs (refer to Chapter 8).

Chapter 3

Methodology

3.1 Introduction

The most pressing issues in the field of fluid mechanics include huge dynamical systems that represent a variety of effects on a wide range of sizes. Studies of computational fluid dynamics frequently make use of models that require solving the Navier–Stokes equations with a number of degrees of freedom that are on the order of magnitude of 10^6 or more. In the work that Lumley did in 1967 [119], model order reduction techniques were first used for the purpose of gaining a greater insight into the mechanisms and intensity of turbulence as well as large coherent structures that were present in fluid flow problems. This was the first time that these techniques had been used. Simulate order reduction is also used in current aeronautics to model the flow over the body of an aircraft. This use is one of the modern applications of model order reduction [173]. A good illustration of this may be seen in the work of Lieu [114], in which the complete order model of an F16 fighter aircraft, which originally had over 2.1 million degrees of freedom, was simplified down to a model with only 90 degrees of freedom.

Various reviews on Proper Orthogonal Decomposition (POD) have already been published and offer a more in-depth, theoretical description of the method [27, 82]. POD is a modal decomposition technique which extracts modes by optimising the mean square of the variables of interest [163]. The basic approach consists of two steps: the first steps is the calculation of a reduced basis using the POD of an ensemble of flow-field realisations either from numerical simulations or experiments. The governing PDEs are then projected onto the basis of the POD modes in some appropriate inner product using the Galerkin projection method. The kinematic information of the flowfield of interest, often calculated from high-fidelity calculations, is firstly rewritten as a set of POD modes. Then the dynamic information is rewritten in terms of these POD modes. On implementation of the Galerkin method, the governing partial differential equations can be described as

a set of ordinary differential equations (ODEs) in terms of amplitudes of the POD modes. A detailed overview of the traditional uniform POD-Galerkin ROM method is introduced in this chapter, further modifications based on this basic idea, namely the modification to balance accuracy and efficiency (Chapter 4) and to solve moving and/or deforming interface problems (refer to Chapter 5 and 6) will be introduced in the following chapters.

3.2 Governing Equations

In this chapter, two and/or three dimensional non-hydrostatic Navier-Stokes equations describing the conservation of mass and momentum of a fluid are considered. For instance, the three-dimensional Navier-Stokes equations are given as follows:

$$\begin{aligned}\nabla \cdot \mathbf{u} &= 0 \\ \rho \left(\frac{\partial \mathbf{u}}{\partial t} + \mathbf{u} \cdot \nabla \mathbf{u} \right) &= \nabla p + \nabla \cdot \boldsymbol{\tau}\end{aligned}\quad (3.1)$$

where the term $\mathbf{u} \equiv (u_x, u_y, u_z)^T$ and p denote the velocity vector and the perturbation pressure term respectively. The term $\boldsymbol{\tau}$ denotes the stress tensor defined in terms of rate-of-strain tensor $\boldsymbol{\varepsilon}$ which is given by,

$$\begin{aligned}\boldsymbol{\tau} &= 2\mu\boldsymbol{\varepsilon} \\ \varepsilon_{ij} &= \frac{1}{2} (\nabla \mathbf{u} + \nabla \mathbf{u}^T) \\ &= \frac{1}{2} \left(\frac{\partial \mathbf{u}_i}{\partial \mathbf{x}_j} + \frac{\partial \mathbf{u}_j}{\partial \mathbf{x}_i} \right) - \frac{1}{3} \sum_{i=1}^3 \frac{\partial \mathbf{u}_i}{\partial \mathbf{x}_i} \delta_{ij} \quad i, j = \{x, y, z\}\end{aligned}\quad (3.2)$$

where δ_{ij} denotes the Kronecker delta, μ denotes the kinematic viscosity and it is assumed that there is no summation over repeated indices.

3.3 Modelling Reduction via Proper Orthogonal Decomposition

3.3.1 Proper Orthogonal Decomposition

The Proper Orthogonal Decomposition (POD) approach is firstly proposed by Berkooz, Holmes and Lumley in 1993 [27]. To start, some definitions are introduced. The inner product is a generalisation of the dot product and follows the same basic rules as the dot product. In fluid dynamics, the inner product is defined in the following way: in the

space \mathbb{R} , for two vector field f and g defined in $\Omega \in \mathbb{R}$, the definition of inner product is given by:

$$\langle f, g \rangle = \int_{\Omega} f(x) \overline{g(x)} dx \quad (3.3)$$

For instance, the inner product of two vectors in the real n -space \mathbb{R}^n is given by:

$$\langle x, y \rangle = \left\langle \begin{bmatrix} x_1 \\ \vdots \\ x_n \end{bmatrix}, \begin{bmatrix} y_1 \\ \vdots \\ y_n \end{bmatrix} \right\rangle = \mathbf{x}^T \mathbf{y} = \sum_{i=1}^n x_i y_i \quad (3.4)$$

where \mathbf{x}^T is the transpose matrix of \mathbf{x} .

In this chapter, vectors \mathbf{x} and \mathbf{y} are represented by the velocity flow fields \mathbf{u}_1 and \mathbf{u}_2 , refer to Chapter 3.4. For instance, the inner product of the two velocity flow fields \mathbf{u}_1 and \mathbf{u}_2 defined in a two-dimensional domain yield the following:

$$\langle \mathbf{u}_1, \mathbf{u}_2 \rangle_{\Omega} := \int_{\Omega} \mathbf{u}_1 \cdot \mathbf{u}_2 dx = \int_{\Omega} (u_{1x} u_{2x} + u_{1y} u_{2y}) dx \quad (3.5)$$

where u_{1x} and u_{1y} are the velocity components of \mathbf{u}_1 of in the x -direction and y -direction, respectively, namely, in a two-dimensional analysis. The induced norm of a vector \mathbf{u} is then defined as:

$$\|\mathbf{u}\|_{\Omega} := \sqrt{\langle \mathbf{u}, \mathbf{u} \rangle_{\Omega}} \quad (3.6)$$

3.3.1.1 Singular Value Decomposition

In practice of the Proper Orthogonal Decomposition (POD), the Singular Value Decomposition (SVD) is used to solve the subspace. Detailed review of the SVD method can be found in [157], only a brief review is presented in this project. The SVD is a factorisation of a real or complex matrix that generalizes the eigen decomposition of a square normal matrix with an orthonormal eigenbasis to any matrix via an extension of the polar decomposition. Specially, a $m \times n$ real Matrix \mathbf{M} can be decomposed as the follow form:

$$\mathbf{M} = \mathbf{U} \mathbf{\Sigma} \mathbf{V}^T \quad (3.7)$$

where \mathbf{U} is an $m \times m$ orthonormal matrix, $\mathbf{\Sigma}$ is an $m \times n$ rectangular diagonal matrix with non-negative real numbers on the diagonal, and \mathbf{V}^T is the transpose matrix of an $n \times n$ orthonormal matrix \mathbf{V} . Given the SVD of \mathbf{M} , the following two relations hold:

$$\mathbf{M}^T \mathbf{M} \mathbf{V} = \mathbf{V} (\mathbf{\Sigma}^T \mathbf{\Sigma}) \quad (3.8)$$

$$\mathbf{M}\mathbf{M}^T\mathbf{U} = \mathbf{U}(\boldsymbol{\Sigma}\boldsymbol{\Sigma}^T) \quad (3.9)$$

The right-hand sides of these relations describe the eigenvalue decompositions of the left-hand sides. The columns of \mathbf{V} are eigenvectors of $\mathbf{M}^T\mathbf{M}$ and the columns of \mathbf{U} are eigenvectors of $\mathbf{M}\mathbf{M}^T$. The SVD approach has been transformed to the eigenvalue and the eigenvector problem, which is more common in numerical studies and much easier to solve.

3.3.1.2 The Proper Orthogonal Decomposition

The main use of the POD method is to decompose a physical field, for instance, the velocity field in this thesis, seeking the most important variables that influence its physical behaviour. The reduced order model is based on the velocity flow field $\mathbf{u}(\mathbf{x}, t)$ on the time interval $[0, T]$, the time averaged of the velocity flow field $\mathbf{u}(\mathbf{x}, t)$ is defined as:

$$\mathbf{u}_0(\mathbf{x}) = \frac{1}{T} \int_0^T \mathbf{u}(\mathbf{x}, t) dt \quad (3.10)$$

The fluctuating velocity flow field $\mathbf{u}'(\mathbf{x}, t)$ is defined as follows:

$$\mathbf{u}'(\mathbf{x}, t) = \mathbf{u}(\mathbf{x}, t) - \mathbf{u}_0(\mathbf{x}) \quad (3.11)$$

The goal of this process is to decompose the fluctuating velocity flow field $\mathbf{u}'(\mathbf{x}, t)$ by the POD approach:

$$\mathbf{u}'(\mathbf{x}, t) = \sum_{i=1}^{\infty} a_i(t) \mathbf{u}_i(\mathbf{x}) \quad (3.12)$$

where $\mathbf{u}_i(\mathbf{x})$ is the POD orthogonal basis and the temporal dependency is described by the amplitudes of $a_i(t)$. This can be proved by the POD theorem of probability, where a random function can be expanded as a series of deterministic functions with random coefficients, so that it is possible to separate the deterministic part from the random one [117, 12].

Recapping that the term $\mathbf{M}\mathbf{M}^T$ is required to solve eigenproblems using the SVD approach, the two-point autocorrelation tensor \mathbf{R} for the flow field is defined as:

$$\mathbf{R}_{ij} = \frac{1}{T} \int_0^T \mathbf{u}'(\mathbf{x}_i, t) \cdot \mathbf{u}'(\mathbf{x}_j, t) dt \quad (3.13)$$

On implementing the SVD approach on the following equation:

$$\int_{\Omega} \mathbf{R}\mathbf{U}dx = \boldsymbol{\Lambda}\mathbf{U} \quad (3.14)$$

where Λ is a diagonal matrix, thus the Proper Orthogonal Decomposition of a given vector, namely $\mathbf{u}'(\mathbf{x}_i, t)$ is found. The POD modes \mathbf{u}_i with corresponding eigenvalues λ_i are obtained by solving the above equation, where \mathbf{u}_i is the i -th column of the matrix \mathbf{U} , and λ_i is the square root of the i -th component of the diagonal of the matrix Λ , ordered with respect to the decreasing positive eigenvalues, i.e., $\lambda_1 \geq \lambda_2 \geq \dots > 0$. It should be noted that the autocorrelation tensor \mathbf{R} is self-adjoint, which ensures that all the POD modes \mathbf{u}_i are orthogonal, i.e.,

$$\langle \mathbf{u}_i, \mathbf{u}_j \rangle_{\Omega} = \delta_{ij} \quad (3.15)$$

where δ_{ij} is the Kronecker delta. Using the orthonormality of the POD modes, a temporal amplitude satisfies the equation 3.12 is given as follows:

$$\mathbf{a}_i(t) = \langle \mathbf{u}', \mathbf{u}_i \rangle_{\Omega} \quad (3.16)$$

Thus, the fluctuating velocity flow field is decomposed as a combination of a series of temporal independent terms times its corresponding temporal amplitude.

Thus, the velocity profile is composed between The spatial modes \mathbf{u}_i and temporal coefficients a_i , however the equation 3.12 can be read as an expansion with a_i and the spatial coefficients, \mathbf{u}_i , as well. In other words, this symmetry implies that time and space can be interchanged, this leads to the temporal decomposition of the velocity profile. Integration over domain Ω is replaced by the integration over the time domain $[0, T]$. Similarly, the spatial correlation 3.13 is exchanged for the temporal correlation function as follows:

$$\mathbf{C}(s, t) = \langle \mathbf{u}'(\mathbf{x}, s), \mathbf{u}'(\mathbf{x}, t) \rangle_{\Omega} \quad (3.17)$$

The eigenproblem for the eigenfunction a_i with eigenvalue μ_i becomes:

$$\frac{1}{T} \int_0^T \mathbf{C}(s, t) \mathbf{a}_i(s) ds = \mu_i \mathbf{a}_i(t) \quad (3.18)$$

Similarly, the modes are ordered with respect to the decreasing real positive eigenvalues $\mu_1 \geq \mu_2 \geq \mu_3 \geq \dots > 0$. It should be noted that these eigenvalues are identical to the ones obtained from the decomposition in the spatial domain, i.e. $\mu_i = \lambda_i$. The POD modes are computed as:

$$\mathbf{u}_i(\mathbf{x}) = \frac{1}{T\lambda_i} \int_0^T a_i(t) \mathbf{u}'(\mathbf{x}, t) dt \quad (3.19)$$

3.3.1.3 Temporal discretisation of the POD method (Method of Snapshots)

In this thesis, the rebuilt solution is obtained from the ensemble of analytical or numerical solutions. To further reduce the computational cost, the method of snapshots, a discretisation approach of the POD procedure in the temporal domain proposed by Sirovich in 1987 [154], is implemented. Let an ensemble of M snapshots be given at the discrete times as follows:

$$\mathbf{u}^{(i)}(\mathbf{x}) = \mathbf{u}(\mathbf{x}, t^{(i)}), \quad i = 1, \dots, M \quad (3.20)$$

Similar to Equation 3.10, the time averaged of the velocity flow field $\mathbf{u}(\mathbf{x}, t)$ and the fluctuational velocity flow field $\mathbf{u}'(\mathbf{x}, t)$ are defined as:

$$\mathbf{u}_0(\mathbf{x}) = \frac{1}{M} \sum_{i=1}^M \mathbf{u}^{(i)}(\mathbf{x}) \quad (3.21)$$

$$\mathbf{u}'(\mathbf{x}, t^{(i)}) = \mathbf{u}^{(i)}(\mathbf{x}) - \mathbf{u}_0(\mathbf{x}), \quad i = 1, \dots, M \quad (3.22)$$

The discrete form of the matrix \mathbf{R} , which is a $M \times M$ matrix yields following:

$$R_{ij} = \frac{1}{M} \langle \mathbf{u}'(\mathbf{x}, t^{(i)}), \mathbf{u}'(\mathbf{x}, t^{(j)}) \rangle, \quad i, j = 1, \dots, M \quad (3.23)$$

Similar to the continuous case, the method of snapshots solves the following eigenvalue problem:

$$\mathbf{R}\mathbf{a}^{(i)} = \lambda_i \mathbf{a}^{(i)}, \quad i = 1, \dots, M \quad (3.24)$$

where $\mathbf{a}^{(i)} = (a_1^{(i)}, \dots, a_M^{(i)})$ and λ_i are the eigenvectors and eigenvalues, respectively. Thus, the POD modes \mathbf{u}_i and the coefficients are computed as:

$$\mathbf{u}_i(\mathbf{x}, t) = \frac{1}{M\lambda_i} \sum_{j=1}^M a_j^{(i)}(t) \mathbf{u}'(\mathbf{x}, t^{(j)}) \quad (3.25)$$

$$\mathbf{a}_i = \frac{\mathbf{a}^{(i)}}{\sqrt{M\lambda_i}} \quad (3.26)$$

The method of snapshot yields a $M \times M$ correlation matrix, while the same discretisation in the spatial domain yields a matrix with size $N_g N_d \times N_g N_d$, where N_g is the number of grid points and N_d is the dimension of the problem of interest. Normally $N_g N_d$ is much greater than M , making the method of snapshot more suited for CFD data, whereas the POD in the spatial domain is more suitable for long time samples of few experimental measurements.

3.3.2 Galerkin method

The Galerkin approach involves projecting the functions that define the initial equation onto a finite-dimensional subspace of the whole phase space [13]. This is done in order to simplify the analysis. It is necessary for the phase space to be an inner product space that is covered by an appropriate group of basis functions in order to carry out the Galerkin technique. The appropriate option for the basis function can range from mathematical models like the Fourier modes and the Chebyshev polynomials to empirical models like the POD modes. Both types of models can be included in this category. However, in this thesis, only the POD approach is included. Considering a dynamic problem described by:

$$\frac{d\mathbf{u}}{dt} = f(\mathbf{u}) \quad (3.27)$$

where f is a general operator on the velocity profile \mathbf{u} , namely the Navier-Stokes equation and \mathbf{u} can be decomposed in terms of suitable orthogonal basis functions via the POD method as follows:

$$\mathbf{u}(\mathbf{x}, t) = \sum_{i=0}^{\infty} a_i(t) \mathbf{u}_i(\mathbf{x}) \quad (3.28)$$

By projecting the equation onto the set of the basis functions, the dynamics of the temporal coefficients can be described as:

$$\frac{da_i}{dt} = \langle f(\mathbf{u}, \mathbf{u}_i(\mathbf{x})) \rangle, \quad i = 0, \dots, \infty \quad (3.29)$$

where $\mathbf{u}_0(x)$ denotes the average velocity profile defined in equation 3.21. The truncation in both the POD and the Galerkin method yields a model of equation as:

$$\mathbf{u}(\mathbf{x}, t) = \sum_{i=0}^N a_i(t) \mathbf{u}_i(\mathbf{x}) \quad (3.30)$$

$$\frac{da_i}{dt} = \langle f(\mathbf{u}), \mathbf{u}_i(\mathbf{x}) \rangle, \quad i = 0, \dots, N \quad (3.31)$$

3.4 Implementation of a POD-Galerkin based ROM for fluid mechanics

Considering an incompressible fluid in a rigid domain Ω , with the density ρ_F and viscosity μ_F , the coupled approach can be applied to the governing Navier-Stokes equation [82] is given as follows:

$$\rho_F \left[\frac{\partial \mathbf{u}}{\partial t} + (\mathbf{u} \cdot \nabla) \mathbf{u} \right] = -\nabla p + \mu \Delta \mathbf{u} \quad (3.32)$$

where \mathbf{u} is the velocity vector, p is the pressure. Using the POD method, the velocity flow field can be decomposed on the truncated POD modes ϕ_i at N modes as follows:

$$\mathbf{u}(\mathbf{x}, t) = \mathbf{u}_0(\mathbf{x}) + \sum_{i=1}^N a_i(t) \mathbf{u}_i(\mathbf{x}) = \sum_{i=0}^N a_i(t) \mathbf{u}_i(\mathbf{x}) \quad (3.33)$$

where $a_0 \equiv 1$, $u_0(x)$ is the mean velocity flow field; when $i > 1$, $a_i(t)$ are the temporal coefficients, and $\mathbf{u}_i(x)$ are the corresponding POD modes. An ordinary equation governing the temporal coefficients $a_i(t)$ is obtained by substituting the velocity flow field decomposition (Equation 3.33) into the governing Navier-Stokes equation (Equation 3.32) and projecting onto the subspace spanned by the POD modes $\mathbf{u}_i(x)$:

$$\langle \rho_F \left[\frac{\partial \mathbf{u}}{\partial t} + (\mathbf{u} \cdot \nabla) \mathbf{u} \right] + \nabla p - \mu \Delta \mathbf{u}, \mathbf{u}_i(\mathbf{x}) \rangle_{\Omega} = 0, \quad i = 1, \dots, N \quad (3.34)$$

where $\langle \mathbf{u}, \mathbf{v} \rangle_{\Omega} := \int_{\Omega} \mathbf{u} \cdot \mathbf{v} d\mathbf{x}$ denotes the inner product defined on the subspace. Due to the orthogonality and the free divergence of the POD modes $\mathbf{u}_i(\mathbf{x})$, Equation 3.34 becomes:

$$\rho_F \frac{d}{dt} a_i = \mu_F \sum_{j=0}^N d_{ij} a_j + \mu_F \sum_{j,k=0}^N c_{ijk} a_j a_k + f_i^p, \quad i = 1, \dots, N \quad (3.35)$$

where

$$d_{ij} = \langle \mathbf{u}_i, \Delta \mathbf{u}_j \rangle_{\Omega} \quad (3.36)$$

$$c_{ijk} = -\langle \mathbf{u}_i, (\mathbf{u}_j \cdot \nabla) \mathbf{u}_k \rangle_{\Omega} \quad (3.37)$$

It should be noted that the incompressibility of the POD modes can be used to express f_i^p in a boundary integral form as follows (Aubry et al., 1988):

$$f_i^p = -\langle \mathbf{u}_i, \nabla p \rangle_{\Omega} = -\int_{\partial\Omega} p \mathbf{u}_i \cdot \mathbf{n} d\mathbf{x} \quad (3.38)$$

where n is the outward norm to the domain Ω considered for the boundary $\partial\Omega$. The coefficient f_i^p which contains the pressure term p can be avoided. Indeed, for more cases (for example the driven cavity) the velocity field is equal to zero on the boundary, and, as the POD vector complies with the homogeneous boundary conditions, f_i^p is zero. In other cases, some particular methods have been developed. Refer to Rempfer (Rempfer, 1996), who uses a vorticity formulation and Aubry et al. (Aubry et al., 1988)

who modelled this term for the study of the viscous sublayer in a channel flow and Allery (Allery, 2002) uses a penalisation method.

3.5 Evaluation of POD-Galerkin Applications

In this section several aspects of particular POD-Galerkin methods are presented to evaluate the performance in terms of accuracy and efficiency. A discussion related to the POD basis computation is presented.

3.5.1 Error Estimation

For the temporally discretised POD model, the difference between the POD solution and the referenced numerical solution using i POD modes can be computed as:

$$err_p(i) = \sqrt{\sum_{k=0}^N t_k |\tilde{\mathbf{u}}(t, P) - \mathbf{u}_{ref}(t, P)|_{\Omega}^2} \quad (3.39)$$

where N is the number of snapshots, t_k is the time-stamp difference between the k -th and $k+1$ -th snapshots. $\tilde{\mathbf{u}}(t, P)$ describes the approximated solution of the displacement at the node P and $\mathbf{u}_{ref}(t, P)$ is the corresponding reference solution, obtained either from the analytical solution or the baseline numerical solution. The theoretical approximation errors of the i -th POD mode is defined as:

$$err_t(i) = \sqrt{\sum_{j=i+1}^{N_{POD}} a_j} \quad (3.40)$$

where $\{a_i\}$ are the POD modes, N_{POD} is the targeted number of POD modes. Note that the theoretical error can also be obtained computed using the trace for the matrix of Equation 3.23, i.e.,

$$err_t(i) = \sqrt{trace(\bar{\mathbf{R}}) - \sum_{j=1}^i a_j} \quad (3.41)$$

The experimental solution and numerical simulation without reduction are used as the reference. The relative error at a certain time t is given by

$$\varepsilon_P(t) = \frac{|\tilde{\mathbf{u}}(t, P) - \mathbf{u}_{ref}(t, P)|}{|\mathbf{u}_{ref}(t, P)|} \quad (3.42)$$

Two errors are defined in order to compare the different POD-Galerkin methods. On the one hand, the maximum error of the velocity component at all points within the grids Ω is defined as follows:

$$\varepsilon_{\Omega}(t) = \max_{P \in \Omega} \varepsilon_P(t) \quad (3.43)$$

and the weighted difference is given by

$$\varepsilon_{\Omega} = \sum_{P \in \Omega} \varepsilon_P(t) d_x d_y \quad (3.44)$$

where d_x and d_y are the dimensions of the corresponding grids of the point P in the x- and y- direction. For a comparison of the computational effort of the different ROM methods, the time ratio is employed. This is defined by the computational time of the simulation with the reduction with respect to the computational time of the unreduced simulation at the same scale of time, e.g. the time ratio of the numerical solution is one.

The stability and error estimates, as addition to the corresponding inner products for the Galerkin ROMs, have only been published thus far in continuous form. This has been the case up to this point. They are only true if the relevant integrals are assessed exactly, which is a circumstance that also arises during the numerical analysis of spectrum approaches. When using spectrum approaches, this issue is typically solved by employing a high-precision numerical quadrature that is in a position to integrate the spectral projections precisely.

3.5.2 Computation of the POD basis

A discretised POD model is selected as the numerical application. The details of this problem can be found in Chapter 4.3.1, as the problem settings are not the points of the interest in this chapter.

The decay of the eigenvalues $\{\lambda_i^y\}_{i=1}^{d_y}$ is essential to obtain a good POD approximation. If the eigenvalues decay too slow, either the resulting reduced order model is of large dimension or one obtains large approximation errors. Figure 3.1 shows the comparison between SVD and POD both implementing on the same testing case with same computation settings. For both cases, only the first 50 modes are investigated. It should be noted that for singular values then should be squared to compare WHAT with the corresponding eigenvalues. It is clear that the initial values are identical to one another. Both approaches produce results that are accurate to the same degree, therefore the disparity that appears after around 20 values may be attributed to a problem with the

numbers. The only reason for the disparity to exist is because the singular values were squared before being compared. Due to the fact that we are only concerned with the greatest eigenvalues, this problem does not have any bearing on the POD technique. Therefore, the gain in accuracy brought about by employing the singular value decomposition does not constitute a substantial step forward.

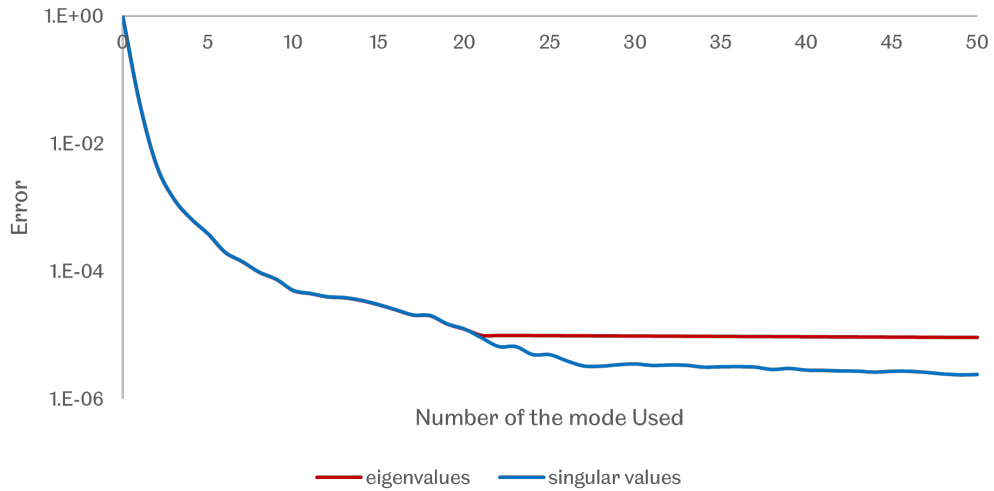


Figure 3.1: A comparison of the decay of the singular values and eigenvalues.

Figure 3.2 presents a comparison of the approximation errors that occur on the applications when the SVD technique and the POD approach are utilised. It has been discovered that the outcomes of using either strategy are comparable. The increased computing precision brought about by the singular value decomposition has no effect on the inaccuracies brought about by the approximation. The two methods that have been discussed produce results that are virtually identical in nature when it is necessary to use only a small number of basis functions. When the projected result is compared to the theoretical outcome, i.e. err_t , refer to (3.41), it is possible to notice that they can be identical up until the point when the accuracy of the eigenvalue solver is exceeded. As a result of the fact that we compute the error by first subtracting the eigenvalues from the trace, we find that the results eventually plateau. This is due to the fact that the total of the eigenvalues is not equal to the trace of matrix \mathbf{R} ; rather, there is a difference of around 10^{-10} . This is the root cause of the problem. In the computation of the error, this results in a value of 10^{-5} due to the use of a square root. In addition, it is important to highlight that the degree of precision in the projection error is comparable to the degree of accuracy in the projection error produced by the finite element approach.

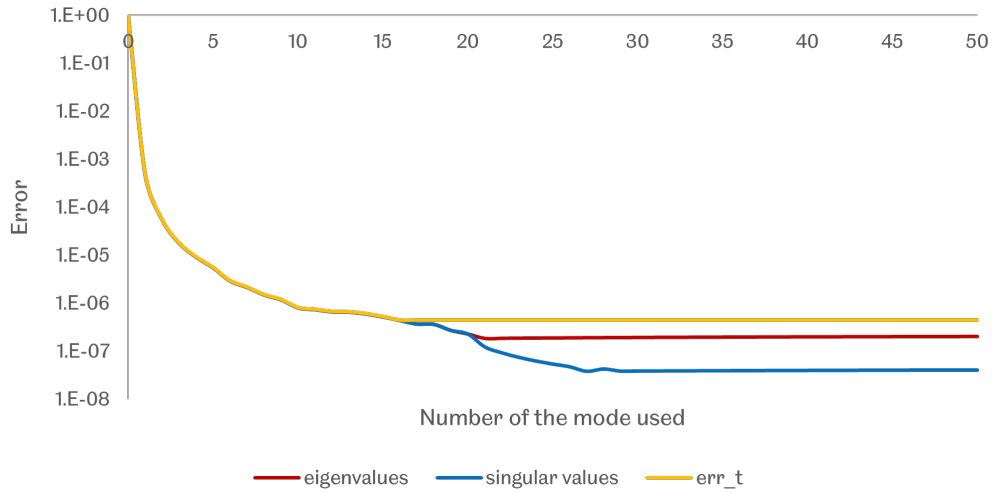


Figure 3.2: A comparison of the decay of the approximation errors.

When we consider the cost of the calculation, it is important to point out that the computation of the POD basis using the SVD is more expensive than the computation using the eigenvalue decomposition. The reason for this is that the equations (3.9) and (3.8) need the matrices \mathbf{M} and \mathbf{M}^T to refer to one other. In actual practice, only the first components of the eigenvalue or singular value decomposition need to be calculated; it is not necessary to calculate the whole eigenvalue or singular value decomposition. Iterative techniques, such as the Lanczos algorithm [175], can thus be used to solve the problem. These techniques provide extremely accurate approximations and have a lower processing overhead than other approaches.

Improving the time discretization is one way that the POD base may be strengthened even more. An ideal snapshot placement strategy can be utilised to accomplish this goal [106]. To produce fresh snapshots without incurring additional computing burden, a linear combination of the existing snapshots was opted upon. This method may also be expanded to an adaptive strategy, in which the POD basis is improved by the addition of information on the behaviour of the system when the parameter is altered (for more information, see Chapter 4).

3.6 Numerical examples of the POD-Galerkin ROM

In this section, the performance of the POD-Galerkin method is evaluated via a simple two-dimensional flow example. In fluid dynamics, vortex shedding is an oscillating flow that takes place when a fluid, such as air or water, flows past a cylindrical body at certain velocities, depending on the size and shape of the body.

The test case is carried out on the configuration described in Figure 3.3, where a cylindrical rigid body is attached to a spring that has been immersed in a fluid flow at a relatively low Reynolds number, $Re = 1690$. In addition, a relatively high Reynolds number, namely $Re = 5000$, is simulated to challenge the capability and stability in cases of unsteady flow problems.

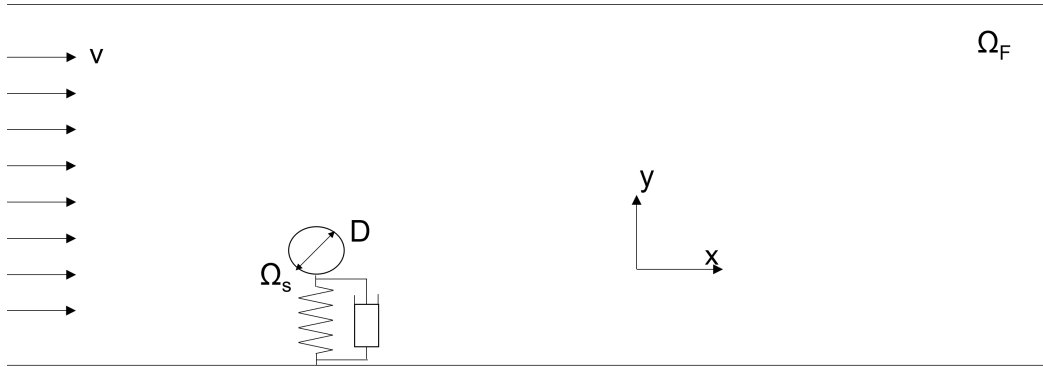


Figure 3.3: Schematic description of the flow induced vibration of an oscillating circular cylinder.

The cylinder oscillates due to the fluid forces along the y -axis, and the body is modelled as a cylindrical rigid solid body, that is attached to a linear spring-damping system. The motion of the fluid and solid domains are solved using the ANSYS Fluent and Mechanical solvers, respectively, and coupled by a semi-implicit coupled algorithm. The full details of the problem can be found in [112], and the main parameters are summarized in Table 3.1.

Table 3.1: Basic parameters of the structural dynamics and aerodynamics for flow around an oscillating circular cylinder, reproduced from [112].

Parameters	Values
Diameter, D [m]	0.05
Mass, m [kg]	1.178
Stiffness, k [N/m]	0.559
Damping coefficient, c [kg/s]	2.7825

where Diameter D is used to determine the geometry of the solid domain, the motion profile of the cylinder is obtained from parameters mass m , stiffness k , and damping coefficient c ,

$$m\ddot{\mathbf{x}} + c\dot{\mathbf{x}} + k\mathbf{x} = 0 \quad (3.45)$$

where \mathbf{x} is the location of the cylinder. The problem domain is $[-0.6 \text{ m} \times 0.6 \text{ m}] \times [-0.4 \text{ m} \times 0.4 \text{ m}]$, and the cylinder is located at $(0, 0)$ at time $t = 0$ second. The fluid flows past the oscillating cylinder and exit the domain through the right hand side of the boundary. No slip and zero outward flow conditions are applied to the upper and lower edges of the rectangle, whilst FSI boundary conditions are applied to the cylinder's wall ensuring that the velocity at the surface equals the motion of the solid domain. Velocity inlet boundary condition is applied to the left hand side of the domain, where velocity profile is set to 0.0422 m/s for $Re = 1690$ and 0.130 m/s for $Re = 5000$. Outlet boundary condition is applied to the right hand side. From the full model simulation, 100 snapshots were obtained at regularly spaced time intervals $\Delta t = 0.01 \text{ s}$ for each of the u , v and p solution variables.

The full order model is established using ANSYS FLUENT and the Transient Structure modules. In the case of the Reynolds number being 1690, the upstream inlet velocity was set to 0.0338 m/s in order to produce the Reynolds number of 1690, as employed in [112]. Since the fluid is incompressible, the density and viscosity of the fluid are considered to be constant at 1000 kg/m^3 , and 0.001 kg m s , respectively.

The turbulence model used is the $k-\omega$ SST model and the transport equations for the SST model used to calculate the turbulent kinetic energy k and the specific dissipation rate ω are those used in ANSYS FLUENT. This two-equation model is suitable for modelling the boundary layers as well as the far field flows, and therefore it has been used extensively in studies involving wind turbine blades and aeroelastic problems with reasonable results [80, 75].

On considering the computational time and accuracy, the mesh size of 1 mm and the time size of 1×10^{-4} seconds are deemed as the appropriate mesh size and time size for the modelling in this study, for a detailed mesh and time step convergence study please refer to Section 5.3.1.1. The fluid model consists of 158,610 nodes and 579,632 elements while the structural part consists of 2595 nodes and 2422 elements. The time-step size is 1×10^{-4} seconds and the number of nonlinear iterations per time step is 500. A loose coupling strategy was applied in order to couple both the fluid and structural domains.

The POD snapshot solution has been computed using the ANSYS Mechanical and ANSYS Fluent with a RANS $k-\omega$ turbulence model using the overset method to adapt the mesh around the oscillating cylindrical body. A loosely coupled algorithm couples both the structural and fluid domains. During one oscillation period, one hundred snapshots are taken, and these are interpolated on a rectangular grid to build a POD basis using Equation 3.34. By implementing the POD-Galerkin ROM approach, Equation (3.33), the velocity field is decomposed as follows:

$$\mathbf{u}(\mathbf{x}, t) = \sum_{i=0}^M a_i(t) \mathbf{u}_i(\mathbf{x}) \quad (3.46)$$

where $\mathbf{u}_i(\mathbf{x})$ and $a_i(t)$, $i = 1, \dots, M$ are the POD eigenmode functions and the amplitude of each mode, respectively. $\mathbf{u}_0(\mathbf{x})$ is the average velocity profile over the computational time and $a_0(t) = 1$. Detailed discussion of the POD modes and the corresponding please refer to Section 5.3.1, as shown in Figures 5.7. Here, only the brief discussion of the traditional uniform POD-Galerkin ROM is presented.

The solutions for the flow past the cylinder at time instances 5.0 and 10.0 seconds are depicted in Figure 3.4. These solutions were computed using the two ROM models (uniform ROM and the new proposed model) as well as the full high-fidelity model employing 12 POD basis functions. The solutions are shown in the figure as a bar graph. In this particular instance, the Reynolds number was 100. The uniform POD-Galerkin technique demonstrates a satisfactory level of congruence with the CFD solution. Because of the truncation of the POD modes that occurred during the computation, the difference is most pronounced in the region that surrounds the oscillating cylinder. Increasing the number of POD modes is one way to reduce the impact of this.

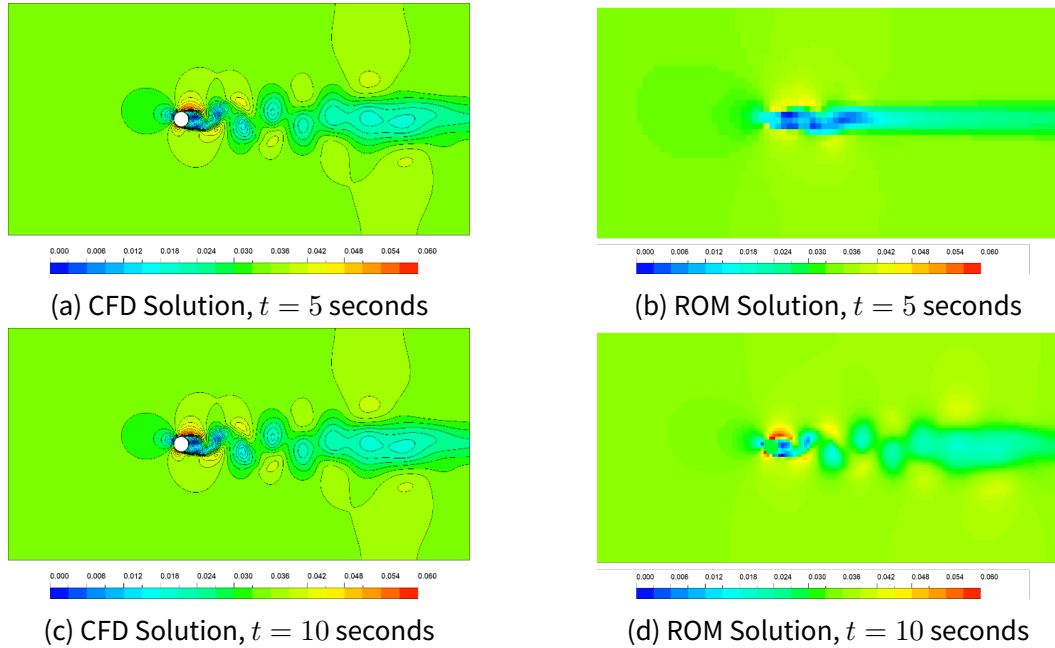


Figure 3.4: Comparison between the CFD solution and the proposed ROM solution using 12 POD modes for the flow past a oscillating cylinder at $Re = 1690$ and time instances 5.0s and 10.0s.

In this analysis, the velocity flowfield is computed by the uniform POD-Galerkin method

using various POD modes, namely 12 and 24 POD modes. These solutions show that the POD model have performed particularly well at resolving the flow field at both time instances. Although the standard POD models via 12 POD modes are able to capture the wave pattern, the solution via the 12 POD modes has a large error near the peak of the waves during the spin-up period of modelling, as shown in Figure 3.5. Although the error between the POD and the CFD solution is inevitable, this error can be minimise to an acceptable value by increasing the number of the POD modes and changing the grid used, please refer to Chapter 4.

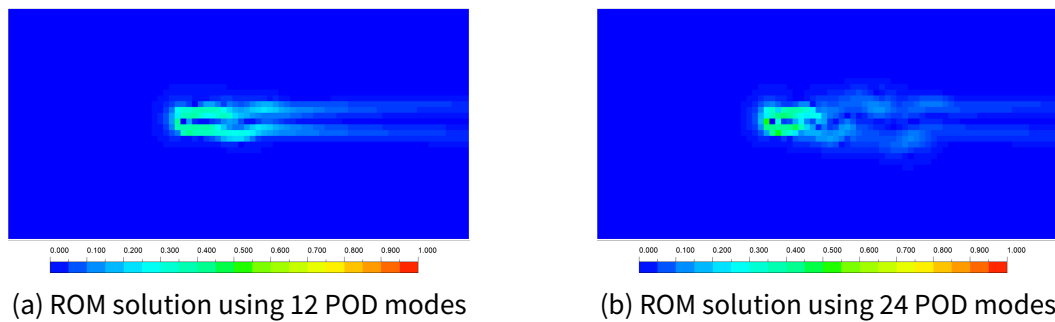


Figure 3.5: Errors in the flow past an oscillating cylinder problem at $Re = 1690$ predicted by the proposed ROM using 12 and 24 POD modes.

The uniform POD-Galerkin method presented in this chapter can be applied on various flow conditions. To challenge further the capability of the ROM, the Reynolds number was then increased to $Re = 5000$ and the number of POD bases are guided from the decrease of eigenvalues, shown in Figure 3.6. The larger number of POD bases that are chosen, the more energy is captured. In this case, 12, 24 and 36 POD bases are used to evaluate the performance of the ROM.

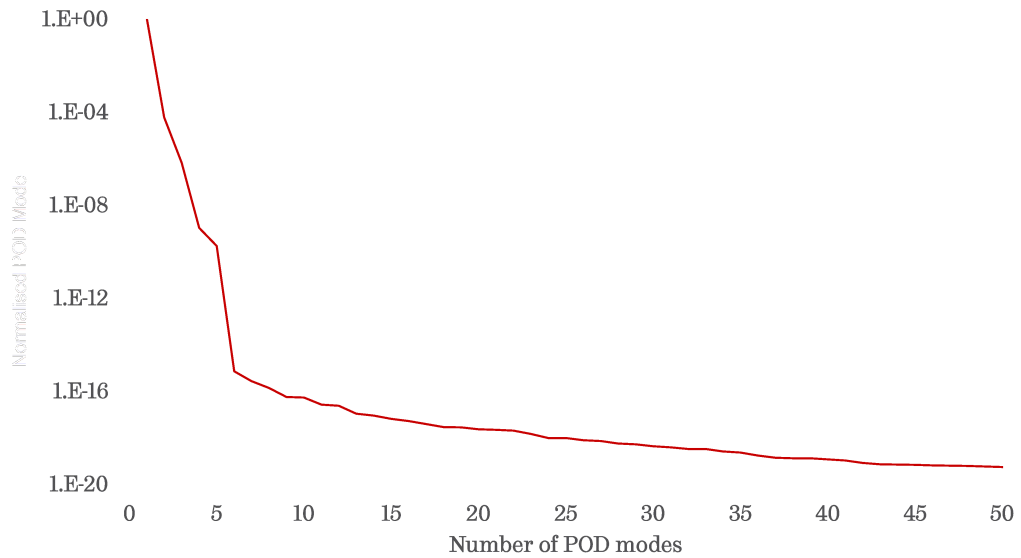


Figure 3.6: Singular eigenvalues in order of decreasing magnitude of the ROM for the Flow past a cylinder at $Re = 5000$

The comparison of results between the full and POD models (the standard uniform approach via different number of POD modes) was carried out. Figure 3.7 shows the simulated flow patterns at time instances 5.0 and 10.0 (where 12 POD bases are used). As shown in the figures, the proposed model performs well for this Reynolds number. Figure 3.4 shows the difference between the full model and proposed refined POD method and the standard POD of the flow past a cylinder problem at time instances 10.0 and 20.0 using 12 POD basis functions. The ROM model still shows a good agreement to the full order modelling solution, however the model fails to compute the wake contour in several timesteps at higher Reynolds number cases.

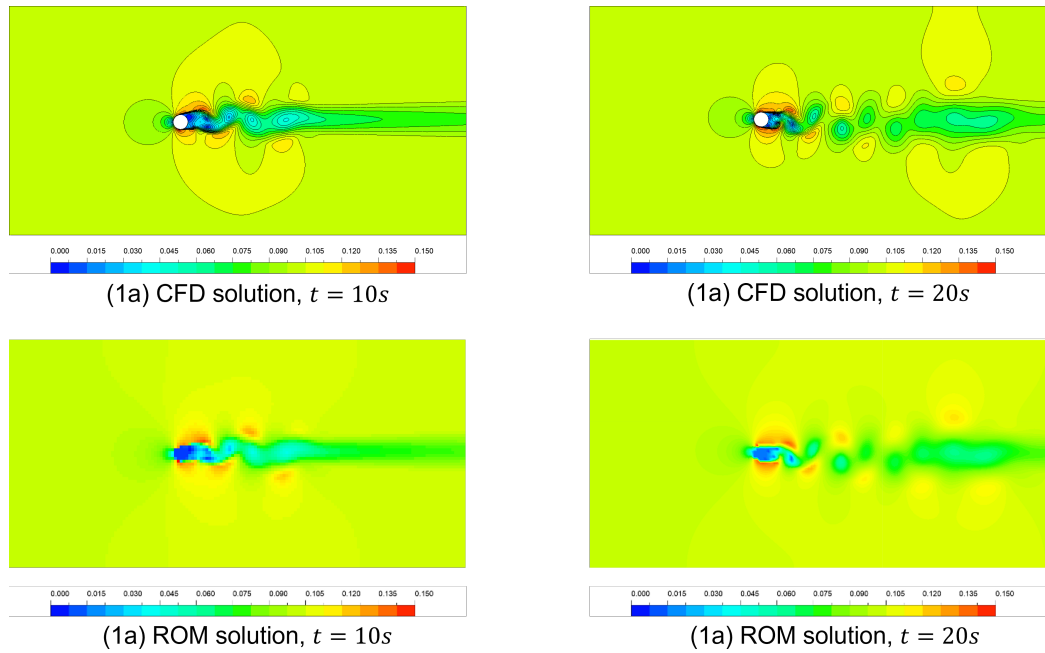


Figure 3.7: Comparison of the solutions of the flow past an oscillating cylinder problem at $Re = 35000$ and time instances 10.0 and 20.0 between CFD solution and the proposed ROM using 12 basis functions.

In addition, by increasing the total number of POD bases, the accuracy of the findings obtained from the POD ROM may be increased even more. The entire solution and the suggested improved reduced order model are compared head-to-head in Figure 3.8. The figure shows the results for 12, 24, and 36 POD basis functions, respectively. When comparing the answers produced by the conventional POD ROM to the predictions made by the ROM, there is a discernible improvement in the predictions made by the ROM when fewer basis functions are utilised in both situations.

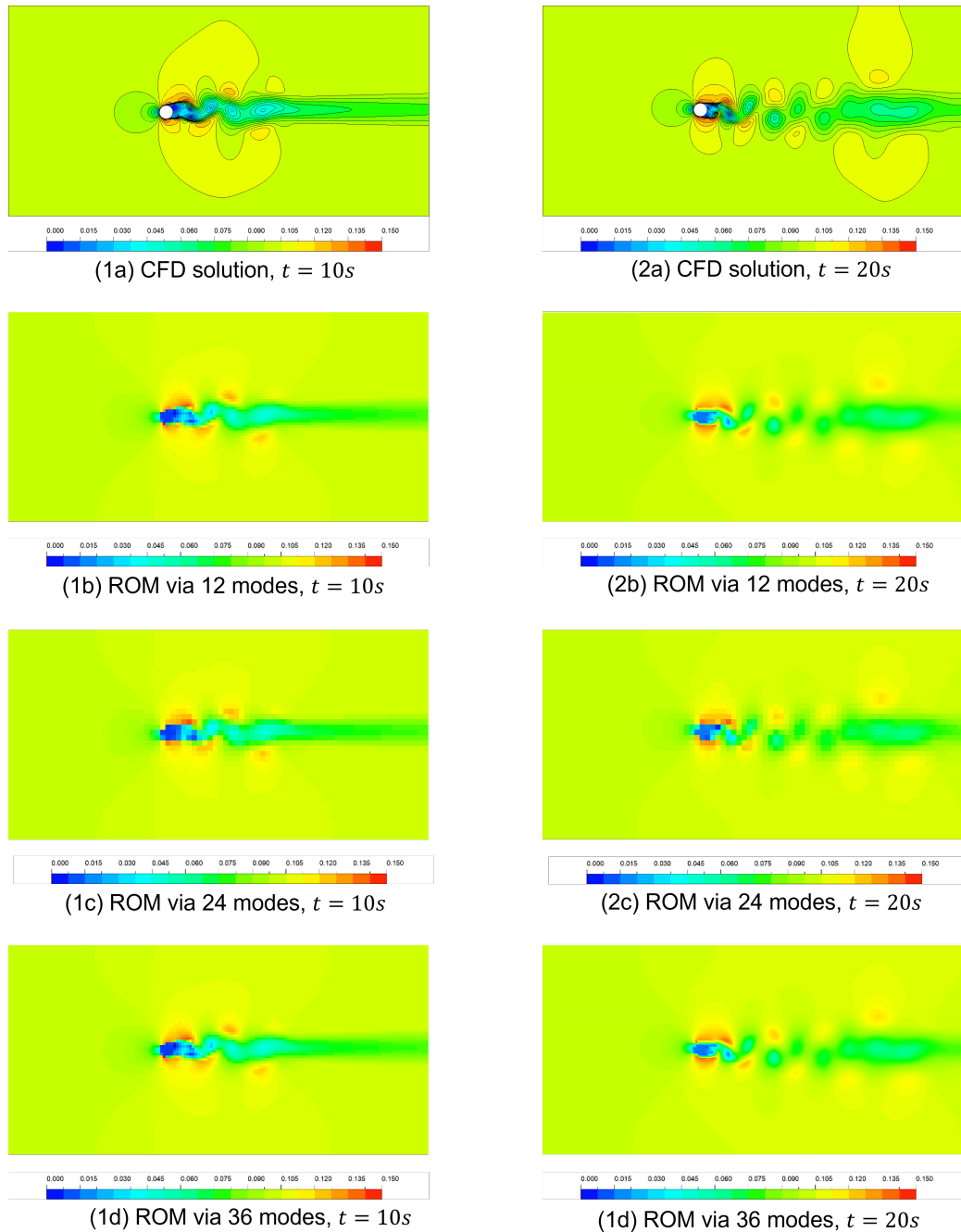


Figure 3.8: Comparison of the solutions of the flow past a oscillating cylinder problem at $Re = 35000$ and time instances 10.0 (1) and 20.0 (2) between CFD solution (a) and the proposed ROM using 12 (b), 24 (c) and 36 (d) basis functions.

Figure 3.9 illustrates the difference in velocity that results from rebuilding the flow-field using either 12 or 36 POD bases, as compared to utilising the full order solution. Once more, it is demonstrated that bringing the total number of POD bases up to 36 results in an improvement in the accuracy of the velocity solution. The root mean square

error (RMSE) of the velocity measurements produced from the revised grid ROM that was proposed gets less as the number of POD bases gets higher. While there is no sudden shift in the solutions, the suggested ROM can work effectively when employing only 12 POD bases. However, when there is an abrupt change in time, it is possible to capture it by increasing the number of POD bases.

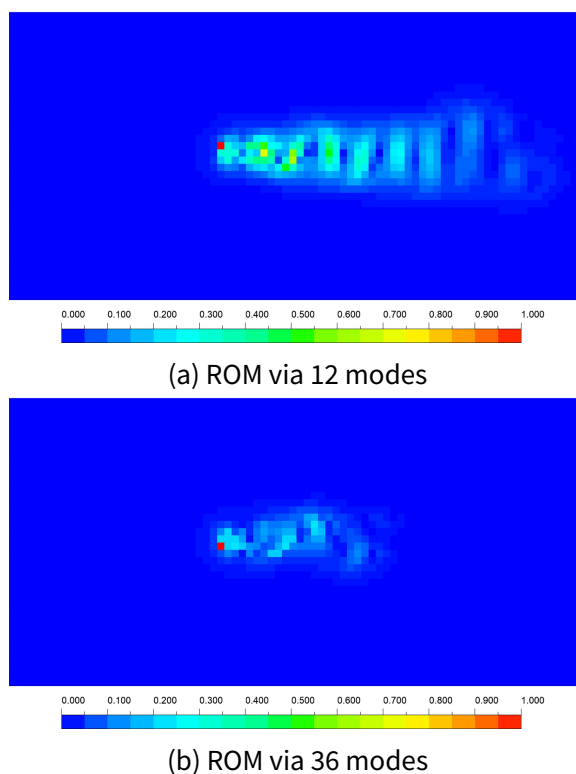


Figure 3.9: The error for the flow past a oscillating cylinder problem at $Re = 35000$ predicted by the proposed ROM using 12 (a) and 36 (b) basis.

Another way to increase the accuracy of the ROM method is to refine the grid density in the projection process. Figure 3.11 compares the full model and the refined grid ROM using different sparse grid refinement levels i with $i \in \{1, 2, 3\}$ and using 12 POD bases. Each grid has the number of nodes $n_l = 2^{(i-1)} + 1$ in which l denotes the number of levels, as shown in Figure 3.10. As can be seen from Figure 3.11, even level one (3 points at each dimension) performs well, while level zero (one point at each dimension, mean value of each dimension) failed to capture the energy in the flows.

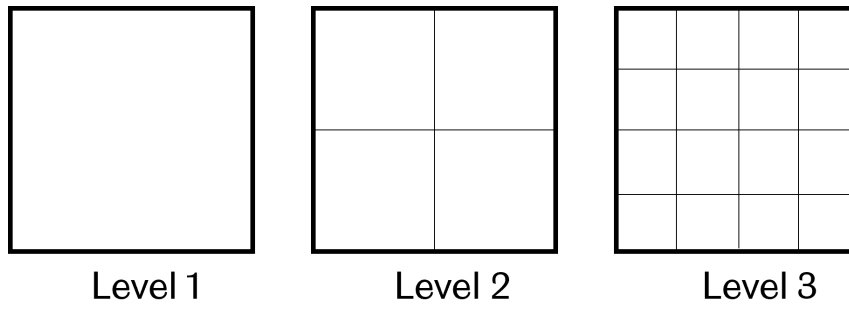
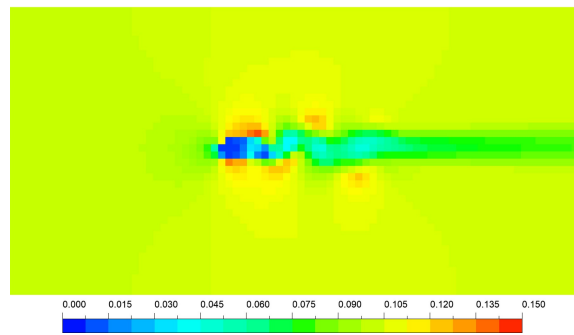
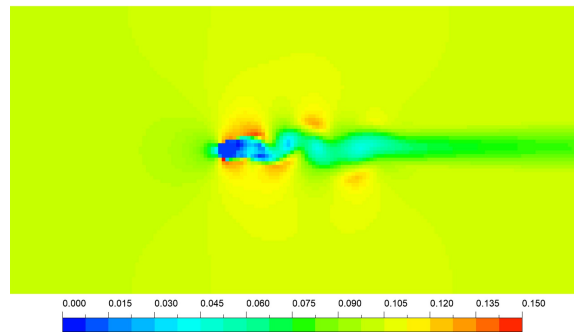


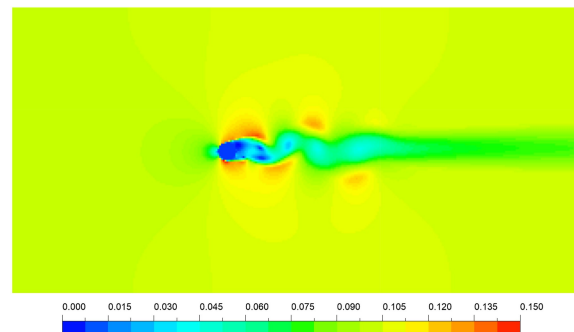
Figure 3.10: Schematic presentation of the grid dimension used in different levels of uniformly refined ROMs.



(a) Grid dimension - Level 1



(b) Grid dimension - Level 2



(c) Grid dimension - Level 3

Figure 3.11: Comparison of the solutions of the flow past an oscillating cylinder problem at $Re = 35000$ between the CFD solution and the proposed ROM obtained from different refinement levels at $t=10s$.

Although the performance of the ROM method can be improved spatially and temporally, these refinements result in an increase in the computational cost which undermines the advantage of the ROM methods to the full order solution. Figure 3.12 shows the online and offline CPU time required to compute up to 200 timesteps with varying mesh size. It shows that the cost of the ROM models remains static with an increased resolution of mesh, and that significant CPU speed-ups are obtained when using the mesh with the largest number of nodes. For the largest mesh, the CPU costs were reduced by a factor of 100 compared to the cost of the high-fidelity model. The offline CPU time listed here includes the time for assembling and solving the matrix for the full model and projecting the POD solution onto the full space, as shown in Figure 3.13. It can be seen that although the ROM is efficient, the increase in terms of mesh density still slows the computational speed of the ROMs, since it involves assembling and solving different dimensional matrices.

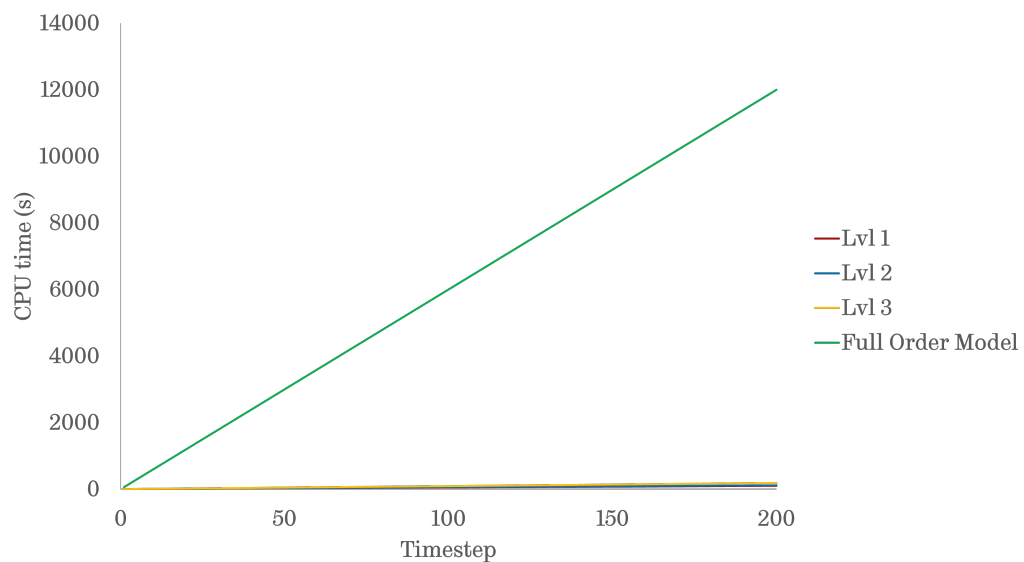


Figure 3.12: Comparison of the online CPU time history on the flow past an oscillating cylinder problem at $Re=5000$ between the full-order CFD solution and ROMs.

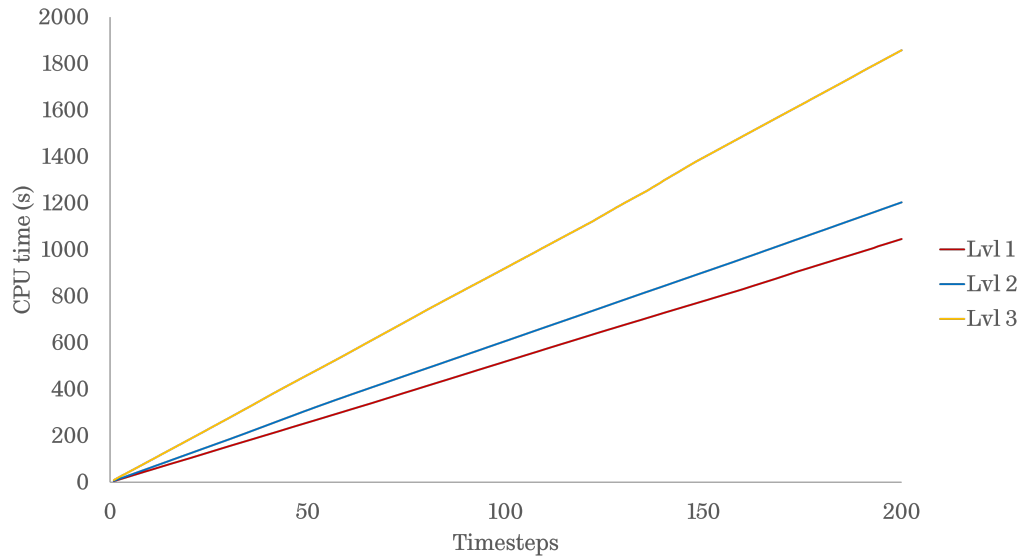


Figure 3.13: Offline CPU time history for the ROM on the flow past an oscillating cylinder at $Re=5000$ (up to 200 snapshots).

3.7 Conclusion

In this chapter, an a-priori comparison of the approximation errors using different POD basis generation approaches is made. In addition, some important outlines for an improved POD basis computation are presented. Finally, the empirical interpolation method is introduced in order to overcome the numerical complexity when evaluating the non-linear term in the reduced order model. A detailed evaluation of the ROM method is presented in a simple case, although the ROM methods can be improved by adding snapshots and/or grids. However, this hinders the performance of the ROM method. Therefore, it is necessary to propose a new multiple and adaptive snapshot method to balance the accuracy and efficiency of ROMs. For multiple and adaptive snapshot details, please refer to Chapter 4. In addition, the ROM has shows a relatively good behaviour in lower Reynolds number cases, however it is not capable of predicting accurate results in high Reynolds number flows, which is common in VAWT applications, or in cases of moving/deforming FSI problems. By introducing the strain tensor, the ROM method shows a good potential to solve FSI problems, and for a detailed discussion please refer to Chapters 5 and 6.

Chapter 4

Locally Refined POD-Galerkin Based ROM

4.1 Introduction

In this chapter, a novel POD-Galerkin based ROM method is presented and discussed as well as some general results obtained in the last decade in the field of reduced order modelling in fluid mechanics. The idea of the original Galerkin method is to project the governing equations onto a finite-dimensional subspace of the full phase space by Holmes [82]. To perform the Galerkin method, the phase space must be an inner product space spanned by a suitable set of basis functions. The novel ROM method is realised by coupling the original POD-Galerkin based ROM with a locally refined algorithm thus improve the computational accuracy without sacrificing the efficiency.

4.2 Methodology

In Chapter 3, a detailed methodology of the traditional uniform POD-Galerkin ROM has been presented and investigated. In this section, a modification based on the traditional uniform ROM method, the adaptive POD-Galerkin ROM is proposed.

4.2.1 Adaptive Snapshot Subspaces

In situations when there is a significant shift in velocity or where there are thin solid entities, the conventional uniform POD-Galerkin ROM does not accurately reflect the flow-field [167]. Therefore, it is necessary to perform a local “refinement” strategy to improve its accuracy. The idea of the adaptive grid refinement process applied in this study is presented in Figure 4.1.

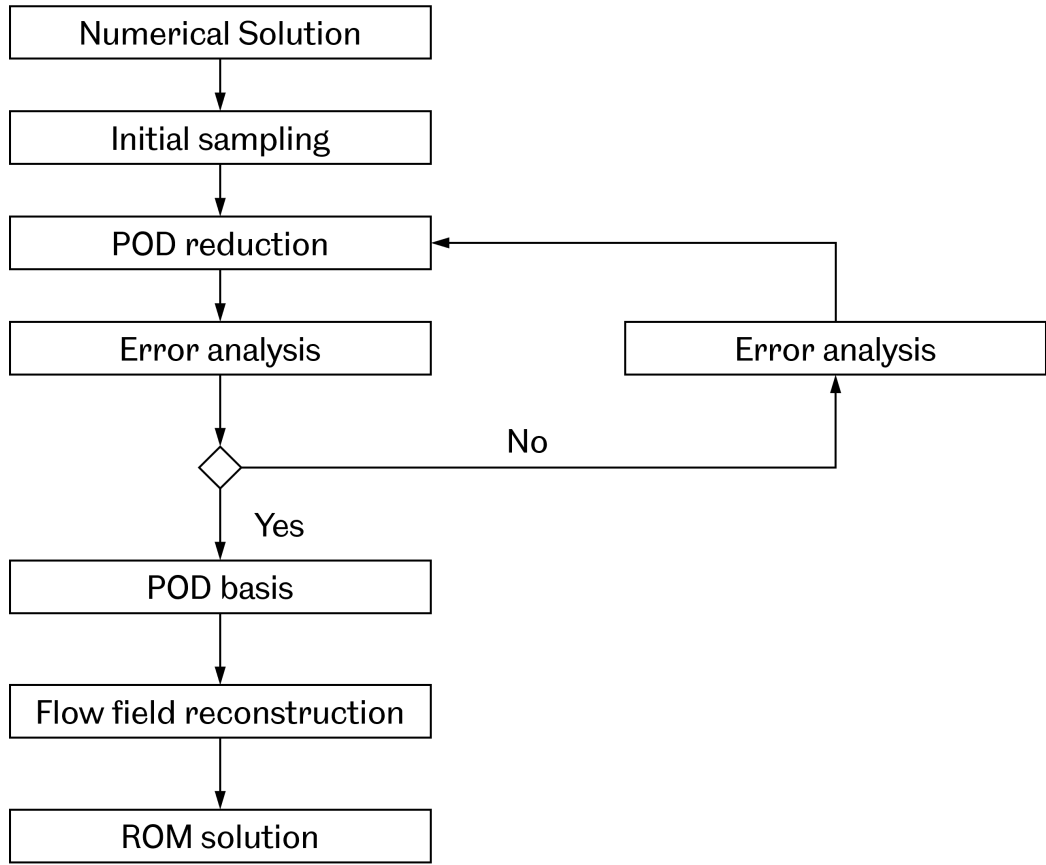


Figure 4.1: Flowchart of the proposed self-adaptive POD-Galerkin ROM

In order to calculate a collection of snapshots, it is necessary to discretise the issue of interest using adaptive finite elements in space. Let $V_1, \dots, V_N \subset V$ be adapted finite element spaces, so that $u_1 \in V_1, \dots, u_N \in V_N$. Let M_1, \dots, M_N be the dimensions of the respective spaces. In this section, an H-adaptive Cartesian Lagrangian finite elements algorithm with a fixed polynomial degree will be built [182]. As a result, the level of refinement that each snapshot finite element space is defined by will be changed.

For discretisation on a fixed domain, linear combinations of snapshots can be represented by linear combinations of finite element coefficient vectors. However, the original snapshots is no longer capable in cases of adaptive spatial discretisation. One possible solution is to replace the original snapshots in terms of a suitable common finite element basis. an additional space $V_+ \subset V$ with finite dimension M_+ is introduced, which satisfies:

1. V_+ is a finite element space of the same type as V_1, \dots, V_N
2. $V_1 + \dots + V_N \subset V_+$ in terms of a vector sum

The first property ensures that all snapshots, once interpolated onto V_+ , function in the same manner as if they were all calculated on a fixed discretization. This is because the first property assures that all discretizations are fixed. Because of the second characteristic, the difference in accuracy between any snapshot and its representation in V_+ is now zero.

In general, setting $V_+ = V_1 + \dots + V_N$ would be too restrictive in the sense that it does not necessarily fulfil the first property. When the snapshots are modified using the quad-tree approach, beginning with a standard starting grid, the resulting scenario is one that is more convenient to deal with. It is well known that the overlay of two such meshes is the smallest common refinement that they share, which means that $V_1 + \dots + V_N = V_+$. A sketch is given in Figure 4.2, where refining different regions of common grid V_0 results in V_1 and V_2 , the finite element space V_+ equals the overlay of both refined meshes, and therefore $V_+ = V_1 + V_2$. Moreover, the mesh of V_+ can be found by repeated local refinements of any snapshot mesh.

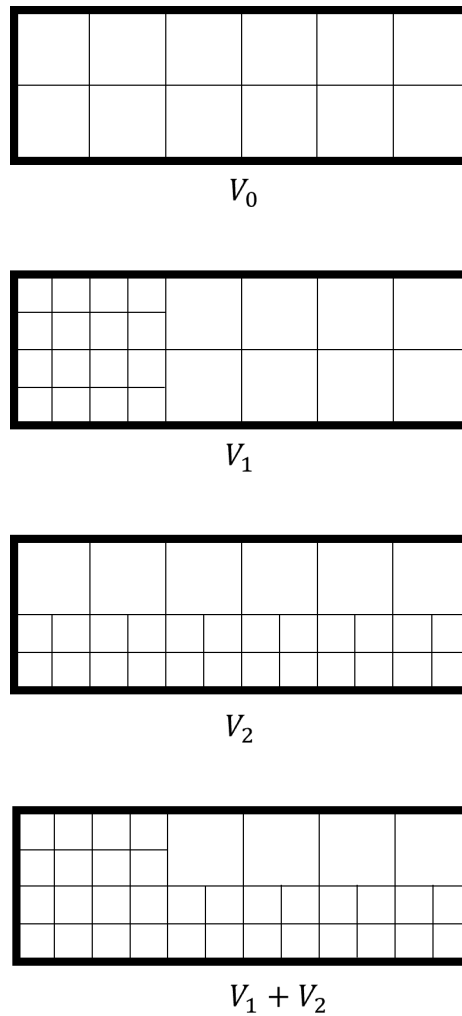


Figure 4.2: Illustration of meshes resulting from refinement by newest vertex refinement based on a common initial grid corresponding to a finite element space V_0

A typical example of the employed adaptive discretisation process is illustrated in Figure 4.1. At the beginning of the adaptive refinement process, the initial POD grid is applied on the entire domain, i.e., the subspace is computed by means of the snapshot data basis. At the beginning of the simulation, this subspace is used to reduce the size of the nonlinear governing matrix, as illustrated in Figure 4.3 (a). From then on, in a loop over all the grids, the differences are detected. If the accumulated difference is larger than a user defined tolerance value, the grid subspace affiliation is changed from the initial to a local-refined sub-domain, as illustrated in Figure 4.3 (b) and (c). It should be noted that, at each time step after the same number of iteration loops, the number and size distribution of the subspace grid are determined by the baseline flow field. In addition, the process can be suppressed manually by adding a local refinement to the area of interest, for example, the area near the aerofoils and tower in the VAWT simulations.

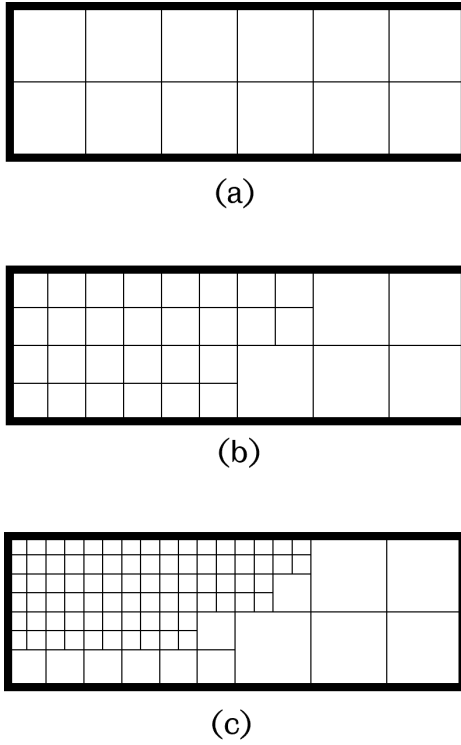


Figure 4.3: A typical example of an adaptive discretisation at different time steps

4.2.1.1 Preparation for the POD method

Recalling that the first step in the computation of a POD with the method of snapshots is the creation of the snapshot, see Section 3.3. For the case of space adapted snapshots, two different ways can be achieved: The first option is to represent all snapshots as members of a common finite element space of all snapshots. The second option is to represent pairs of snapshots as members of common finite element spaces of these pairs.

The implementation for adaptive finite element snapshots is provided in terms of a common finite element space of all snapshots, where $u_1, \dots, u_N \in V_+$. The finite element coefficients of the snapshots are represented with respect to a basis of V_+ in a set of snapshot coefficient vectors $u_1, \dots, u_N \in V_+$ and define a snapshot matrix $U_1, \dots, U_N \in \mathbb{R}^{M_+ \times N}$. Let M_+ be the matrix associated with the V-inner product of functions in V_+ , so that for $u_i, u_j \in V_+$ $(u_i, u_j)_V = U_i^T M_+ U_j$. Then the snapshot Gramian matrix is given by $G = U^T M_+ U$.

Another way to compute the Gramian matrix used in the POD is to create common finite element spaces of pairs of snapshots. For instance, the computation of a single entry of the snapshot Gramian matrix for a pair consisting of $u_i \in V_i$ and $u_j \in V_j$. Let

U_i^{ij} and U_j^{ij} be the finite element coefficient vectors of u_i and u_j with respect to a basis of their common finite element space V_{ij} and let M_{ij} be the matrix associated with the V -inner product of functions in V_{ij} , so that $(u_i, u_j)_V = (U_i^{ij})^\top M_{ij} U_j^{ij}$. This means that the Gramian matrix can be filled by creating finite element spaces V_{ij} of all pairs of snapshots.

Either approach may be used to successfully get the Gramian matrix matrix required for the eigenvalue decomposition that is linked with the method of snapshots. In any event, because of the characteristics of the typical finite element spaces, the only Gramians that need to be determined are the precise ones. The first technique has the benefit of requiring the creation of only a single common finite element space, which is a significant time saver. However, the dimensions of this region are not known, and it is possible that they are exceptionally high. In addition, the second method necessitates the generation of a somewhat higher quantity of lower-dimensional finite element spaces. However, both approaches are adequate in terms of the precision and efficiency with which they compute results.

4.2.1.2 POD basis functions and approximation

The POD basis functions are determined as linear combinations of snapshots by Chapter 3. If the snapshots are represented as members of V_+ , the POD basis functions are automatically members of V_+ and can be computed by linearly combining the snapshot finite element coefficient vectors corresponding to a basis of V_+ . The POD basis functions are able to be implicitly specified as linear combinations of snapshots if the snapshots are represented as members of the original adapted finite element spaces V_1, \dots, V_N . By doing things in this manner, it is possible to prevent the formation of a basis for V_+ ; but, applying a linear operator on a single POD basis function means applying this operator to all snapshots. A POD approximation can be represented in a number of different ways, including in terms of V_+ , in terms of a linear combination of POD basis functions, or in terms of snapshots. All of these approaches are related to the preceding notion. It is possible to develop POD Galerkin models based on adaptive snapshots without having to first establish the common discretisation space if one expresses the POD approximation and the POD basis in terms of the snapshots.

In the very final paragraph of Chapter 3, the theoretical conclusions concerning the V -orthogonal POD projection have been provided in the context of functions in V . Because of this, the outcomes do not change depending on whether the snapshots were generated using a static or an adaptive discretisation. On the other hand, the V -orthogonal projection calls for prior knowledge of the function that is going to be projected; for this

reason, it is only useful as a reference. However, the accuracy of the POD approximation is affected by the snapshot discretisation, which is done during the computation of POD coefficients using a reduced-order model that was produced using Galerkin projection.

When performing the analysis, an adaptive grid discretisation based on a two-dimensional refinement strategy in which an internal node has exactly four children is developed. The strategy is implemented using a quad-tree data structure which was first introduced by Finkel and Bentley [59], and it can be implemented automatically and/or manually. The adaptive discretisation approach employed is initiated on a fixed grid, and at each iteration an inner node is introduced which has four child grids when the velocity difference exceeds the threshold as given by the user.

The self-adaptive iteration computation of the new subspace can be achieved in different ways. The first approach uses the snapshot data bases of the whole n -dimensional precomputed model. At each time step, the refined sub-domain is selected by means of the governing matrix. The eigenvalue problem of the corresponding matrix leads to the refined subspace. Although this method presents the most accurate results, it is necessary to compute the eigenvalue problem for each update, and this is much more computationally inefficient in cases of a smaller tolerance value or when predicting the flow field with dramatic changes. To minimise this additional drawback, a second grid update strategy is proposed. In each update, the new subspace is constructed by using only the relevant grids of the initial subspace or the subspace at the previous iteration loop. However, to keep the extracted are orthonormalized, and therefore the Gram-Schmidt algorithm is added to the adaptive solver.

For the error assessment of u^R , the main results for the uniform discretisation is firstly recalled, then the adaptive case is studied and compared to the uniform discretisation case. In this chapter, it is assumed that $\mu \in S_N$. This indicates that the snapshot set is precise enough for practical applications, to the point where the error introduced by the discretization process is minimal.

4.2.1.3 Uniform discretisation

Assume $V^R \subset V_n$ for $n = 1, \dots, N$. This assumption holds if the snapshots have been computed with static finite elements. From $V^R \subset V_n$, a Galerkin orthogonality between this error and the POD space yields, for all $\forall v \in V^R$

$$a \langle \mathbf{u}_i - \mathbf{u}^R(\mu_i); \mu_i \rangle = 0, \quad i = 1, \dots, N \quad (4.1)$$

Following from coercivity and continuity, the Céa's lemma states the error between the snapshots and the reduced-order solution evaluated at the corresponding values for the training parameters, also known as the POD approximation error. This error is calculated by comparing the reduced-order solution to the snapshots.

$$\|\mathbf{u}_i - \mathbf{u}^R(\mu_i)\| \leq \frac{\gamma(\mu_i)}{\alpha(\mu_i)} \|\mathbf{u}_i - \mathbf{P}^R \mathbf{u}_i\|, \quad i = 1, \dots, N \quad (4.2)$$

Moreover, Equation 4.2 implies $u^D(\mu_i) = u_n$ for $i = 1, \dots, N$. The fact that the snapshots are recovered for large enough R is called asymptotic snapshot reproducibility. For the error with respect to the numerical solution,

$$\begin{aligned} \|\mathbf{u}(\mu_i) - \mathbf{u}^R(\mu_i)\|_V &\leq \|\mathbf{u}(\mu_i) - \mathbf{u}_i\|_V + \|\mathbf{u}_i - \mathbf{u}^R(\mu_i)\|_V \\ &\leq \frac{\gamma(\mu_i)}{\alpha(\mu_n)} \|\mathbf{u}(\mu_i) - \mathbf{P}_n \mathbf{u}(\mu_i)\|_V \\ &\quad + \frac{\gamma(\mu_i)}{\alpha(\mu_i)} \|\mathbf{u}_i - \mathbf{P}^R \mathbf{u}_i\|_V, \quad i = 1, \dots, N \end{aligned} \quad (4.3)$$

It is important to note, however, that the first term derives from the offline discretisation, which is only relevant for the setup of the reduced-order model, whereas the second term derives from the online discretisation, which is also relevant for the evaluation time of the reduced-order model. Both of these points should be taken into consideration. In order to achieve the highest possible level of computing efficacy, it is necessary to strike a compromise between the mistakes caused by the finite element discretisation and the POD truncation.

4.2.1.4 Adaptive discretisation

For more general cases, where the snapshots are members of different finite element spaces, the inequalities are no longer true. The assumption $V^R \subset V_i$ for $i = 1, \dots, N$ is usually not satisfied in the adaptive case, instead, $V^R \subset V_+$ and $V_i \subset V_+$ for $i = 1, \dots, N$. As a consequence, the Galerkin orthogonality between the reduced-order error $u_i - u^R(\mu_i)$ and the reduced space V^R for $i = 1, \dots, N$ cannot be implemented directly. Starting with the error between the solution of the reduced-order model and the baseline solution. Due to $V^R \subset V$, for any $\mu \in S$ Galerkin orthogonality and the corresponding Céa's lemma can still be derived as follows, for all $\forall v \in V^R$

$$a \langle \mathbf{u}_i - \mathbf{u}^R(\mu_i), \mathbf{v}; \mu_i \rangle = 0 \quad (4.4)$$

$$\|\mathbf{u}_i - \mathbf{u}^R(\mu_i)\|_V \leq \frac{\gamma(\mu_i)}{\alpha(\mu_i)} \|\mathbf{u}(\mu) - \mathbf{P}^R \mathbf{u}(\mu)\|, \quad i = 1, \dots, N \quad (4.5)$$

Contributions from the snapshot computation and the POD truncation are able to be separated out on the right-hand side of Céa's lemma 4.5. Only $\mu \in S_N$ is taken into consideration so that the mistake that is related with the discretization of the adaptively refined domain may be eliminated. The Céa lemma for the reduced-order model and the characteristics of orthogonal projections are derived after the first step of adding a zero to the right-hand side of the lemma, for $i = 1, \dots, N$,

$$\begin{aligned} & \|\mathbf{u}(\mu_i) - \mathbf{u}^R(\mu_i)\|_V \\ & \leq \frac{\gamma(\mu_i)}{\alpha(\mu_i)} \|\mathbf{u}_i - \mathbf{P}^R \mathbf{u}_i\|_V + \frac{\gamma(\mu_i)}{\alpha(\mu_i)} \|\mathbf{u}(\mu_i) - \mathbf{u}_i\|_V, \quad i = 1, \dots, N \end{aligned} \quad (4.6)$$

and this yields, for $i = 1, \dots, N$,

$$\begin{aligned} & \|\mathbf{u}(\mu_i) - \mathbf{u}^R(\mu_i)\|_V \\ & \leq \|\mathbf{u}_i - \mathbf{P}^R \mathbf{u}_i\|_V + \frac{\gamma(\mu_i)^2}{\alpha(\mu_i)^2} \|\mathbf{u}(\mu_i) - P_i \mathbf{u}(\mu_i)\|_V, \quad i = 1, \dots, N \end{aligned} \quad (4.7)$$

This means that for parameter values in S_N , the error between the numerical and the reduced-order solution can be split into contributions from the projection of the respective snapshot onto the POD space and from the projection of the true solution onto the respective snapshot finite element space. Additionally, this means that the error can be broken down further into contributions from the projection of the true solution onto the respective snapshot finite element space. The POD projection error disappears when there is no POD truncation, which means that for $R=D$, and this is a variation of the conclusions that are already known from the greedy reduced basis theory [32].

However, in general $V^R \not\subseteq V_i$ for $i = 1, \dots, N$, and the Céa's lemma for $u_i - u^R(\mu_i)$ is no longer be true. A straightforward approach is using the results from above to obtain

$$\begin{aligned} & \|\mathbf{u}(\mu_i) - \mathbf{u}^R(\mu_i)\|_V \\ & \leq \|\mathbf{u}_i - \mathbf{u}(\mu_i)\|_V + \|\mathbf{u}(\mu_i) - \mathbf{u}^R(\mu_i)\|_V \\ & \leq \frac{\gamma(\mu_i)}{\alpha(\mu_i)} \left(1 + \frac{\gamma(\mu_i)}{\alpha(\mu_i)} \right) \|\mathbf{u}(\mu_i) - \mathbf{P}_i \mathbf{u}(\mu_i)\|_V \\ & \quad + \frac{\gamma(\mu_i)}{\alpha(\mu_i)} \|\mathbf{u}_i - \mathbf{P}^R \mathbf{u}_i\|_V \end{aligned} \quad (4.8)$$

In any situation, the error that occurs between a snapshot and the solution of the reduced-order model at the corresponding parameter value includes a component from the finite element calculation. This component was absent when the snapshots were taken in a static state.

4.3 Applications

The proposed method is firstly applied to model a special flow field for which there is an analytical solution, and then to a two-dimensional flow past an oscillatory cylinder. The reconstructed ROM solutions are compared to the numerical results as well as analytical solution when it is approachable. In addition, for each case, the error estimation and time analysis results are compared to the corresponding uniform grid ROM solution. It should be noted that this method is not particularly applied for solving wind turbine problems. In contrast, it shows a good capability on solving general FSI simulation. It shows a good compatibility with FSI problems with moving and/or deforming problems, please refer to Chapters 5 and 6. In this chapter, only two simple cases are chosen to validate its accuracy, and for more complicated implementations in 3D, especially in VAWT problems, see Chapters 7 and 8.

4.3.1 Adaptive ROM simulation for Stuart Vortices

To stress the necessity and importance of the adaptive grid refinement, the Stuart vortices, a special flow field with an analytical solution is selected as another application of the approaches proposed in this chapter. In 1967, Stuart [158] introduced an exact solution of the steady two-dimensional Euler equations which has since become well-known in the fluid dynamics community as the "Stuart vortices". The vorticity equation for two-dimensional motion of an inviscid incompressible fluid flow is given as follows:

$$\frac{\partial}{\partial t} \Delta \psi + \frac{\partial \psi}{\partial y} \frac{\partial}{\partial x} \Delta \psi - \frac{\partial \psi}{\partial x} \frac{\partial}{\partial y} \Delta \psi = 0 \quad (4.9)$$

where ψ is the stream function, t is the time, x is the coordinate in the direction of the mean flow and y is the coordinate normal to that direction. Stuart's solution to Equation (4.9) consists of an infinite periodic array of vortices described by the stream function:

$$\psi(x, y) = \ln \left(\sqrt{A^2 - 1} \cosh(y) + A \cos(x) \right) \quad (4.10)$$

Since $A \geq 1$, the flow ranges from the laminar shear layer to the flow due to a set of point vortices on the x axis. For a non-trivial demonstration of the local refined POD-Galerkin based ROM, the time-dependent solution is required. Applying the Galilean transformation to the steady state solution, the time-varying solution yields the following:

$$u_x = \frac{A \sinh(y)}{\sqrt{A^2 - 1} \cosh(y) + A \cos(x - ct)} + c \quad (4.11)$$

$$u_y = \frac{\sqrt{A^2 - 1} \sinh(x - ct)}{\sqrt{A^2 - 1} \cosh(y) + A \cos(x - ct)} \quad (4.12)$$

where c is the convection velocity. It should be noted that the solution is periodic in the x -direction, in the y -direction the velocity flow field extends to $\pm\infty$, and for all practical calculations the domain is bounded in the range $y = \pm 3$. Hence the spatial domain is defined by the rectangular domain $\Omega = [-2\pi, 2\pi] \times [-3, 3]$. For the numerical examples, the convection velocity c is set to be $c = 1$ and a characteristic snapshot of the Stuart vortices is shown in Figure 4.4.

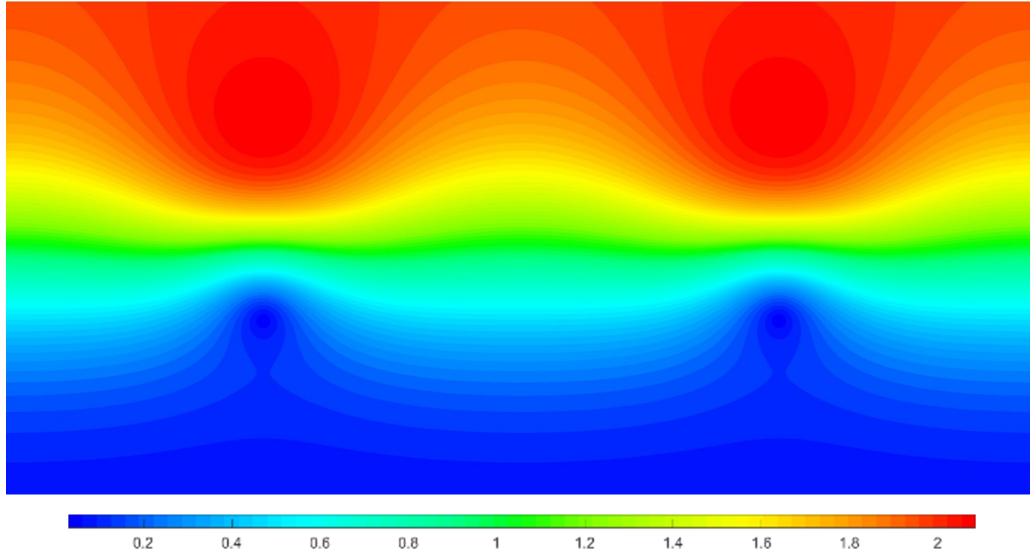


Figure 4.4: Velocity field snapshot of the Stuart vortices at $t = 10\pi$ second.

The ensemble of snapshots for the ROM consists of 100 uniformly distributed snapshots over the period $T = 2\pi$ second. The domain is then uniformly discretised in 30×15 , 60×30 , 120×60 , 240×120 and 480×120 grids in the x - and y - directions, respectively. In each case, the Galerkin method is applied to predict the velocity flow field at $T = 10\pi$ second, and the rebuilt ROM solution is compared to the analytical solution obtained from Equations 4.11 and 4.12. The first six dominant POD modes, which cover

more than 99.9% of the overall kinematic energy, are selected to perform the following calculation. The Galerkin integration is performed by substituting equation (3.33) onto the first six POD modes. The rebuilt velocity flow fields and the differences to the analytical solution of 5 cases are shown in Figure 4.5. For each case, the overall time cost, error and the weighted velocity difference (Equation (4.15)) between the rebuilt velocity flow field and the analytical solution are presented in Table 4.1.

Table 4.1: Time costs and velocity differences for the uniform discretisation.

Grids	Time (s)	Error (%)	Weighted Difference
30×15	0.593	45.5	1.88
60×30	0.688	25.0	0.0817
120×60	0.884	10.0	0.00303
240×120	3.09	2.78	0.000298
480×240	9.31	1.02	0.0000257

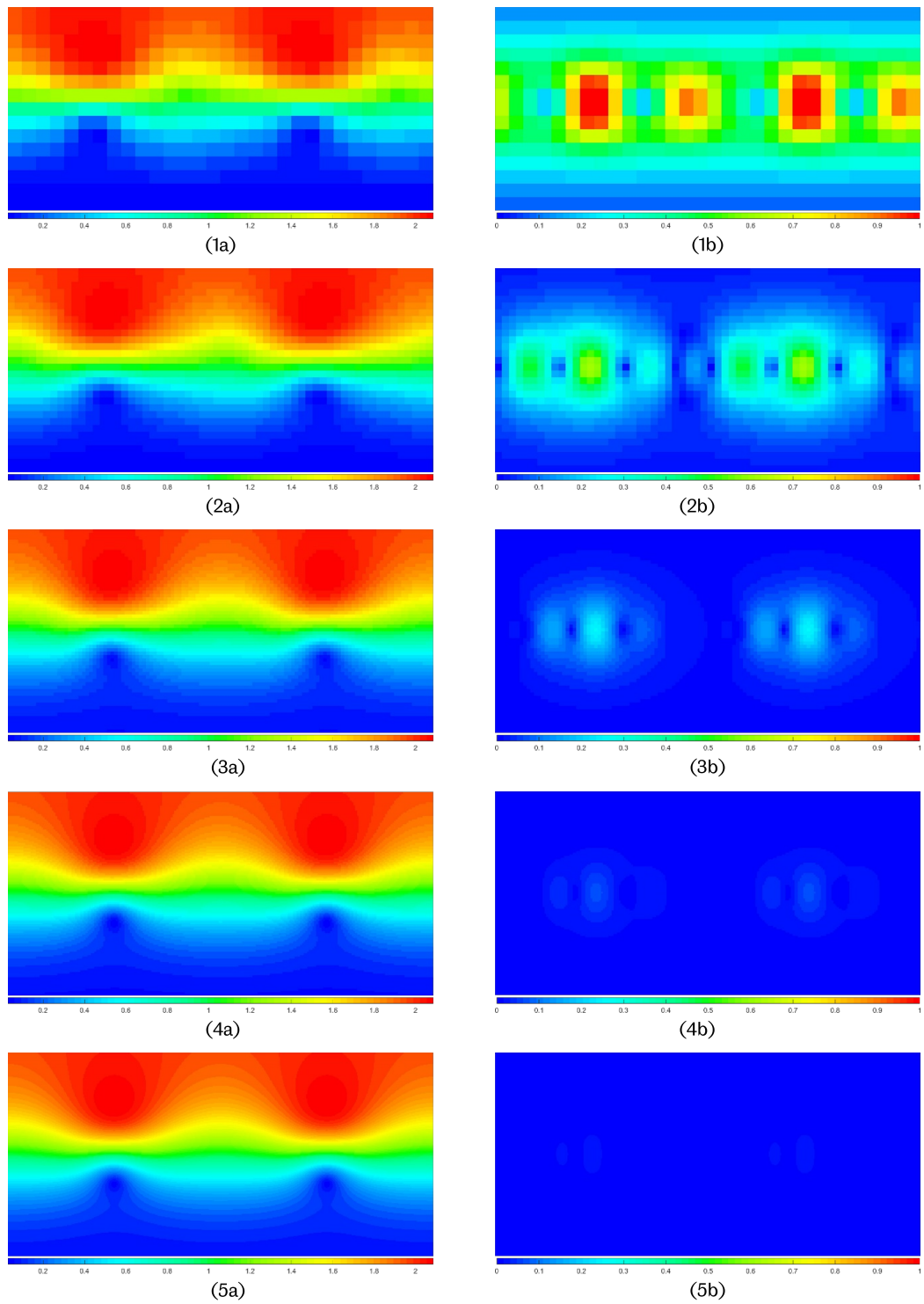


Figure 4.5: Rebuilt velocity flow field and the velocity difference at $t = 10\pi$ second to the analytical solution obtained from different uniform grids. (1). 30×15 grids, (2). 60×30 grids, (3). 120×60 grids, (4). 240×120 grids and (5). 480×240 grids; (a). the rebuilt velocity flow field and (b). the velocity difference to the analytical solution.

In the cases of the adaptive refinement POD-Galerkin ROM, the ensemble of snapshots is the same as the ones for the uniform discretisation. A typical example of the adaptive local refinement strategy is shown in Figure 4.6, where the region I and III are the original mesh discretisation and the region II is the refined discretisation with one level mesh refinement. As explained in Chapter 3, this grid is quadrupled when the gradient of the velocity components of the snapshots at the vortices exceeds the user-defined criteria. An illustrative example is shown in Figure 4.7.

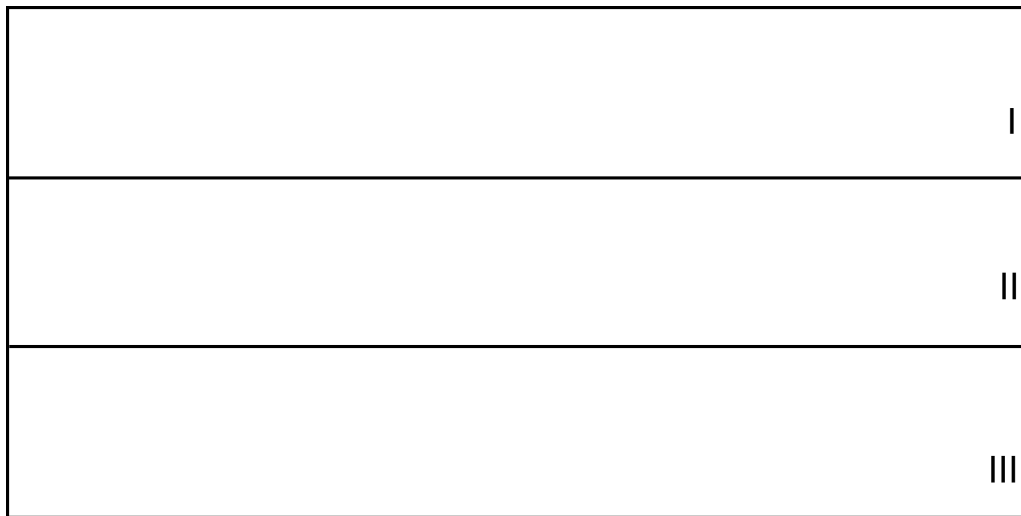


Figure 4.6: Adaptive discretisation for the Stuart vortices reduced order modelling.

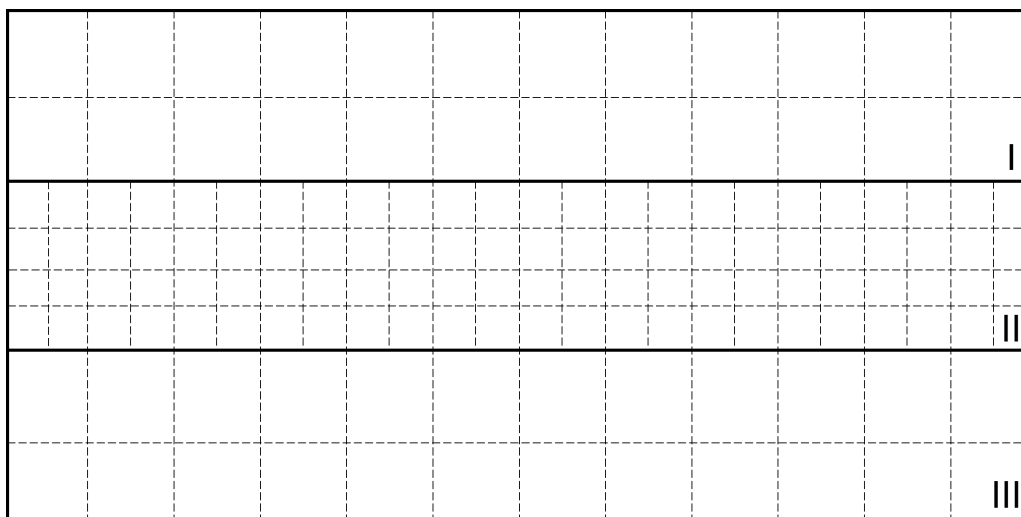


Figure 4.7: Illustrative example of the adaptive mesh refinement for the Stuart vortices solution.

Similar to the uniform discretisation, the first six dominant POD modes are selected

to perform the following calculation. The rebuilt velocity flow fields at time 10π second, using the adaptively refined mesh and the differences to the corresponding analytical solution of 4 cases, namely 30×15 – adaptive, 60×30 – adaptive, 120×60 – adaptive, 240×120 – adaptive, are shown in Figure 4.8. For each case, the overall time cost, maximum velocity difference, weighted difference between the rebuilt velocity flow field and the analytical solution are summarised in Table 4.2.

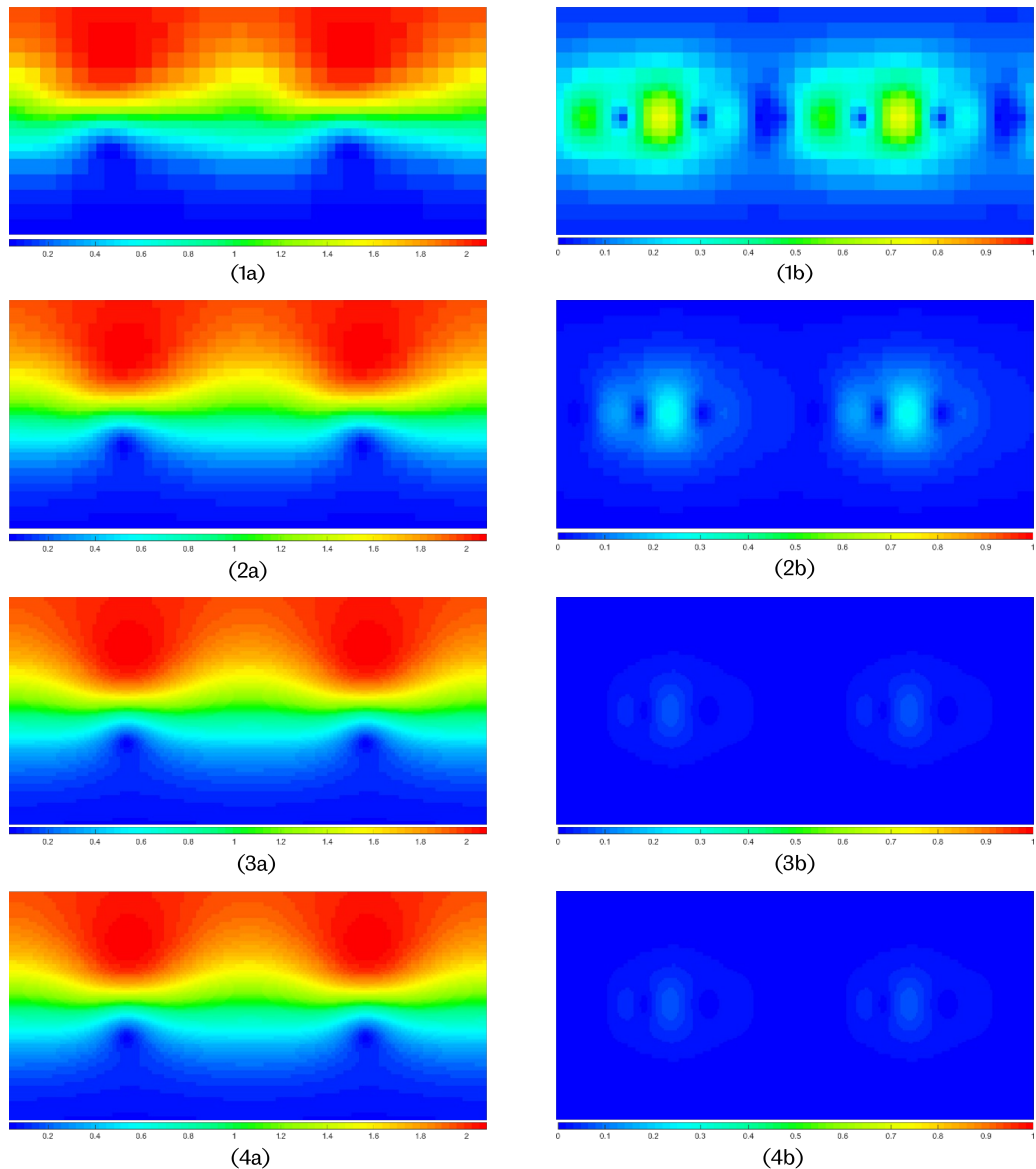


Figure 4.8: Rebuilt velocity flow field and the velocity difference at $t = 10\pi$ second to the analytical solution obtained from different adaptively refined grids. (1). 30×15 – adaptive grids, (2). 60×30 – adaptive grids, (3). 120×60 – adaptive grids, and (4). 240×120 – adaptive grids; (a). the rebuilt velocity flow field and (b). the velocity difference to the analytical solution.

Table 4.2: Time costs and velocity differences for the adaptively refined discretisation.

Grids	Time [s]	Maximum Difference	Weighted Difference
30×15 - adaptive	0.628 (+5.84%)	0.362 (-57.10%)	0.805 (-20.50%)
60×30 - adaptive	0.866 (+25.77%)	0.138 (-42.74%)	0.0468 (-44.8%)
120×60 - adaptive	2.07 (+133.90%)	0.0376 (-19.19%)	0.00245 (-62.46%)
240×120 - adaptive	6.23 (+101.54%)	0.0125 (-47.11%)	0.000158 (-55.14%)

As shown in Table 4.2 and Figure 4.9, the new adaptive POD-Galerkin ROM approach shows a much better accuracy compared to the base uniform discretisation. Although the overall time cost of the adaptive discretisation strategy is longer than the uniform strategy, and it is much quicker than the refined strategy. For instance, the maximum difference of the 120×60 - adaptive, the locally refined grid discretisation based on the uniform grid 120×60 , is 62.46% less than the uniform grid discretisation 120×60 . However, the time cost is increased by 133.90% compared to the uniform grid discretisation 120×60 , but this is still much shorter than for the overall refined discretisation 240×120 takes. Although the increase in the time cost may overshadow the merit of this method, compared to the benefits of improving the accuracy and the computational cost between the ROM approach and the numerical method, this sacrifice in the computational cost due to the self-adaptive spatial discretisation is therefore beneficial.

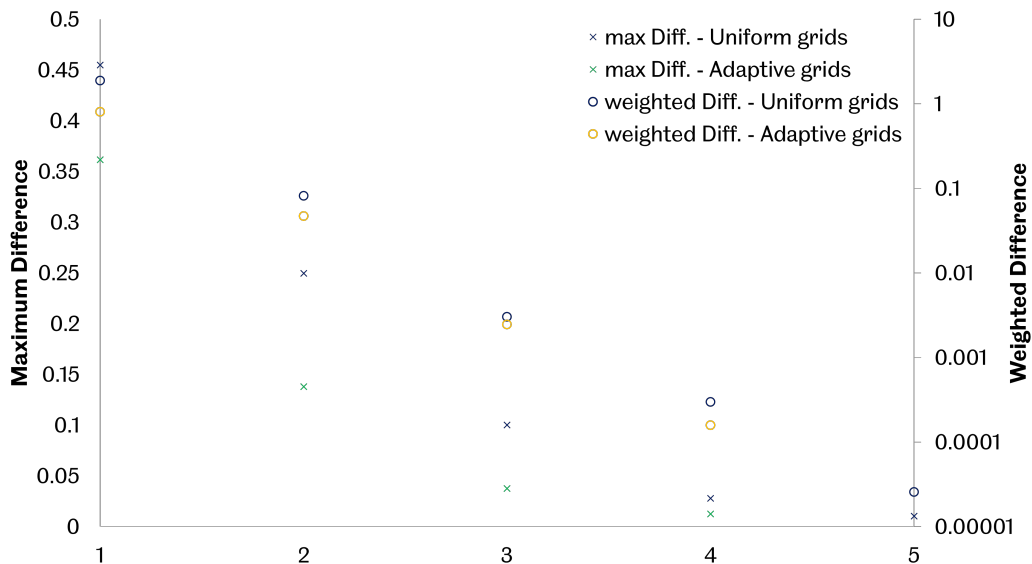


Figure 4.9: Velocity differences for different numerical discretisations at $t = 10\pi$ second.

4.3.2 Adaptive ROM simulation for flow around an oscillating aerofoil

The proposed new method is applied to model an oscillating aerofoil. A two-dimensional pitching and plunging aerofoil is studied as the application of the self-adaptive POD-Galerkin model, but other motions can also be applied using a similar approach. The numerical solution is based on the aerofoil oscillation experiments performed by Sidlof, Vıcek and Stepan [191] and CFD snapshots are pre-calculated in order to build the ROM.

The CFD snapshots are modelled according to [191]. For more details of the simulation, please refer to Section 5.3.2. Here, only the results related to the locally refinement approach is listed.

The self-adaptive POD-Galerkin ROM procedure was executed by implementing a MATLAB subroutine and the results obtained are discussed. The ROM is built using a pre-calculated numerical solution.

The self-adaptive ROM modes are computed from 400 snapshots of the simulation data that covers four whole periods of oscillation. The domain is uniformly discretised in 160×40 , 320×80 , 640×160 , and 1280×320 grids in x - and y - direction, respectively. Then, three different self-adaptive ROM models based on the firstly created uniform ones, namely 160×40 , 320×80 , 640×160 , are built. For each case, the overall computational cost, maximum velocity difference, weighted difference between the rebuilt velocity flow field and the analytical solution are summarised. An example of the POD results is shown in Figure 4.11. For each case, the energy percentage that the POD mode covers decreases monotonically. As shown in Figure 4.10, the POD modes decrease monotonically. 99.5% of the overall energy is covered by at least first 10 POD modes, which are selected to perform the following calculation. The flow field patterns of the limit cycle oscillation (LCO) at $Re = 173,000$ are chosen in order to demonstrate the vorticity contours of each of the POD modes, and the mean flow of the LCO, as shown in Figure 4.11. The selected POD modes associated with the velocity are qualitatively presented. These modes do not present the flow structures but can provide valuable information about the sparse correlations, see for example [30]. The symmetric/antisymmetric patterns about the wake line have been previously reported [133]. Compared to the flow pattern of the POD modes when using the uniform ROM approach, the self-adaptive ROM presents more details in the region where there is a large velocity deviance, such as in the vicinity of the aerofoil, and this provides the capability to predict more accurate results.

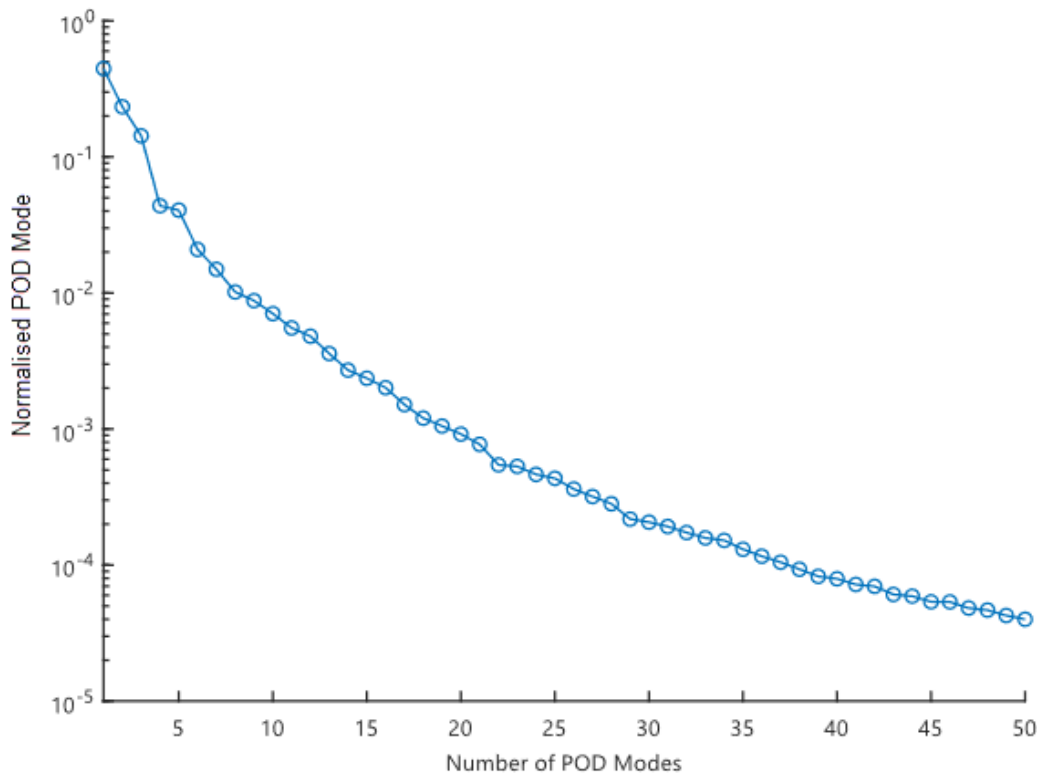


Figure 4.10: The energy spectrum of the POD modes in the case of the limit cycle oscillation at the Reynolds number $Re = 173,000$.

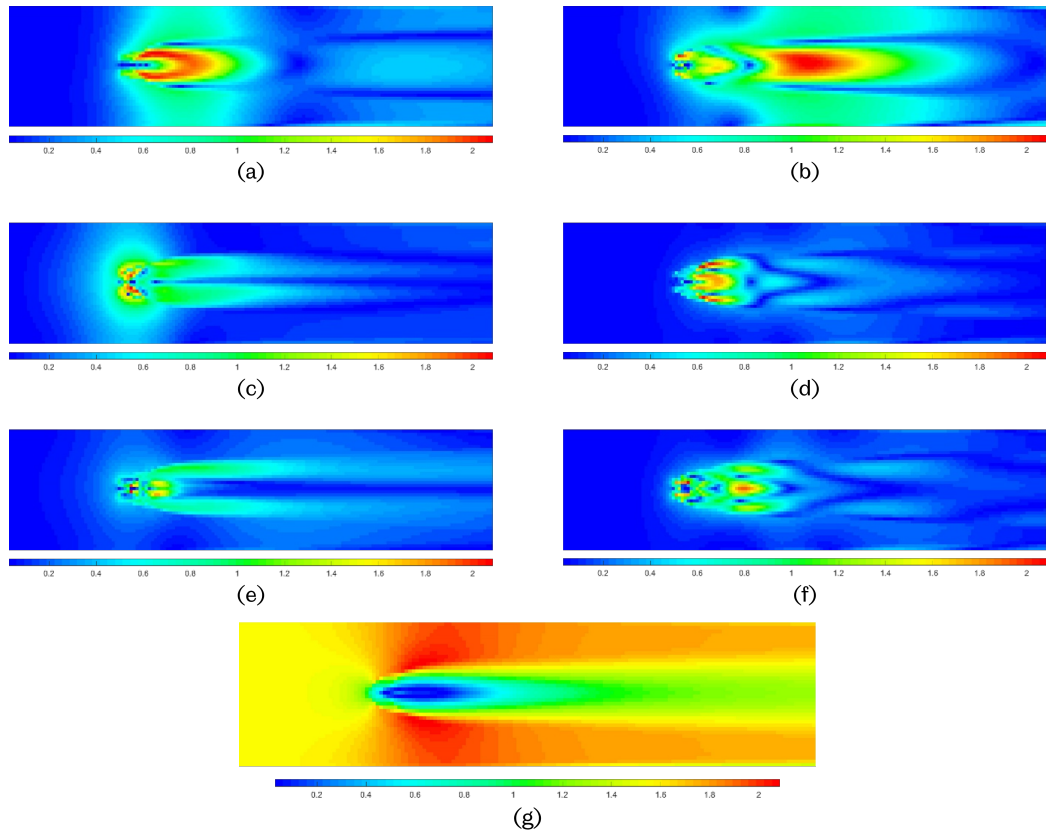


Figure 4.11: Vorticity contours of the first 6 POD modes and the mean flow for a two-dimensional pitching and plunging aerofoil in the case of the limit cycle oscillation ($Re=173,000$) (a) – (f): first six POD modes, (g): Vorticity contours of the mean flow.

Three different kinds of flow structures at the same time step have been investigated: the velocity flow field computed by the CFD approach, the rebuilt flow field from the uniform ROM with the same quality of discretisation, and the self-adaptive POD-Galerkin reduced order models (after five iterations). For the uniform POD-Galerkin ROM, with the dissipation of the temporal coefficients, the vortex structures have disappeared after several periods, and it degenerates to a flow that is similar to its mean flow. In addition, the results show a similar trend compared to the those obtained in the application with a stationary flow field. Compared to the numerical CFD solution, all the rebuilt flow fields are not perfectly accurate due to the large motion of the aerofoil. However, compared to the uniform POD-Galerkin approach, the self-adaptive POD-Galerkin reduced order models are more accurate close to the aerofoil due to the adaptive grid discretisation but with an acceptable sacrifice in the computational cost. In other words, the adaptive ROM is more computationally efficient than the uniform ROM when the acquired accuracy level is given.

To further show the capacity of the model more clearly, three different kinds of flow structure at the same time steps have been investigated: the velocity flow field computed by the numerical approach, the rebuilt flow field from the ROM with a uniform grid, and the self-adaptive POD-Galerkin ROM models. Five different time step snapshots of the limit cycle oscillation at Reynolds number $Re = 173,000$ are selected as an example. With this decomposed solid domain, the dynamics for this prescribed large solid motion problem and the corresponding adapted discretisation which have been shown in Figure 4.12, where different grayscales indicate five different adapted grid iterations. The local refinement concentrates in the vicinity of the aerofoil as well as the wake region to minimise the velocity variance within reduced order modelling process, and it varies at different time step. The accuracy of the adaptive reduced order model is preserved to be almost the same in comparison to the numerical solution after five iteration. On the contract, the reconstruct flow fields using the uniform ROM are not perfectly accurate due to the large motion of the aerofoil. It fails to accurately predict the flow field at several time steps, and the vortex structure disappeared after several periods, and it degenerates to a flow that is similar to its mean flow.

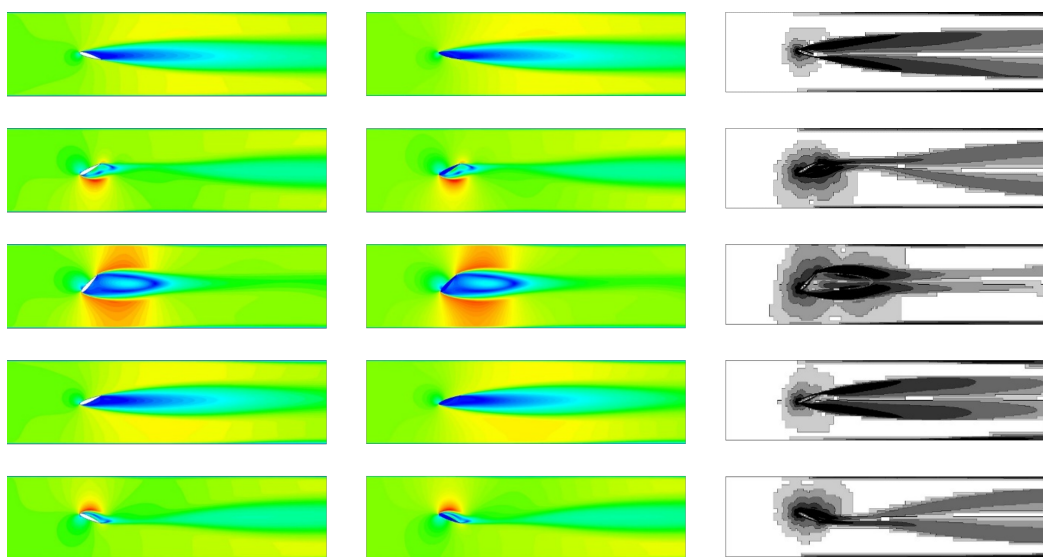


Figure 4.12: Self-adaptive solution for a two-dimensional pitching and plunging aerofoil in the case of the limit cycle oscillation ($Re=173,000$) at different snapshots. Left: numerical solution; Middle: reconstructed flow field using self-adaptive ROM; Right: grid refinements.

To quantify the performance of the self-adaptive POD-Galerkin ROM, the reconstructed dynamic system of the most dominant modes, i.e. the first ten modes, and these are obtained by determining the adaptive projection onto these modes, and this is compared

to the ROM using the same quality of the uniform grids. The phase portrait for the case of the limit cycle oscillation at $Re = 173,000$ is shown in Figure 4.13, where the different lines and symbols indicate the results obtained from the experimental data, which is considered as the benchmark case, the self-adaptive Galerkin-based ROM and the POD-Galerkin projection using a uniform mesh. The presentation of the plunge profile against the pitch angle is plotted after the convergence to the limit cycle. The phase trajectory rotates counter clockwise, which increases the plunge amplitude, decreases the pitch amplitude and decreases the phase difference. This approach shows the very good capability in the capturing of the basic dynamics and the sustaining of the system energy by using the first ten POD modes, whereas, in contrast, the traditional Galerkin-based ROM fails to accurately capture the flow field.

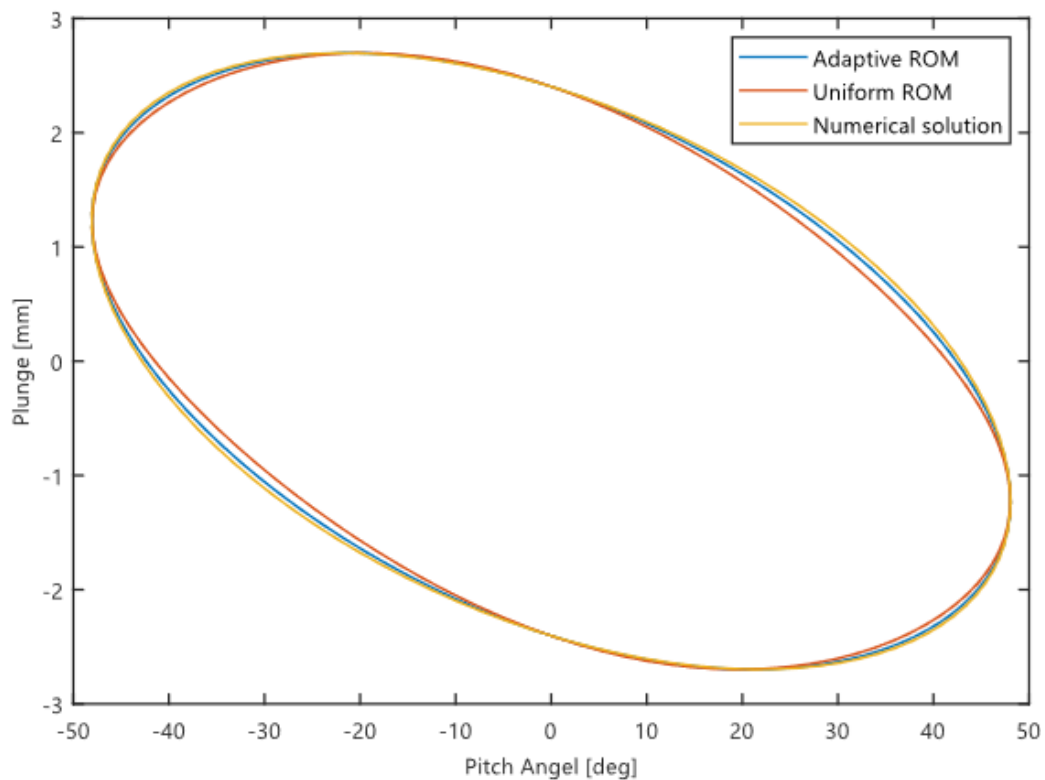


Figure 4.13: A comparison of the POD-Galerkin results using the adaptive and uniform grid discretisation for the flow passing a pitching and plunging aerofoil in the case of a limit damping oscillation at a Reynolds numbers $Re = 173,000$.

Compared to the uniform ROM approach, the proposed novel ROM more accurately predicts results for both limit cycle oscillation cases, as summarised in Table 4.3. Although this new method is slightly more time-consuming than the uniform ROM approach with the same level of minimum grid size, the shape, frequency and amplitudes

are closer to the experimental data and numerical solution, the maximum difference to the experimental data is much smaller than the uniform ROM solution. Compared to the substantial benefits of improving the accuracy and the computational cost between the ROM approach and the numerical method, this sacrifice in the computational cost due to employing the self-adaptive spatial discretisation is therefore very beneficial. The proposed ROM method is still more computationally accurate and efficient compared to the same level uniform ROM solution.

Table 4.3: Time costs and velocity differences for the uniform adaptively refined discretisation.

Grids	Time [s]	Maximum Difference	Weighted Difference
160×40	20.14	4.23	1.23
320×80	20.37	2.34	0.102
640×160	32.25	1.38	0.0931
1280×320	163.35	0.56	0.0198

4.4 Conclusion

In this chapter, a much more accurate and efficient strategy for solving the reduced order problems is presented. The underlying system of governing equations is motivated by implementing adaptive snapshot subspaces. The new proposed method is first applied to model a two-dimensional flow passing an oscillating circular cylinder with adaptively refinement, and then for a special flow field for which there is an analytical solution with a custom region refinement strategy. The reconstructed ROM solutions are compared to the numerical results as well as the analytical solution when it is approachable. In addition, for each case, error estimation and time analysis are compared to the corresponding uniform grid ROM solution. Both the ROM results show a relatively good agreement with the CFD and analytical solution regarding the velocity and displacement fluctuations. Overall, the new adaptive ROM approach is much more computationally efficient than the uniform ROM when the required accuracy level is given.

Chapter 5

Locally Refined POD-Galerkin Based ROM with Moving Fluid-Solid Interface

5.1 Introduction

In this chapter, a POD-Galerkin based reduced-order model with moving fluid-solid interface has been proposed by projecting the governing Navier-Stokes equation onto the POD modes. Some general results obtained in the last decade in the field of reduced order modelling in fluid mechanics are presented. The idea of the Galerkin method is to project the governing equations onto a finite-dimensional subspace of the full phase space [82]. To perform the Galerkin method, the phase space must be an inner product space spanned by a suitable set of basis functions. The POD is employed to capture more energy with a small number of basis functions.

In this chapter, only rigid domains are taken into consideration. The methodology of the proposed approach is firstly introduced, and then, the method applied to the flow past an oscillatory cylinder, and additional cases where flow past a large amplitude pitching and plunging aerofoil at higher Reynolds numbers. For FSI problems with flexible solid bodies, please refer to Chapter 6.

5.2 Methodology

In this part, a novel POD-Galerkin based ROM is suggested for the purpose of solving scenarios in which the interface between the solid domain and the fluid domain flows while the solid itself is assumed to be stiff. Please refer to Chapter 6 for examples whose interfaces have been known to distort. The purpose of this method is to solve the problem of a moving solid body by first considering a fixed grid that contains the entire time-variant grid (both fluid and solid), and then interpolating the fluid and the solid velocity field

from the time variant grid to the locally refined grid. This method was proposed in order to solve the problem. Following this step, the POD basis is computed for the global velocity field (both fluid and solid) on the fixed uniform grid. After this, a characteristic function is inserted in order to monitor the various domains.

Considering an incompressible fluid in a rigid domain Ω , with the density ρ_F and viscosity μ_F . coupled approach can be applied to the governing Navier-Stokes equation [82]:

$$\rho_F \left[\frac{\partial \mathbf{u}}{\partial t} + (\mathbf{u} \cdot \nabla) \right] = -\nabla p + \mu \Delta \mathbf{u} \quad (5.1)$$

where \mathbf{u} is the velocity vector, and p is the pressure. Using the POD method, the velocity flow field can be decomposed onto the truncated POD modes ϕ_i at N modes:

$$\mathbf{u}(\mathbf{x}, t) = \mathbf{u}_0(\mathbf{x}) + \sum_{i=1}^N a_i(t) \mathbf{u}_i(\mathbf{x}) = \sum_{i=0}^N a_i(t) \mathbf{u}_i(\mathbf{x}) \quad (5.2)$$

where $a_0 \equiv 1$, $\mathbf{u}_0(\mathbf{x})$ is the mean velocity flow field; when $i > 1$, $a_i(t)$ are the temporal coefficients, and $\mathbf{u}_i(\mathbf{x})$ are the corresponding POD modes. An ordinary equation governing the temporal coefficients $a_i(t)$ is obtained by substituting the velocity flow field decomposition (Equation (3.33)) into the governing Navier-Stokes equation (Equation (5.1)) and projecting this onto the subspace spanned by the POD modes $\mathbf{u}_i(\mathbf{x})$:

$$\langle \rho_F \left[\frac{\partial \mathbf{u}}{\partial t} + \nabla p - \mu \Delta \mathbf{u}, \mathbf{u}_i(x) \right] \rangle_{\Omega} = 0, \quad i = 1, \dots, N \quad (5.3)$$

where $\langle \mathbf{u}, \mathbf{v} \rangle := \int_{\Omega} \mathbf{u} \cdot \mathbf{v} d\mathbf{x}$ denotes the inner product defined on the subspace. Due to the orthogonality and the free divergence of the POD modes $\mathbf{u}_i(x)$, Equation (3.34) becomes:

$$\rho_F \frac{d}{dt} a_i = \mu_F \sum_{j=0}^N b_{ij} a_j + \mu_F \sum_{j,k=0}^N c_{ijk} a_j a_k + f_i^p, \quad i = 1, \dots, N \quad (5.4)$$

where

$$b_{ij} = \langle \mathbf{u}_i, \Delta \mathbf{u}_j \rangle_{\Omega} \quad (5.5)$$

$$c_{ijk} = -\langle \mathbf{u}_i, (\mathbf{u}_j \cdot \nabla) \mathbf{u}_k \rangle_{\Omega} \quad (5.6)$$

It should be noted that the incompressibility of the POD modes can be used to express f_i^p in a boundary integral form as follows:

$$f_i^p = -\langle \mathbf{u}_i, \nabla \mathbf{p} \rangle_{\Omega} = - \int_{\partial\Omega} \mathbf{p} \mathbf{u}_i \cdot \mathbf{n} dx \quad (5.7)$$

where \mathbf{n} is the outward norm of the domain Ω and the boundary is $\partial\Omega$. The coefficient f_i^p which contains the pressure term \mathbf{p} - can be avoided.

5.2.1 POD-Galerkin based ROM for fluid-structure interactions

5.2.1.1 The governing equations

Consider a rigid body with two dimensions that is submerged in a fluid that cannot be compressed. In Figure 5.1, a simplified diagram of the problem domain of interest is presented. **No slip velocity boundary conditions are applied at the four lateral boundaries.** In this diagram, $\Omega_S(t)$ represents the domain occupied by the moving rigid body, the centre of mass of which is denoted by M ; $\Omega_F(t)$ represents the moving spatial domain upon which the fluid motion is described; and $\Gamma_I(t)$ represents the interface between $\Omega_S(t)$ and $\Omega_F(t)$. The interface $\Gamma_I(t)$ shifts suitably in response to any positional changes made by the stiff body $\Omega_S(t)$.

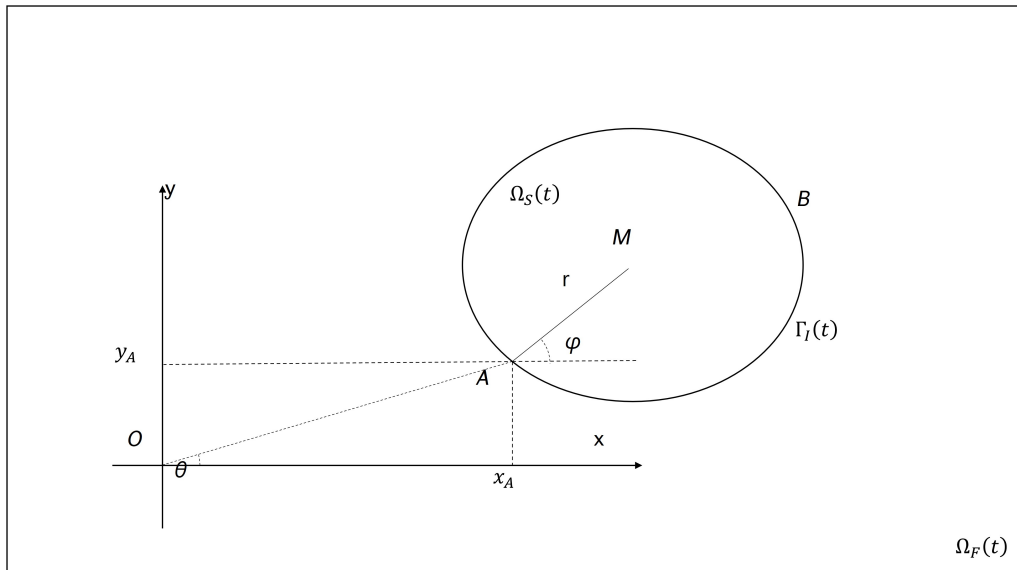


Figure 5.1: Schematic description of problem domain and the notation of FSI problems

The governing equations for fluid motion are given by:

$$\rho_F \left(\frac{\partial \mathbf{u}}{\partial t} + (\mathbf{u} \cdot \nabla) \mathbf{u} \right) = \nabla \cdot \boldsymbol{\sigma}, \quad \forall \mathbf{x} \in \Omega_F(t) \quad (5.8)$$

$$\nabla \cdot \mathbf{u} = 0, \quad \forall \mathbf{x} \in \Omega_F(t) \quad (5.9)$$

$$\mathbf{u}_F = \mathbf{u}_S = \mathbf{u}_{\Gamma_I}(t), \quad \forall \mathbf{x} \in \Gamma_I(t) \quad (5.10)$$

$$\boldsymbol{\sigma}_f \cdot \mathbf{n} = \boldsymbol{\sigma}_s \cdot \mathbf{n}, \quad \forall \mathbf{x} \in \Gamma_I(t) \quad (5.11)$$

$$\mathbf{u}_F = \mathbf{u}_F(\mathbf{x}, t)|_{t=0}, \quad \forall \mathbf{x} \in \Omega_F|_{t=0} \quad (5.12)$$

where $\boldsymbol{\sigma}$ is the viscous stress tensor defined as:

$$\boldsymbol{\sigma} = -p\mathbf{I} + 2\mu\mathbf{E}(\mathbf{u}) \quad (5.13)$$

where \mathbf{I} is the second-order identity tensor and $\mathbf{E}(\mathbf{u})$ is the strain rate tensor:

$$\begin{aligned} \mathbf{E}(\mathbf{u}) &= \frac{1}{2} \left[\nabla \mathbf{u} + (\nabla \mathbf{u})^T \right] \\ &= \begin{bmatrix} \frac{\partial \mathbf{u}_x}{\partial x} & \frac{1}{2} \left(\frac{\partial \mathbf{u}_x}{\partial y} + \frac{\partial \mathbf{u}_y}{\partial x} \right) \\ \frac{1}{2} \left(\frac{\partial \mathbf{u}_x}{\partial y} + \frac{\partial \mathbf{u}_y}{\partial x} \right) & \frac{\partial \mathbf{u}_y}{\partial y} \end{bmatrix} \end{aligned} \quad (5.14)$$

Equations (5.8) and (5.9) are the governing equations of incompressible fluid. Equations (5.10) and (5.11) assume that the interface $\Gamma_I(t)$ between the solid domain $\Omega_S(t)$ and fluid domain $\Omega_F(t)$ is perfect contact. Equation (5.12) is the initial condition where the initial velocity flow field $\mathbf{u}_F(\mathbf{x}, t)$ has to satisfy Equation (5.9). Specifically, in the VAWT simulations, the rotational speed of the blades is given and, moreover, in this chapter, it is assumed to be constant. The translational speed of the solid domain is zero and thus $\mathbf{u}_{\Gamma_I}(t)$ is expressed as:

$$\mathbf{u}_{\Gamma_I}(t) = \boldsymbol{\omega} \times \mathbf{r}, \quad (5.15)$$

where $\boldsymbol{\omega}$ is the angular velocity of the solid domain, namely, a VAWT, \mathbf{r} is the distance vector between the point of interest and the centre of the tower.

The fictitious domain method was developed by Patankar et al [137]. It involves treating the entire fluid-solid rigid domain, also known as the fictitious domain, as if it were a fluid. This is accomplished by extending the Navier-Stokes equations to the solid rigid domain and setting the rigidity constraint on the solid domain to $\Omega_S(t)$, the governing equations for solid domain are given by:

$$\rho_S \left(\frac{\partial \mathbf{u}}{\partial t} + (\mathbf{u} \cdot \nabla) \mathbf{u} \right) = \nabla \cdot \boldsymbol{\sigma}, \quad \forall \mathbf{x} \in \Omega_S(t) \quad (5.16)$$

$$\nabla \cdot \mathbf{u} = 0, \quad \forall \mathbf{x} \in \Omega_S(t) \quad (5.17)$$

$$\nabla \cdot E(\mathbf{u}) = 0, \quad \forall \mathbf{x} \in \Omega_S(t) \quad (5.18)$$

$$\mathbf{u}_F = \mathbf{u}_S = \mathbf{u}_{\Gamma_I}(t), \quad \forall \mathbf{x} \in \Gamma_I(t) \quad (5.19)$$

$$\boldsymbol{\sigma}_f \cdot \mathbf{n} = \boldsymbol{\sigma}_s \cdot \mathbf{n}, \quad \forall \mathbf{x} \in \Gamma_I(t) \quad (5.20)$$

$$\mathbf{n} : \mathbf{E}(\mathbf{u}) = 0, \quad \forall \mathbf{x} \in \Gamma_I(t) \quad (5.21)$$

$$\mathbf{u}_S = \mathbf{u}_S(\mathbf{x}, t)|_{t=0}, \quad \forall \mathbf{x} \in \Omega_S|_{t=0} \quad (5.22)$$

$$(5.23)$$

Combining governing equations of fluid domain and solid domain, the governing equation of the whole domain yields the following:

$$\begin{aligned} \int_{\Omega} \rho \left(\frac{\partial \mathbf{u}}{\partial t} + (\mathbf{u} \cdot \nabla) \mathbf{u} \right) \cdot d\mathbf{x} - \int_{\Omega_S} \mathbf{p} (\nabla \cdot \mathbf{v}) d\mathbf{x} \\ - \int_{\Omega_F} (\boldsymbol{\sigma} \cdot \mathbf{n}) \cdot \mathbf{v} d\mathbf{x} + \int_{\Omega_F} \mathbf{q} (\nabla \cdot \mathbf{u}) d\mathbf{x} = 0 \end{aligned} \quad (5.24)$$

where $\Omega = \Omega_F(t) \cup \Omega_S(t)$. It should be noted that on selecting the appropriate boundary conditions, the pressure terms are cancelled. The Equation (5.24) becomes:

$$\int_{\Omega} \rho \left(\frac{\partial \mathbf{u}}{\partial t} + (\mathbf{u} \cdot \nabla) \mathbf{u} \right) \cdot \mathbf{v} d\mathbf{x} + 2\mu \int_{\Omega} E(\mathbf{u}) : E(\mathbf{v}) d\mathbf{x} + \int_{\Omega_S} E(\boldsymbol{\lambda}) : E(\mathbf{v}) d\mathbf{x} = 0 \quad (5.25)$$

Indicator function \mathbb{I}_{Ω_F} is introduced to determine the location of the solid domain,

$$\mathbb{I}_{\Omega_F}(\mathbf{x}, t) = \begin{cases} 1, & \mathbf{x} \in \Omega_F(t) \\ 0, & \mathbf{x} \in \Omega_S(t) \end{cases} \quad (5.26)$$

Similar to Equation (3.33), the POD method can be applied to the Lagrange multiplier λ and the indicator function \mathbb{I}_{Ω_F} as well. The decompositions of the indicator function and the Lagrange multiplier yields the following:

$$\mathbb{I}_{\Omega_F}(\mathbf{x}, t) = \sum_{i=0}^{N_I} b_i(t) \mathbf{v}_i(\mathbf{x}) \quad (5.27)$$

$$\lambda(\mathbf{x}, t) = \sum_{i=0}^{N_{\lambda}} c_i(t) \mathbf{w}_i(\mathbf{x}) \quad (5.28)$$

where N_I and N_λ denote the number of POD modes truncated for the indicator function \mathbb{I}_{Ω_F} and the Lagrange multiplier λ , respectively. It should be noted that in Equation (5.28), $\mathbf{w}_i(x) \equiv \mathbf{u}_i(x)$, $i = 1, \dots, N$. On substituting the decomposition of the velocity flow field and Equations (5.27) and (5.28) into the modified governing equations (5.26) and projecting onto the corresponding subspace spanned by the POD modes, the governing equation (5.24) for the Galerkin method for FSI problems yield:

$$\begin{aligned} \rho_F \frac{da_i}{dt} + (\rho_S - \rho_F) \sum_{j=1}^{N_I} \sum_{k=0}^{N_u} b_j b_{ijk} \frac{da_i}{dt} + (\rho_S - \rho_F) \sum_{j=1}^{N_I} \sum_{k,l=0}^{N_u} c'_{ijkl} a_k a_l b_j \\ + 2\mu_F \sum_{k=0}^{N_u} d_{ik} a_k + 2(\mu_S - \mu_F) \sum_{j=1}^{N_I} \sum_{k=0}^{N_u} d'_{ijk} a_k b_j \\ = \sum_{j=1}^{N_I} \sum_{k=0}^{N_\lambda} e_{ijk} b_j c_k, \quad i = 1, \dots, N; j = 1, \dots, N_I \end{aligned} \quad (5.29)$$

$$\frac{db_j}{dt} + \sum_{k=0}^{N_u} \sum_{l=1}^{N_I} f_{jkl} a_k b_l = 0 \quad (5.30)$$

$$\sum_{j=1}^{N_I} \sum_{k=0}^{N_u} g_{ijk} a_k b_j = 0 \quad (5.31)$$

where

$$\mathbf{b}_{ijk} = \langle \mathbf{v}_i, \langle \mathbf{u}_j, \mathbf{u}_k \rangle \rangle_\Omega$$

$$\mathbf{c}_{ikl} = \langle \mathbf{u}_i, (\mathbf{u}_k, \nabla) \mathbf{u}_l \rangle_\Omega \quad (5.32)$$

$$\mathbf{c}'_{ijkl} = \langle \mathbf{v}_i \cdot \langle \mathbf{u}_i, (\mathbf{u}_j \cdot \nabla) \mathbf{u}_k \rangle \rangle_\Omega \quad (5.33)$$

$$\mathbf{d}_{ik} = \langle \mathbf{u}_i \cdot \Delta \mathbf{u}_k \rangle_\Omega \quad (5.34)$$

$$\mathbf{d}'_{ijk} = \langle \mathbf{v}_j \cdot \langle \mathbf{u}_i \cdot \Delta \mathbf{u}_k \rangle \rangle_\Omega \quad (5.35)$$

$$\mathbf{e}_{ijk} = \langle \mathbf{v}_j \cdot \langle \mathbf{u}_i \cdot \Delta \mathbf{u}_k \rangle \rangle_\Omega \quad (5.36)$$

$$\mathbf{f}_{jkl} = \langle \mathbf{v}_j \cdot (\mathbf{u}_k \cdot \nabla) \mathbf{v}_l \rangle_\Omega \quad (5.37)$$

$$\mathbf{g}_{ijk} = \langle \mathbf{v}_j \cdot \langle \mathbf{u}_i \cdot \Delta \mathbf{u}_k \rangle \rangle_\Omega \equiv d'_{ijk} \quad (5.38)$$

It should be noted that when N_λ is chosen to be the same as N_u , the number of POD modes truncated for the velocity flow field, the matrix \mathbf{e}_{ijk} becomes identical to the matrix \mathbf{d}'_{ijk} .

5.2.1.2 Mesh motion description

The mesh velocity vector \mathbf{w} may be arbitrarily specified though it has to satisfy the following conditions on boundaries,

$$\begin{cases} \mathbf{w} = \mathbf{v}_S & \text{on } \Gamma_I(t) \\ \mathbf{w} = 0 & \text{on } \partial\Omega_F(t) \setminus \Gamma_I(t) \end{cases} \quad (5.39)$$

where \mathbf{v}_S is the velocity vector of the rigid body nodes on the interface.

In this study, the mesh velocity in the fluid domain is determined by solving the following equation

$$\begin{cases} \nabla \cdot (\lambda(\mathbf{x}) \nabla \mathbf{w}) = 0 & \text{on } \partial\Omega_F(t) \\ \mathbf{w} = \mathbf{v}_S & \text{on } \Gamma_I(t) \\ \mathbf{w} = 0 & \text{on } \partial\Omega(t) \setminus \Gamma_I(t) \end{cases} \quad (5.40)$$

where $\lambda(x)$ is judiciously chosen to control the mesh deformation. In this case, $\lambda(x)$ is taken equal to 1 for all $x \in \Omega_F(t)$.

5.2.1.3 Fluid-rigid body interaction algorithm

The solid Equation (5.32) can be solved by coupling the finite difference and the method of successive displacement. It can be rewritten as follows

$$\begin{cases} \dot{\mathbf{Y}} = \mathbf{A}\mathbf{F} + \mathbf{b} + \left(\frac{d\mathbf{M}}{dt} - \mathbf{C}\right) \\ \mathbf{M}\dot{\Psi} = \mathbf{Y} \end{cases} \quad (5.41)$$

Then, from initial conditions on Ψ and $\dot{\Psi}$, the solution is obtained through iterations until a fixed error of accuracy is reached. To solve the coupling equations, following explicit scheme is used [2]. Suppose that time $t = t_n$, the fluid velocity and pressure fields, the rigid body displacement and position are known. The time step (Δt) of the Navier-Stokes equations solver is same the rigid body equation.

5.3 Applications of the proposed model on FSI of moving interface

The proposed method is first applied to model the two-dimensional flow past an oscillatory circular cylinder, and then a flow-induced vibration simulation on a NACA 0015 aerofoil at various Reynolds numbers. Finally, a forced vibration case of a NACA 0015 aerofoil at Reynolds number 500,000 is introduced to simulate the working condition of

VAWTs. For each case, the reconstructed ROM solutions from the proposed methodology are compared to the numerical results as well as experimental solution when it is possible in order to validate the accuracy and performance of the model. In addition, in order to test the compatibility of the proposed method, refinement strategies introduced in Chapter 4 are applied to both these simulations, and error estimations and time analyses are compared to the corresponding uniform grid ROM solution.

5.3.1 ROM simulation for flow around an oscillating circular cylinder

5.3.1.1 Simulation modelling

The first test case is carried out on the configuration described in Figure 5.2 , where a cylindrical rigid body is attached to a spring that has been immersed in a fluid flow at a relatively low Reynolds number, $Re = 1690$, as described in Section 3.

Mesh and time size sensitivity studies are carried out to determine the appropriate cell face and time step. In the case of the mesh sensitivity study, the Reynolds number is 1690. Five different mesh sizes are investigated, i.e., 8 mm, 4mm, 2 mm, 1 mm, and 0.5 mm, and the associated total number of elements and calculated oscillation amplitudes are presented in Figure 5.2. The amplitude converges at a mesh size of 1 mm and on further refining the mesh size then a 5.4% relative difference is obtained.

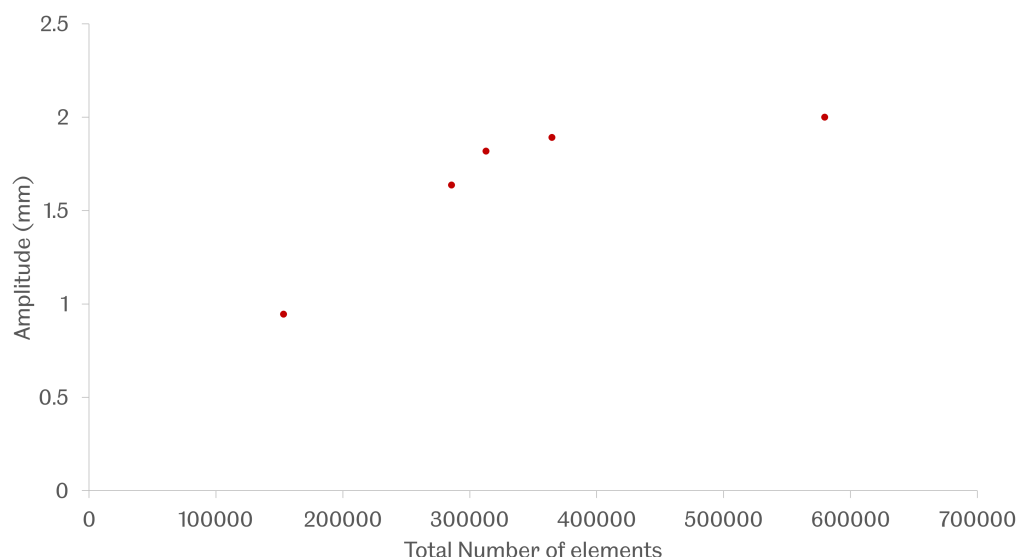


Figure 5.2: Mesh convergence study of the flow-induced vibration of an oscillating circular cylinder.

In the time size sensitivity study, five time steps are investigated, i.e. 1×10^{-5} seconds, 1×10^{-4} seconds, 2×10^{-4} seconds, 5×10^{-4} seconds, and 1×10^{-3} seconds. The associated total number of elements and oscillation frequencies are presented in Figure 5.4 and the amplitude converges at a time size of 1×10^{-4} seconds.

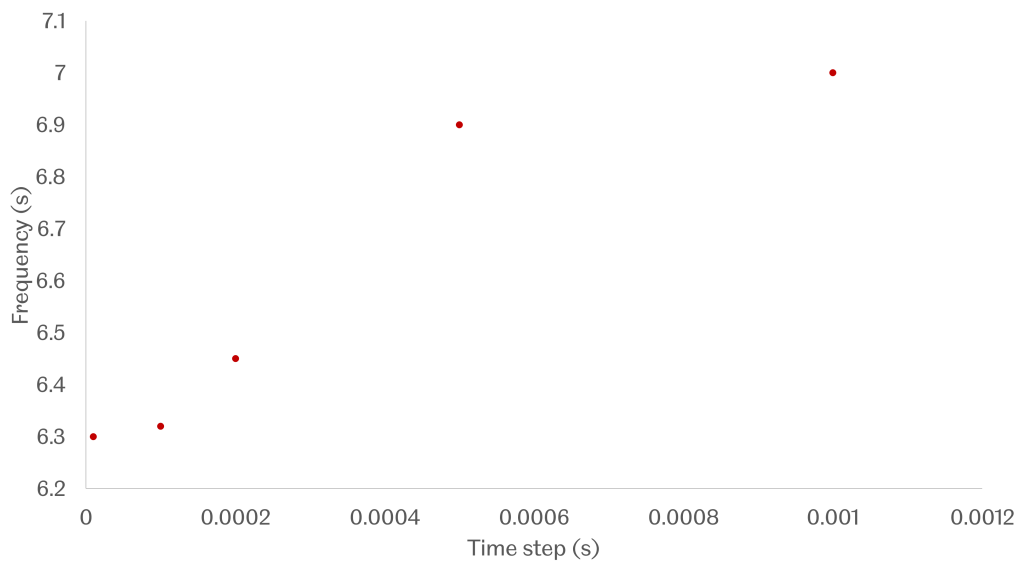


Figure 5.3: Time step convergence study of the flow-induced vibration of an oscillating circular cylinder.

On considering the computational time and accuracy, the mesh size of 1 mm and the time size of 1×10^{-4} seconds are deemed as the appropriate mesh size and time size for the modelling in this study.

As can be seen in Figure 5.5, the simulation's meshes are made up of two separate domains, each with their own set of structural meshes, which are then combined with an overset mesh. When the flow is initially generated, the necessary connection between the background mesh and the overset mesh is immediately established automatically. The process of converting additional solve cells into receptor cells and turning unnecessary receptors into dead cells, such as the cylinder region in the background mesh, is part of the overlap minimisation technique. This technique is used to reduce the amount of overlap that exists between the various component meshes and the background mesh. In the course of this procedure, a solution cell will transform into a receptor cell if it is able to locate an appropriate donor cell with a higher donor priority. By default, higher donor preference is given to cells with smaller sizes. Therefore, the solver will attempt to derive the solution on the finest local mesh without requiring any more input from the user in locations where there is mesh overlap. The fluidic model consists of 158,610

nodes and 579,632 elements while the structural part consists of 2595 nodes and 2422 elements, as shown in Figure 5.4. The time-step size is 1×10^{-4} seconds and the number of nonlinear iterations per time step is 500. A loose coupling strategy was applied in order to couple both the fluidic and structural domains.

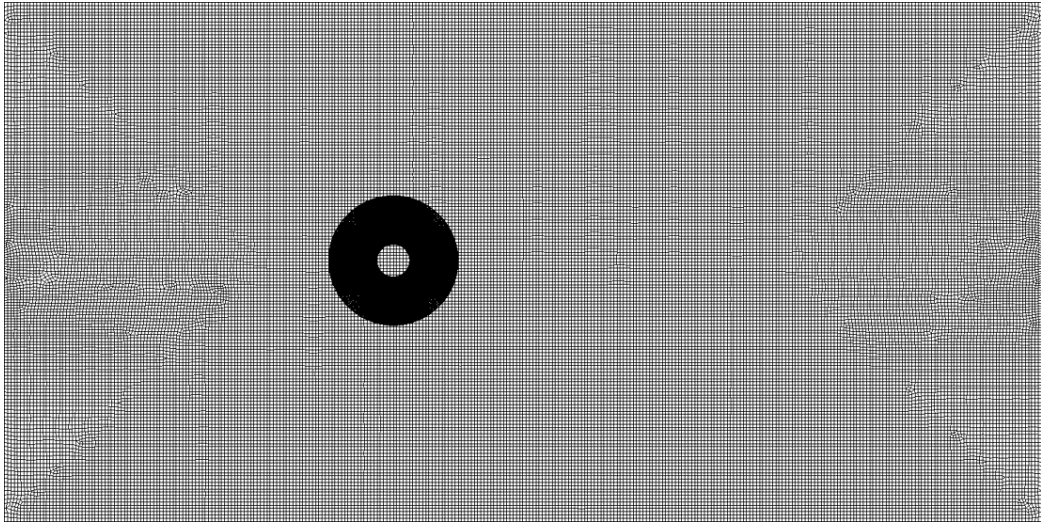


Figure 5.4: Schematic diagram of the meshes of interest of the flow-induced vibration of an oscillating circular cylinder.

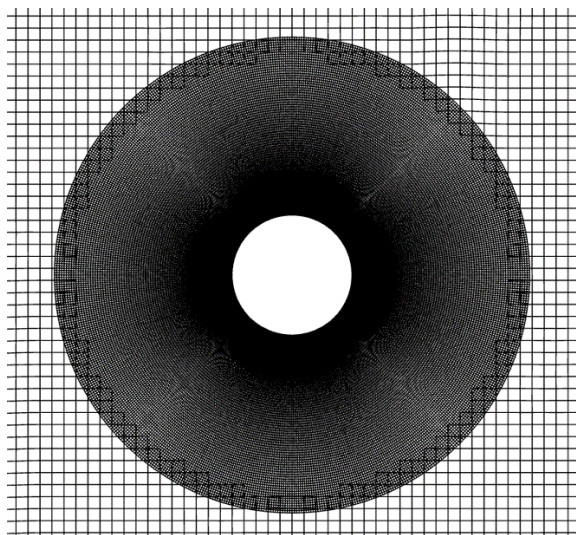


Figure 5.5: Overset mesh combination of domain of interest of the flow-induced vibration of an oscillating circular cylinder.

5.3.1.2 POD construction

The POD snapshot solution has been computed using the ANSYS Mechanical and ANSYS Fluent with a RANS $k-\omega$ turbulence model using the ALE method to adapt the mesh

around the oscillating cylindrical body. A loosely coupled algorithm couples both the structural and fluid domains. During one oscillation period, one hundred snapshots are taken, and these are interpolated on a rectangular grid to build a POD basis using Equation (3.5). Recapping that the computational results of (5.30) define the velocity profile on the time-dependent grid, thus the location of the solid cylinder cannot be computed via the traditional POD-Galerkin based ROM method. An indicator function $\mathbb{I}_{\Omega_F}(\mathbf{x}, t)$ is introduced to indicate the membership of a point \mathbf{x} in the fluid domain $\Omega_F(t)$:

$$\mathbb{I}_{\Omega_F}(\mathbf{x}, t) = \begin{cases} 1 & \text{if } \mathbf{x} \in \Omega_F(t) \\ 0 & \text{if } \mathbf{x} \in \Omega \setminus \Omega_F(t) \end{cases} \quad (5.42)$$

With the indicator function $\mathbb{I}_{\Omega_F}(\mathbf{x}, t)$, the parameters defined on the computational domain Ω , such as the velocity, density and viscosity, denoted by $\mathbf{u}(\mathbf{x}, t)$, $\rho(\mathbf{x}, t)$ and $\mu(\mathbf{x}, t)$ respectively, are decomposed as follows:

$$\forall \mathbf{x} \in \Omega$$

$$\mathbf{u}(\mathbf{x}, t) = \mathbb{I}_{\Omega_F}(\mathbf{x}, t) \mathbf{u}_F(\mathbf{x}, t) + (1 - \mathbb{I}_{\Omega_F}(\mathbf{x}, t)) \mathbf{u}_S(\mathbf{x}, t) \quad (5.43)$$

$$\rho(\mathbf{x}, t) = \mathbb{I}_{\Omega_F}(\mathbf{x}, t) \rho_F + (1 - \mathbb{I}_{\Omega_F}(\mathbf{x}, t)) \rho_S \quad (5.44)$$

$$\mu(\mathbf{x}, t) = \mathbb{I}_{\Omega_F}(\mathbf{x}, t) \mu_F + (1 - \mathbb{I}_{\Omega_F}(\mathbf{x}, t)) \mu_S \quad (5.45)$$

where ρ_F and ρ_S are the density of the fluid and solid domains, respectively, μ_F is the fluid viscosity, and μ_S is a penalisation factor in the rigidity constraint.

Taking this technique is the same as taking the solid domain to be Eulerian, and several other ways have been offered in the research that has been done on this topic. The Immersed Boundary Method, which can be found in Peskin [138], is the most well-known and has inspired a few more similar approaches. This technique involves simulating the solid with a membrane that is moving through a fluid flow so that it may be modelled. In order to take into consideration this membrane, a force component is first included into the fluid equation. Following this step, the fluid constraint is then interpolated on the membrane. The non-physical representation of the fluid-solid interface is one of the primary problems with the traditional method. Because of this, the author proposes a new alternate method, the so-called fictitious domain method, which was developed for fluid-solid-rigid interaction problems by Glowinski et al. [69] and Patankar et al [137].

By implementing the POD-Galerkin ROM approach, Equation (5.30), the velocity profile of all domains in the simulation is decomposed as the following form:

$$\mathbf{V}(\mathbf{x}, t) = \sum_k a_k(t) \mathbf{u}^k(\mathbf{x}) \quad (5.46)$$

where $\mathbf{u}^k(\mathbf{x})$ and $a_k(t)$, $k = 1, \dots, M$ are the POD eigenmode functions and the amplitude of each mode, respectively. Figures 5.6 shows the first four POD modes of the velocity field and the mean flow of the POD snapshots, respectively.

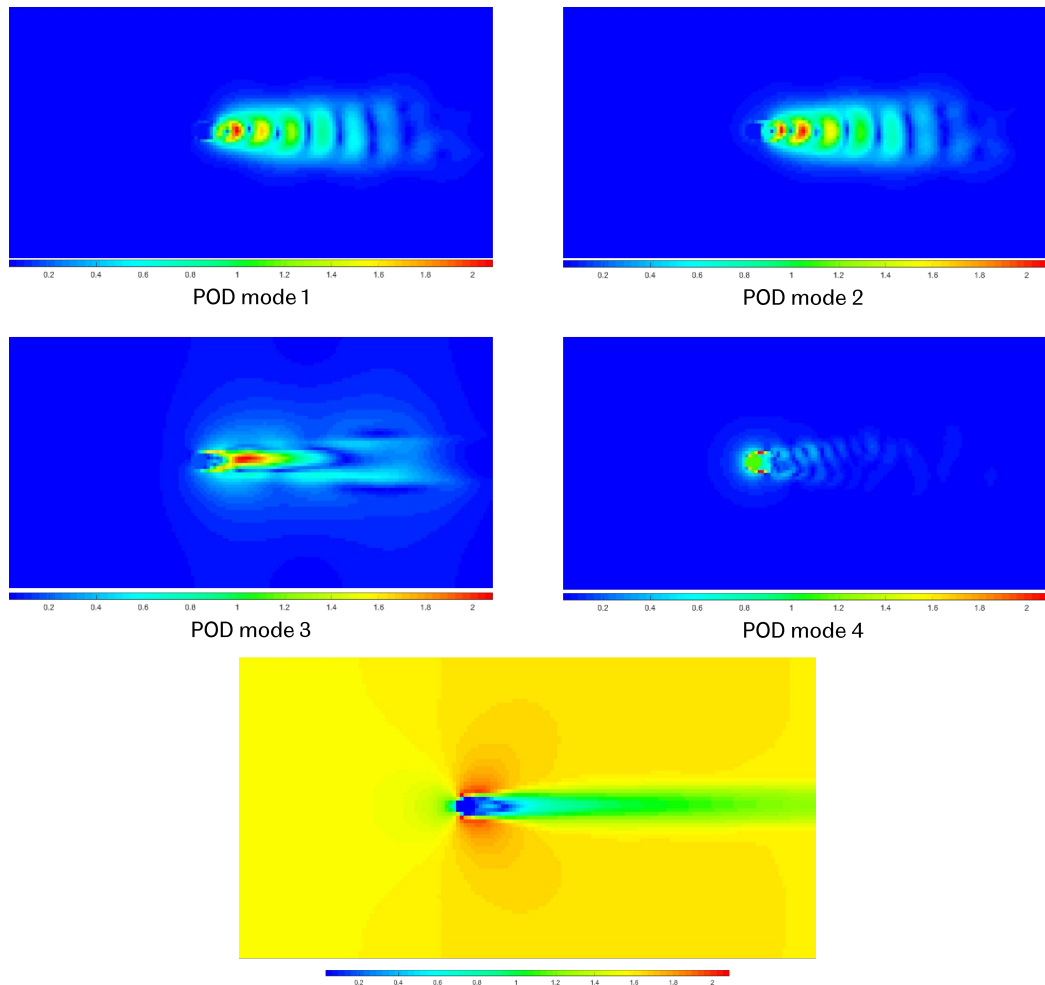


Figure 5.6: Schematic diagram of the normalised POD modes and the mean flow of the velocity field of the cylinder oscillating at $Re = 1690$.

The first POD mode is the temporal average velocity field and the other modes capture the additional velocity fluctuations as giving by equation (5.47). Figure 5.7 illustrates the energy accuracy with different POD modes used and it can be observed that 10 POD modes are sufficient to construct the velocity field within an error in the kinetic energy captured less than 1%.

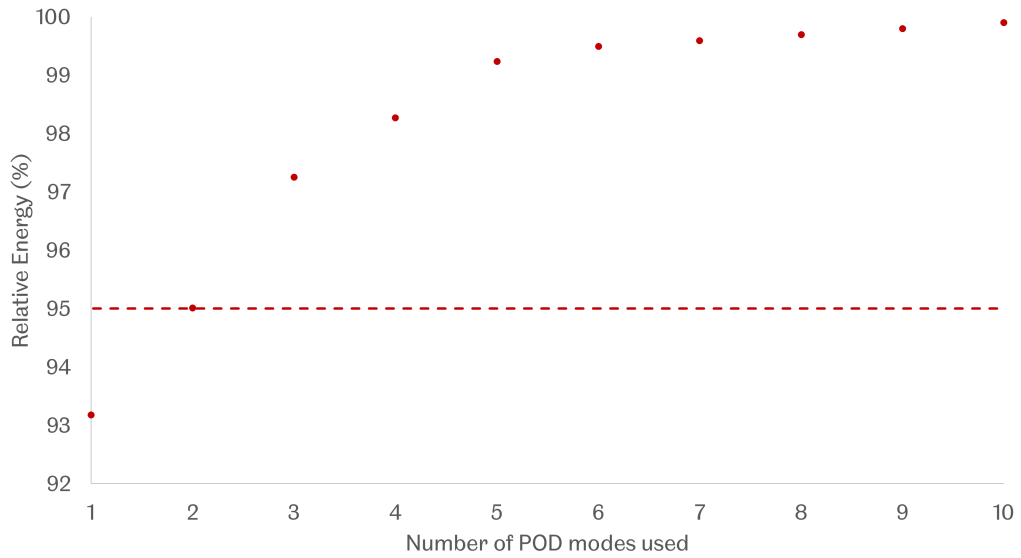


Figure 5.7: ROM accuracy regarding the energy coverage with different number of POD modes.

5.3.1.3 ROM simulation results

A pivotal parameter of the fluid-induced vibration, namely the displacement of the centre of gravity of the circular cylinder is selected to validate the performance of the proposed ROM using different number of POD modes, as illustrated in Figure 5.8. Although, 3 POD modes is good enough to capture at least 95% of the kinetic energy using the energy criterion, six POD modes are necessary to present a relatively precise displacement field at the centre of gravity of the rigid body.

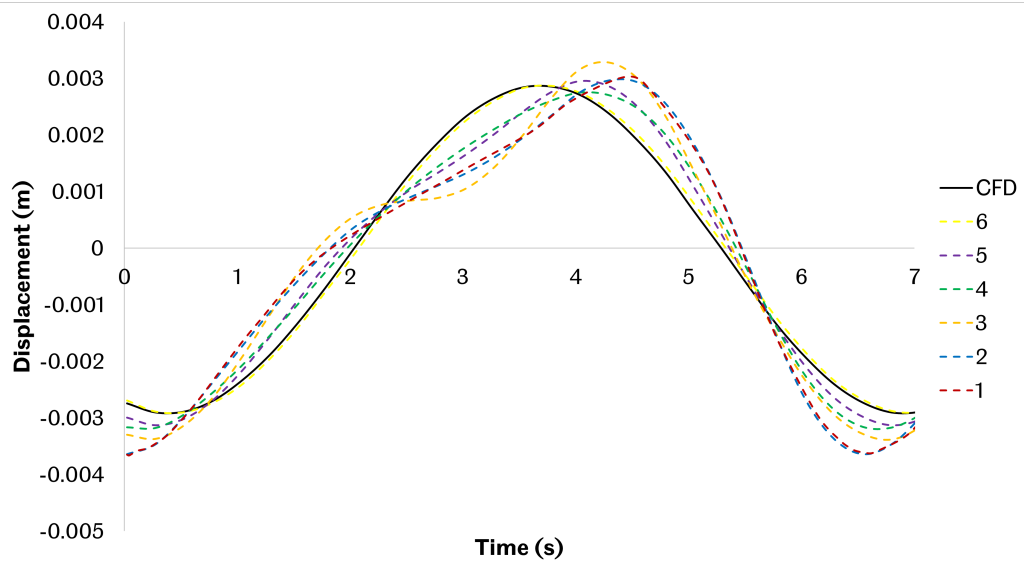


Figure 5.8: The reconstructed displacement of the centre of gravity of the circular cylinder in the first six seconds of one oscillation period using POD modes of different size.

The ROM shown in Figures 5.9 and 5.10 is built using 6 POD modes. Figures 5.9 and 5.10 show a comparison between the CFD results and the results obtained at a time snapshot during one oscillating period in terms of the x -axis and y -axis velocity contours, respectively.

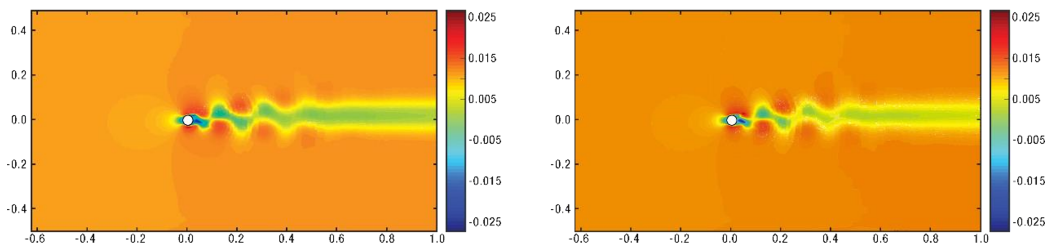


Figure 5.9: Comparison between the computational x -axis velocity field (left, reproduced from [112, 151]) and the result obtained using the snapshot ROM method (right).

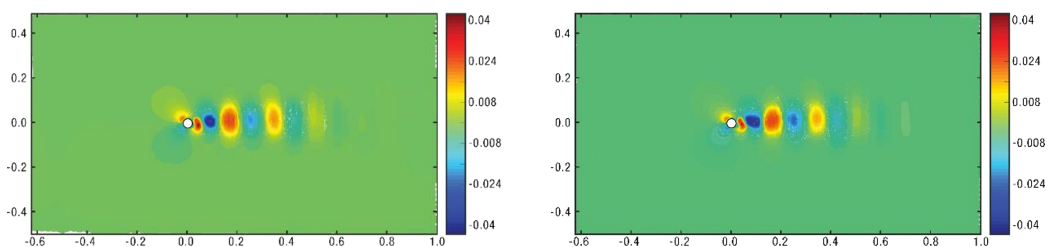


Figure 5.10: Comparison between the computational y -axis velocity field (left, reproduced from [112, 151]) and the result obtained using the snapshot ROM method (right).

Figure 5.11 shows the solutions for the flow past the cylinder at time instances 5.0 and 10.0, as calculated using the two ROM models (traditional reduced order modelling using uniform grids and the proposed model using adaptive grid), and the full high fidelity model using 12 POD basis functions. In this particular instance, the Reynolds number was 100. These results demonstrate that the POD model has done exceptionally well when it comes to resolving the flow field at both of the different times considered. As shown in Figure 3.4, the standard POD models are able to capture the wave pattern using all 6 POD modes, but they have a significant error near the peak of the waves during the spin-up period of modelling.

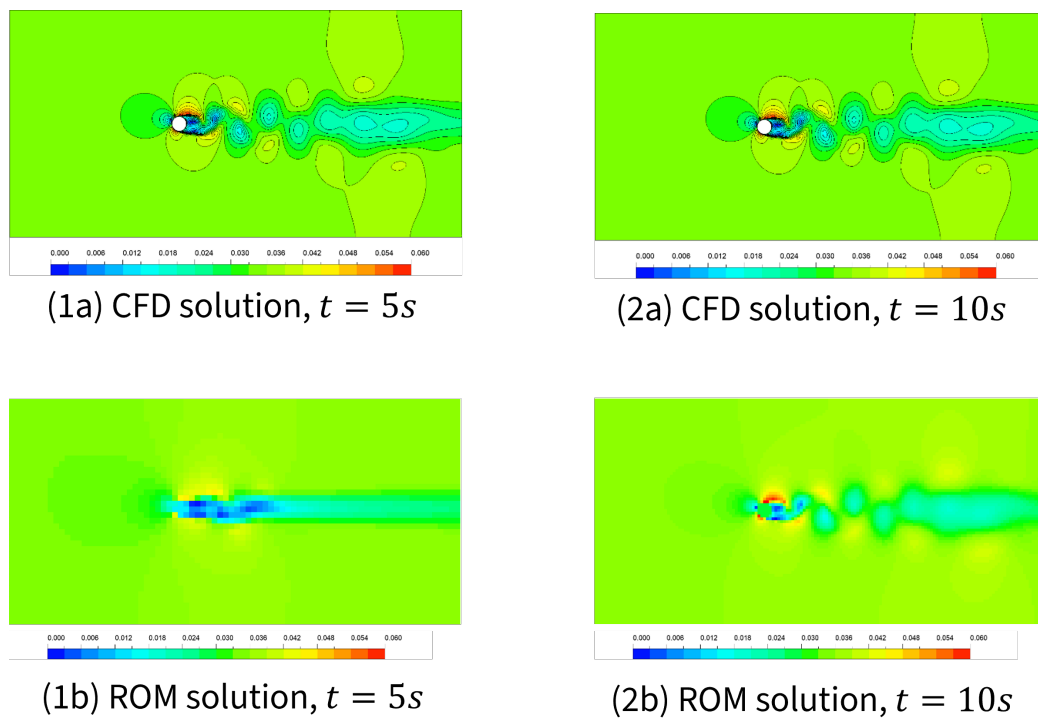


Figure 5.11: Comparison of the solutions of the flow past a oscillating cylinder problem at $Re = 1690$ and time instances 10.0 and 30.0 between full order solution and the proposed ROM using 12 basis functions.

The comparison between the computational results and the result obtained using the proposed adaptive ROM results for the centre of the gravity of the cylinder in the first six seconds of the oscillation is illustrated in Figure 5.13.

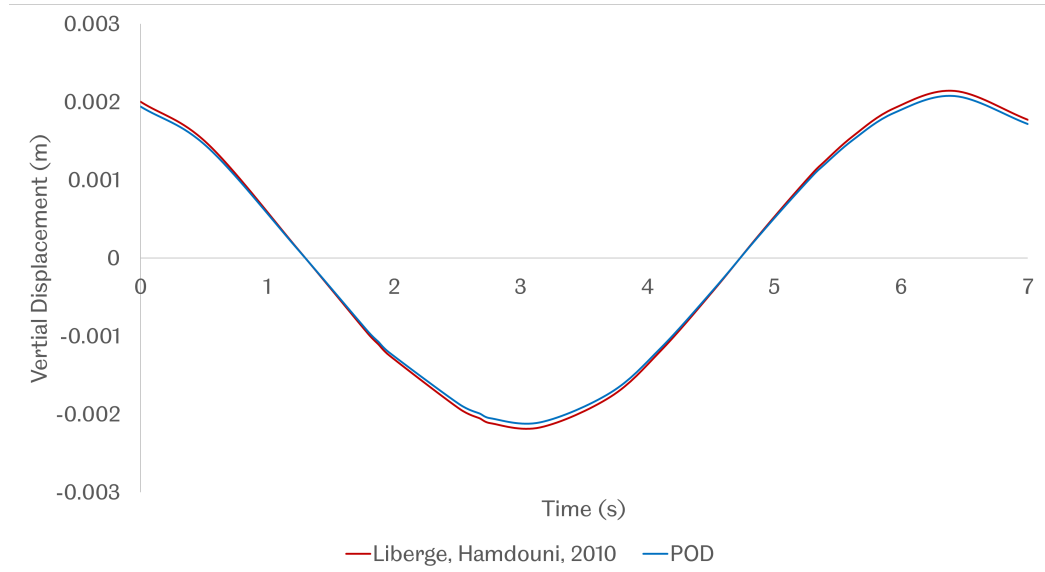


Figure 5.12: Displacement of the position of the centre of gravity of the circular cylinder within the first seven seconds of one oscillation period.

Recapping that in section 3.5, several aspects of the particular POD-Galerkin methods are presented to evaluate the performance in terms of accuracy and efficiency. The error function of this particular problem is defined as follows,

$$err(N) = \frac{\|V - V_N\|_{(0,T)}}{\|V\|_{(0,T)}} \quad (5.47)$$

where V and V_N are the referenced solution and the solution truncated at the N -th POD mode, $\|\cdot\|$ indicates the induced norm of the vector of interest, refer to Equation (3.6).

As discussed in previous figures, the proposed POD-Galerkin ROM shows a good agreement between the results obtained using the ROM and the published results [112]. It is observed that the error of the proposed method in the prediction of the displacement and velocity fluctuations is about 0.05%. The proposed ROM method shows a better performance compared to the traditional uniform ROM method, as shown in Figure 5.13. This is due to the errors being compounded when truncating the POD eigenfunctions, when constructing the POD basis, having insufficient sampling and the errors in the inner product and the numerical integration of the ROM.

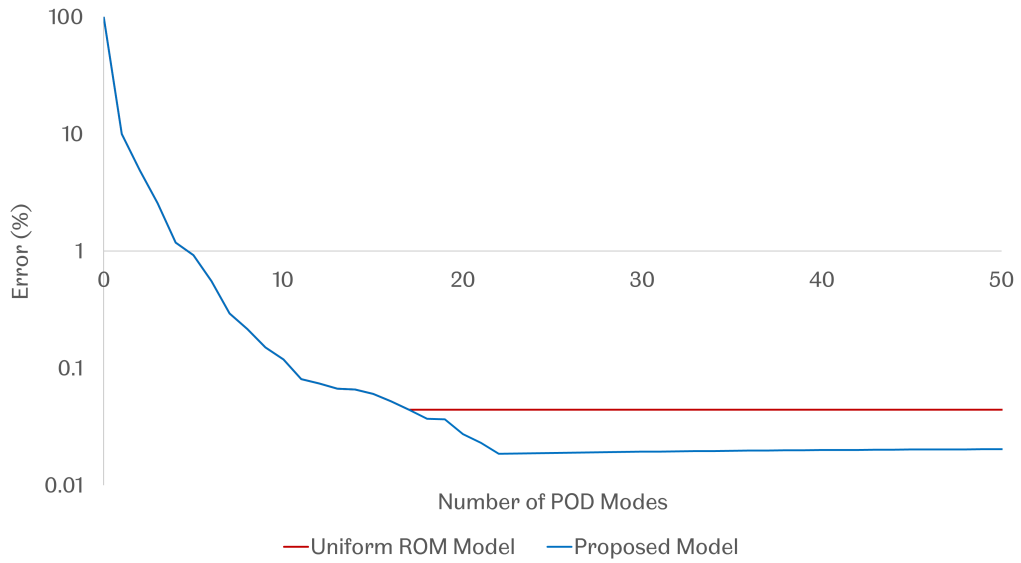


Figure 5.13: The error of velocity profile obtained via different numbers of POD modes in the case of the flow induced vibration of a cylinder oscillating at $Re = 1690$.

5.3.2 ROM simulation for flow around an oscillating aerofoil

A two-dimensional pitching and plunging aerofoil with more complicated flowing condition at various Reynolds number is studied to further challenge the proposed POD-Galerkin model in this section, but other motions can also be easily applied by the use of a similar approach. The numerical solutions are based on the aerofoil oscillation experiments performed by Sidlof, et al. [191].

The CFD snapshots are modelled as per the literature then used to build the reduced order models. The flow-induced vibration of a NACA 0015 aerofoil freely moves normal to the direction of inlet, as shown in Figure 5.14. **No-slip boundary conditions are applied to the top and bottom side of the domain. Inlet boundary condition is applied to the left side, inlet velocity is set to 44.7 m/s for $Re = 173000$ and 125.8 m/s for $Re = 570000$ and outlet boundary condition is applied to the right hand side of the domain. FSI boundary condition is applied to the aerofoil where the velocity at the boundary equals to the solid domain motion.** For more detailed information, please refer to Sidlof, et al. [191]. The NACA 0015 aerofoil, with a chord length $c = 59.5$ mm and a span 76.6 mm, is fixed in an 80×210 mm test section of a wind tunnel. The aerofoil rotates around a miniature ball bearings located at $1/3$ of the chord, with the restoring moment is realised by a spiral torsion spring built inside the aerofoil profile. The parameters employed in the model are summarised in Table 5.1, and these are the same values as those used in the experimental investigation.

Table 5.1: Properties employed in the aerofoil model for the flow-induced vibration of the NACA 0015 aerofoil.

Parameters	Values
Chord [mm]	59.5
Mass [kg]	0.148
Linear Stiffness [N/m]	16.383
Linear Damping [kg/s]	5.6
Torsion Stiffness [Nm/deg]	0.00753
Torsion Damping [kgm^2/s]	0.00078

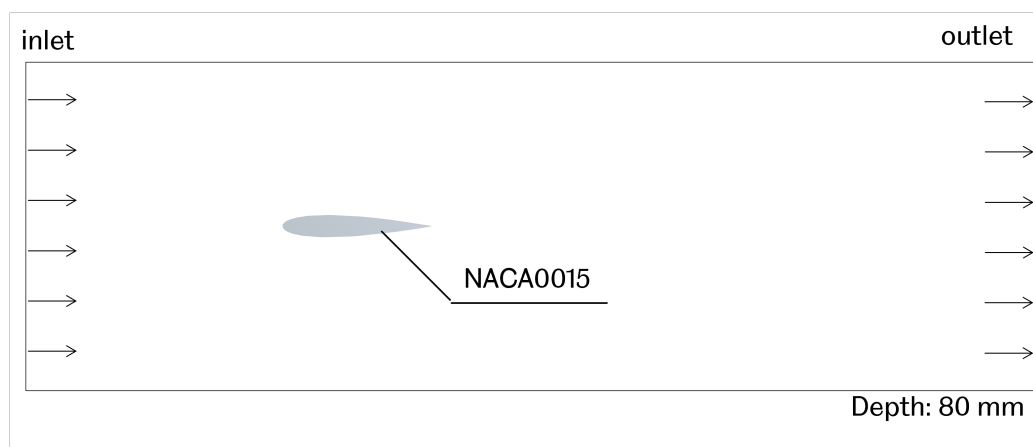


Figure 5.14: Schematic of the domain of the flow-induced vibration of the NACA 0015 aerofoil.

Figure 5.15 illustrates the computational domain used in the CFD modelling. The fluid model consists of 854,625 nodes and 879,632 elements. The mesh is split into two parts: background fluid domain and the refined overset domain near to the aerofoil. The time-step size is 5×10^{-5} second and the number of nonlinear iterations per time step is 1500. A loose coupling strategy was applied to couple both the fluid and structural domains at each time step. The aerofoil is assumed as a rigid body, and the corresponding rigidity is modelled in the structural solver.

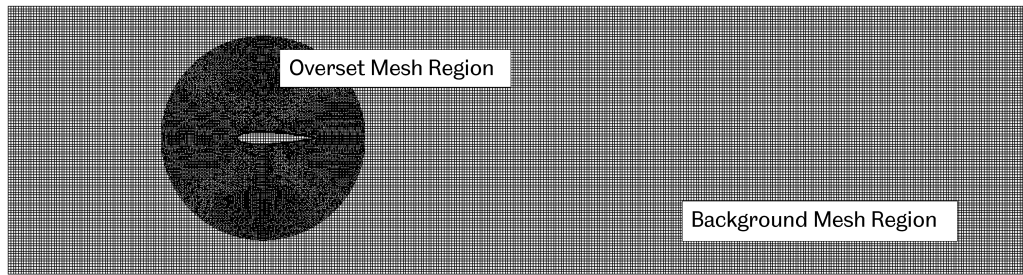


Figure 5.15: Schematic of the mesh used in the case of the flow-induced vibration of the NACA 0015 aerofoil.

The structural model of the aerofoil is illustrated in Figure 5.16. The aerofoil of interest is modelled as a 2D rigid body, and the vertical guide is modelled as a point mass at the rotational centre of the aerofoil. The aerofoil is attached to a linear spring-damping system which fits the linear stiffness and damping ratio employed in the experiment. The point mass and the aerofoil are then connected using a torsional spring-damping system which fits the experimental torsion stiffness and damping ratio. The stiffness parameters used in this validation simulation are summarised in Table 5.1.

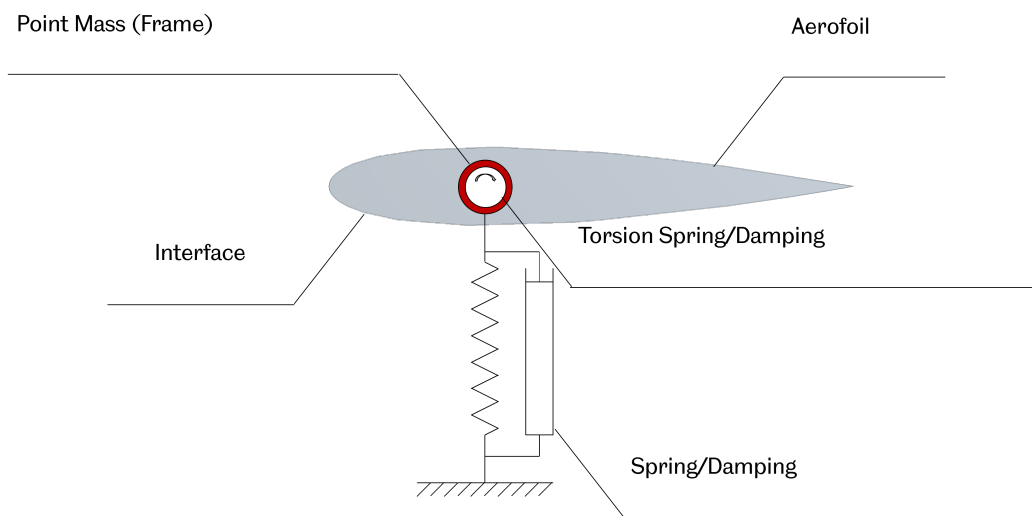


Figure 5.16: Structural model of the flow-induced vibration of the NACA 0015 aerofoil.

The governing motion equation of the solid domain is determined by the structural model introduced in Section 5.2.2. A simple, linear, 2-D spring model coupled to the fluid dynamics model is employed, as shown in Figure 5.17. The aerofoil modelled is free to translate along the y-axis, fluid dynamics model generates the lift and moment coefficients that are introduced into the structural model that in turn determines the incremental motion of the aerofoil. This process is then executed in a stepwise fashion

for each time increment. The previous time increment fluid dynamics model is used to compute the next time increment aerofoil position and then the aerodynamics of that position are calculated.

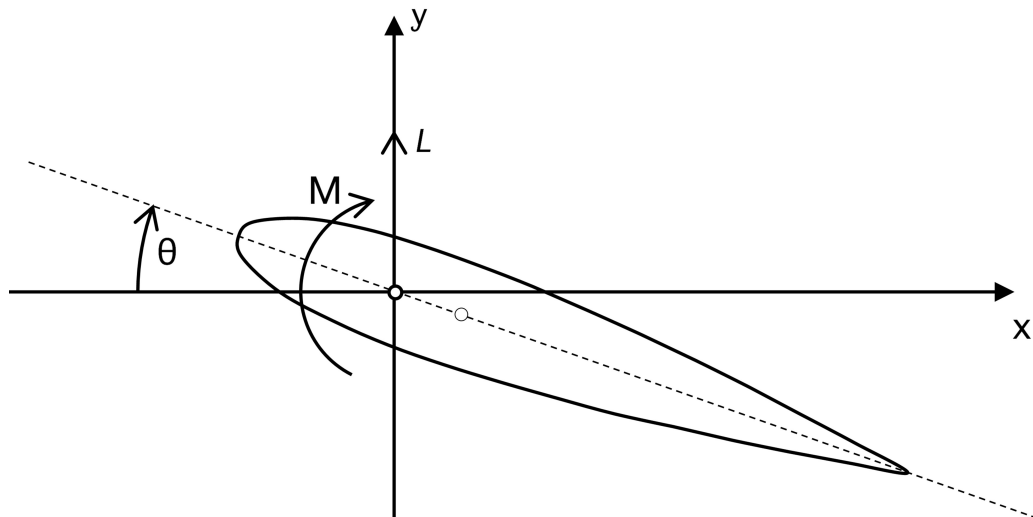


Figure 5.17: Schematic illustration of a 2-D pitching and plunging aerofoil.

The proposed POD-Galerkin approach is applied to model the two-dimensional flow-induced pitching and plunging aerofoil in the cases of limit cycle oscillating at different Reynolds numbers. The amplitudes stabilize at the limit cycle oscillations due to the structural and/or aerodynamic nonlinearities. The accuracy and computational cost of the model in the case of a limit cycle oscillation is investigated. Accuracy and order reduction are discussed with respect to the full-order numerical model and the traditional POD strategy with uniform grids.

The model is established using ANSYS FLUENT coupled with the Transient Structure modules using the $k-\omega$ SST turbulence model. This two-equation model is suitable for modelling the boundary layers as well as the far field flows, and therefore it has been used extensively in studies involving wind turbine blades and aeroelastic problems with reasonable results [80, 75].

5.3.2.1 Flow-induced vibration of a NACA 0015 aerofoil at Reynolds number $Re = 173,000$

As shown in Figure 5.18, the first case of limit cycle oscillations is chosen at the Reynolds number 173,000, defined by the incoming velocity of 44.7 m/s, the chord length of the

NACA 0015 aerofoil is $c = 59.5$ mm. The aerofoil starts to oscillate at the initial displacement of $y_0 = 3.3$ mm, and the initial pitch angle of $\theta_0 = 0^\circ$. The two-way fluid-structure interaction strategy is selected to simulate the motion of the aerofoil.

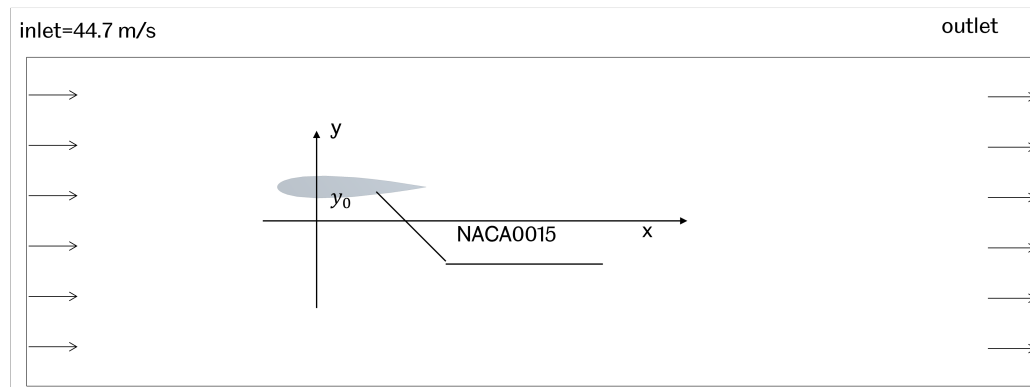


Figure 5.18: Schematic of the domain settings of the flow-induced vibration of the NACA 0015 aerofoil at Reynolds number $Re = 173,000$.

The accuracy of the numerical model has been validated by comparing the full order CFD results to the experimental data. The presentation of the pitch angle against the plunge at $Re = 173,000$ is presented in Figure 5.19. The phase trajectory rotates counterclockwise, which increases the plunge amplitude, decreases the pitch amplitude and decreases the phase difference. In addition, the time history of the plunge and pitch angle for the limit cycle oscillation is shown in Figure 5.20. The time history is plotted after convergence to the limit cycle. It has been shown that the accuracy of the numerical case is preserved to be almost the same as the experimental data, where the average error in both the pitch and plunge solutions are underestimated by about 5% in comparison to the experimental data. However, the frequency and phase are almost identical to the experimental data for both cases. The error in the amplitude is due to only two dimensions being considered in the numerical solution, and although the third dimension is negligible, it still has an effect on some of the results. Therefore, both limit cycle cases are considered to be sufficiently accurate to construct the reduced order models.

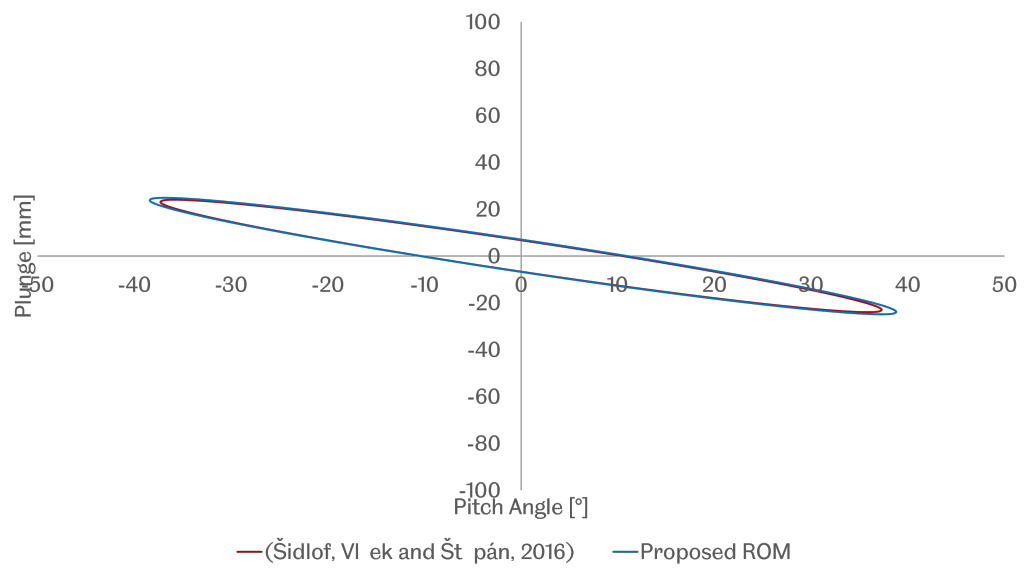


Figure 5.19: Comparison of the phase between the pitch angle and plunge of the NACA 0015 aerofoil limit cycle oscillation at $Re = 173,000$.

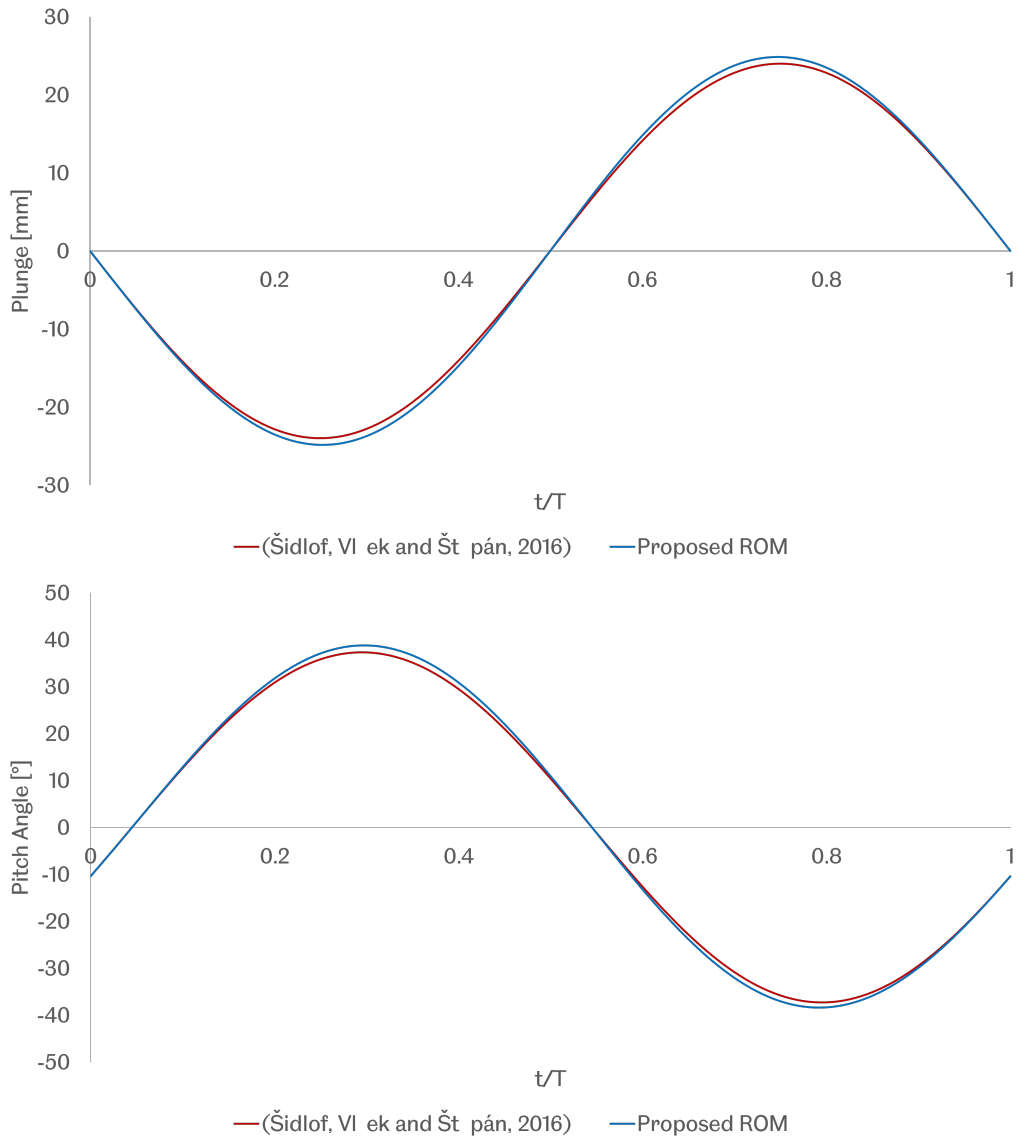


Figure 5.20: Time history of the pitch and plunge of the NACA 0015 aerofoil limit cycle oscillation over normalised periods at $Re = 173,000$.

The proposed POD-Galerkin ROM procedure was executed by implementing a MATLAB subroutine as per the methodology listed in Section 5.2, and the results obtained are discussed and compared to the experimental data.

The ROM is built using a pre-calculated numerical solution. The proposed ROM modes are computed from 400 uniformly distributed snapshots of the simulation data over four complete periods of oscillation. In addition, as a validation case of the proposed locally refined strategy, the domain is uniformly discretised in 160×40 , 320×80 , 640×160 , and 1280×320 grids in the x - and y - direction, respectively. Thus, three different proposed ROM models based on the created uniform grids, namely 160×40 - uniform, 320×80 -

uniform, 640×160 - uniform, are built. For each case, overall computational cost, error of the ROM solution against the baseline CFD solution, maximum velocity difference, error weighted difference between the rebuilt velocity flow field and the analytical solution are summarised.

For every cases, the energy percentage of the POD mode decreases monotonically, as shown in Figure 5.21. The first 20 dominant POD modes, which cover more than 99.5% of the overall kinematic energy, are selected to perform the following calculation. Various ROM solutions via three different iteration levels of the adaptive refinement, namely 160×40 - adaptive, 320×80 - adaptive, 640×160 - adaptive, are compared to the corresponding ROM models using uniform grids. In the first case, the flow field patterns of the limit cycle oscillation at $Re = 173,000$, an additional case at higher Reynolds number will be conducted to challenge the performance and robustness of the proposed adaptive ROM.

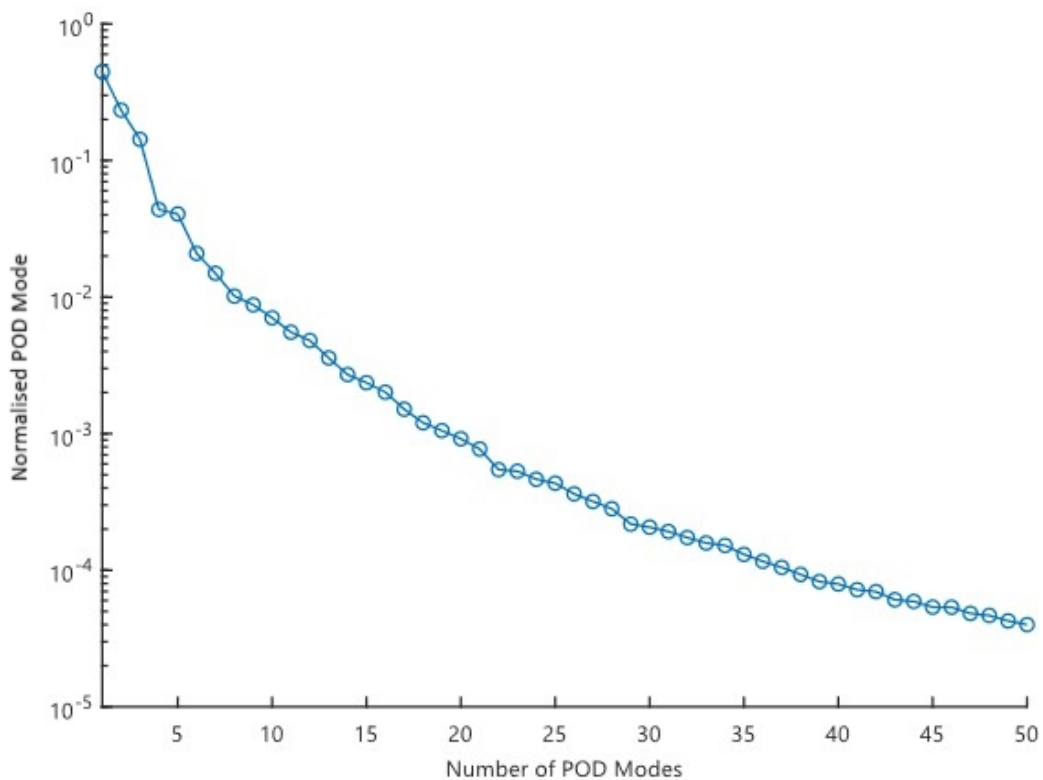


Figure 5.21: The energy spectrum of the POD modes in the case of the limit cycle oscillation at $Re = 173,000$.

Figure 5.22 demonstrates the vorticity contours of first six POD modes, and the mean flow of the limit cycle oscillation (LCO). Selected POD modes associated with the velocity are qualitatively presented. These modes do not present the flow structures but can be

informative assistances providing additional good information about the sparse correlations [30]. The symmetric/antisymmetric patterns about the wake line have been previously reported [133]. Compared to the flow pattern obtained from the POD modes of the uniform ROM approach, the proposed ROM presents much more detail in the region with large velocity deviance, such as in the vicinity of the aerofoil, which provides the capability of predicting much more accurate results.

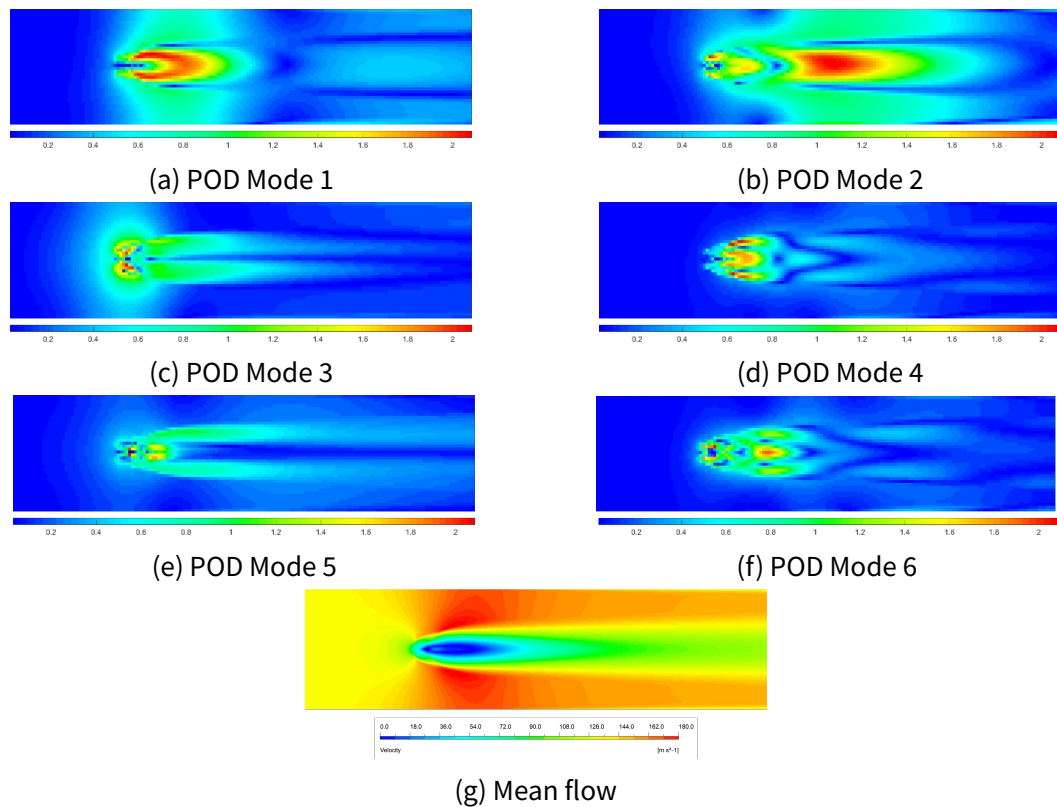


Figure 5.22: Vorticity contours of the first 6 POD modes and the mean flow for a two-dimensional pitching and plunging aerofoil in the case of the limit cycle oscillation ($Re = 173,000$) (a) - (f): first six POD modes, (g): vorticity contours of the mean flow.

To further show the capacity of the model more clearly, the flow structure at the same time steps have been investigated: the velocity flow field computed by the numerical approach and the proposed POD-Galerkin ROM models. Five different time step snapshot of the limit cycle oscillation at $Re = 173,000$ are selected as an example. With this decomposed solid domain, the dynamics for this prescribed large solid motion problem and the corresponding adapted discretisation are shown in Figure 5.23. The accuracy of the adaptive ROM is preserved to be almost the same in comparison to the numerical solution after five iterations.

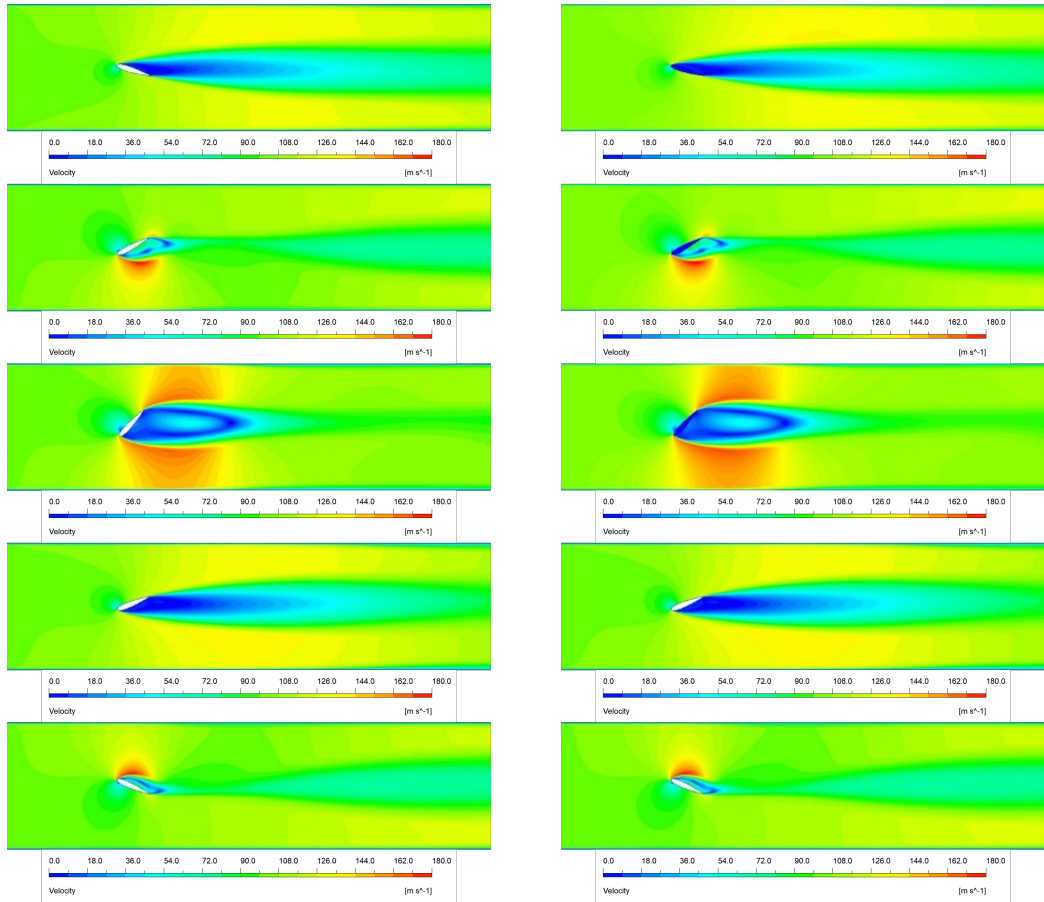


Figure 5.23: Proposed solution for a two-dimensional pitching and plunging aerofoil in the case of the LCO at $Re = 173,000$ at different snapshots. Left: numerical solution; Right: reconstructed flowfield using the new proposed ROM.

The reconstructed dynamic system of the most dominant modes, i.e. the first ten modes, are achieved by the adaptive projection onto these modes, and it is compared to the ROM using the same quality of uniform grids to quantify the performance of the proposed POD-Galerkin ROM. The phase portrait of the case of at $Re = 173,000$ is plotted in Figure 5.24, where a comparison is made between the numerical solution and the Galerkin-based ROM with and without the proposed method. The presentation of the plunge profile against the pitch angle is plotted after convergence onto the limit cycle. The phase trajectory rotates counterclockwise, which increases the plunge amplitude, decreases the pitch amplitude and decreases the phase difference.

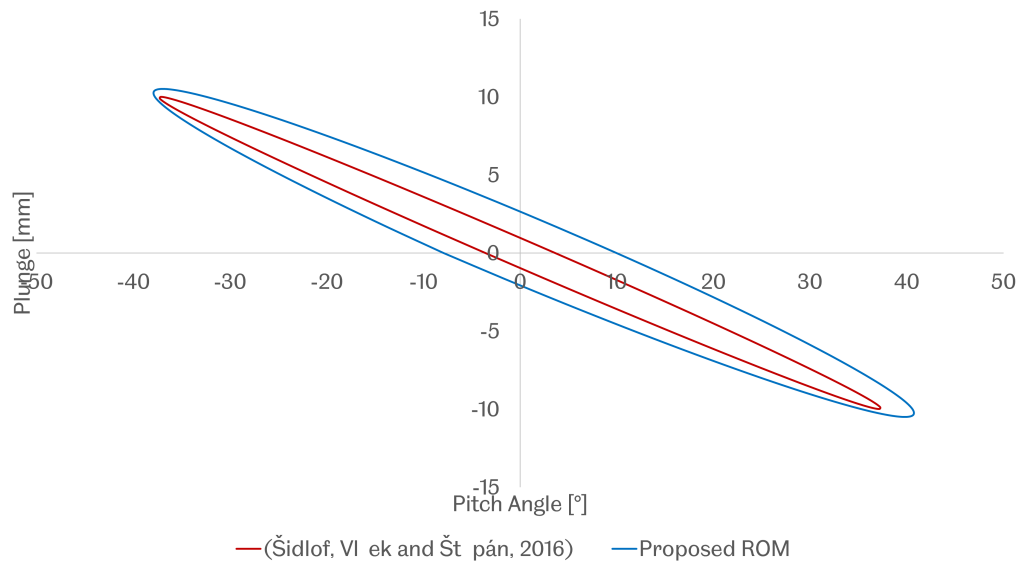


Figure 5.24: A comparison of the POD-Galerkin results using the adaptive and uniform grid discretisation for the flow passing a pitching and plunging aerofoil in the case of a limit damping oscillation at $Re = 173,000$.

Compared to the uniform ROM approach, the proposed ROM more accurately predicts results for both limit cycle oscillation cases. Figure 5.25 shows the normalised error between the benchmarked numerical solution and the ROM method via the uniform approach and the proposed method. The shape, frequency and amplitudes are much closer to the experimental and numerical solution [191]. The proposed adaptive discretisation concentrates on the vicinity of the aerofoil, as well as in the wake region to minimise the velocity variance within the reduced order modelling process, and it varies at different time steps. The accuracies of the adaptive reduced order model are observed to be almost the same in comparison to the numerical solution after five iterations. In contrast, the reconstructed flow fields using the uniform ROM are not perfectly accurate due to the large motion of the aerofoil.

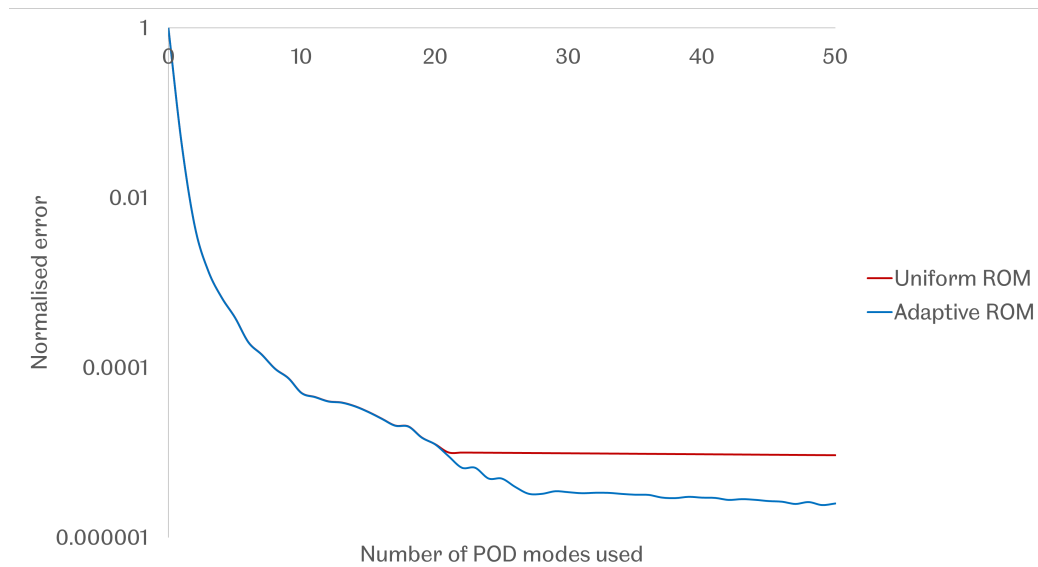


Figure 5.25: Decay of the normalized error for the POD basis using the adaptive and uniform grid discretisation for the flow passing a pitching and plunging aerofoil at the Reynolds number $Re=173,000$.

Similar to the first case, the computational cost up to 200 timesteps is investigated. Figure 5.26 shows the online and offline CPU time required to compute up to 200 timesteps with varying mesh size. The computational cost of the full order CFD simulation is compared against those of a uniform discretisation and the proposed ROMs. It shows that the cost of the ROM models remains static with an increasing resolution of the mesh, and that significant CPU speed-ups are obtained when using the mesh with the largest number of nodes. The CPU costs were reduced by a factor of about 100 compared to the cost of the high-fidelity model. The offline CPU time listed here includes the time for assembling and solving the matrix for the full model and projecting the POD solution onto the full space, as shown in Figure 5.27. It can be seen that the proposed ROM is much more computationally efficient than the traditional uniform ROM, and this is because the decrease in terms of mesh density speeds the computational speed of the ROMs, since it involves assembling and solving different dimensional matrices.

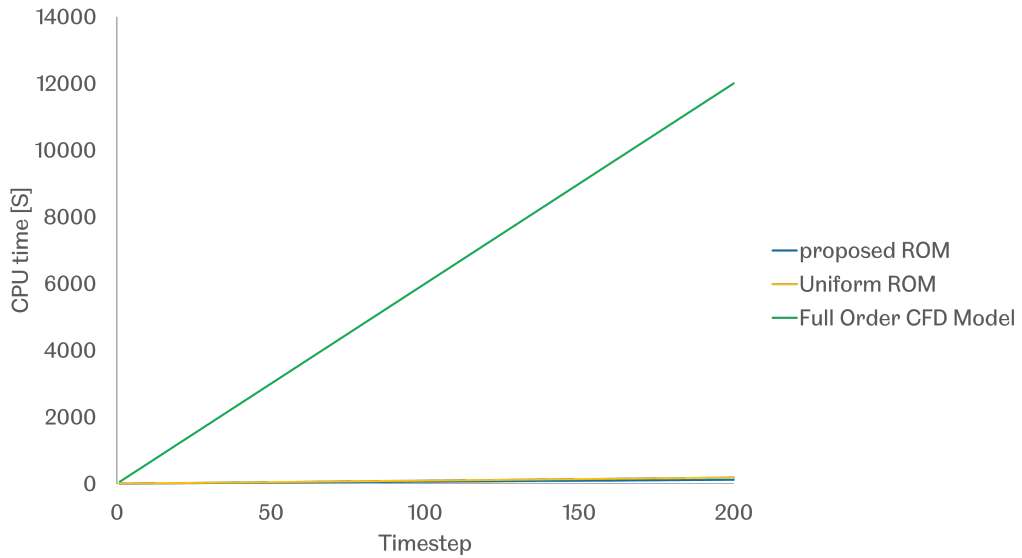


Figure 5.26: Comparison of the online CPU time history on the the two-dimensional pitching and plunging aerofoil in the case of the limit cycle oscillation at the Reynolds number $Re=173,000$ between the full-order CFD solution and the ROMs.

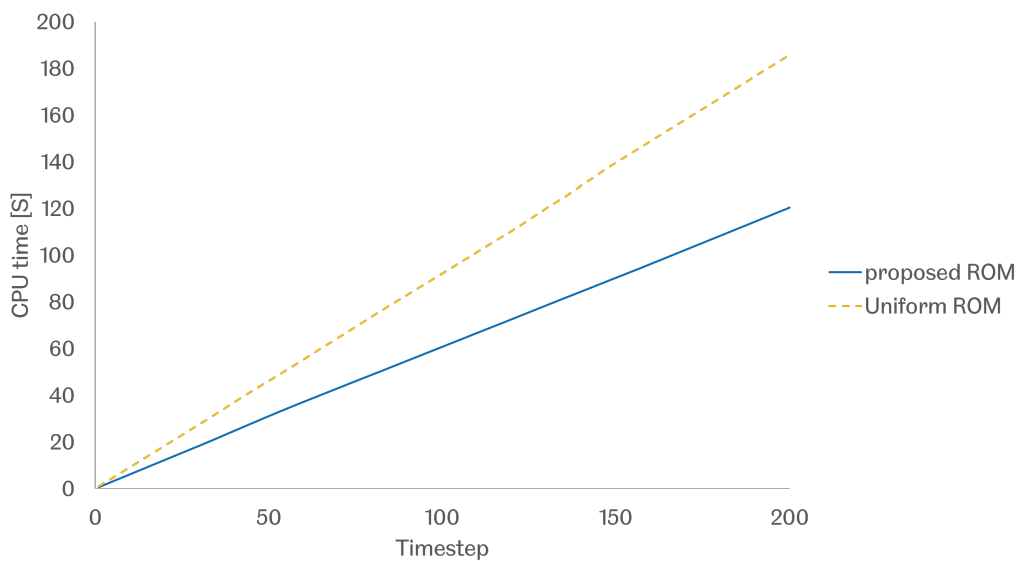


Figure 5.27: CPU time history for the ROMs on a two-dimensional pitching and plunging aerofoil in the case of the limit cycle oscillation at the Reynolds number $Re=173,000$.

The proposed ROM more accurately predicts the results for the limit cycle oscillation cases compared to the uniform ROM with the same level of grid. The reconstructed ROM solutions are compared to the existing numerical results as well as the experimental data. The results show a relatively good agreement with the CFD solution regarding

the velocity and displacement fluctuations. Compared to the accuracy and the computational cost between the ROM approach and the numerical method, the proposed ROM shows a very good potential for use in fluid-structure interaction simulations (FSI) problems.

5.3.2.2 Flow-induced vibration of a NACA 0015 aerofoil at $Re = 570000$

In order to challenge the performance of the proposed methodology at higher Reynolds numbers, in the second case, the Reynolds number is increased to 570,000, defined by the incoming velocity of 125.8 m/s, as shown in Figure 5.28. The chord length of the NACA 0015 aerofoil is $c = 59.5$ mm, the same as the first case. The aerofoil starts to oscillate at the initial displacement of $y_0 = 0$ mm, and the initial pitch angle of $\theta_0 = 0^\circ$. The two-way fluid-structure interaction strategy is selected to simulate the motion of the aerofoil.

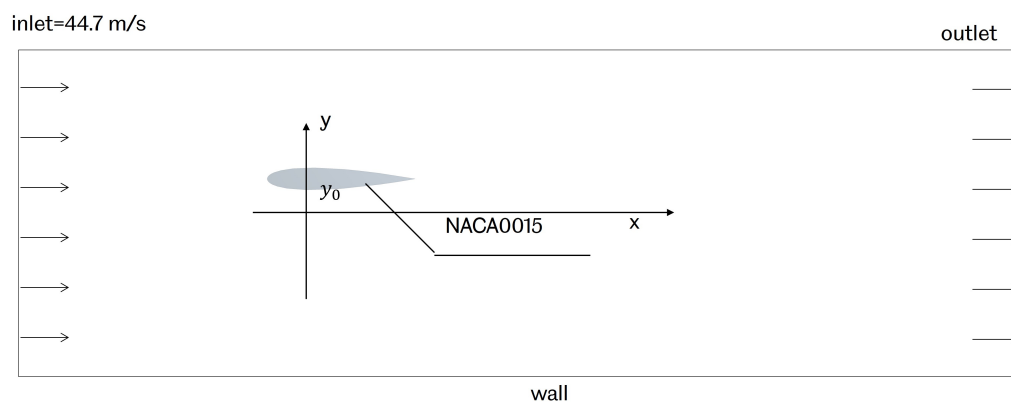


Figure 5.28: Schematic of the domain settings of the flow-induced vibration of the NACA 0015 aerofoil at $Re = 570000$.

Similar to the first case, the accuracy of the numerical model has been validated by comparing the new predicted results to the experimental data. The presentation of the pitch angle against the plunge at a Reynolds number 570,000. The time history of the plunge and pitch angle for the limit cycle oscillation is shown in Figure 5.29. The time history is plotted after convergence to the limit cycle.

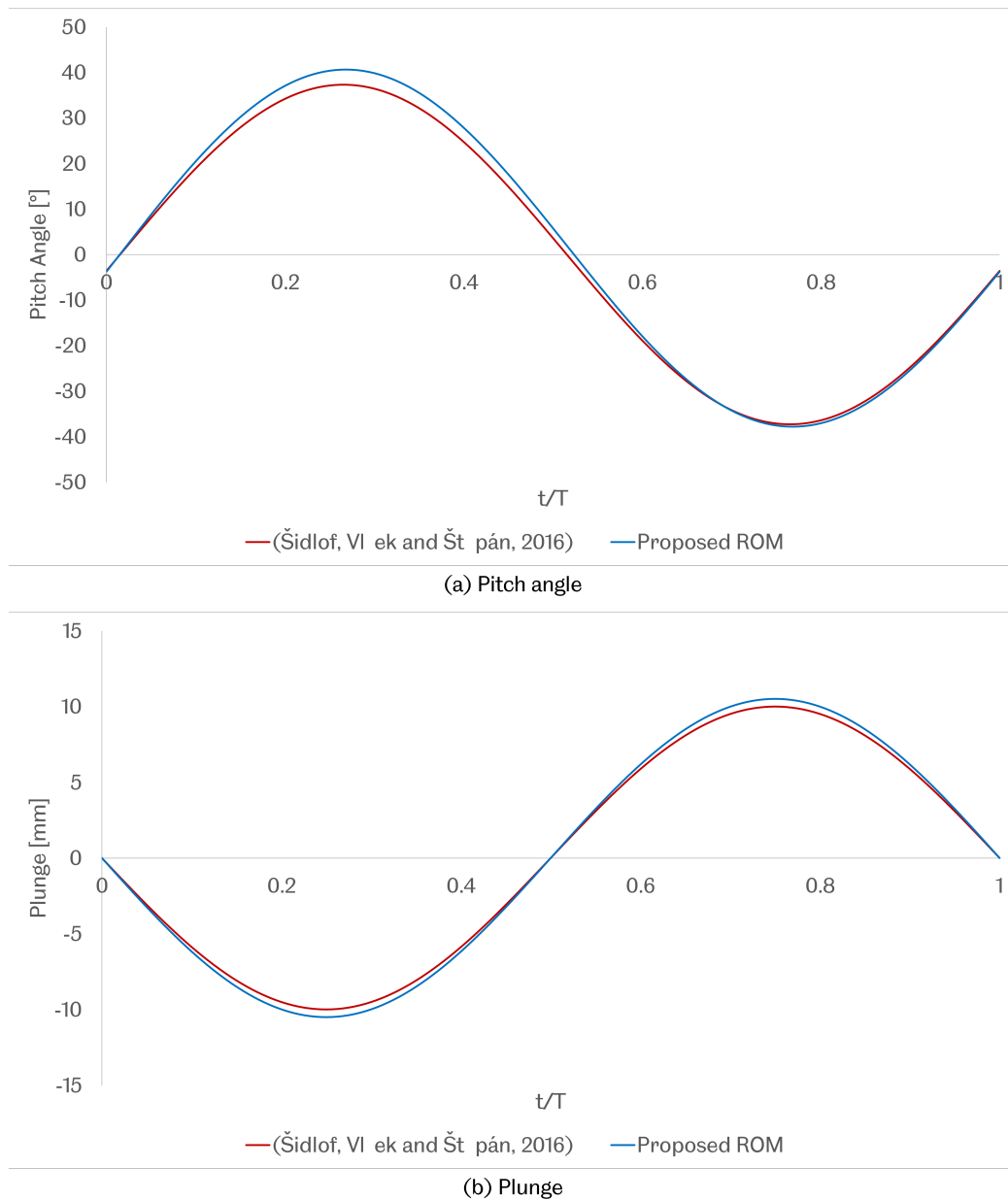


Figure 5.29: Time history of the pitch (a) and plunge (b) of the NACA 0015 aerofoil limit cycle oscillation over normalised periods $Re = 570000$

The proposed POD-Galerkin ROM procedure was executed by implementing the proposed methodology via MATLAB subroutines and the results obtained are discussed. The reduced order model is built using a pre-calculated numerical solution.

The proposed ROM modes are computed from 400 snapshots of the simulation data that covers four complete periods of oscillation. The domain is uniformly discretised in 160×40 , 320×80 , 640×160 , and 1280×320 grids, respectively. Then, three different proposed ROM models based on firstly on the created uniform grids, namely 160×40

- adaptive, 320×80 - adaptive, 640×160 - adaptive, are built as per the methodology shown in Chapter 4. For each case, overall computational cost, maximum velocity difference, weighted difference between the rebuilt velocity flow field and the analytical solution are summarised.

Similar to the first case, the energy percentage of the POD mode decreases monotonically, as shown in Figure 5.30. The first ten dominant POD modes, which cover more than 99.5% of the overall kinematic energy, are selected to perform the following calculation. The maximum difference of the velocity profile within each grid no larger than the 1/100 of the inlet velocity is selected as the threshold of the adaptive discretisation. The flow field patterns of the limit cycle oscillation at a Reynolds number 570,000 are chosen to demonstrate the vorticity contours of each POD modes, and the mean flow of the LCO, as shown in Figure 5.31. Selected POD modes associated with the velocity are qualitatively presented. These modes do not present the flow structures but can provide good information about the sparse correlations for example [30]. The symmetric/antisymmetric patterns about the wake line have been previously reported in [133]. Compared to the flow pattern obtained from the POD modes of the uniform ROM approach, the proposed ROM presents much more detail in the region with large velocity deviance, such as in the vicinity of the aerofoil, which provides the capability of predicting much more accurate results.

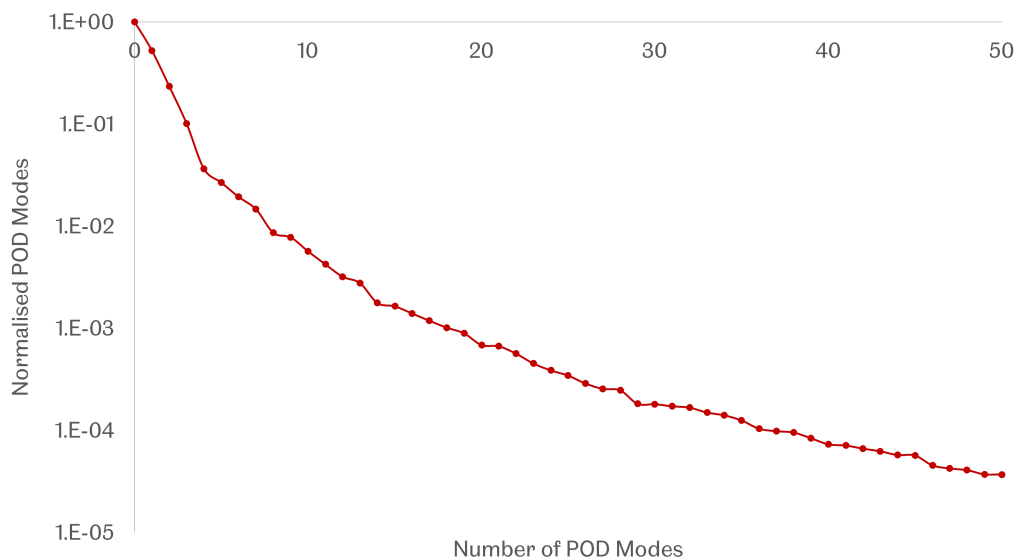


Figure 5.30: The normalised POD modes of the POD modes in the case of the limit cycle oscillation of the NACA 0015 aerofoil at $Re = 570000$.

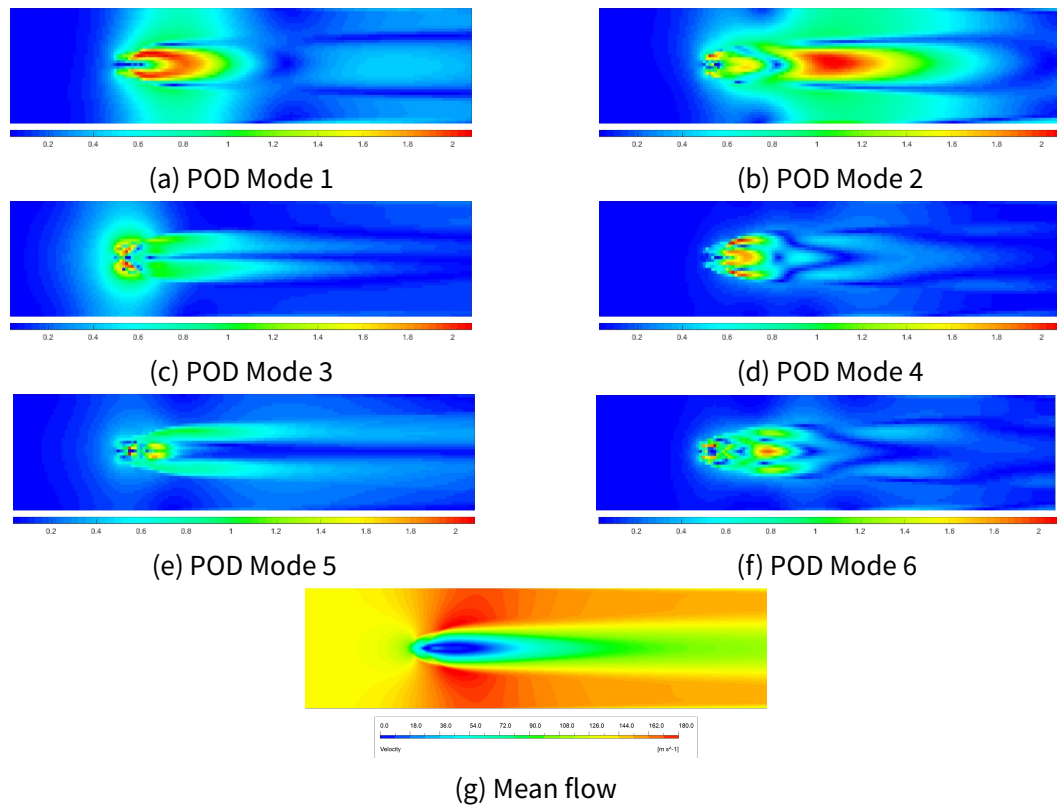


Figure 5.31: Vorticity contours of the first 6 POD modes and the mean flow for a two-dimensional pitching and plunging aerofoil in the case of the limit cycle oscillation at $Re = 570000$ (a) - (f): first six POD modes, (g): Vorticity contours of the mean flow.

To further show the capacity of the model more clearly, the flow structure at the same time steps have been investigated: the velocity flow field computed by the numerical approach and the proposed POD-Galerkin ROM models. Five different time step snapshot of the limit cycle oscillation at $Re = 570000$ are selected as an example. With this decomposed solid domain, the dynamics for this prescribed large solid motion problem and the corresponding adapted discretisation are shown in Figure 5.32. The accuracy of the adaptive reduced order model is preserved to be almost the same in comparison to the numerical solution after five iterations.

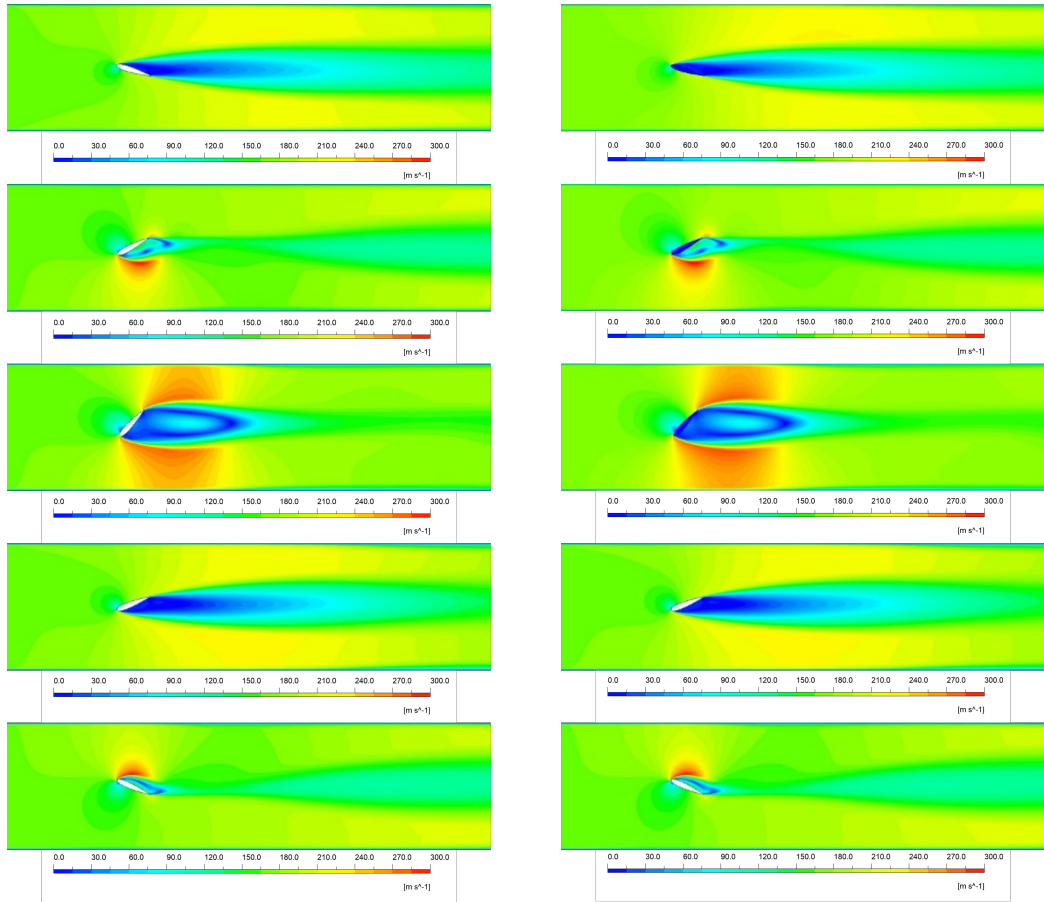


Figure 5.32: Proposed solution for a two-dimensional pitching and plunging aerofoil in the case of the limit cycle oscillation at $Re = 570000$ at different snapshots. Left: numerical solution; Right: reconstructed flowfield using the new proposed ROM.

The reconstructed dynamic system of the most dominant modes, i.e. the first ten modes, are achieved by the adaptive projection onto these modes, and it is compared to the ROM using the same quality of uniform grids to quantify the performance of the proposed POD-Galerkin ROM. The phase portrait of the case of the limit cycle oscillation at the Reynolds number 570,000 is plotted in Figure 5.33, where a comparison is made between the numerical solution and the Galerkin-based ROM with and without the proposed method. The presentation of the plunge profile against the pitch angle is plotted after convergence onto the limit cycle. The phase trajectory rotates counter clockwise, which increases the plunge amplitude, decreases the pitch amplitude and decreases the phase difference.

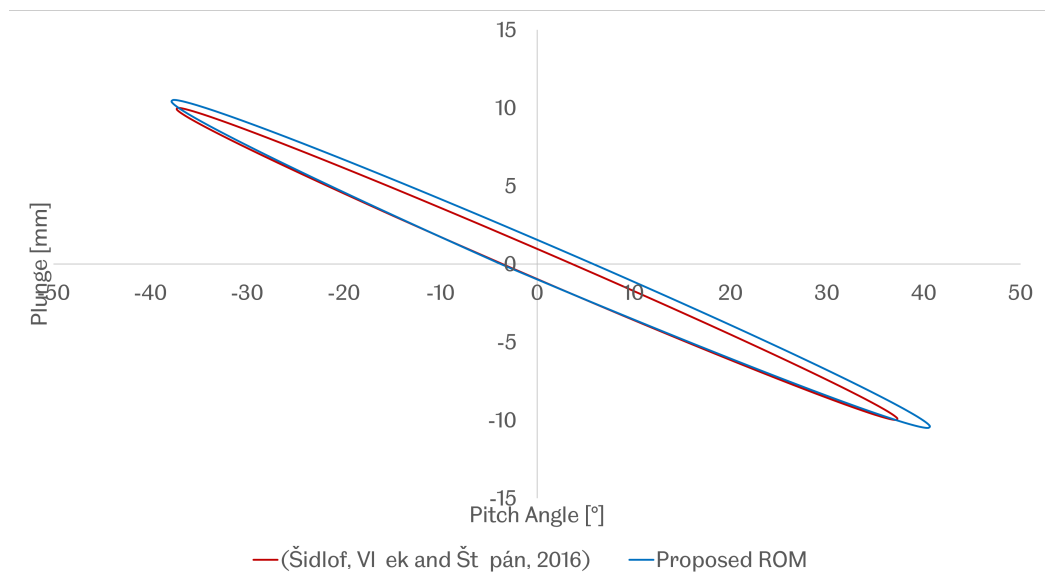


Figure 5.33: A comparison of the POD-Galerkin results using the adaptive and uniform grid discretisation for the flow passing a pitching and plunging aerofoil in the case of a limit damping oscillation at the Reynolds number $Re=570,000$.

Compared to the uniform ROM approach, the proposed ROM more accurately predicts results for both limit cycle oscillation cases. Figure 5.34 shows the normalised error between the benchmarked numerical solution and the ROM method via the uniform approach and the proposed method. The shape, frequency and amplitudes are much closer to the experimental and numerical solution [191]. The proposed adaptive discretisation concentrates on the vicinity of the aerofoil, as well as in the wake region to minimise the velocity variance within the reduced order modelling process, and it varies at different time steps. The accuracies of the adaptive reduced order model are observed to be almost the same in comparison to the numerical solution after five iterations. In contrast, the reconstructed flow fields using the uniform ROM are not perfectly accurate due to the large motion of the aerofoil.

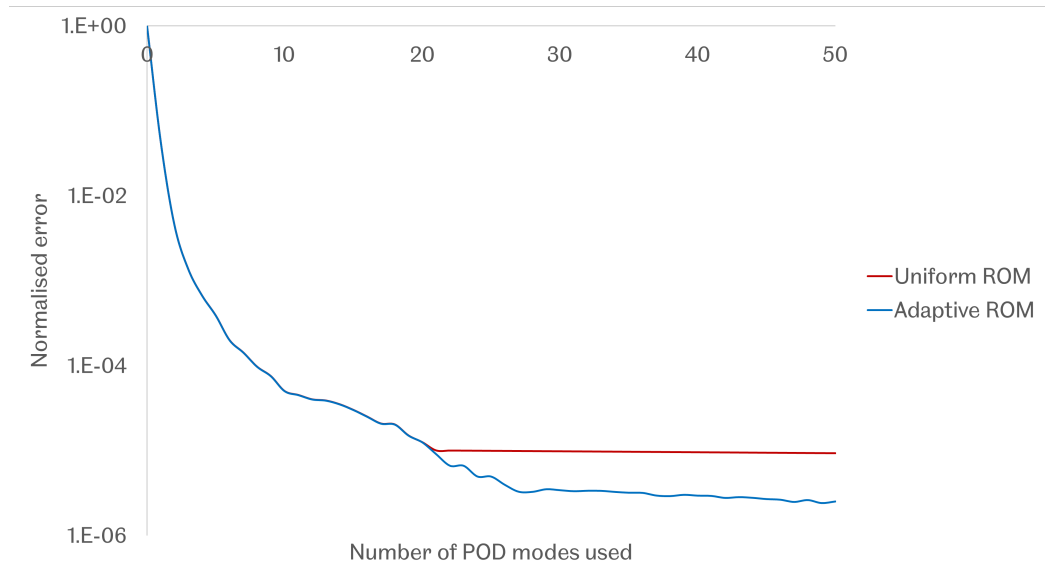


Figure 5.34: Decay of the normalized error for the POD basis using the adaptive and uniform grid discretisation for the flow passing a pitching and plunging aerofoil at the Reynolds number $Re=5700,000$.

Figure 5.35 and 5.36 shows the online and offline CPU time required to compute up to 200 timesteps with varying mesh size. The computational cost of the full order CFD simulation is compared against those of a uniform discretisation and the proposed ROMs. It shows that the cost of the ROM models remains static with an increasing resolution of the mesh, and that significant CPU speed-ups are obtained when using the mesh with the largest number of nodes. The CPU costs were reduced by a factor of about 100 compared to the cost of the high-fidelity model. The offline CPU time listed here includes the time for assembling and solving the matrix for the full model and projecting the POD solution onto the full space, as shown in Figure 5.36. It can be seen that the proposed ROM is much more computationally efficient than the traditional uniform ROM, and this is because the decrease in terms of mesh density speeds the computational speed of the ROMs, since it involves assembling and solving different dimensional matrices.

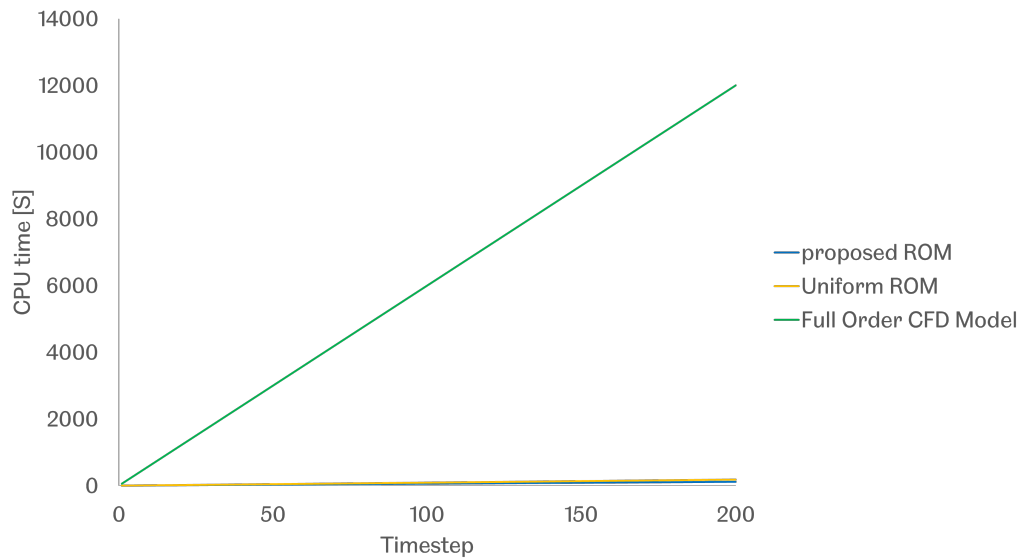


Figure 5.35: Comparison of the online CPU time history on the the two-dimensional pitching and plunging aerofoil in the case of the limit cycle oscillation at the Reynolds number $Re=570,000$ between the full-order CFD solution and the ROMs.

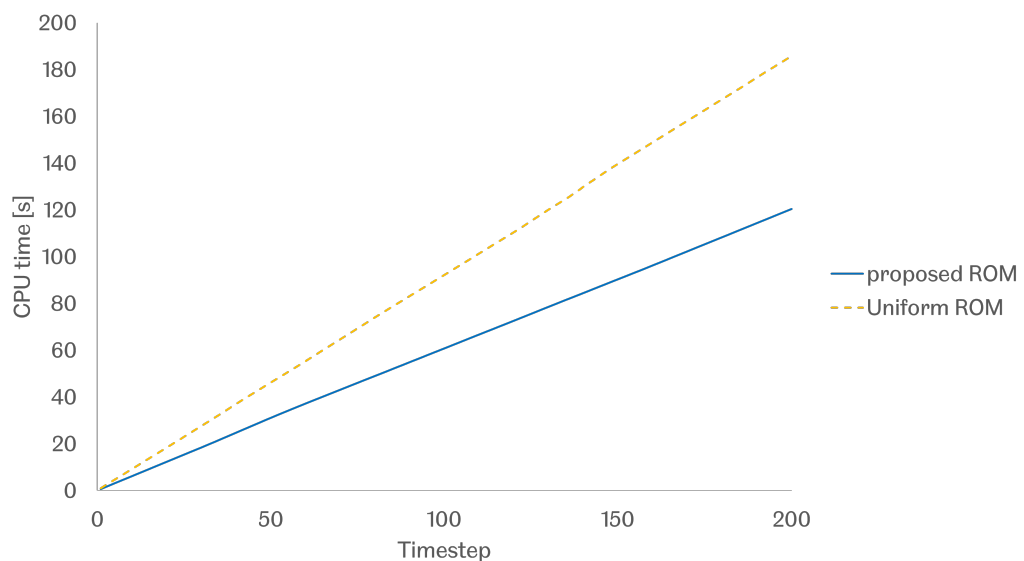


Figure 5.36: CPU time history for the ROMs on a two-dimensional pitching and plunging aerofoil in the case of the limit cycle oscillation at the Reynolds number $Re=570,000$ between the proposed ROM and the uniform ROMs solution.

The proposed ROM more accurately predicts the results for the limit cycle oscillation cases compared to the uniform ROM with the same level of grid. The reconstructed ROM solutions are compared to the existing numerical results as well as the experimental data. The results show a relatively good agreement with the CFD solution regarding

the velocity and displacement fluctuations. Compared to the accuracy and the computational cost between the ROM approach and the numerical method, the proposed ROM shows a very good potential for use in fluid-structure interaction simulations (FSI) problems.

5.3.2.3 Forced Vibration of an Oscillating Aerofoil

In this part, the aerofoil is subject to kinematic limitations that have been imposed (i.e., the oscillating motion is prescribed). The following statement describes the combined motion of pitching and heaving when it is limited to an axis of pitching that is set on the chord line at point x_p from the leading edge:

$$\theta(t) = \theta_0 \sin(\gamma t), \quad h(t) = H_0 \sin(\gamma t + \phi) \quad (5.48)$$

where θ_0 and H_0 are initial pitch angle and plunge, respectively. γ is the angular frequency (which is $2\pi f$), and ϕ is the phase difference with respect to the pitching motion (taken as $\phi = 90^\circ$ in this investigation), as shown in Figure 5.37. The oscillation frequency f is characterized by a reduced frequency f^* defined as

$$f^* = \frac{f c}{U_\infty} \quad (5.49)$$

where U_∞ is the inlet velocity.

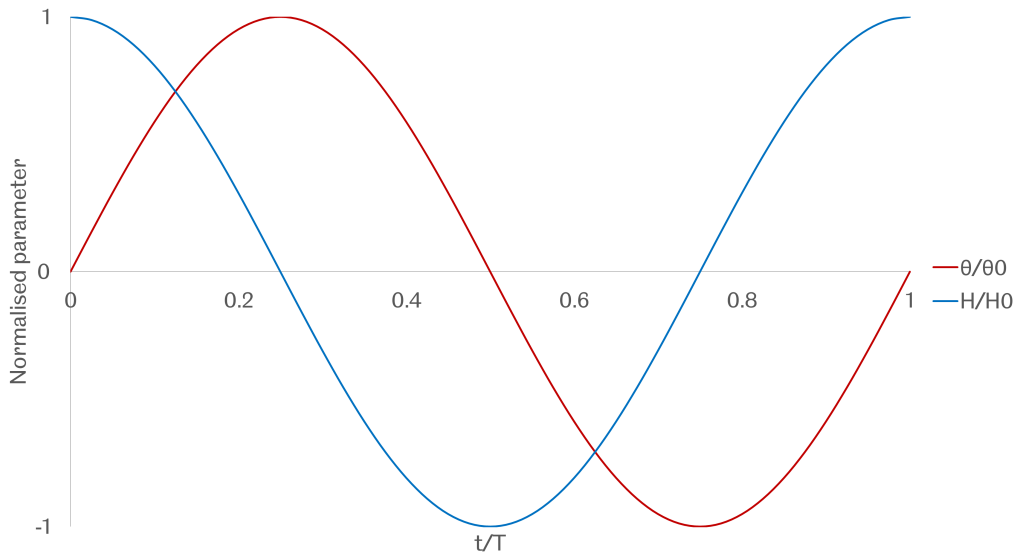


Figure 5.37: Normalised pitch and plunge profiles of the NACA 0015 aerofoil.

The motion profiles of the fluid and solid domains are solved using the ANSYS Fluent and Mechanical solvers, respectively, and coupled by a semi-implicit coupled algorithm. The model is established using ANSYS FLUENT and the Transient Structure modules. The upstream inlet velocity was set to 122.75 m/s in order to produce the Reynolds number of 570,000 as employed in [103], as shown in Figure 5.38. Since the fluid is incompressible, the density and viscosity of the fluid are considered to be constant at 1.225 kg/m^3 , and $1.7894 \times 10^{-5} \text{ kg/(m.s)}$, respectively.

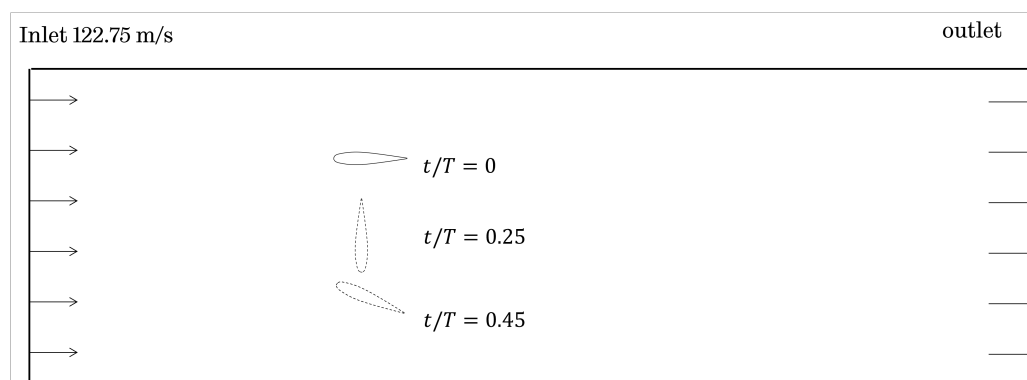


Figure 5.38: Schematic diagram of the domain of the NACA 0015 aerofoil forced vibrating at $Re = 570000$.

The turbulence model used is the $k-\omega$ SST model and the transport equations for the SST model used to calculate the turbulent kinetic energy k and the specific dissipation rate ω are those used in ANSYS FLUENT. This two-equation model is suitable for modelling the boundary layers as well as the far field flows, and therefore it has been used extensively in studies involving wind turbine blades and aeroelastic problems with reasonable results [80, 75].

On considering the computational time and accuracy, the mesh size of 1 mm and the time size of 1×10^{-5} seconds are deemed as the appropriate mesh size and time size for the modelling in this study. The meshes of the simulation consists of two individual domains with structural meshes together with the overset mesh, the fluid model consists of 158,610 nodes and 579,632 elements while the structural part consists of 2595 nodes and 2422 elements, identical to previous cases, as shown in Figure 5.15. The time-step size is 1×10^{-5} seconds and the number of nonlinear iterations per time step is 500. A loose coupling strategy was applied in order to couple both the fluid and structural domains.

The POD snapshot solution has been computed using the ANSYS Mechanical and ANSYS Fluent with a RANS $k-\omega$ SST turbulence model using the ALE method to adapt the

mesh around the oscillating cylindrical body. A loosely coupled algorithm couples both the structural and fluid domains. During one oscillation period, one hundred snapshots are taken, and these are interpolated on a rectangular grid to build a POD basis using Equation (3.5).

The first POD mode is the temporal average velocity field, and the other modes capture the additional velocity fluctuations as given by equation (5.47). As shown in Figure 5.39, the POD modes decrease monotonically. Figure 5.40 illustrates the energy accuracy with different POD modes used and it can be observed that 18 POD modes are sufficient to construct the velocity field within an error in the kinetic energy captured less than 1%. Therefore, the first 18 POD modes are selected in this analysis.

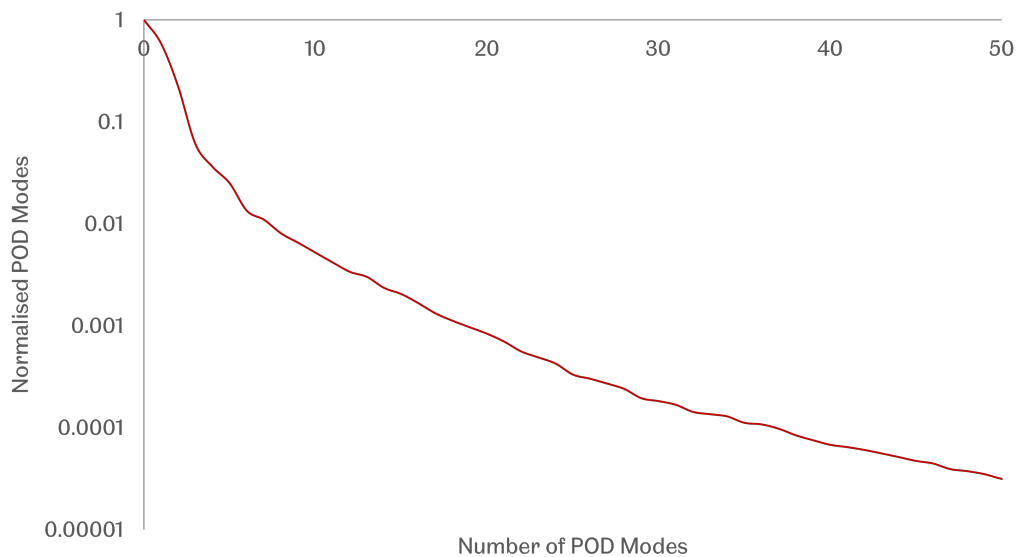


Figure 5.39: The normalised POD modes in the case of the forced oscillation at the Reynolds number $Re = 570,000$.

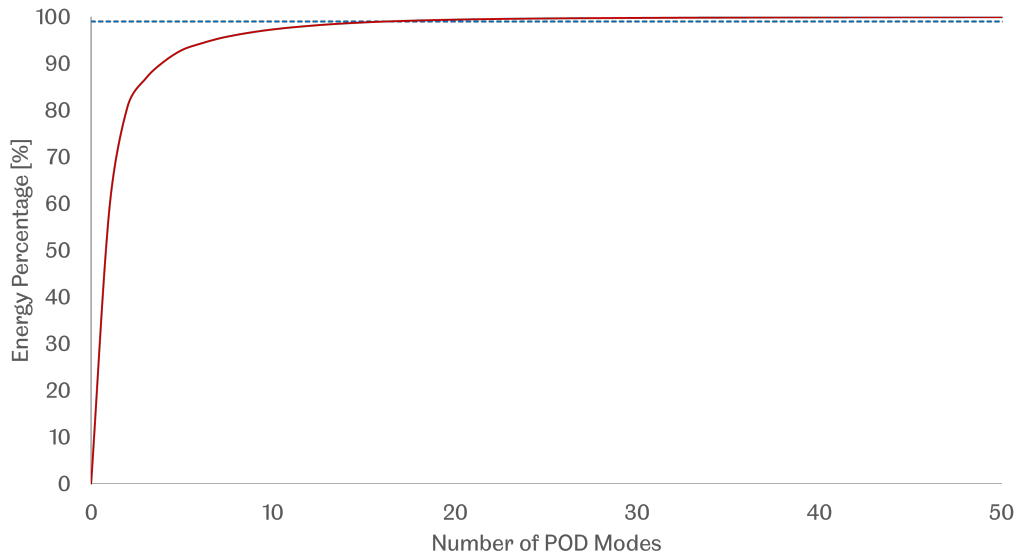


Figure 5.40: ROM accuracy regarding the energy with different number of POD modes in the case of the forced oscillation at $Re = 570000$.

In this section, the rebuilt ROM solutions from the proposed adaptive methodology, namely the solution 80×40 -adaptive, are compared against the corresponding uniform ROM solutions, namely 80×40 -uniform and the proposed adaptive methodology via different refinement levels, namely 40×20 -adaptive. For all the cases, the reduced order models are built using 18 POD modes which covers more than 99% of energy.

Two typical timesteps, i.e., $t/T=0.25$ and 0.45 are selected for ROM solutions to be computed as per (Kinsey and Dumas, 2014). ROM solutions are evaluated and compared in terms of accuracy and computational efficiency.

In order to make the comparison clearer, the rebuilt ROM solution via the proposed adaptive ROM methodology is compared against the ROM solution via the uniform ROM model whose grid size is same as the minimum grid size of the adaptive ROM model. For instance, as an illustrative example shown in Figure 5.41, the "adaptive ROM solution - Level 2" is compared against the "uniform ROM solution - Level 2".

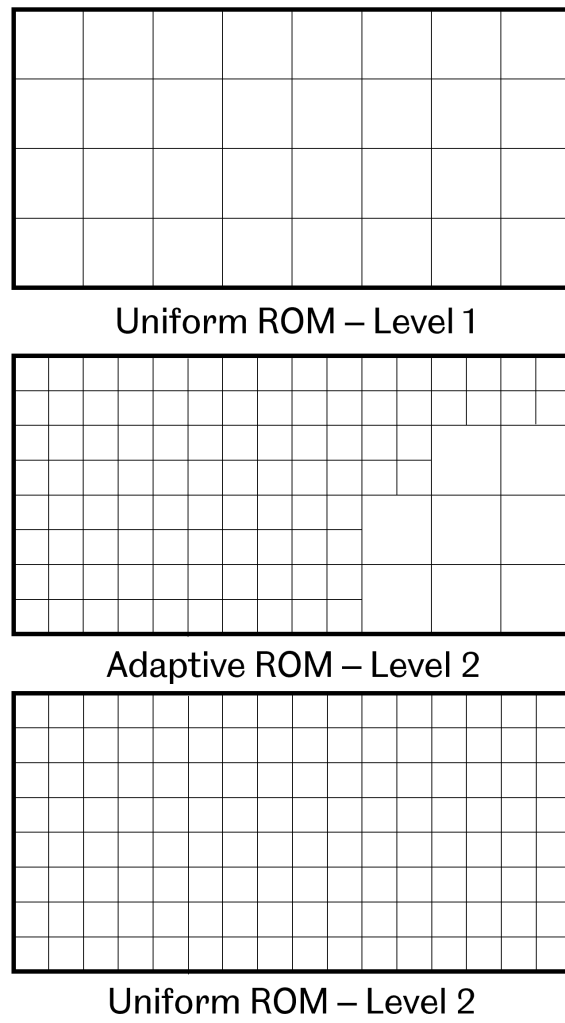
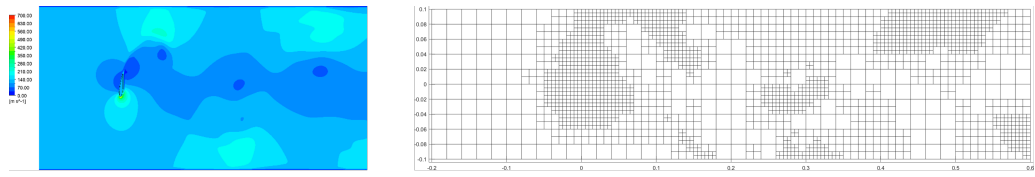
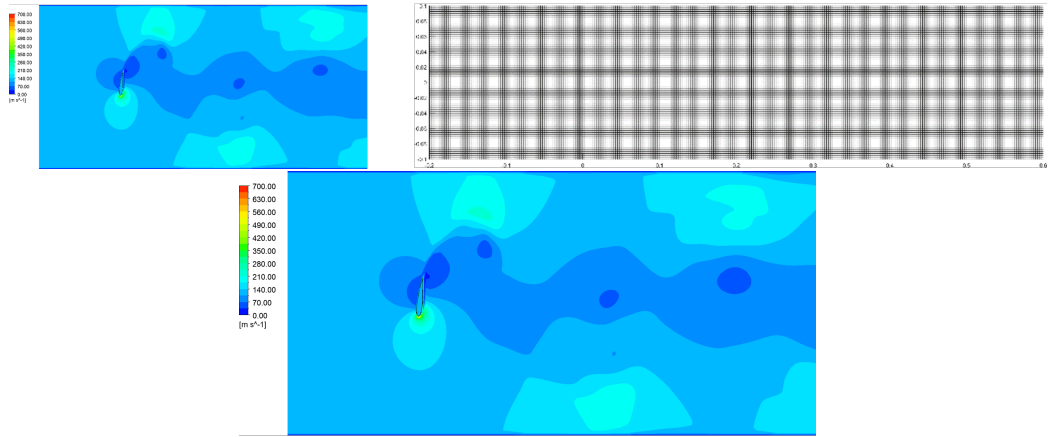


Figure 5.41: Comparison between the adaptive ROM solution and the corresponding uniform ROM solution in the case of the forced oscillation at $Re = 570000$.

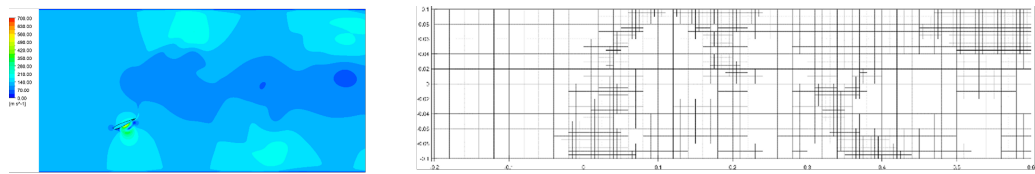
Figure 5.42 shows the solutions for the flow past the cylinder at time instances $t/T = 0.25$ and 0.45 , as calculated using the proposed ROM models (80×40 - adaptive), the corresponding ROM solutions via uniform grids (80×40 - uniform) using 18 POD basis functions, and the referenced full order CFD solution at Reynolds number $Re=500,000$. The proposed POD-Galerkin ROM model with/without adaptively refinement strategy have performed particularly well at resolving the flow field at both time instances. The proposed uniform ROM models are able to capture the wave pattern but have a large error near the peak of the waves during the spin-up period of the modelling.



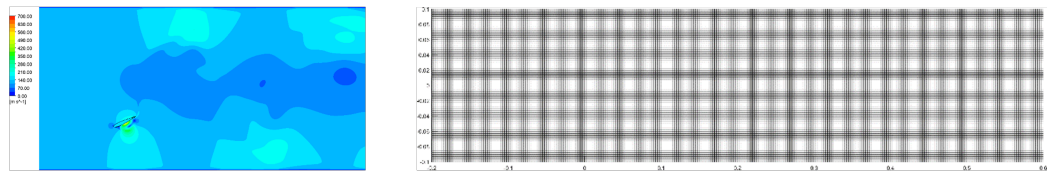
(1a) Reconstructed adaptive ROM solution at $t/T = 0.25$



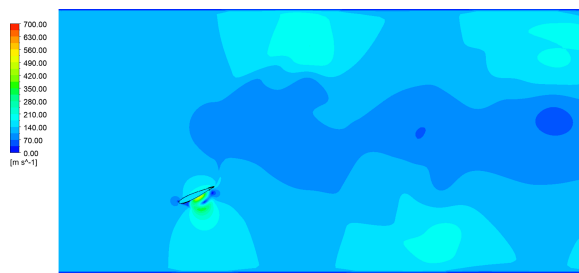
(1b) Reconstructed uniform ROM solution at $t/T = 0.25$



(2a) Reconstructed adaptive ROM solution at $t/T = 0.45$



(2b) Reconstructed uniform ROM solution at $t/T = 0.45$



(2c) Reconstructed uniform ROM solution at $t/T = 0.45$

Figure 5.42: Comparison between the proposed adaptive solution and the uniform ROM for a two-dimensional forced vibration aerofoil at $Re = 570000$ at timesteps $t/T=0.25$ (1) and 0.45 (2).

The $err(N)$ of the proposed method in the prediction of the displacement and veloc-

ity fluctuations is around 0.2% close to those of the uniform ROM model which is around 0.3%, as shown in Figure 5.43.

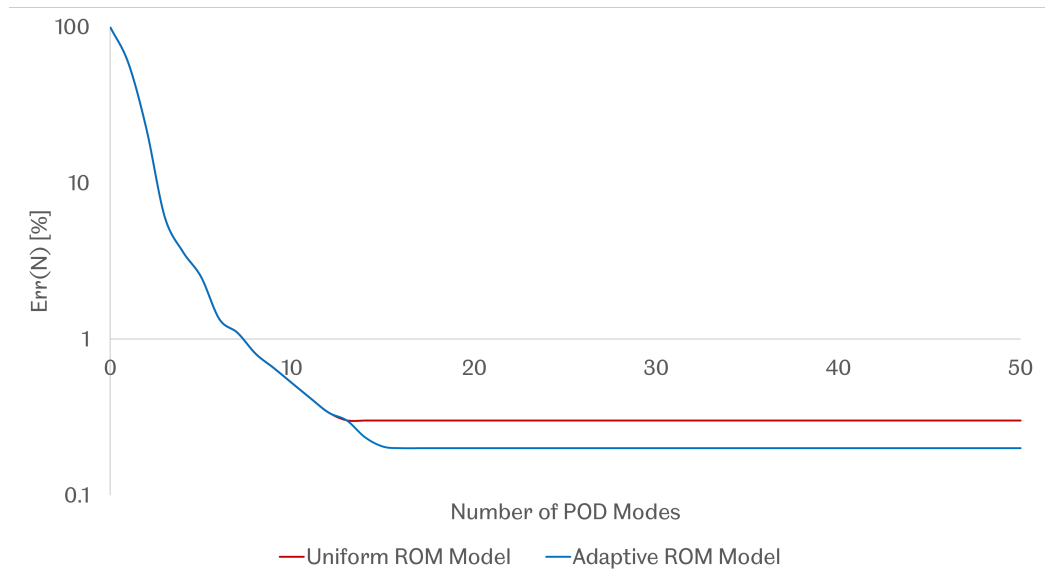


Figure 5.43: Error $err(N)$ of velocity profile obtained via different numbers of POD modes in the case of the flow induced vibration of the oscillating aerofoil NACA 0015 at $Re = 570000$.

Figure 5.45 summarises the computational costs of both the uniform and adaptive ROM models. The adaptive ROM model is much more computationally efficient than the uniform model as the proposed adaptively refinement reduces the size of matrices used in the ROM calculation while maintaining same level of accuracy.

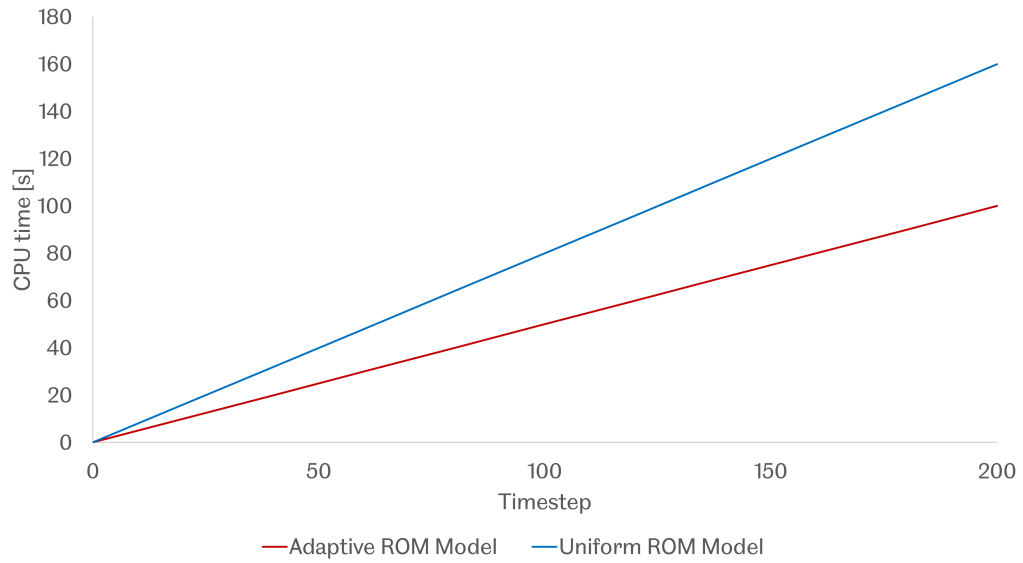


Figure 5.44: Comparison of CPU time history between the proposed ROM and the uniform ROM on the prescribed of the NACA 0015 aerofoil at $Re = 570000$.

As shown in the previous figures, both proposed POD-Galerkin ROMs show a good agreement with the CFD solution. It is observed that error $err(N)$ of the proposed method in the prediction of the displacement and velocity fluctuations is around 0.2%. The proposed ROM method shows a better performance compared to the proposed ROM method via uniform grid, as shown in Figure 5.14. This is due to the errors being compounded when truncating the POD eigenfunctions, when constructing the POD basis, having insufficient sampling and the errors in the inner product and the numerical integration of the ROM.

In addition, the rebuilt ROM solution via the proposed adaptive ROM is compared against the proposed ROM solution via different refinement levels. For instance, as an illustrative example shown in Figure 5.45, the "adaptive ROM solution - Level 1" is compared against the "adaptive ROM solution - Level 2" in this section, as the minimum grid size of these two models is identical.

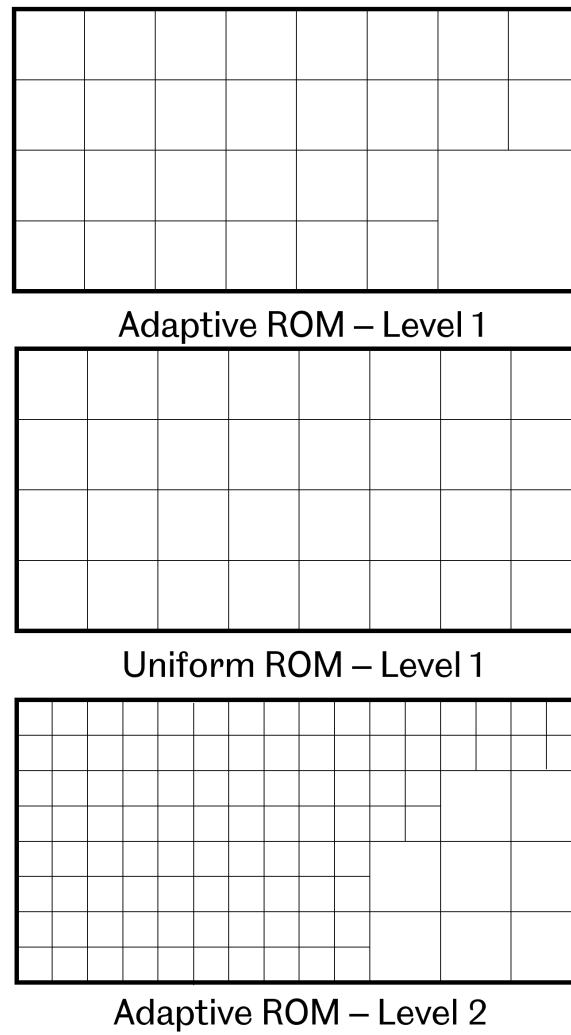
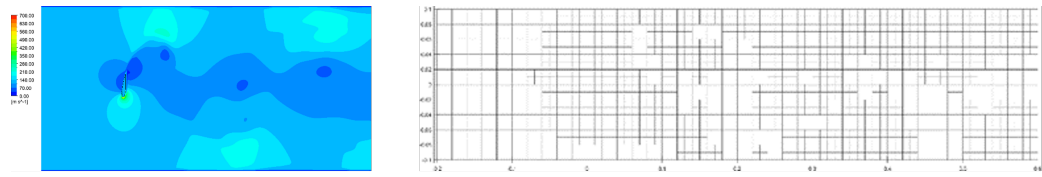
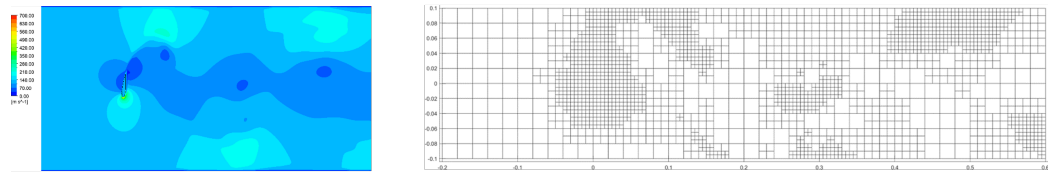


Figure 5.45: Illustrative demonstration of the adaptive ROM solution and the corresponding uniform ROM solutions.

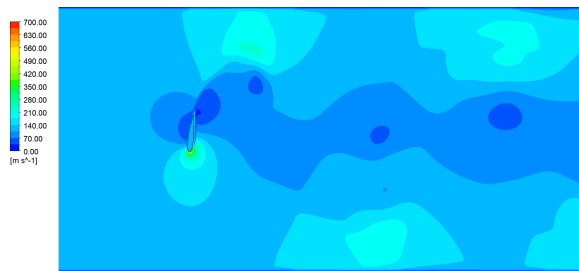
Figure 5.46 shows the solutions for the flow past the cylinder at time instances $t/T = 0.25$ and 0.45 , as calculated using the proposed ROM models (80×40 -adaptive), the corresponding ROM solutions via uniform grids (80×40 -uniform) using 18 POD basis functions, and the referenced full order CFD solution at $Re = 570000$. The POD-Galerkin ROM model that was developed with and without an adaptively refined technique has done exceptionally well when it comes to resolving the flow field at both time occurrences. The wave pattern can be captured by the suggested uniform ROM models, however these models have a significant amount of inaccuracy at the peaks of the waves during the spin-up phase of the modelling process.



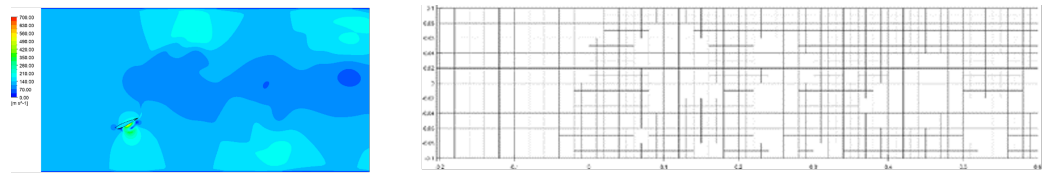
(1a) Reconstructed adaptive ROM – Level 1 solution at $t/T = 0.25$



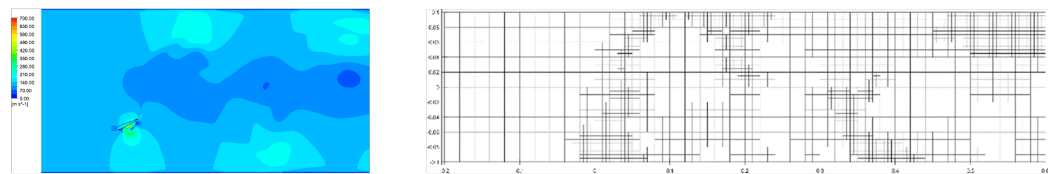
(1b) Reconstructed adaptive ROM – Level 1 solution at $t/T = 0.25$



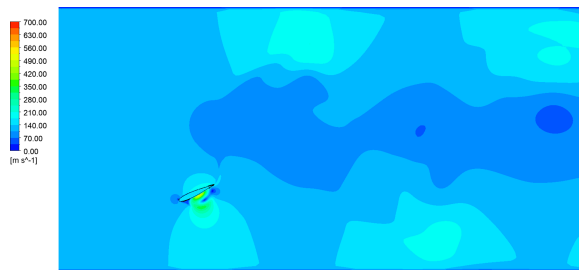
(1c) Full order CFD solution at $t/T = 0.25$



(2a) Reconstructed adaptive ROM – Level 1 solution at $t/T = 0.45$



(2b) Reconstructed adaptive ROM – Level 2 solution at $t/T = 0.45$



(2c) Full order CFD solution at $t/T = 0.45$

Figure 5.46: Comparison of the proposed adaptive solutions for a two-dimensional forced vibration aerofoil at $Re = 570000$ at timesteps $t/T = 0.25$ (1) and 0.45 (2).

The relative error between the proposed ROM solution via two different levels and the referenced CFD solution is illustrated in Figure 5.47. As a result of the increased size of matrices used in the POD-Galerkin projection, one additional level of adaptive refinement successfully reduces the error profile of the velocity fluctuations from around 1% (Adaptive ROM Model - Level 1) close to around 0.3% (Adaptive ROM Model - Level 2).

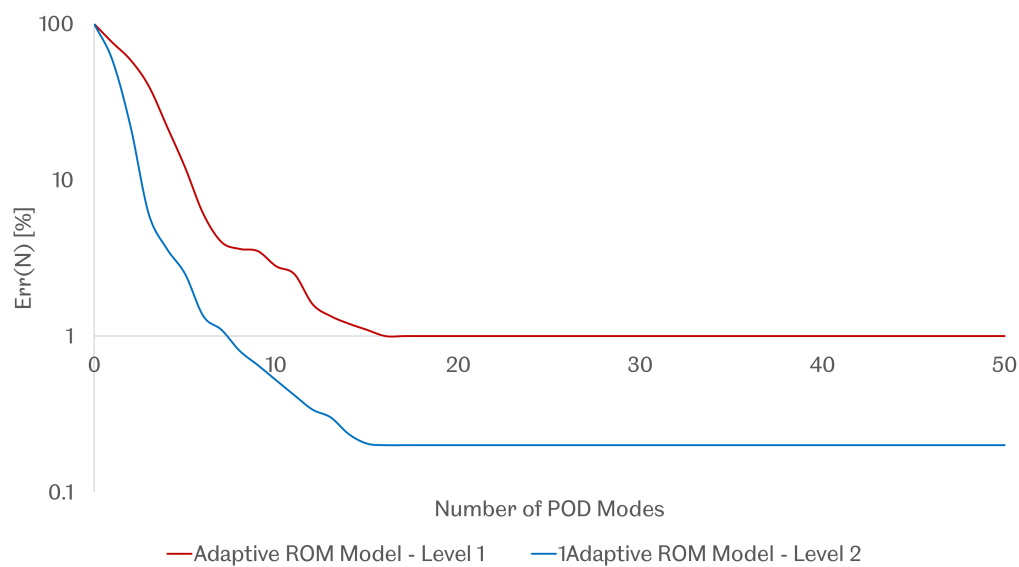


Figure 5.47: Error $err(N)$ of velocity profile obtained via different numbers of POD modes using adaptive ROM models in the case of the flow induced vibration of an oscillating aerofoil NACA at $Re = 570000$.

However, this improvement in terms of accuracy sacrifices the computational efficiency as summarised in Figure 5.48. It shows the computational costs of both adaptive ROM models via different refinement level. The so called "Adaptive ROM model - level 2" is less computationally efficient than the "Adaptive ROM model - level 1" as the additional adaptive refinement reduces the size of grids therefore increases the size matrices used in the ROM calculation. It should be noted that the additional refinement levels sometime not necessary when the loss of computational efficiency is considered. In addition, compared to the proposed uniform ROM model with same grid size, the proposed adaptive ROM method still shows a performance in terms of computational efficiency.

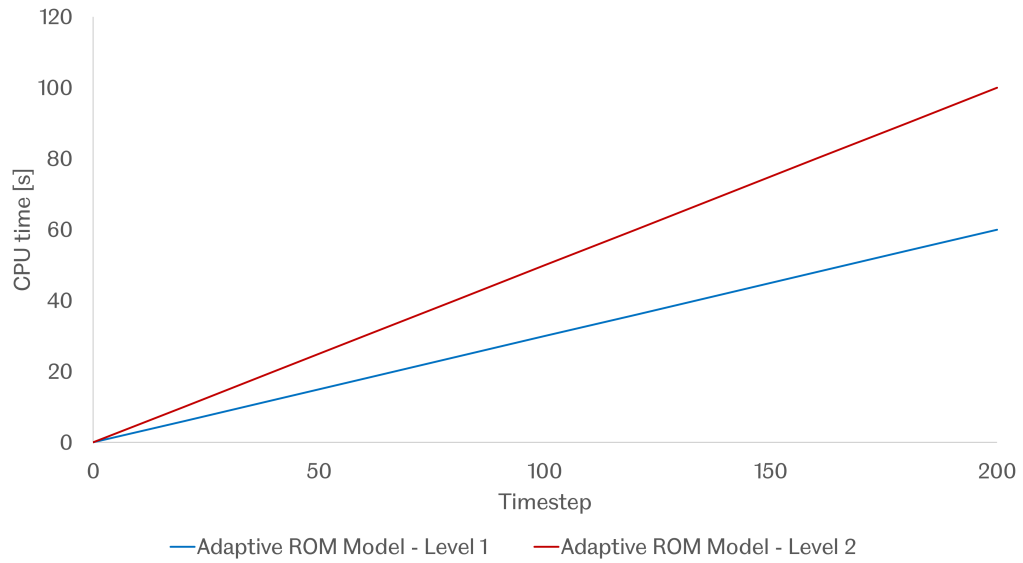


Figure 5.48: CPU time history for the proposed adaptive ROMs on the prescribed of the NACA 0015 aerofoil at $Re = 570000$.

5.4 Conclusion

In this chapter a new ROM model that deals with moving fluid-solid interfaces is proposed. This new method that has been proposed solves the problem of a moving solid body by first considering a fixed grid that contains the entire time-variant grid (both fluid and solid), and then interpolating the fluid and the solid velocity field from the time variant grid to the locally refined grid. In other words, the problem is solved by considering a fixed grid that contains the entire time-variant grid (both fluid and solid). After that, the POD basis for the global velocity field (both fluid and solid) is generated using the fixed uniform one as the starting point. After then, a distinctive function that follows each of the different domains is brought into play. In addition, the compatibility to the proposed adaptively refinement strategy (Chapter 4) is investigated. The proposed method is first applied to model a two-dimensional flow passing an oscillating circular cylinder at relatively low Reynolds number, then under a more complicated flow condition, namely flow-induced vibration of a pitching and plugin aerofoil. The reconstructed ROM solutions are compared to the existing numerical results as well as the experimental data when it is possible. Additional cases are added to investigate the performance of the proposed model in the case of higher Reynolds number, namely at 500,000. The proposed model is applied to the flow-induced vibration and the prescribed oscillation of the aerofoil NACA0015 at $Re = 570000$. For each case, error estimations and time analy-

ses are compared to the corresponding uniform grid ROM solution. Both the ROM results show a relatively good agreement with the CFD solution regarding the velocity and displacement fluctuations. In addition, the proposed method presents a better capability and accuracy to deal with FSI problems compared to the traditional uniform reduced order model at various Reynolds numbers. The adaptive refinement strategy shows a good compatibility with the proposed ROM model for FSI problems. The adaptive ROM model is computationally more efficient than the proposed uniform one, and the size of grid employed is same as the minimum grid size of the adaptive ROM.

Chapter 6

Locally Refined POD-Galerkin Based ROM with Deforming Fluid-Solid Interface

6.1 Introduction

In this chapter, a POD-Galerkin based reduced-order model with deforming fluid-solid interface has been proposed by projecting the governing Navier-Stokes equation onto the POD modes. Some general results obtained in the last decade in the field of reduced order modelling in fluid mechanics are presented. The idea of the Galerkin method is to project the governing equations onto a finite-dimensional subspace of the full phase space (Holmes, et al., 1996). To perform the Galerkin method, the phase space must be an inner product space spanned by a suitable set of basis functions. The Proper Orthogonal Decomposition (POD) approach is employed to capture more energy with a small number of basis functions.

Differ from the previous chapter, this chapter focuses on the fluid-structure interaction problems with deforming fluid-solid interface, where rigid domain is no longer considered as flexible other than rigid in the Chapter 5. Computer simulations of the dynamics of complicated structural systems using first-principles models may sometimes be prohibitively costly. This is similar to the situation with fluid mechanical systems. In order to analyse and optimise the design of complex structures, methods are required that may decrease the number of degrees of freedom possessed by the models while yet maintaining all of the pertinent physics. One strategy for achieving model flexibility for structures is to first create a full finite element model, and then use a component approach that is borrowed from the finite segment method. This allows for a significant reduction in the number of degrees of freedom, while still incorporating the essential

physics and nonlinearities of the system.

Validation entails making a comparison between the results achieved through the use of the model presented and the findings acquired through the use of various simulation models or those gained through the use of experimental measurements. The proposed method is first applied to model a two-dimensional flow around a flexible plate, and then a three-dimensional flow-induced and forced vibration simulation on both NACA 0015 aerofoil and teardrop shape aerofoil at various Reynolds numbers. For each case, the reconstructed ROM solutions from the proposed methodology are compared to the numerical results as well as experimental solution when it is possible in order to validate the accuracy and performance of the model. In addition, in order to test the compatibility of the proposed refinement strategies introduced in Chapter 4 are applied to both these simulations, and error estimations and time analyses are compared to the corresponding uniform grid ROM solution.

6.2 Modelling of a slender body using the finite segment method

The discretisation of a flexible link into stiff parts (segments) that represent the link's inertial properties is the fundamental concept behind the finite segment technique. This method is also known as the finite element method. Joints made out of massless and non-dimensional spring-damping devices that reflect the stiffness properties of the connection are used to connect the segments together, as shown in Figure 6.1, where a flexible body $\mathbf{P}_0\mathbf{P}_n$ is modelled as a chain of rigid segments $\mathbf{P}_{i-1}\mathbf{P}_n$, $i = 1, \dots, n$.

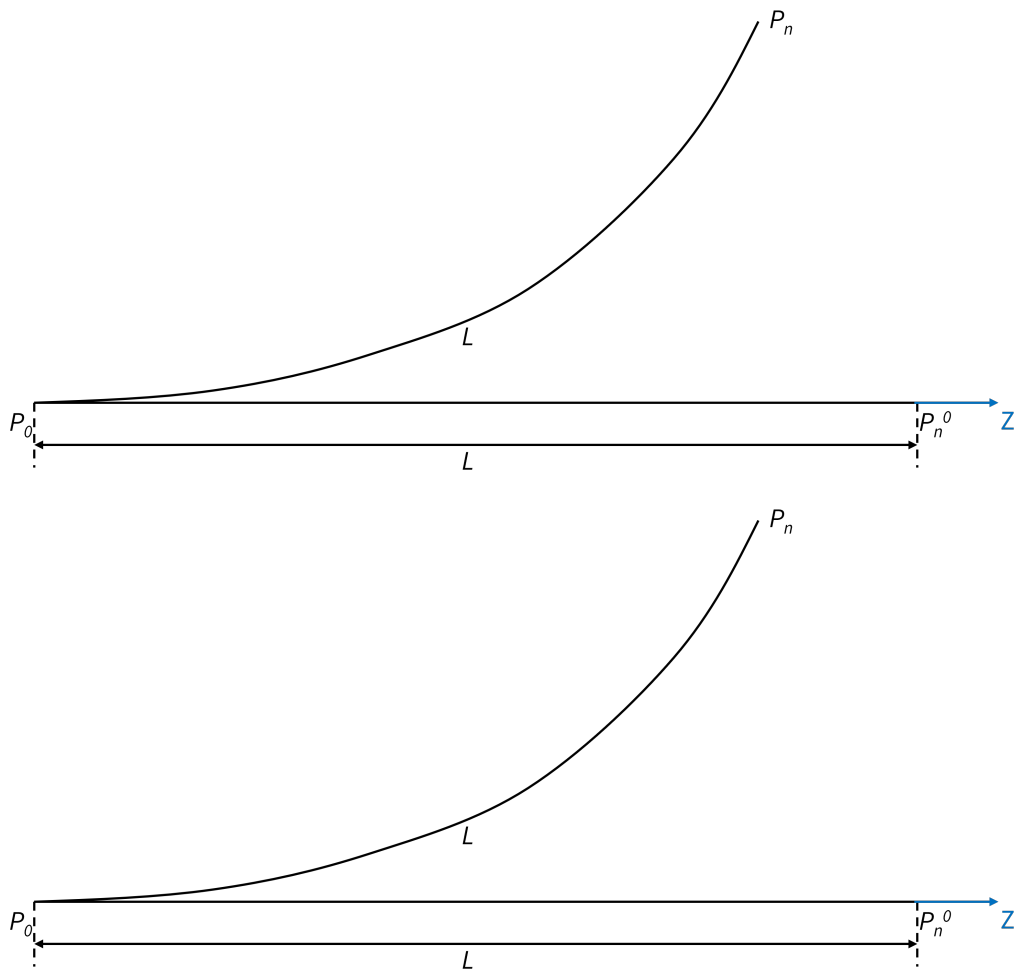


Figure 6.1: Flexible link before and after solid body deformation and its discretisation.

6.2.1 Coordinates

When the longitudinal flexibility is omitted, the following relation is valid:

$$L = \widehat{P_0 P_n} = \sum_{i=1}^n L_i \quad (6.1)$$

This indicates that the length of the deformed link along its curvature remains unchanged, and this makes it possible to take into consideration the amount Δ depicted in Figure 6.1, which is the result of significant deformations in the flexible link. The notation that is shown in Figure 6.3 is added because it is necessary to be able to specify the location of any point on the neutral axis of the connection that is located in the i th segment [4].

The Euler angles presented in Figure 6.2 are introduced in order to describe the orientation of a rigid segment, namely $P_{i-1}P_i^0$. These angles define absolute rotations, in which the Euler angles ZYX define the orientation of the system $\{i\}$ with respect to the preceding segment $\{i-1\}$.

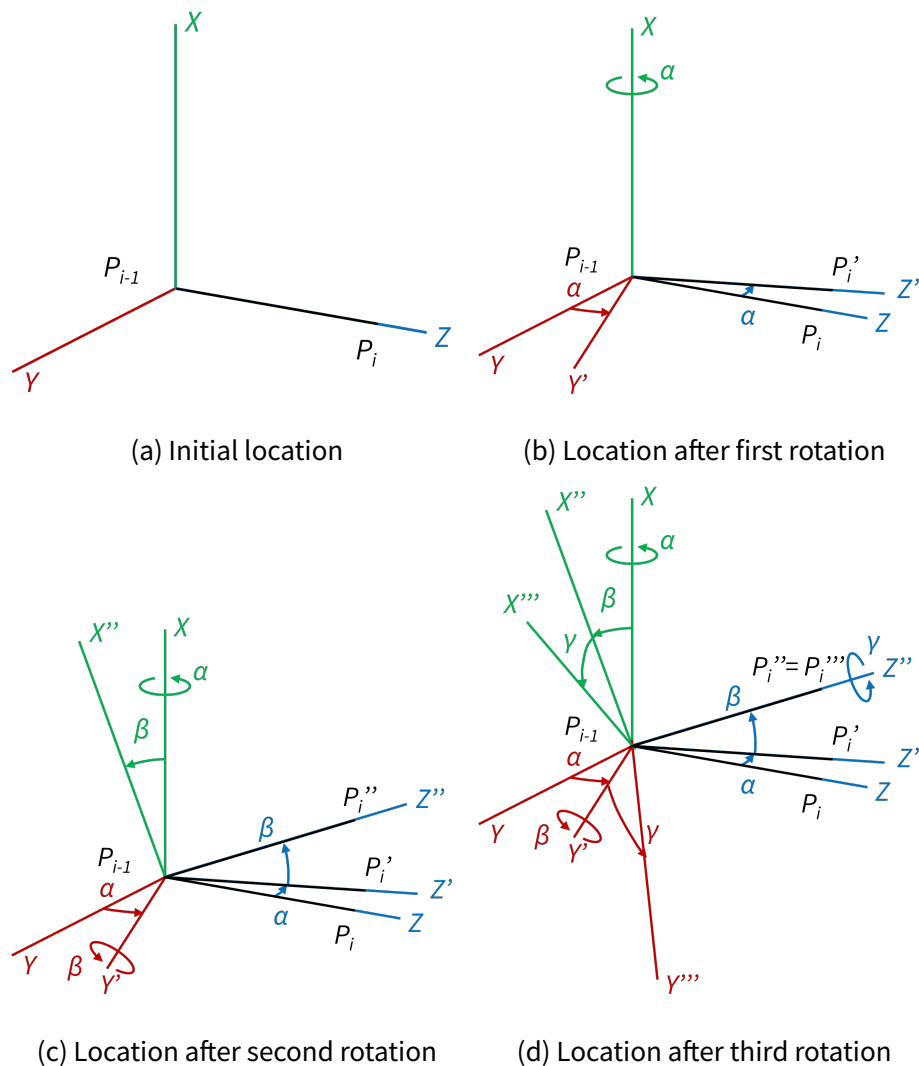


Figure 6.2: Illustrative demonstration of the Euler angles used for solid body rotation.

Initially the i -th segment $P_{i-1}P_i^0$ lies parallel to the z axis of the inertial frame, as shown in Figure 6.2a. The order of rotations which leads to the end of the i -th segment from point P_i^0 to the point P_i is as follows:

1. The first rotation around the X axis by an angle α_i to form $X'Y'Z'$, as shown in Figure 6.2b.

2. The second rotation around the Y' axis by an angle β_i to form $X''Y''Z''$, as shown in Figure 6.2c.
3. The third rotation around the Z''' axis by an angle γ_i to form $X'''Y'''Z'''$, as shown in Figure 6.2d.

The rotation matrix of each rotation yields the following

$$\begin{aligned}
 \mathbf{R}_x &= \begin{bmatrix} 1 & 0 & 0 \\ 0 & \cos \alpha_i & -\sin \alpha_i \\ 0 & \sin \alpha_i & \cos \alpha_i \end{bmatrix}, \\
 \mathbf{R}_y &= \begin{bmatrix} \cos \beta_i & 0 & \sin \beta_i \\ 0 & 1 & 0 \\ -\sin \beta_i & 0 & \cos \beta_i \end{bmatrix}, \\
 \mathbf{R}_z &= \begin{bmatrix} \cos \gamma_i & -\sin \gamma_i & 0 \\ \sin \gamma_i & \cos \gamma_i & 0 \\ 0 & 0 & 1 \end{bmatrix},
 \end{aligned} \tag{6.2}$$

The combined rotation matrix \mathbf{R}_i yields

$$\begin{aligned}
 \mathbf{R}_i &= \mathbf{R}_x \mathbf{R}_y \mathbf{R}_z \\
 &= \begin{bmatrix} \cos \beta_i \cos \gamma_i & -\cos \beta_i \sin \gamma_i & \sin \beta_i \\ \cos \alpha_i \sin \gamma_i + \sin \alpha_i \sin \beta_i \cos \gamma_i & \cos \alpha_i \cos \gamma_i - \sin \alpha_i \sin \beta_i \sin \gamma_i & -\sin \alpha_i \sin \beta_i \\ \sin \alpha_i \sin \gamma_i - \cos \alpha_i \sin \beta_i \cos \gamma_i & \sin \alpha_i \cos \gamma_i + \cos \alpha_i \sin \beta_i \sin \gamma_i & \cos \alpha_i \cos \beta_i \end{bmatrix} \\
 &= \begin{bmatrix} \uparrow & \uparrow & \uparrow \\ \mathbb{A}_i & \mathbb{B}_i & \mathbb{C}_i \\ \downarrow & \downarrow & \downarrow \end{bmatrix}
 \end{aligned} \tag{6.3}$$

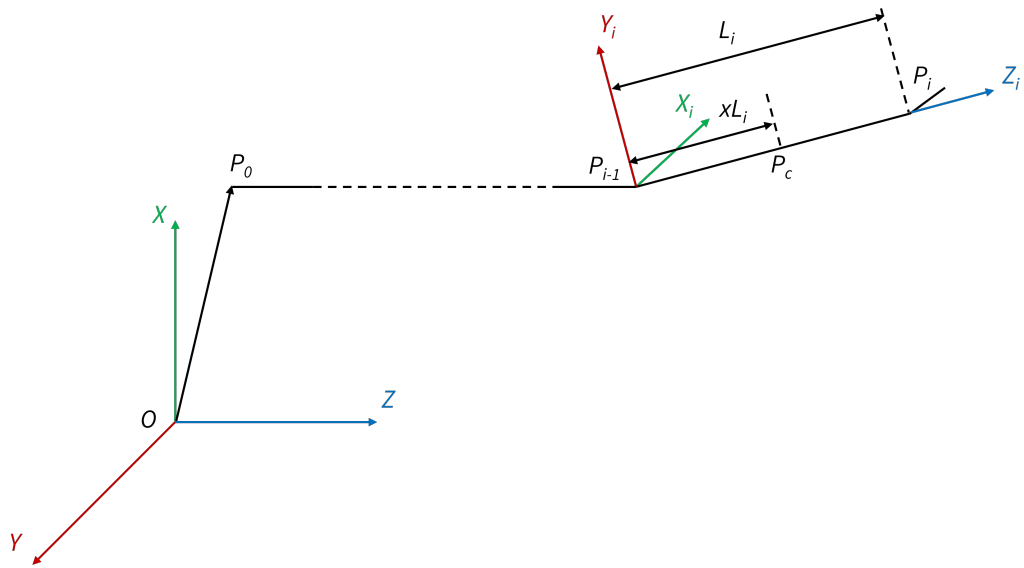


Figure 6.3: Illustrative demonstration of the notation used for the i -th segment

Figure 6.3 shows the notation used in the i -th segment $P_{i-1}P_i$ whose length is L_i . For any point P_c in the neutral axis of the i -th segment lying at a distance $xL_i, 0 \leq x \leq 1$ from the point P_{i-1} with respect to axes of the inertial frame of reference, the coordinate of P_{i-1} takes the following form:

$$\begin{aligned}
 \mathbf{r}_{P_{i-1}} &= \overrightarrow{OP_0} + \sum_{j=1}^{i-1} \overrightarrow{P_{j-1}P_j} \\
 &= \mathbf{r}_0 + \sum_{j=1}^{i-1} \mathbf{R}_j \begin{pmatrix} 0 \\ 0 \\ L_j \end{pmatrix} \\
 &= \mathbf{r}_0 + \sum_{j=1}^{i-1} L_j \mathbf{C}_j
 \end{aligned} \tag{6.4}$$

where \mathbf{r}_0 is the coordinate of the point P_0 , and \mathbf{C}_i is the third column of the matrix \mathbf{R}_i .

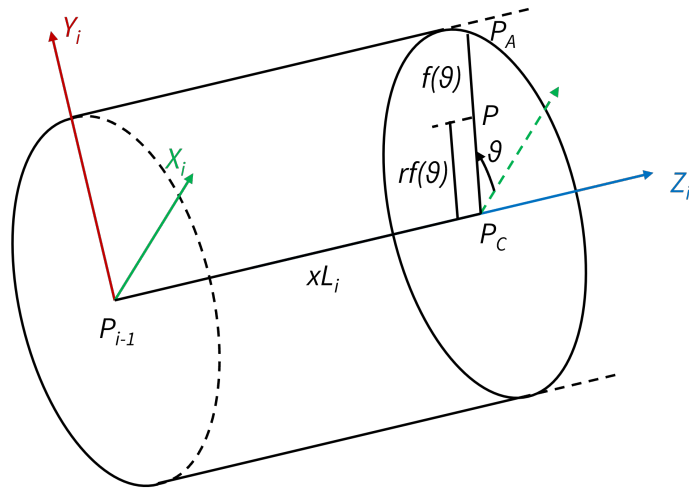


Figure 6.4: Illustrative demonstration of the additional notation used for the i-th segment

Several additional parameters are introduced to describe the coordinate of any point in the i-th segment $P_{i-1}P_i$. For any point P located at the interface of the segment, let $rf_i(\theta)$, $0 \leq r \leq 1$ be the radial distance from the Z_i -axis to the point P, θ be the azimuth angle between the X_i -axis and P_cP , the coordinate of the point P with respect to the coordinate system $X_iY_iZ_i$ becomes $(rf_i(\theta) \cos \theta, rf_i(\theta) \sin \theta, xL_i)$

Thus, for any point P on the i-th segment $P_{i-1}P_i$, the coordinate is defined as follows:

$$\begin{aligned}
 \mathbf{r}_P &= \overrightarrow{OP_0} + \sum_{j=1}^{i-1} \overrightarrow{P_{j-1}P_j} + \overrightarrow{P_{i-1}P} \\
 &= \mathbf{r}_0 + \sum_{j=1}^{i-1} \mathbf{R}_j \begin{pmatrix} 0 \\ 0 \\ L_j \end{pmatrix} + \mathbf{R}_i \begin{pmatrix} rf_i(\theta) \cos \theta \\ rf_i(\theta) \sin \theta \\ xL_i \end{pmatrix} \\
 &= \mathbf{r}_0 + \sum_{j=1}^{i-1} L_j \mathbf{C}_j + rf_i(\theta) \cos \theta \mathbf{A}_i + rf_i(\theta) \sin \theta \mathbf{B}_i + xL_i \mathbf{C}_i
 \end{aligned} \tag{6.5}$$

where \mathbf{A} , \mathbf{B} , and \mathbf{C} are the first, second and third column of the matrix \mathbf{R}_i , respectively.

When a solid domain is modelled as a combination of N segments $P_{i-1}P_i$, $i = 1, \dots, n$, and the whole system is defined by the components of a vector of $N = 3 + 3(n + 1) = 3n + 6$ elements:

$$\mathbf{q} = [\mathbf{r}_0 \quad \mathbf{q}_0 \quad \cdots \quad \mathbf{q}_i \quad \cdots \quad \mathbf{q}_n] \tag{6.6}$$

where $\mathbf{q}_i = [\alpha_i \quad \beta_i \quad \gamma_i]$ is the vector of coordinates describing relative of motion of the i-th segments.

6.2.2 Equations of motion

The governing equations of motion are derived from the general form of the Euler-Lagrange equations:

$$\frac{d}{dt} \frac{\partial T}{\partial \dot{\mathbf{q}}_i} - \frac{\partial T}{\partial \mathbf{q}_i} + \frac{\partial V}{\partial \mathbf{q}_i} + \frac{\partial D}{\partial \dot{\mathbf{q}}_i} = \mathbf{Q}_i, \quad i = 1, \dots, N \quad (6.7)$$

where T and V are the kinetic energy and potential energy of the system, respectively, D is the dissipation function. q_i is the i -th row of the vector \mathbf{q} , and it can be either the coordinates or angles. N is the number of the coordinates used in the system, in this case, $3n + 6$.

6.2.2.1 Kinetic energy

For a rigid segment, namely the i -th segment $P_{i-1}P_i$, the kinetic energy takes the following equation:

$$\begin{aligned} T_i &= \frac{1}{2} \rho \int_V \dot{\mathbf{r}}_P \cdot \dot{\mathbf{r}}_P dV \\ &= \frac{1}{2} \rho \int_{x=0}^1 \int_{r=0}^1 \int_{\theta=0}^{2\pi} \dot{\mathbf{r}}_P \cdot \dot{\mathbf{r}}_P \cdot L_i \cdot r dr \cdot dx \cdot [f_i(\theta)]^2 d\theta \end{aligned} \quad (6.8)$$

On substituting Equation 6.5 into Equation 6.8 yields

$$\begin{aligned}
T_i &= \frac{1}{2} \rho \int_V \left[\mathbf{v}_0 + \sum_{j=1}^{i-1} L_j \mathbf{C}'_j + r f_i(\theta) \cos \theta \mathbb{A}'_i + r f_i(\theta) \sin \theta \mathbb{B}'_i + x L_i \mathbf{C}'_i \right]^T \\
&\quad \cdot \left[\mathbf{v}_0 + \sum_{j=1}^{i-1} L_j \mathbf{C}'_j + r f_i(\theta) \cos \theta \mathbb{A}'_i + r f_i(\theta) \sin \theta \mathbb{B}'_i + x L_i \mathbf{C}'_i \right] dV \\
&= \frac{1}{2} \rho L_i \left[\left(\frac{1}{2} \mathbf{v}_0 \cdot \mathbf{v}_0 + \sum_{j=1}^{i-1} L_j \mathbf{v}_0 \cdot \mathbf{C}'_j + \frac{1}{2} \sum_{j=1}^{i-1} \sum_{k=1}^{i-1} L_j L_k \mathbf{C}'_j \cdot \mathbf{C}'_k \right. \right. \\
&\quad \left. \left. + \frac{1}{2} L_i \mathbf{v}_0 \cdot \mathbf{C}'_i + \frac{1}{2} L_i \sum_{j=1}^{i-1} L_j \mathbf{C}'_i \cdot \mathbf{C}'_j + \frac{1}{6} L_i^2 \mathbf{C}'_i \cdot \mathbf{C}'_i \right) \int_0^{2\pi} (f_i(\theta))^2 d\theta \right. \\
&\quad \left. + \left(\frac{1}{3} L_i \mathbf{C}'_i + \frac{2}{3} \mathbf{v}_0 + \frac{1}{3} \sum_{j=1}^{i-1} L_j \mathbf{C}'_j \right) \cdot \mathbb{A}'_i \int_0^{2\pi} [f_i(\theta)]^3 \cos \theta d\theta \right. \\
&\quad \left. + \left(\frac{1}{3} L_i \mathbf{C}'_i + \frac{2}{3} \mathbf{v}_0 + \frac{1}{3} \sum_{j=1}^{i-1} L_j \mathbf{C}'_j \right) \cdot \mathbb{B}'_i \int_0^{2\pi} [f_i(\theta)]^3 \sin \theta d\theta \right. \\
&\quad \left. + \frac{1}{4} \mathbb{A}'_i \cdot \mathbb{A}'_i \int_0^{2\pi} [f_i(\theta)]^4 \cos^2 \theta d\theta \right. \\
&\quad \left. + \frac{1}{4} \mathbb{B}'_i \cdot \mathbb{B}'_i \int_0^{2\pi} [f_i(\theta)]^4 \sin^2 \theta d\theta \right. \\
&\quad \left. + \frac{1}{2} \mathbb{A}'_i \cdot \mathbb{B}'_i \int_0^{2\pi} [f_i(\theta)]^4 \sin \theta \cos \theta d\theta \right] \tag{6.9}
\end{aligned}$$

It should be noted that

$$\int_0^{2\pi} [f_i(\theta)]^2 d\theta = 2A_i \tag{6.10}$$

$$\int_0^{2\pi} [f_i(\theta)]^3 \sin \theta d\theta = 3S_{i,x} \tag{6.11}$$

$$\int_0^{2\pi} [f_i(\theta)]^3 \cos \theta d\theta = 3S_{i,y} \tag{6.12}$$

$$\int_0^{2\pi} [f_i(\theta)]^4 \sin^2 \theta d\theta = 4I_{i,x} \tag{6.13}$$

$$\int_0^{2\pi} [f_i(\theta)]^4 \cos^2 \theta d\theta = 4I_{i,y} \tag{6.14}$$

$$\int_0^{2\pi} [f_i(\theta)]^4 \sin \theta \cos \theta d\theta = 4I_{i,xy} \tag{6.15}$$

where A_i is the cross-section area of the i -th segment, $S_{i,x}$ and $S_{i,y}$ are the first moments of the area about the x and y directions respectively, $I_{i,x}$ and $I_{i,y}$ are the second

moments of the area around the x and y directions respectively, and $I_{i,xy}$ is the product of area of the i-th segment.

On substituting Equations 6.10 - 6.15 onto Equation 6.9, the kinetic energy of the i-th segment $P_{i-1}P_i$ yields the following:

$$\begin{aligned}
T_i = & \frac{1}{2}\rho A_i L_i \mathbf{v}_0 \cdot \mathbf{v}_0 + \rho A_i L_i \sum_{j=1}^i L_j^{(i,1)} \mathbf{v}_0 \cdot \mathbf{C}'_j + \frac{1}{2}\rho A_i L_i \sum_{j=1}^i \sum_{k=1}^i L_{j,k}^{(i,2)} \mathbf{C}'_j \cdot \mathbf{C}'_k \\
& + \rho S_{i,x} L_i \sum_{j=1}^i L_j^{(i,1)} \mathbb{B}'_j \cdot \mathbf{C}'_j + \rho S_{i,x} L_i \mathbf{v}_0 \cdot \mathbb{B}'_i + \rho S_{i,y} L_i \sum_{j=1}^i L_j^{(i,1)} \mathbb{A}'_j \cdot \mathbf{C}'_j \\
& + \rho S_{i,y} L_i \mathbf{v}_0 \cdot \mathbb{A}'_i + \frac{1}{2}\rho I_{i,x} L_i \mathbb{B}'_i \cdot \mathbb{B}'_i + \frac{1}{2}\rho I_{i,y} L_i \mathbb{A}'_i \cdot \mathbb{A}'_i + \rho I_{i,xy} L_i \mathbb{A}'_i \cdot \mathbb{B}'_i \quad (6.16)
\end{aligned}$$

where

$$\begin{aligned}
\mathbf{L}^{(i,1)} &= \begin{bmatrix} L_1 \\ \vdots \\ L_j \\ \vdots \\ L_{i-1} \\ \frac{1}{2}L_i \end{bmatrix} \\
\mathbf{L}^{(i,2)} &= \begin{bmatrix} L_1^2 & \cdots & L_1 L_j & \cdots & L_1 L_{i-1} & \frac{1}{2}L_1 L_i \\ \vdots & & \vdots & & \vdots & \vdots \\ L_j L_1 & \cdots & L_j^2 & \cdots & L_j L_{i-1} & \frac{1}{2}L_j L_i \\ \vdots & & \vdots & & \vdots & \vdots \\ L_{i-1} L_1 & \cdots & L_{i-1} L_j & \cdots & L_{i-1}^2 & \frac{1}{2}L_{i-1} L_i \\ \frac{1}{2}L_i L_1 & \cdots & \frac{1}{2}L_i L_j & \cdots & \frac{1}{2}L_i L_{i-1} & \frac{1}{3}L_i L_i \end{bmatrix}
\end{aligned}$$

Thus the kinetic energy of the whole system is given by

$$T = \sum_{i=1}^n T_i \quad (6.17)$$

$$\mathbb{A}_i^{(1)} = \begin{bmatrix} \frac{\partial \mathbb{A}_i}{\partial \alpha_i} \\ \frac{\partial \mathbb{A}_i}{\partial \beta_i} \\ \frac{\partial \mathbb{A}_i}{\partial \gamma_i} \end{bmatrix} \quad (6.18)$$

$$\mathbb{A}_i^{(2)} = \begin{bmatrix} \frac{\partial^2 \mathbb{A}_i}{\partial \alpha_i^2} & \frac{\partial^2 \mathbb{A}_i}{\partial \alpha_i \partial \beta_i} & \frac{\partial^2 \mathbb{A}_i}{\partial \alpha_i \partial \gamma_i} \\ \frac{\partial^2 \mathbb{A}_i}{\partial \alpha_i \partial \beta_i} & \frac{\partial^2 \mathbb{A}_i}{\partial \beta_i^2} & \frac{\partial^2 \mathbb{A}_i}{\partial \beta_i \partial \gamma_i} \\ \frac{\partial^2 \mathbb{A}_i}{\partial \alpha_i \partial \gamma_i} & \frac{\partial^2 \mathbb{A}_i}{\partial \beta_i \partial \gamma_i} & \frac{\partial^2 \mathbb{A}_i}{\partial \gamma_i^2} \end{bmatrix} \quad (6.19)$$

$$\begin{aligned}
\frac{d}{dt} \frac{\partial T}{\partial \mathbf{v}_0} - \frac{\partial T}{\partial \mathbf{r}_0} &= \frac{d}{dt} \sum_{i=1}^n \left(\rho A_i L_i \mathbf{v}_0 + \rho S_{i,y} L_i \mathbb{A}'_i + \rho S_{i,x} L_i \mathbb{B}'_i + \rho A_i L_i \sum_{j=1}^i L_j^{(i,1)} \mathbb{C}'_j \right) \\
&= \sum_{i=1}^n \rho A_i L_i \dot{\mathbf{v}}_0 + \sum_{i=1}^n \rho S_{i,y} L_i \left[\mathbb{A}_i^{(1)} \mathbf{q}_i'' + \mathbb{A}_i^{(2)} \mathbf{q}'_i \cdot \mathbf{q}'_i \right] \\
&\quad + \sum_{i=1}^n \rho S_{i,x} L_i \left[\mathbb{B}_i^{(1)} \mathbf{q}_i'' + \mathbb{B}_i^{(2)} \mathbf{q}'_i \cdot \mathbf{q}'_i \right] \\
&\quad + \sum_{i=1}^n \rho A_i \sum_{j=1}^i L_j^{(i,1)} \left[\mathbb{C}_j^{(1)} \mathbf{q}_i'' + \mathbb{C}_j^{(2)} \mathbf{q}'_i \cdot \mathbf{q}'_i \right]
\end{aligned} \tag{6.20}$$

6.2.2.2 Potential energy

In this thesis, the potential energy of the gravitational forces is neglected, therefore only the energy of the spring deformation is considered.

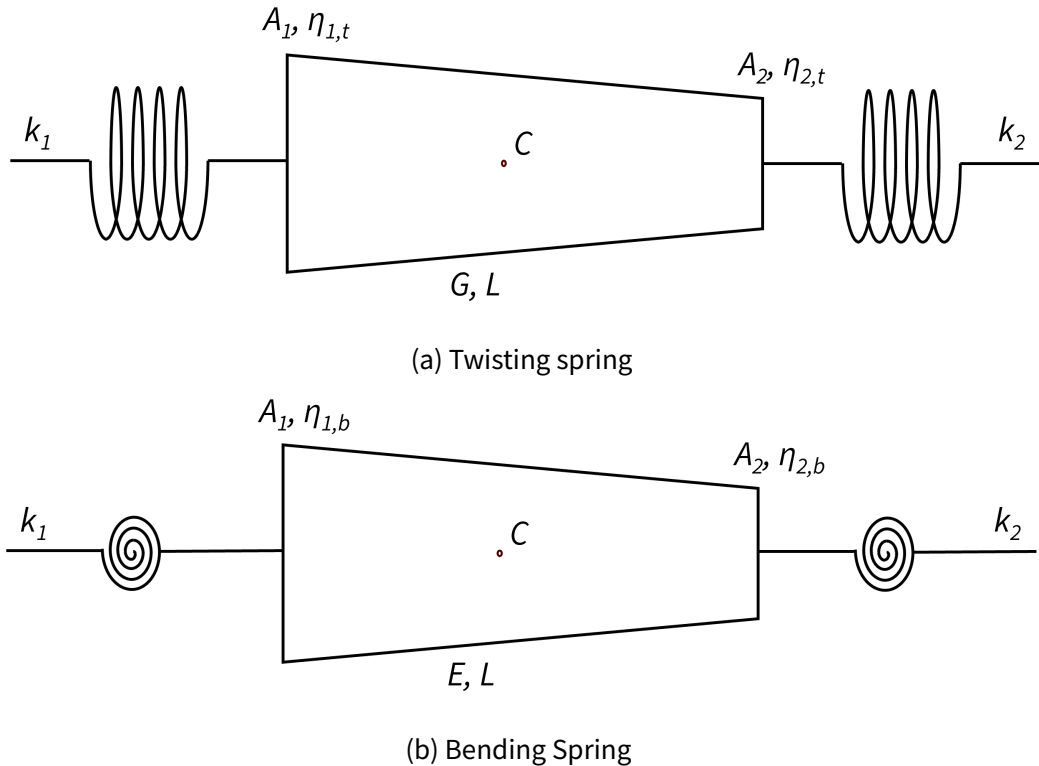


Figure 6.5: Illustrative demonstration of the twisting and bending spring modelling

For the twisting spring, as shown in Figure 6.5a, the stiffness coefficients of the modelled spring at the left and right hand side are defined as follows:

$$k_1 = \frac{G (J_1 - J_c)}{\eta_{1,t} (\ln J_1 - \ln J_c)} \quad (6.21)$$

$$k_2 = \frac{G (J_2 - J_c)}{\eta_{2,t} (\ln J_2 - \ln J_c)} \quad (6.22)$$

where J_1 and J_2 are the polar moments of inertia of the segment at the left and right hand ends, J_c is the polar moment of inertia of the segment at the centre of mass of the segment, A_1 and A_2 are the cross-sectional areas of the segment at the left and right hand ends, and $\eta_{1,t}$, $\eta_{2,t}$ and J_c are defined as follows:

$$\eta_{1,t} = \frac{L (2J_1 + J_2)}{3 (J_1 + J_2)} \quad (6.23)$$

$$\eta_{2,t} = \frac{L (J_1 + 2J_2)}{3 (J_1 + J_2)} \quad (6.24)$$

$$J_c = \frac{2 (J_1^2 + J_1 J_2 + J_2^2)}{3 (J_1 + J_2)} \quad (6.25)$$

For the bending spring, as shown in Figure 6.5b, the stiffness coefficients of the modelled spring at the left and right hand sides are defined as follows:

$$k_1 = \frac{E (I_1 - I_c)}{\eta_{1,b} (\ln I_1 - \ln I_c)} \quad (6.26)$$

$$k_2 = \frac{E (I_2 - I_c)}{\eta_{2,b} (\ln I_2 - \ln I_c)} \quad (6.27)$$

where I_1 and I_2 are the second order moment of inertia of the segment at the left and right hand ends, respectively, I_c is the polar moment of inertia of the segment at the centre of mass of the segment, A_1 and A_2 are the cross-section area of the segment at left and right hand ends, respectively and, $\eta_{1,b}$, $\eta_{2,b}$ and I_c are defined as follows:

$$\eta_{1,b} = \frac{L (2I_1 + I_2)}{3 (I_1 + I_2)} \quad (6.28)$$

$$\eta_{2,b} = \frac{L (I_1 + 2I_2)}{3 (I_1 + I_2)} \quad (6.29)$$

$$I_c = \frac{2 (I_1^2 + I_1 I_2 + I_2^2)}{3 (I_1 + I_2)} \quad (6.30)$$

When the segment is straight, i.e., $J_1 = J_2$ and $I_1 = I_2$, the stiffness coefficients k_1 and k_2 yield

$$k_{1,b} = k_{2,b} = \frac{2EI}{L} \quad (6.31)$$

$$k_{1,t} = k_{2,t} = \frac{2GJ}{L} \quad (6.32)$$

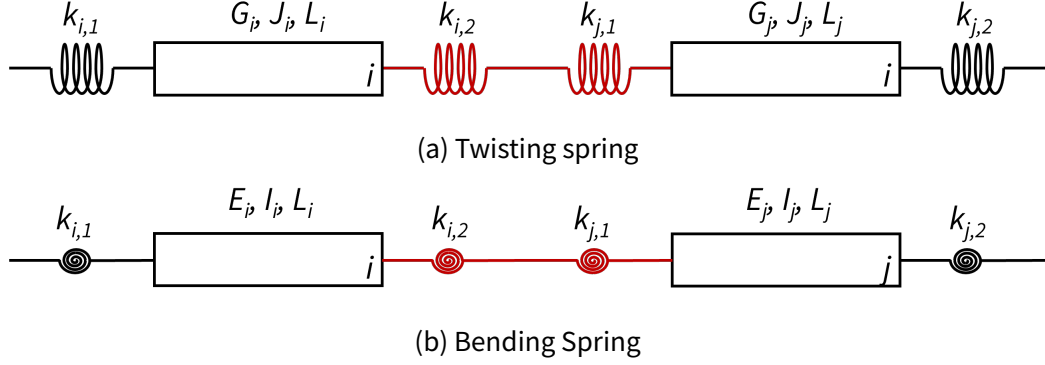


Figure 6.6: Stiffness coefficients of the combined spring

The combined stiffness coefficient between the two straight segments is defined as follows

$$k_{ij} = \frac{2G_i G_j J_i J_j}{G_i J_i L_j + G_j J_j L_i} \quad (6.33)$$

$$k_{ij} = \frac{2E_i E_j I_i I_j}{E_i I_i L_j + E_j I_j L_i} \quad (6.34)$$

As shown in Figure 6.2d, the elastic deformation energy of the spring is defined by the following expression:

$$V_i = \frac{1}{2} k_{i,bx} \alpha_i^2 + \frac{1}{2} k_{i,by} \beta_i^2 + \frac{1}{2} k_{i,t} \gamma_i^2 \quad (6.35)$$

where the coefficients $k_{i,bx}$, $k_{i,by}$ and $k_{i,t}$ are determined from,

$$\begin{aligned} k_{i,bx} &= \frac{k_{i-1,bx} k_{i,bx}}{k_{i-1,bx} k_{i,bx}} \\ &= \frac{2E_{i-1} E_i I_{i-1,x} I_{i,x}}{E_i I_{i,x} L_{i-1} + E_{i-1} I_{i-1,x} L_i} \end{aligned} \quad (6.36)$$

$$\begin{aligned} k_{i,by} &= \frac{k_{i-1,by} k_{i,by}}{k_{i-1,by} k_{i,by}} \\ &= \frac{2E_{i-1} E_i I_{i-1,y} I_{i,y}}{E_i I_{i,y} L_{i-1} + E_{i-1} I_{i-1,y} L_i} \end{aligned} \quad (6.37)$$

$$\begin{aligned} k_{i,t} &= \frac{k_{i-1,t} k_{i,t}}{k_{i-1,t} k_{i,t}} \\ &= \frac{2G_{i-1} G_i J_{i-1} J_i}{G_i J_i L_{i-1} + G_{i-1} J_{i-1} L_i} \end{aligned} \quad (6.38)$$

where E_i is the Young's modulus of the material used in the i -th segment, $I_{i,x}$ and $I_{i,y}$ are the moment of inertia of cross section around X- and Y- axis, $J_i = I_{i,x} + I_{i,y}$ is the polar moment of inertia, L_i is the length of the i -th segment.

Since gravity force is neglected in this case, the potential energy is given by

$$\begin{aligned} V &= \sum_{i=1}^n V_i \\ &= \sum_{i=1}^n \left(\frac{1}{2} k_{i,bx} \alpha_i^2 + \frac{1}{2} k_{i,by} \beta_i^2 + \frac{1}{2} k_{i,t} \gamma_i^2 \right) \end{aligned} \quad (6.39)$$

Thus

$$\frac{\partial V}{\partial \mathbf{q}_i} = \begin{bmatrix} k_{i,bx} \alpha_i \\ k_{i,by} \beta_i \\ k_{i,t} \gamma_i \end{bmatrix} \quad (6.40)$$

6.2.2.3 Dissipation of energy

The visco-elastic characteristics of the rigid segments can be defined by introducing the damping coefficients. Similar to the stiffness coefficients, the damping coefficients can be defined as follows

$$C_\alpha = 2\xi \sqrt{k_i I_{i,x}} \quad (6.41)$$

$$C_\beta = 2\xi \sqrt{k_i I_{i,y}} \quad (6.42)$$

$$C_\gamma = 2\xi \sqrt{k_i J_i} \quad (6.43)$$

The dissipation of energy is therefore given by

$$V_\alpha = \frac{1}{2} C_\alpha \dot{\alpha}^2 \quad (6.44)$$

$$V_\beta = \frac{1}{2} C_\beta \dot{\beta}^2 \quad (6.45)$$

$$V_\gamma = \frac{1}{2} C_\gamma \dot{\gamma}^2 \quad (6.46)$$

The sum of dissipation of energy and its derivative yield

$$\begin{aligned}
 V &= \sum_{i=1}^n V_i \\
 &= \sum_{i=1}^n (V_\alpha + V_\beta + V_\gamma) \\
 &= \sum_{i=1}^n \left(\frac{1}{2} C_\alpha \dot{\alpha}^2 + \frac{1}{2} C_\beta \dot{\beta}^2 + \frac{1}{2} C_\gamma \dot{\gamma}^2 \right)
 \end{aligned} \tag{6.47}$$

$$\frac{\partial V}{\partial \dot{\mathbf{q}}_i} = \begin{bmatrix} C_\alpha \dot{\alpha}_i \\ C_\beta \dot{\beta}_i \\ C_\gamma \dot{\gamma}_i \end{bmatrix} \tag{6.48}$$

6.2.3 The fluid-structure interface

For there to be a successful coupling between the fluid and the multibody system, it is necessary to ensure both the continuity of velocity and the equilibrium of forces at the interface between the fluid and the structure for each component of the multibody system. Let $\Gamma_i^{fs}(0) = \partial\Omega^f(0) \cap \partial\Omega^i(0)$ be the fluid-structure interface at $t = 0$ for the multibody i and $\Gamma_i^{fs}(t) = \varphi^s(\Gamma_i^{fs}(0), t)$ be the evolved interface at time t . The kinematic and dynamic equilibrium conditions can be written as,

$$\begin{aligned}
 \forall \mathbf{X}^s \in \Gamma_i^{fs}(0) \\
 \bar{\mathbf{u}}^f(\varphi^s(\mathbf{X}^s, t), t) = \mathbf{u}^s(\mathbf{X}^s, t)
 \end{aligned} \tag{6.49}$$

$$\begin{aligned}
 \forall \gamma \in \Gamma_i^{fs}(0) \\
 \int_{\varphi^s(\gamma, t)} \bar{\boldsymbol{\sigma}}^f(\mathbf{x}^f, t) \cdot \mathbf{n} d\Gamma + \int_\gamma \mathbf{t}^s d\Gamma = 0
 \end{aligned} \tag{6.50}$$

where φ^s is the position vector that maps the initial position \mathbf{X}^s of the flexible multibody component i to its position at time t and \mathbf{t}^s is the traction on the structure along the interface γ . Here, \mathbf{n} is the outward normal to the fluid-structure interface, γ is any part of the interface $\Gamma_i^{fs}(0)$ in the reference configuration and $\varphi^s(\gamma, t)$ is the corresponding fluid part at time t . The requirements outlined above for the interface are enforced in such a way that the velocity of the fluid is made to perfectly match the velocity of the deformable solid body. The fluid forces, which comprise the integration of the pressure and shear stress effects on the body surface, are what determine the motion of the structure. This motion is called the structural motion.

6.3 Applications of the Proposed Model on the FSI Simulation of the Fluid Solid interface

Validation entails making a comparison between the results achieved through the use of the model presented and the findings acquired through the use of various simulation models or those gained through the use of experimental measurements. The proposed method is first applied to model a three-dimensional flow-induced and forced vibration simulation on a flexible flat plate attached to a rigid aerofoil which oscillates as per a pre-calculated motion. For each case, the reconstructed ROM solutions from the proposed methodology are compared to the numerical results as well as experimental solution when it is possible in order to validate the accuracy and performance of the model. In addition, in order to test the compatibility of the proposed refinement strategies introduced in Chapter 4 are applied to both simulations, error estimations and time analyses are compared to the corresponding uniform grid ROM solution.

6.3.1 Adaptive ROM simulation for teardrop/flat design oscillation

6.3.1.1 Simulation Modelling

The test case is carried out on the configuration illustrated in Figure 6.7, where a flexible flat is attached to a rigid aerofoil NACA0033 moving according to a pre-defined motion profile.

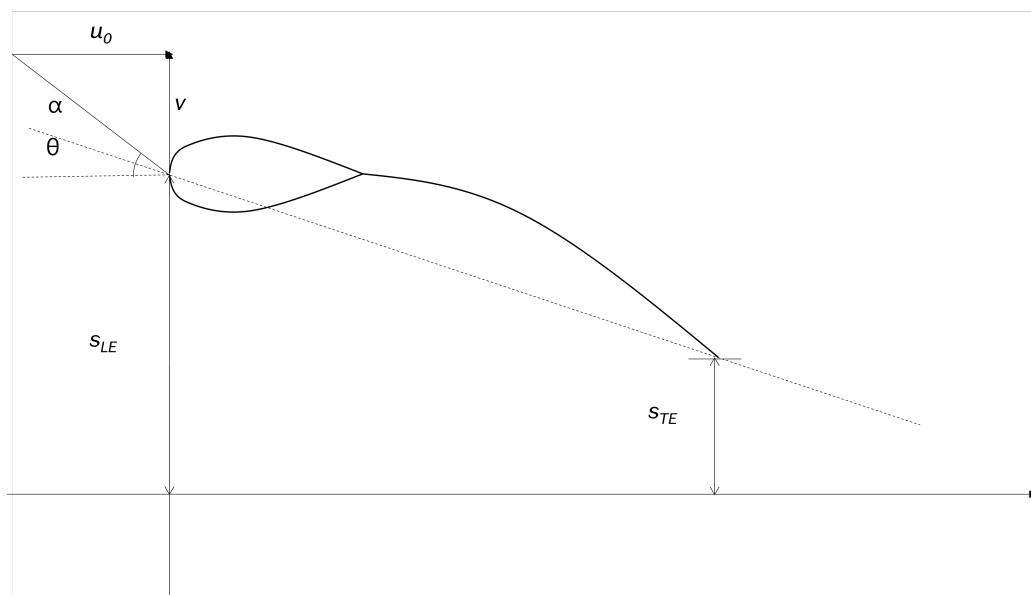


Figure 6.7: Schematic demonstration of the flexible aerofoil heaving periodically.

The flexible flat plate deforms due to the fluid forces; it is modelled as a chain of various number of rigid segments. The motions of the fluid and solid domains are solved using the ANSYS Fluent and Mechanical solvers, respectively, and coupled by a semi-implicit coupled algorithm. A schematic description of this problem is illustrated in Figure 6.8.

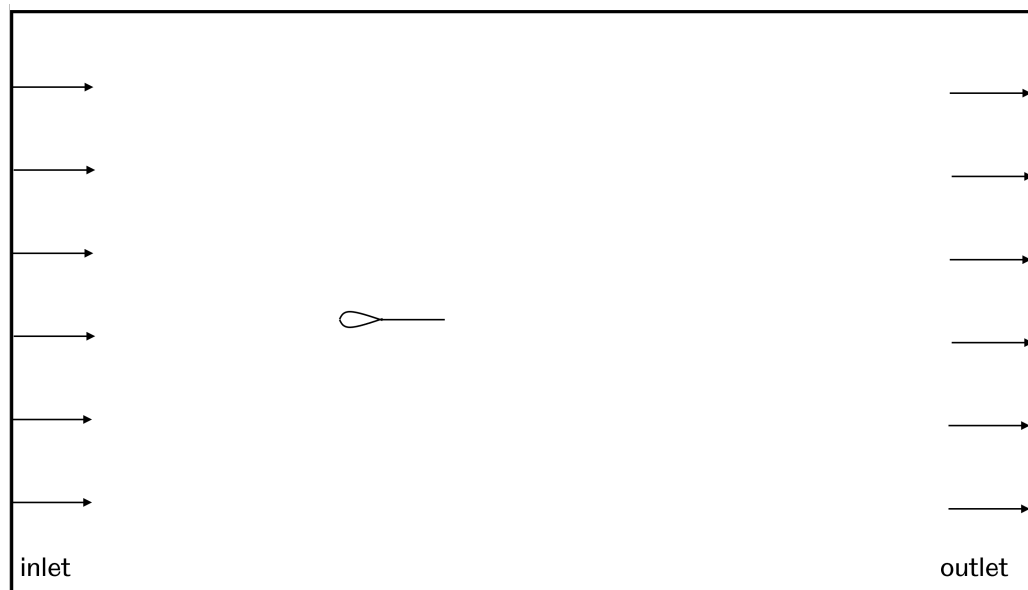


Figure 6.8: Schematic demonstration of the domain of the vibration of the Teardrop/flat design FSI simulation.

Experiments were carried out on 7 plates for a study of chordwise flexibility by varying the thickness of the carbon-manganese steel plate, the full details of the problem can be found in (Heathcote and Gursul, 2007). Identical, apart from their thickness, as summarised in Table 6.1, here only the bending stiffness of the plates relative to the most flexible aerofoil $b/c=0.56 \times 10^{-3}$ is selected which refers to the thickness of 0.05 mm.

Table 6.1: Properties employed in the numerical model for the vibration investigation of the teardrop/flat design.

Parameters	Values
Teardrop	
Chord [mm]	30
Flexible flat plate	
Chord [mm]	60
Thickness [mm]	0.05
Bending stiffness [GPa]	205

Experiments were carried out using tunnel speeds of 0.1 and 0.3 metres per second, which corresponded to Reynolds numbers of 9,000 and 27,000, respectively, when based on the chord length of the 90 millimetre aerofoil. At a constant amplitude of $a = 17.5$ mm, the effects of chordwise flexibility were investigated through a series of experiments, the displacement of the leading-edge was therefore given by $s_{LE} = a \cos(\omega t)$. The parameters employed in the model are summarised in Table 6.1, and these are the same values as those used in the experimental investigation.

The Fluid-Structure Interaction simulations are modelled as per the experiment then used to build the reduced order models using the proposed methodology. The teardrop/flat design are flexible in the chordwise direction only, as shown in Figure 6.8, a schematic of the flexible teardrop/flat design used in this simulation. For more detailed information, please refer to (Heathcote and Gursul, 2007).

Figure 6.9 illustrates the computational domain used in the CFD modelling. The fluid model consists of 2,329,942 nodes and 1,146,915 elements. The mesh is split into four parts: background fluid domain and the refined overset domains near to the solid aerofoil ("Overset domain - 1"), and the flexible flat plate ("Overset domain - 2") and two additional overset domains which link two separate overset domains, as shown in Figure 6.9. The time-step size is 5×10^{-5} second and the number of nonlinear iterations per time step is 1500. A loose coupling strategy was applied to couple both the fluidic and structural domains at each time step. The aerofoil is assumed to be a rigid body, while the flat plate is flexible, the corresponding rigidities are modelled in the structural solver.

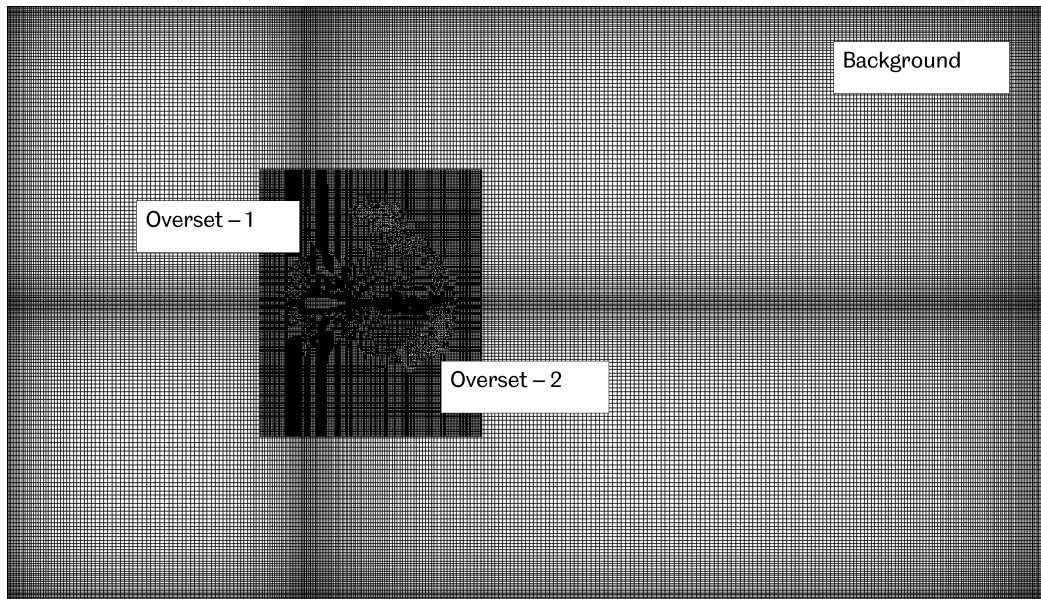


Figure 6.9: Schematic demonstration of the domain of the vibration investigation of the teardrop/flat design FSI simulation.

The governing motion equation of the rigid aerofoil is determined by the predefined equation $s_{LE} = a \cos(\omega t)$. The flexible flat plate modelled is free to deform along the y-o-z plane, fluid dynamics model generates the lift and moment coefficients that are introduced into the structural model that in turn determines the incremental motion of the structural model. This process is then executed in a stepwise fashion for each time increment. The previous time increment fluid dynamics model is used to compute the next time increment aerofoil position and then the aerodynamics of that position are calculated. For more detailed information please refer to Chapter 3.3.1.3.

The model is established using ANSYS FLUENT coupled with the Transient Structure modules using the $k-\omega$ SST turbulence model. This two-equation model is suitable for modelling the boundary layers as well as the far field flows, and therefore it has been used extensively in studies involving wind turbine blades and aeroelastic problems with reasonable results (Heinz, et al., 2016; Halawa, et al., 2017).

Mesh and time size sensitivity studies are carried out to determine the appropriate cell face and time step. In the case of the mesh sensitivity study, the Reynolds number is 9,000. Five different mesh sizes are investigated, i.e., 8 mm, 4 mm, 2 mm, 1 mm, and 0.5 mm, and the associated total number of elements and calculated oscillation amplitudes are presented in Figure 6.10. The amplitude converges at a mesh size of 1 mm and on further refining the mesh size then a 5.4% relative difference is obtained.

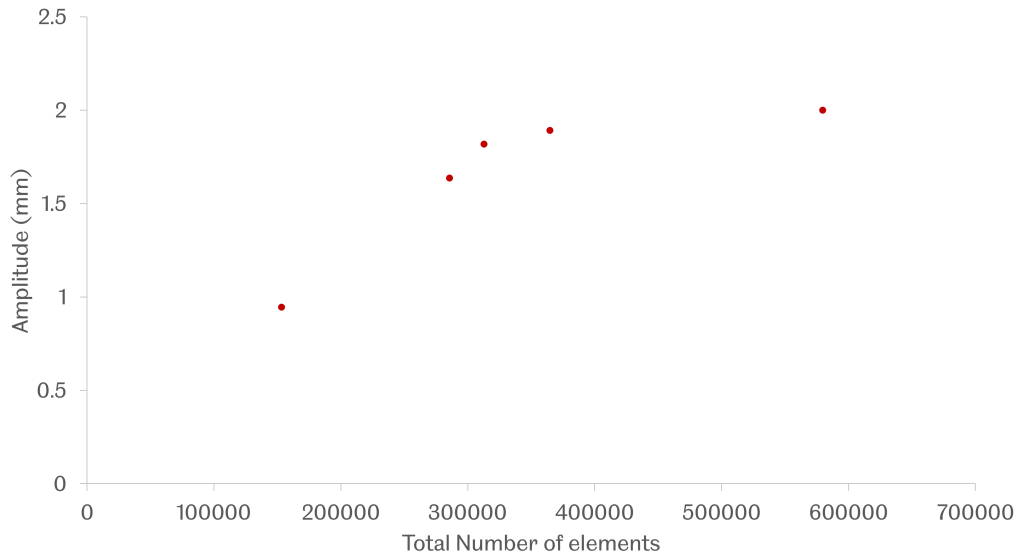


Figure 6.10: Mesh convergence study of the vibration investigation of the teardrop/flat design FSI simulation at Reynolds number $Re=9,000$.

In the time size sensitivity study, five time steps are investigated, i.e. 1×10^{-5} seconds, 1×10^{-4} seconds, 2×10^{-4} seconds, 5×10^{-4} seconds, and 1×10^{-3} seconds. The associated total number of elements and oscillation frequencies are presented in Figure 6.11 and the amplitude converges at a time size of 1×10^{-4} seconds.

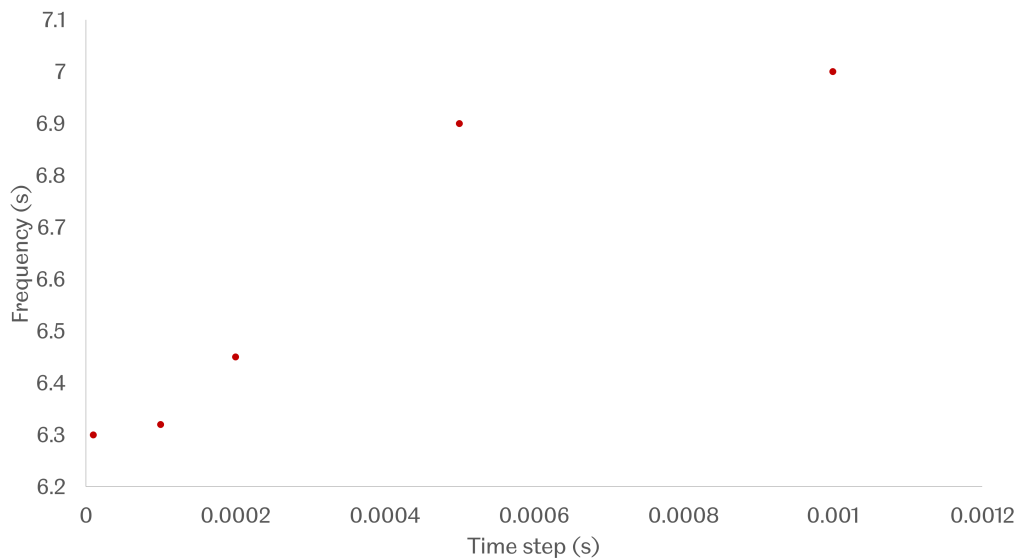


Figure 6.11: Time step convergence study of the teardrop/flat design FSI simulation at Reynolds number $Re=9,000$.

On considering the computational time and accuracy, the mesh size of 1 mm and the

time size of 1×10^{-4} seconds are deemed as the appropriate mesh size and time size for the modelling in this study.

6.3.1.2 Reduced Order Modelling

The proposed POD-Galerkin approach is applied to model the three-dimensional flow-induced vibrating teardrop/flat design at various Reynolds numbers. The motion of the rigid aerofoil is given by $s_{LE} = a \cos(\omega t)$ while the following flexible flat plate is determined by flow-induced vibration. For each case, accuracy and computational cost of the model are investigated. Accuracy and order reduction are discussed with respect to the full-order numerical model and the traditional POD strategy with uniform grids.

The proposed locally refined POD-Galerkin Reduced Order Modelling procedure was executed by implementing a MATLAB subroutine as per the modified ROM methodology for deforming fluid-solid interface listed in Section 6.2 and the refinement approach listed in the Chapter 4, and the results obtained are discussed and compared to the corresponding experimental data.

The computational domain for the proposed reduced order models is $l_x \times l_y \times l_z = (-200 \text{ mm}, 500 \text{ mm}) \times (-200 \text{ mm}, 200 \text{ mm}) \times (-10 \text{ mm}, 10 \text{ mm})$ with initial uniform mesh at $N_x \times N_y \times N_z = 35 \times 20 \times 2$, as shown in Figure 6.12. The flexible teardrop aerofoil was placed on the x-o-z plane along the x-axis, where the leading edge is initially at $(x_0, y_0, z_0) = (0, 0, 0)$. The plate is forced to flap along the y-axis with constant amplitude, $a=17.5 \text{ mm}$. Various simulations were calculated as per the experiments conducted in (Heathcote and Gursul, 2007).

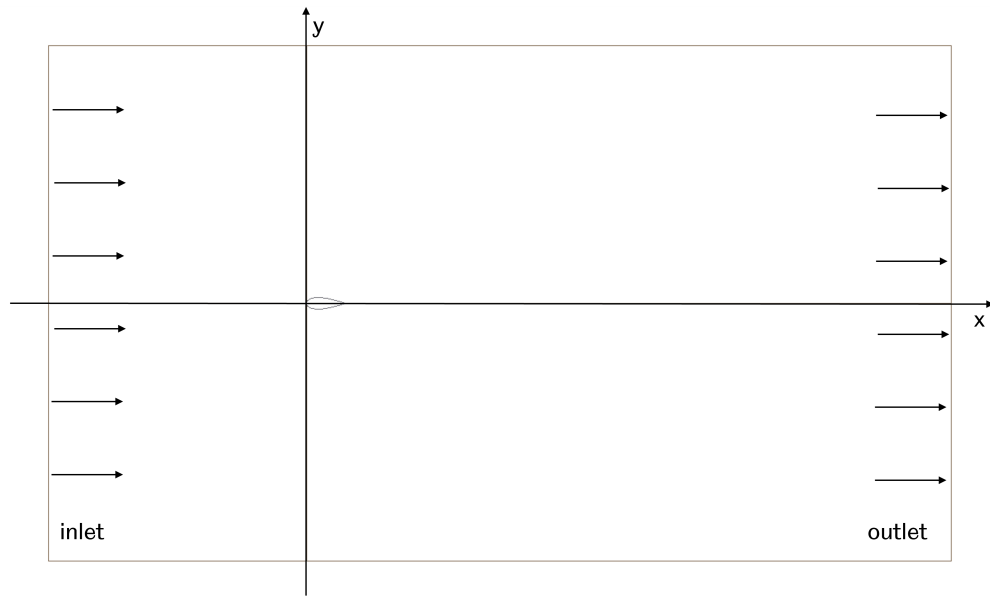


Figure 6.12: Computational domain of flexible flapping teardrop/plate shape oscillation simulation.

The reduced order model is built using a set of pre-calculated numerical solutions. The proposed ROM modes are computed from 400 uniformly distributed snapshots of the simulation data over four complete periods of oscillation. In addition, as a validation case of the proposed locally refined strategy, the domain is uniformly discretised in 35×20 , 70×40 , 140×80 , and 280×160 grids in the x- and y- direction, respectively. Thus, three different adaptived ROM models based on the created uniform grids, namely 70×40 -adaptive, 140×80 -adaptive, and 280×160 -adaptive and four ROM models via uniform grids, namely 35×20 -uniform, 70×40 -uniform, 140×80 -uniform, and 280×160 -uniform are built. For each case, the overall computational cost, error of the ROM solution against the baseline CFD solution, maximum velocity difference, and norm of the error between the rebuilt velocity flow field and the numerical solution are summarised.

The energy percentage of the POD modes decreases monotonically in every cases of the POD simulation. On considering the energy percentage of the most dominant POD modes cover, the first 20 dominant POD modes, which cover more than 99.9% of the overall kinematic energy, are selected to perform the following calculation. for each adaptive ROM cases, the solution is compared against those via two different levels of uniform grids, for instance, the proposed ROM solution with 70×40 -adaptive is compared against the uniform ROM solutions 35×20 -uniform, 70×40 -uniform, in terms computational efficiency and accuracy. In this case, the flow field patterns of the oscillation at a Reynolds number 9,000, additional application cases on Vertical Axis Wind

Turbine and Horizontal Axis Wind turbine at higher Reynolds number will be conducted in Chapter 7 and 8 to challenge the performance and robustness of the proposed adaptive ROM methodology.

The global POD results have been plotted in Figure 6.13 as the energy distribution, the POD modes decrease monotonically, denoting the decreasing energy coverage of each POD modes. In this analysis first 12 POD modes are selected to build the reduced order model.

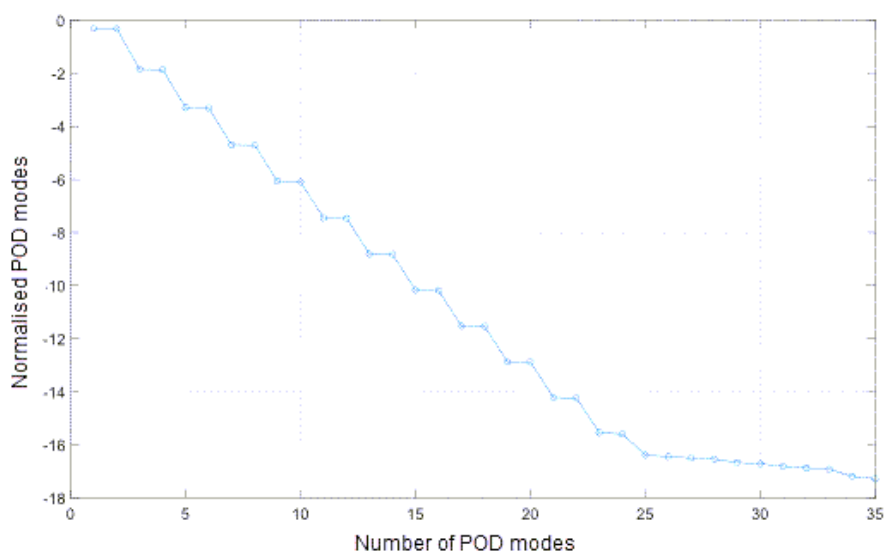


Figure 6.13: Normalised POD modes of the proposed adaptive POD-Galerkin ROM model for the teardrop/plate oscillation simulation.

6.3.1.3 ROM simulation results

Comparison between the proposed and the uniform POD methodology In this section, the ROM solutions via the proposed adaptive POD-Galerkin ROM using various settings are compared to the CFD solutions and experimental in terms of aerodynamic parameters. In addition, the number of finite element segment is analysed.

To show the capacity of the model more clearly, the flow structure at the same timesteps have been investigated: the velocity flow field computed by the full-order CFD solution and the proposed POD-Galerkin ROM models. The vertical displacement of the trailing edge of the teardrop/plate shape at various time step snapshot of the oscillation at Reynolds number $Re=9,000$ are selected as an example. With this decomposed solid domain, the dynamics for this prescribed large solid motion problem and the corresponding adapted discretisation are shown in Figure 6.14. The accuracy of the adaptive re-

duced order model is preserved to be almost the same in comparison to the numerical solution after six iterations, with the maximum error of 5%.

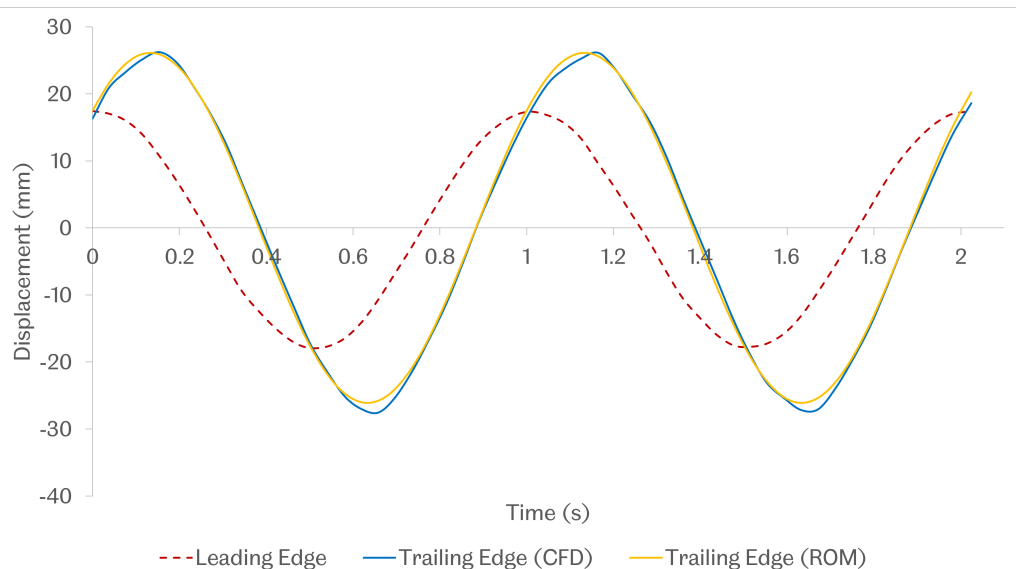


Figure 6.14: Proposed solution for the three-dimensional teardrop/flat design oscillation at Reynolds number $Re=9000$.

The reconstructed dynamic system of the most dominant modes, i.e., the first ten modes, are achieved by the adaptive projection onto these modes, and it is compared to the ROM using the same quality of uniform grids to quantify the performance of the proposed POD-Galerkin ROM. In this discussion the solution via the adaptive ROM 70×40 -adaptive is compared to the reduced order model with the same size of the grid, i.e., 70×40 . The corresponding mesh grid is shown in Figure 6.15. The vertical displacement of the teardrop/flat design oscillation at the Reynolds number $Re=9,000$ is plotted in Figure 6.15, where a comparison is made between the full-order CFD solution and the POD-Galerkin based ROM with and without the proposed methodology. The presentation of the displacement is plotted after convergence.

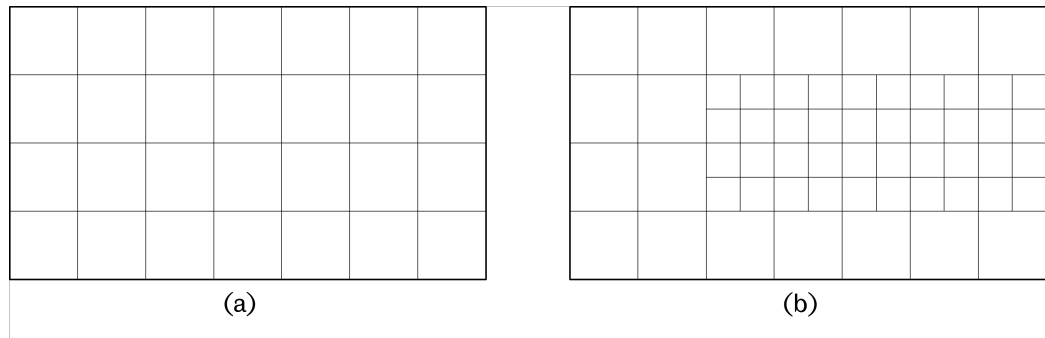


Figure 6.15: A comparison of the POD-Galerkin results using the adaptive (b) and the uniform (a) grid discretisation for the teardrop/flat design oscillation at the Reynolds number $Re=9,000$.

The proposed methodology performs similarly in the case of the FSI simulation at the Reynolds number $Re=27,000$. Figure 6.16 summarises the comparison of the proposed solution to the uniform POD solution. Both the vertical displacement of the teardrop/flat design oscillation and flow pattern are illustrated in the figure. The proposed adaptive POD methodology stills accurately predicts the flow condition despite of a higher percentage error compared to the FSI simulation at the Reynolds number $Re=9,000$. The proposed adaptive POD method overperforms to the uniform POD solution in terms accuracy, and this will be investigated in detail in the following sections.

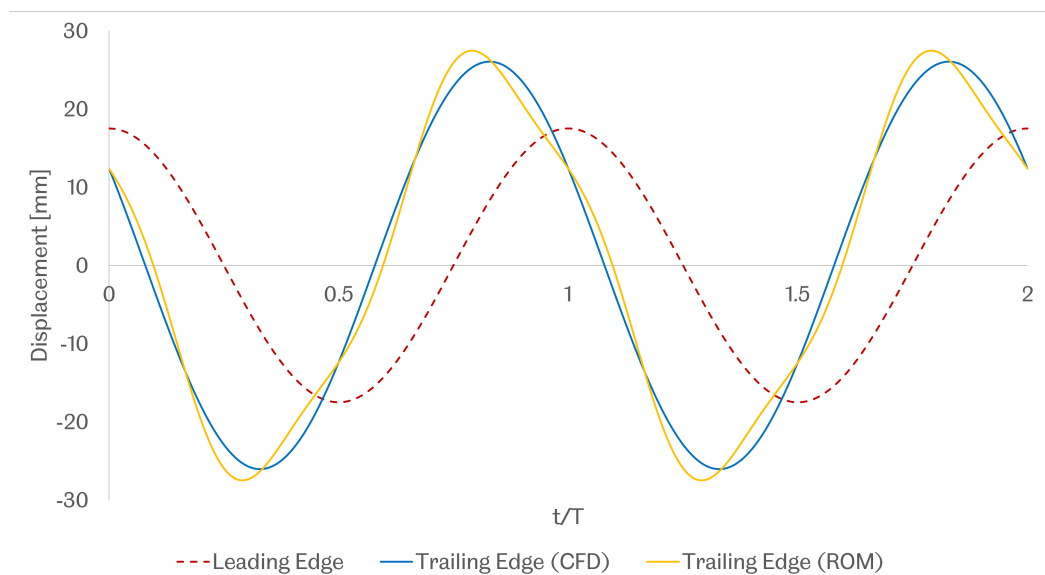


Figure 6.16: Proposed solution for the three-dimensional teardrop/flat design oscillation at Reynolds number $Re=27000$.

Investigation on number of segments In this section, the number of finite segments is investigated. Recapping that the teardrop part is considered to be rigid, and therefore modelled as a rigid segment, while the flexible flat plate is modelled as a chain of different numbers of rigid finite segments, as shown in Figure 6.17. The number of rigid segments varies from 3 to 13, i.e., 2 up to 12 segments used to model the flexible flat plate, is considered in the case of the oscillation at the Reynolds number $Re=9,000$.

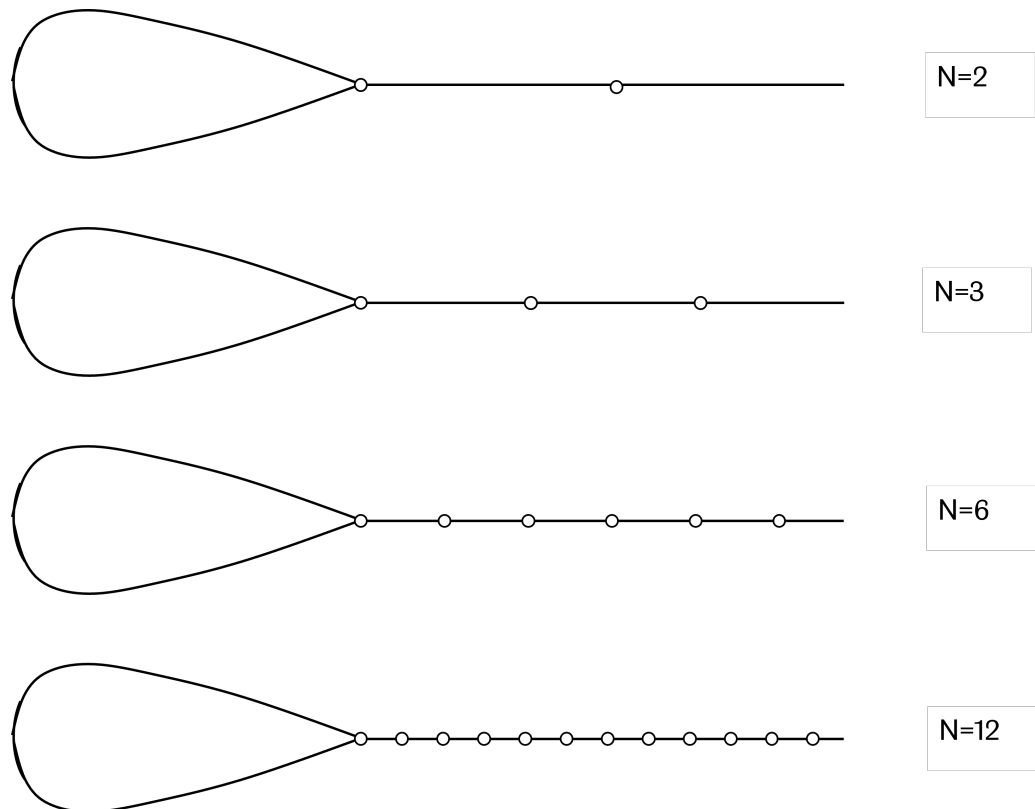


Figure 6.17: Different number of finite element segments used in the teardrop/flat design vibration simulation.

Figure 6.18 plots the vertical displacement profiles of the teardrop/flat plate design oscillation at the Reynolds number, $Re=9,000$. The ROM solutions of the proposed ROM methodology using different number of finite segments are compared to the full-order CFD solution. As shown in the figure, the increase in the number of finite segments reduces the error profile between the full order CFD solution and the corresponding ROM solution.

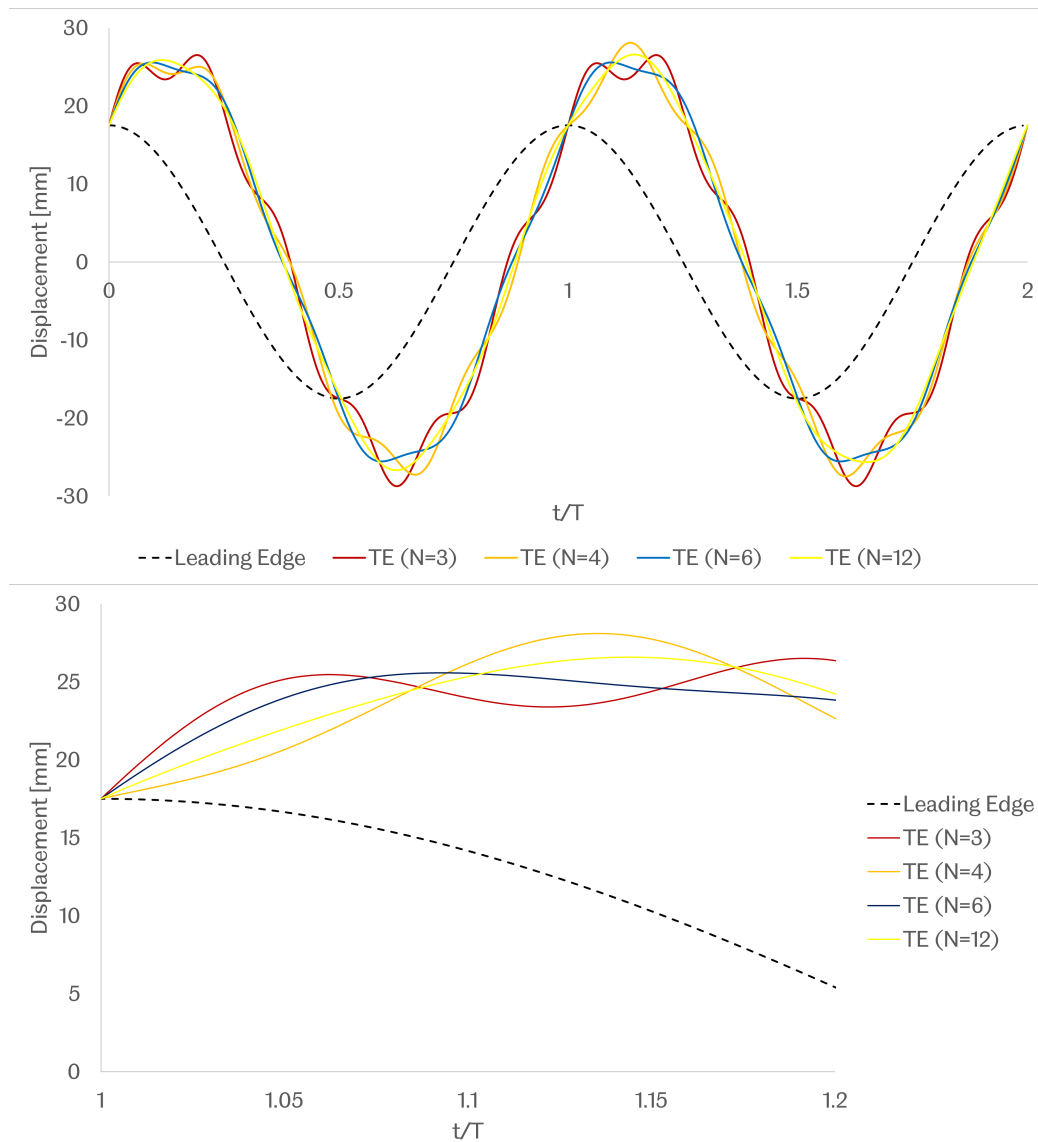


Figure 6.18: Displacement of trailing edge of teardrop/flat aerofoil vibration simulation at Reynolds number 9,000.

Computational efficiency and accuracy In this section the computational cost up to 200 timesteps is investigated. Compared to the uniform POD-Galerkin ROM approach, the proposed adaptive ROM methodology more accurately predicts the results for teardrop/flat design oscillation at the Reynolds number $Re=9,000$. Figure 6.19 shows the normalised error between the benchmarked full order CFD solution and the ROM methods via both the uniform approach and the proposed methods. The shape, frequency and amplitudes are much closer to the experimental and numerical solution (Heathcote and Gursul, 2007). The proposed adaptive discretisation concentrates on the vicinity of the de-

sign, as well as in the wake region to minimise the velocity variance within the reduced order modelling process, and it varies at different time steps. The accuracies of the adaptive reduced model are observed to be almost the same in comparison to the numerical solution after five iterations. In contrast, the reconstructed flow fields using the uniform ROM are not perfectly accurate due to the large motion the flexible flat plate.

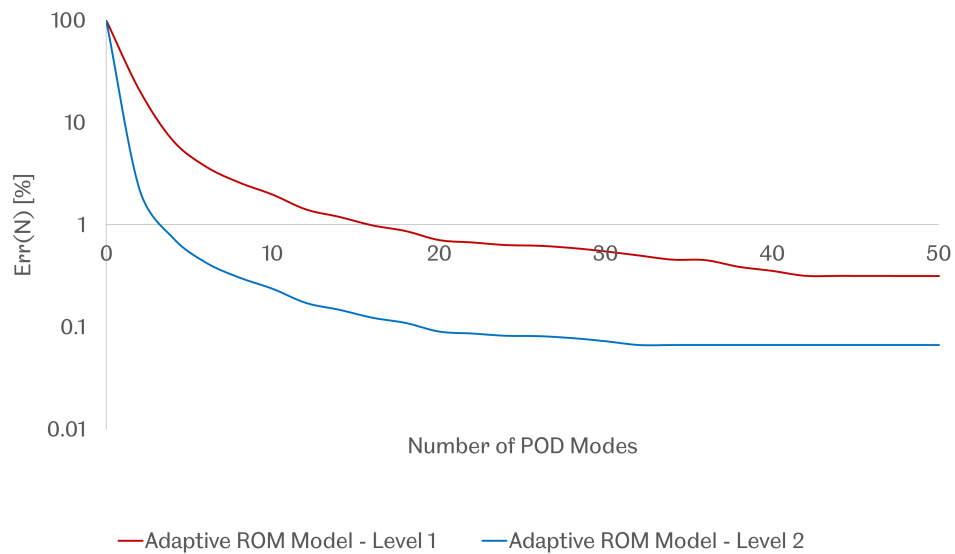


Figure 6.19: Decay of the normalised error for the POD basis using the adaptive and uniform grid discretisation for the teardrop/flat design oscillation at the Reynolds number $Re=9,000$.

Figure 6.20 shows the online and offline CPU time required to compute up to 200 timesteps with varying mesh size. The computational cost of the full order CFD simulation is compared against those of a uniform discretisation and the proposed ROMs. It shows that the cost of the ROM models remains static with an increasing resolution of the mesh, and that significant CPU speed-ups are obtained when using the mesh with the largest number of nodes. The CPU costs were reduced by a factor of about 100 compared to the cost of the high-fidelity model.

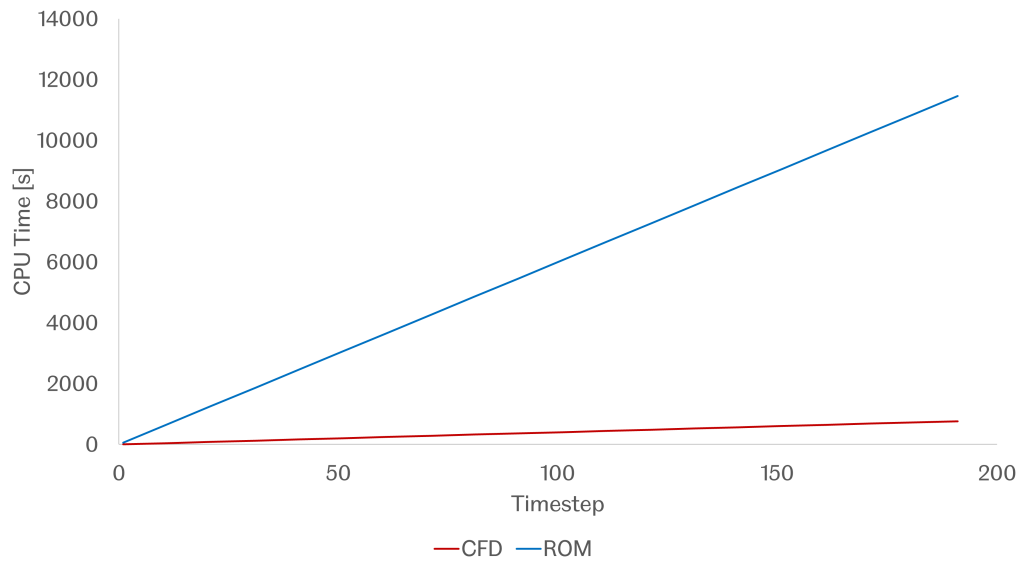


Figure 6.20: Comparison of the CPU time history on the three-dimensional teardrop/flat design oscillation at the Reynolds number $Re=9,000$ between the full-order CFD solution and the ROMs.

Figure 6.21 represents a zoomed figure of the Figure 6.20, which is a comparison of the offline CPU time history of the different Reduced Order Models. The offline CPU time listed here includes the time for assembling and solving the matrix for the full order model and projecting the POD solution onto the uniform/adaptive space. As shown in the figure, the proposed ROM is much more computationally efficient than the uniform POD-Galerkin ROM methodology, and this is because the decrease in terms of mesh density speeds the computational speed of the ROMs, since it involves assembling and solving different dimensional matrices.

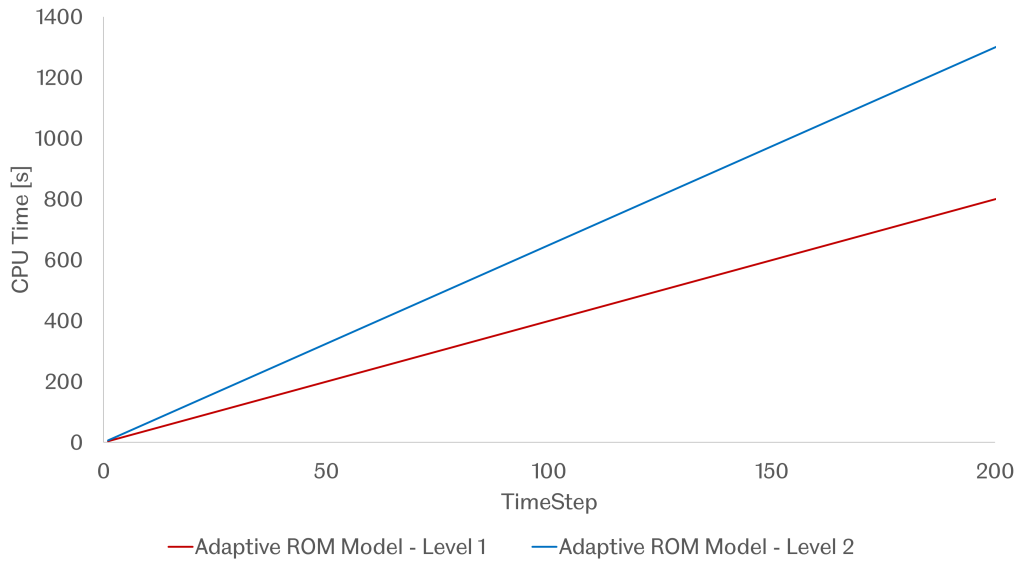


Figure 6.21: Comparison of the offline CPU time history on the three-dimensional teardrop/flat design oscillation at the Reynolds number $Re=9,000$ of different ROMs.

From all the above investigations, the proposed locally refined POD-Galerkin based ROM more accurately predicts the results for the teardrop/flat plate design oscillation compared to the proposed uniform ROM with the same level of grid. The reconstructed ROM solutions are compared to the existing numerical results as well as the experimental data. The results show a relatively good agreement with the full-order CFD solution regarding the velocity and displacement fluctuations. Compared to the accuracy and the computational cost between the ROM approach and the numerical method, the proposed ROM shows a very good potential for use in fluid-structure interaction simulations (FSI) problems. It is demonstrated that the locally refined POD-Galerkin based ROM is capable and robust for deforming boundary problems, the locally refined prediction has been improved significantly from the traditional ROM method.

6.4 Conclusions

In this chapter a novel ROM model that deals with deforming fluid-solid interfaces is proposed. In contrast to Chapter 5, this chapter focuses on the fluid-structure interaction problems with a deforming fluid-solid interface, where rigid domain is no longer considered as being flexible rather than being rigid. In the proposed methodology, the flexibility of the solid domain is modelled as a combination of rigid solid segments. The approach that will be taken for the model flexibility for the structure is to first develop a full finite element model, and then use a component approach that has been borrowed

from the finite segment method in order to significantly reduce the number of degrees of freedom while still incorporating the essential physics of the system, including the nonlinearities. This will be done in order to accommodate the model flexibility for the structure.

In order to validate the model, it is necessary to compare the findings that were achieved through the use of the model presented to the results that were acquired through the use of various simulation models or those that were gained via experimental measurements. The proposed method is first applied to model a two-dimensional flow around a flexible plate, and then a three-dimensional flow-induced and forced vibration simulation on both the NACA 0015 aerofoil and the teardrop shape aerofoil at various Reynolds numbers. For each case, the reconstructed ROM solutions from the proposed methodology are compared to the numerical results as well as the experimental solution when it is possible in order to validate the accuracy and performance of the model. In addition, in order to test the compatibility of the proposed refinement strategies introduced in Chapter 4 are applied to both these simulations, and error estimations and time analyses are compared to the corresponding uniform grid ROM solution.

For each case, error estimations and time analyses are compared to the corresponding uniform grid ROM solution. Both the ROM results show a relatively good agreement with the CFD solution regarding the velocity and displacement fluctuations. In addition, the proposed method presents a better capability and accuracy to deal with FSI problems compared to the traditional uniform reduced order model at various Reynolds numbers. The adaptive refinement strategy shows a good compatibility with the proposed ROM model for FSI problems. The adaptive ROM model is computationally more efficient than the proposed uniform one, and the size of grid is same as the minimum grid size of the adaptive ROM.

6.5 Nomenclature

Nomenclature

α, β, γ	Rotational angle around X-, Y-, Z- axis respectively
\mathbb{A}_i	First column of the combined rotational matrix \mathbf{R}_i
\mathbb{B}_i	Second column of the combined rotational matrix \mathbf{R}_i
\mathbb{C}_i	Third column of the combined rotational matrix \mathbf{R}_i
\mathbf{R}_i	Combined rotational matrix of the i-th segment
$\mathbf{R}_\alpha, \mathbf{R}_\beta, \mathbf{R}_\gamma$	Rotatioanl matrix of α, β and γ respectively
ρ_i	material density used in the i-th segment
A_i	Cross-section area of the i-th segment
$C_\alpha, C_\beta, C_\gamma$	Damping coefficients
E_i	Young's modulus of the material used in the i-th segment
$I_{i,xy}$	Product moment of area of the i-th segment
$I_{i,x}, I_{i,y}$	Second moment of area of the i-th segment around the X-, Y- axis respectively
J_i	Polar moment of inertia of the i-th segment
$k_{i,bx}, k_{i,by}$	Stiffness coefficients of the bending spring of the i-th segment along X and Y axis, respectively
$k_{i,t}$	Stiffness coefficients of the torsion spring of the i-th segment
L_i	Length of the i-th segment
$S_{i,x}, S_{i,y}$	First moment of area of the i-th segment around the X-, Y- axis respectively

T_i Kinetic energy of the i-th segment

V_i Dissipation of energy of the i-th segment

Chapter 7

ROM FSI Simulation of the NREL 5-MW HAWT

7.1 Introduction

In previous chapters, the locally refined POD-Galerkin based ROM approach to solve FSI problems with deforming and/or moving interface is presented and the validity of the resulting deformation and dynamics were confirmed in the cases of both rigid and flexible bodies. In this chapter, the proposed novel ROM method is implemented on a NREL 5MW offshore Horizontal Axis Wind Turbine (HAWT), the NREL 5MW offshore HAWT is simulated and the resulting deflection of the blades with different numbers of segmentation is analysed and compared. Similar simulations have been performed [135], where multiple analysis parameters, including the number of ROM grid of the reduced order modelling, and the number rigid segmentations on each turbine blade are investigated during to the simulation.

7.2 Full Order Modelling on FSI of HAWT

7.2.1 Simulation of the HAWT

The conceptual NREL 5-MW reference offshore wind turbine [90] is used as the geometry for the simulations, as shown in Figure 7.1.



Figure 7.1: Illustrative modelling of the NREL 5-MW offshore wind turbine.

The geometry and fundamental features of the turbine, which comprises of the floating support platform structure, as well as the tower, nacelle, and baseline rotor, are summarised in Table 7.1. The NREL wind turbine is a standard three-bladed upwind variable-speed variable-pitch controlled horizontal axis wind turbine. It has a capacity of 5 MW, which is considered utility-scale. The turbine has a design rated tip speed of 80 metres per second, which results in a Mach number that is lower than 0.3, which justifies the utilisation of an incompressible code as the flow solver. It has seen extensive use as the reference turbine by a variety of different researchers and companies within the wind turbine sector, including the Offshore Code Comparison Collaboration project (OC3) and its continuance (OC4) [93, 91, 92, 94].

Table 7.1: Basic properties of the NREL 5-MW offshore wind turbine. Baseline turbine properties

Baseline turbine properties	
Rating 5MW Rotor orientation, configuration	Upwind, 3 blades
Rotor diameter, hub diameter	126m, 3m
Hub height	90m
Cut-in, rated, cut-out wind speed	3 m/s, 11.4 m/s, 25m/s
Cut-in, rated rotor speed	6.9 RPM, 12.1 RPM
Rated tip speed	80 m/s
Control	Variable speed, collective pitch
Drivetrain	High speed, multiple-stage gearbox
Overhang, shaft tilt, pre-cone angle	5 m, 5°, 2.5°
Tower properties	
Elevation to tower base above SWL	10 m
Elevation to tower top	87.6 m
Platform properties	
Depth to platform base below SWL	120 m
Elevation to platform top above SWL	10 m
Depth to top of taper below SWL 4 m	
Depth to bottom of taper below SWL	12 m
Platform diameter above taper	6.5 m
Platform diameter below taper	9.4 m

7.2.2 Computation Settings

Figure 7.2 shows the computational domain for the 3D CFD simulations. The computational domain consists of the grids defining the turbine, including an accurate geometrical representation of the three blades, tips and tower as documented in [90, 93, 91], and an approximate nacelle and hub due to insufficient geometric information for these components. In addition to the moving overset turbine meshes, a stationary background grid is used to set for the boundary conditions. The background grid extends $-100 \leq x \leq 500$, $-150 \leq y \leq 150$, and $0 \leq z \leq 300$ with the centre of the turbine located at $x=0$ in order to minimise boundary effects. With this configuration, the presence of the turbine does not significantly disturb the inlet flow. Three refinement regions are used at the vicinity of the blade to accurately capture the flow around the blades, and one constructed to resolve the wake flow close to and behind the rotor. There are spaces between the blade roots and the hub, as well as between the hub and the nacelle, to allow for pitching of the blades and rotation of the rotor shaft. The turbulence model calls for the boundary conditions for solid surfaces to be specified as "no-slip," and the grid

spacing must be adjusted accordingly. This is to ensure that the condition $y^+ \leq 1$ is met. Before beginning the transient simulation, stable simulations are calculated for each of the different situations. It is important to note that the fixed tower and support platform are taken into consideration in this chapter, which results in a boundary that cannot be crossed on the open surface of the backdrop grid. This makes advantage of the implementation that is detailed in Huang's work [83] to impose the free surface as an immersed boundary. There is no roughness or wall functions involved in this process.

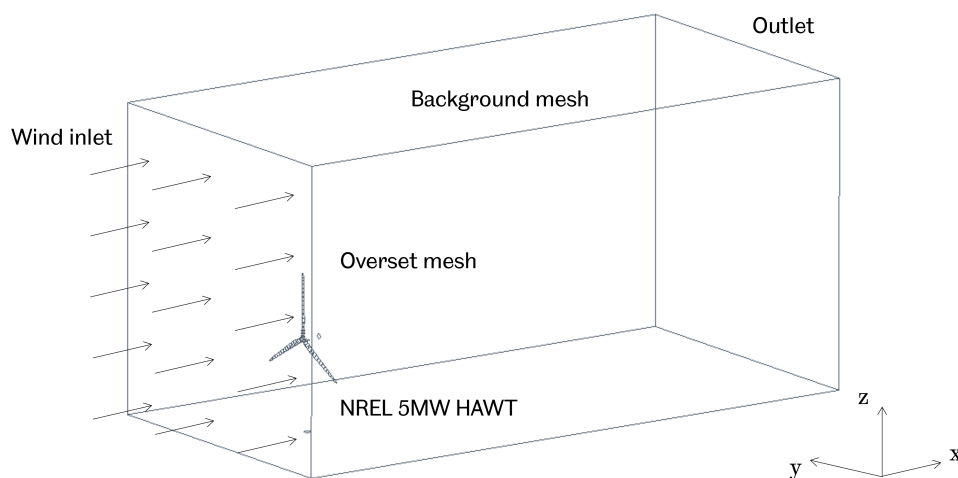


Figure 7.2: Computational domain of NREL 5-MW reference wind turbine for 3D FSI simulation.

The computational domain consists of 14 regions, organised in a parent/child hierarchy, as shown in Figure 7.3, and takes around 6 million meshes. Together, the blades, tips, hub, and blade refinements make up the body rotor overset mesh, which revolves around the shaft. The tower platform, air refinement, and body rotor come together to create the body rotor nacelle. During the simulations, the overset region meshes are the only ones that move; as a result, the total computational cost is reduced as a result of this. At the time of execution, the dynamic overset approach is utilised to do a recalculation of the overset meshing. The revolving rotor, blade, pitch, and yaw control, as well as the deformation of the turbine blades, may all be manipulated using this strategy, allowing for full control or prediction of the turbine. In each and every simulation that was carried out for the purposes of this chapter, a second-order implicit Euler scheme was utilised for the calculation of the temporal terms. When it comes to the spatial discretization, the convective terms are handled with a scheme that has a fourth-order upwind bias, while the viscous terms are handled with a scheme that has a second-order

centred. Because of the way the time step was set up, each time step results in the blades rotating by 0.5 degrees. For each simulation scenario, a total of twenty spins of the rotor were accounted for.

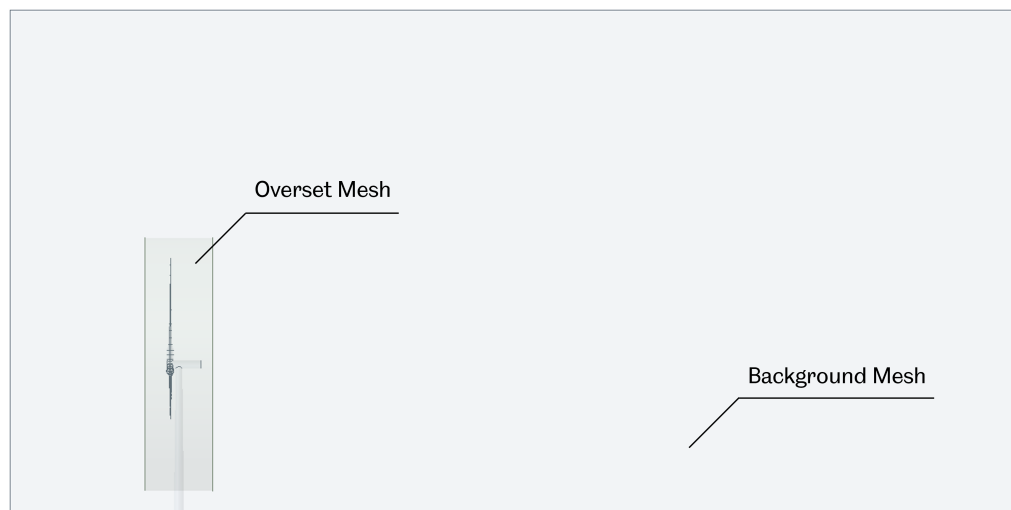


Figure 7.3: Mesh hierarchy of NREL 5-MW reference wind turbine for 3D FSI simulation.

The turbulence model used is the $k-\omega$ SST model and the transport equations for the SST model used to calculate the turbulent kinetic energy k and the specific dissipation rate ω are those used in ANSYS FLUENT. This two-equation model is suitable for modelling the boundary layers as well as the far field flows, and therefore it has been used extensively in studies involving wind turbine blades and aeroelastic problems with reasonable results (Heinz, et al., 2016; Halawa, et al., 2017).

Table 7.1 provides a summary of the structural properties of each component, including the mass and centre of gravity, flap-wise, edge-wise, torsional and extensional section stiffness, as well as flap-wise and edge-wise section inertia. These properties are organised according to the direction of the flaps and edges of the component. The construction of the model adheres to the structural information that is described in Jonkman's papers [90, 93]. The structural model of the turbine is comprised of a total of six components, including three blades, a nacelle, a hub, and a tower. In the flexible turbine simulations, beam force elements are employed as connectors, which results in each body having six degrees of freedom (DOF). It is believed that the tower, nacelle, and hub have a stiff structure. In order to provide a kinematic description of the relationship between the various components of the turbine, the following kinetic joints or constraints are applied: A bracket joint is used at each interface of the blade and hub, thereby restraining relative motions between the components; a revolute joint is used between the hub and

nacelle along the rotational axis of the rotor to allow rotor rotation and constrain other degrees of freedom; similarly, another revolute joint is used at the interface of nacelle and tower for the yaw motion; and finally, a bracket joint is used at each interface of the blade and hub, thereby It is assumed that the entire blade has the same configuration for the sake of simplicity.

Table 7.2: Structural properties of the NREL 5-MW reference wind turbine.

Blade	
Length [m]	61.5
Overall Mass (each) [kg]	17,740
Moment of inertia [$kg \cdot m^2$]	11,776,047
Centre of mass location (along pre-coned axis) [m]	20.475
Flap-wise stiffness (equivalent) [GPa]	92.1
Edge-wise stiffness (equivalent) [GPa]	3.96
Torsional stiffness (equivalent) [MPa]	556.36
Extensional stiffness (equivalent) [GPa]	2.08
Nacelle and Hub	
Overall Mass [kg]	296,780
Tower	
Overall Mass [kg]	347,460

The NREL 5-MW wind turbine is a three-bladed horizontal axis wind turbine. Each turbine blade is 61.5 metre long, as shown in Figure 7.4. The cross-section profile of the blade used in the turbine is illustrated in Figure 7.5. The distributed blade structural properties of each NREL 5-MW wind turbine blade, including torsional and extensional stiffnesses, are illustrated in Figure 7.6. The turbine blade is modelled as a flexible body using equivalent structural properties as per the definition of [90, 93].

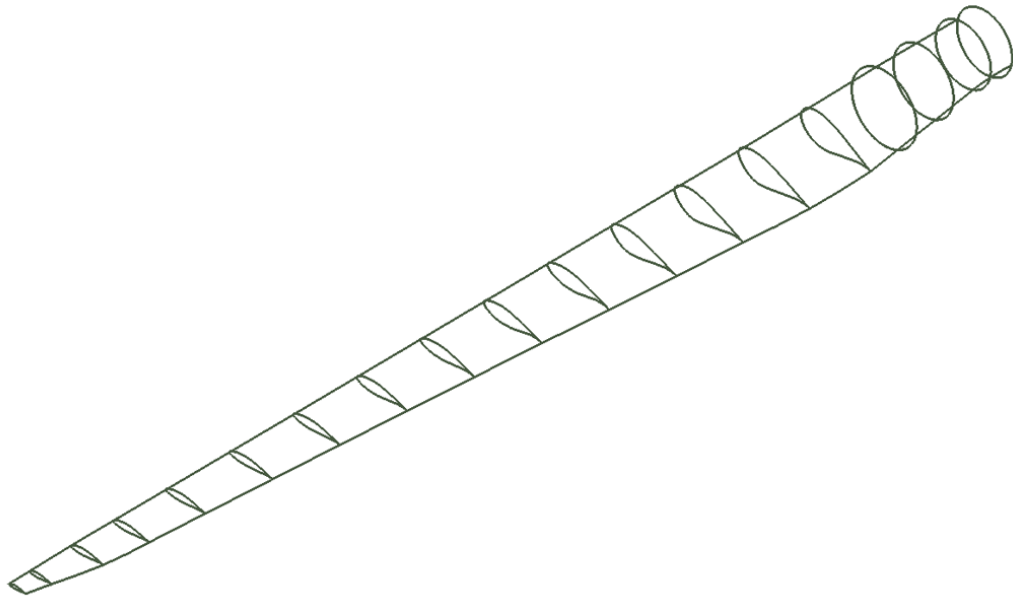


Figure 7.4: Illustrative demonstration of the NREL 5-MW offshore wind turbine blade.

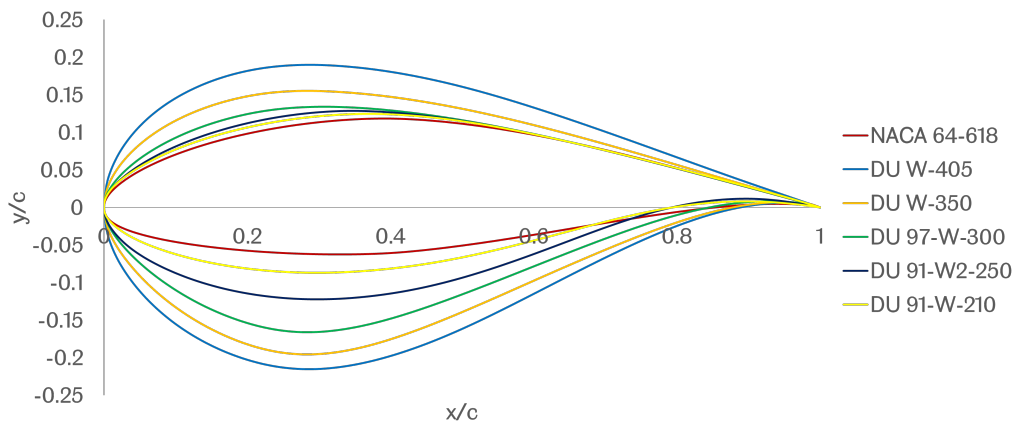


Figure 7.5: Cross sectional aerofoil profile of the NREL 5-MW wind turbine blade.

The test cases were selected from the OC3 findings that were made accessible to the public [93]. The OC3 project is a good benchmark for the utility-scale offshore wind turbine because it involved several revisions for each simulation case, all of which were performed independently by a group of international participants with expertise in wind energy. These participants came from universities, research institutions, and industries. In this chapter, two separate test cases are carried out, and both of them maintain a steady rotating speed. In the OC3 project, the simulation case that has a constant rotor speed of 9 RPM will be used as the basic and simplest validation scenario and the wind speed is 8 metres per second. For wind speeds less than the rated wind speed of 11.4 m/s, the rotor

speed of 12.1 RPM was applied to simulate the case which is maintained at a constant rated power and regulates the generator speed [90]. In addition, this chapter also simulates when the wind turbine operates at the rated rotational speed as the wind speed increases from the cut-in speed to cut-out speed.

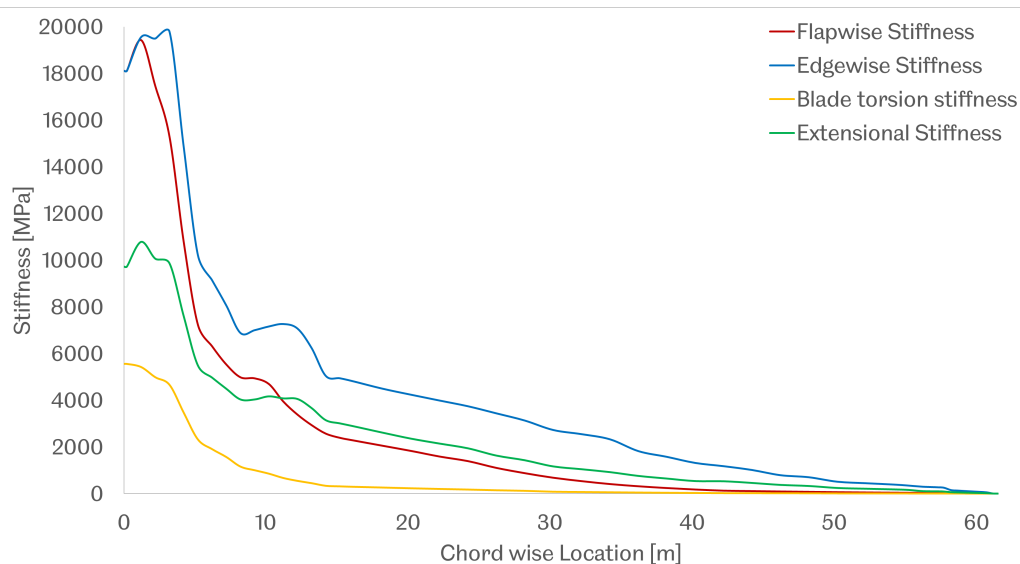


Figure 7.6: Distributed blade structural properties of the NREL 5-MW wind turbine blade.

The baseline full-order CFD simulations results are compared to the OC3 reference simulation that both use the BEM-based aerodynamic code AeroDyn [107] as aerodynamic solver and MBD-based structural solvers [95] prior to reduced order modelling.

Table 7.3 summarised a comparison snapshot between the baseline CFD simulation and the results from OC3 project. On considering the maximum difference between the current FSI simulation and the OC3 project is no larger that 6.5%, the difference is reasonable. The proposed POD-Galerkin will be implemented on the current CFD solution and compared to both the CFD solution and the OC3 project.

Table 7.3

	Current Simulation	OC3
Averaged Thrust [kN]	384.97 (+3.40%)	372.32
Averaged Shaft torque [kN m]	2096.40 (+6.12%)	1975.54
Averaged Power [kW]	1975.81 (+6.12%)	1861.90

7.3 Reduced Order Modelling

The refined ROM methodology (please refer to Chapter 6) has been applied to solve both FSI simulations and stability analyses. The computational domain for the ROM is identical to the those for the FSI simulation with the uniform ROM mesh at $N_x \times N_y \times N_z = 300 \times 150 \times 150$, as shown in Figure 7.7. Mesh and time size sensitivity studies are carried out to determine appropriate cell face and time steps. 200 snapshots over 4 periods are used to build ROM, nacelle, hub and tower are assumed to be rigid, and therefore only the deformation of the blades is considered here. Each NREL 5-MW wind turbine blade is modelled as a combination of up to 30 rigid segments. A detailed analysis of the number of segments is presented in Chapter 7.4.1. Four iterations of the ROM mesh refinement are implemented in this application, refer to Chapter 4, as shown in Figure 7.8. The threshold is set as the difference within each sub-grid is no larger than 0.05% of the maximum velocity difference of the overall domain.

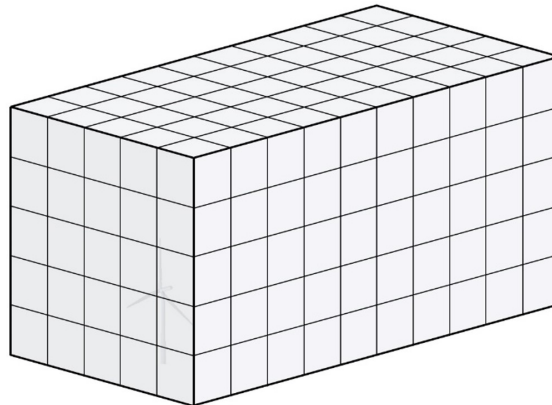


Figure 7.7: Initial uniform ROM mesh of 3D computational domain for NREL 5-MW reference wind turbine FSI simulation. Each grid represents a $5 \times 5 \times 5$ mesh grids in ROM calculation.

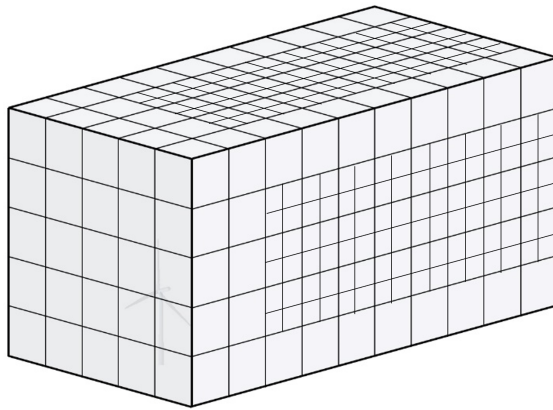


Figure 7.8: Illustrative demonstration of the ROM refined mesh of 3D computational domain for the NREL 5-MW reference wind turbine FSI simulation after one iteration.

During the simulations, the nacelle, hub, and tower are assumed to be rigid. Each HAWT blade is modelled as a chain of rigid segments, please refer Chapter 6. Various numbers of segmentation are investigated, as an example of which uses consists 16 rigid bodies to model one blade is represented in Figure 7.9, which in total the turbine multi-body system has 50 bodies.

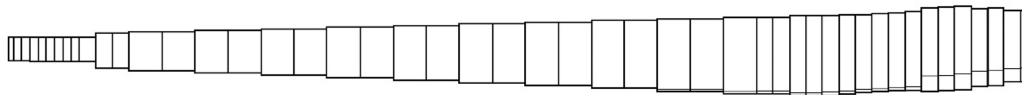


Figure 7.9: An illustration of segment representation of HAWT blade, 16 segments are used in this example.

Figure 7.10 shows the energy spectrum of the POD modes used for the simulation at a wind speed 8m/s. Visual inspection shows that there is a decrease in the eigenvalues satisfies exponential Kolmogorov n-width. This helps us to choose the number of POD bases. The greater the number of POD bases that are chosen, the more energy is captured. The first twelve dominant POD modes, which covers more than 99.9% of the overall kinematic energy, are selected to perform the following calculation. The Galerkin integration is obtained by substituting Equation (3.33) into the first six POD modes.

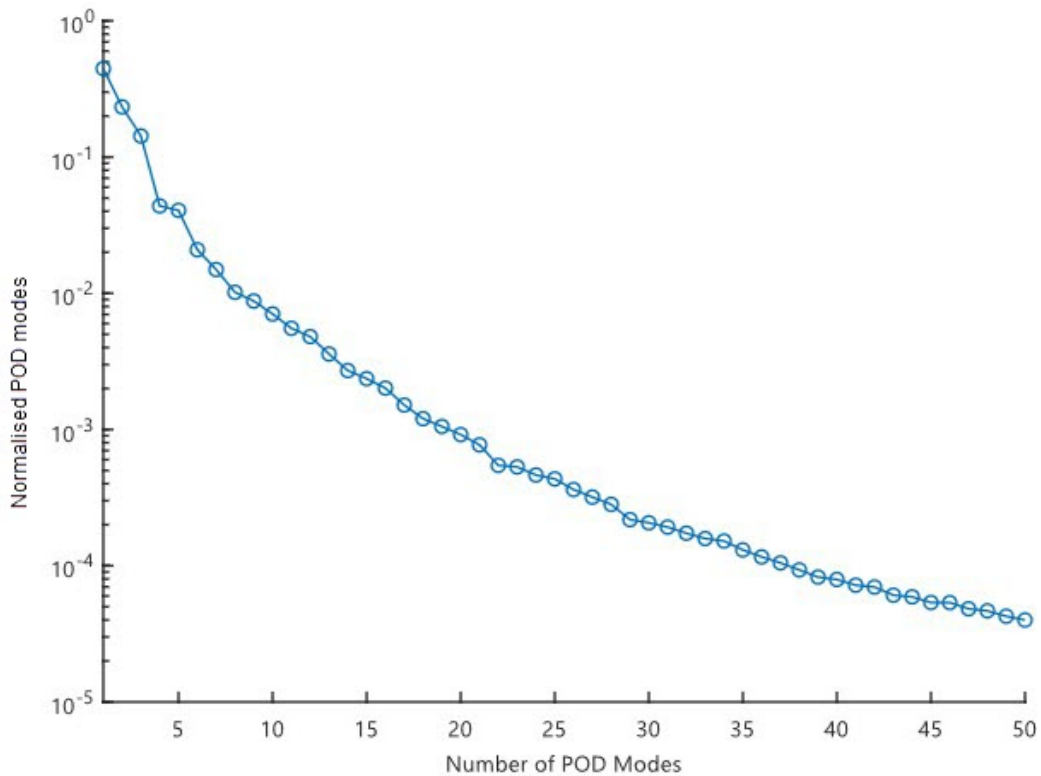


Figure 7.10: Energy spectrum of the POD modes for the NREL 5MW HAWT.

7.4 Results

The application of the proposed ROM methodology in this study is based on numerical simulations and experiments of the NREL 5MW wind turbine. The NREL 5-MW wind turbine is a utility-scale, conventional three-bladed upwind variable-speed variable-pitch controlled horizontal axis wind turbine, and it has been widely used as the reference turbine by other researchers and wind turbine industries, including the Offshore Code Comparison Collaboration project (OC3) and its continuation (OC4). The wind turbine fits in the range of wind velocity from 3 m/s to 25 m/s. The designated rated tip speed of the turbine is 80 m/s, with Mach number less than 0.3, thus justifying the use of an incompressible code as flow solver.

As proposed in the previous chapters, the rigidity of the flexible solid domains is modelled as a combination of several rigid segments. The constraints between the rigid segments are always in 6 DOFs to satisfy structural continuity. In this practical simulation, the NREL 5-MW wind turbine consists of four individual parts: tower, nacelle, three hubs and three blades; tower, nacelle and hubs are considered rigid, and therefore modelled as only one rigid segment for each part. The wind turbine blades are modelled by

multiple rigid segments, varying from 1 to 30 segments for each blade, to capture large deflections in multiple scenarios. A constant time step of 0.01 s was used for all the considered cases. Details on the convergence analysis will be summarised in Section 7.4.1. For all FSI simulations, at the initial time step blade 1 was placed downward immediately in front of the tower, as shown in Figure 7.11. At every complete rotation, the blade 1 is passing the tower while half a rotation later it is at the uppermost position. In addition, the rotor clockwise rotates when seen facing upwind direction.

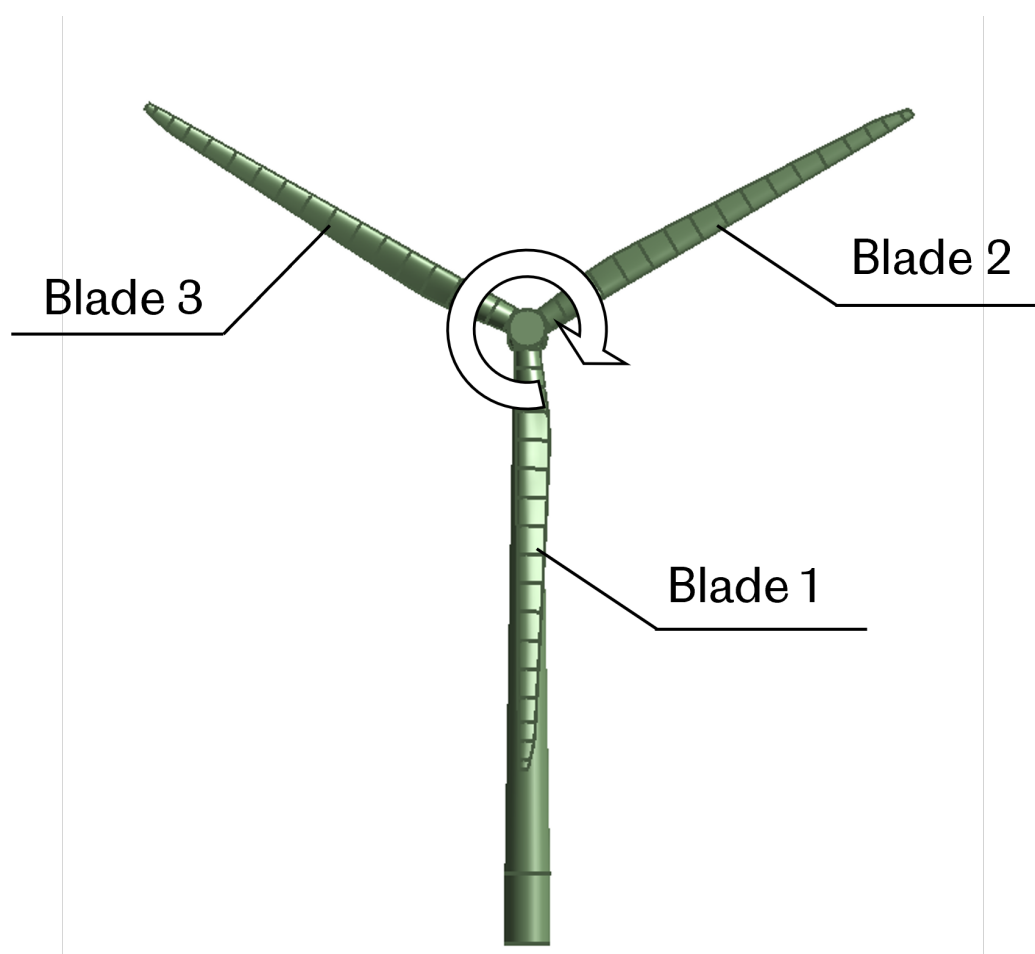


Figure 7.11: Initial wind turbine setting for the HAWT FSI simulation.

7.4.1 Convergence analysis

Before performing the reduced order modelling, a convergence analysis was performed with the steady wind load cases to determine the number of modes to be used in the proposed reduced order model methodology and to observe the effects of large deflections on projection residual. Figure 7.12 shows how the L2 norm of the NREL 5MW reference wind turbine blade projection residual varies with number of finite element segments

of each blade. The linear and nonlinear blade models in the solver are used to calculate the deflections of the blades under a steady wind load of 8 metres per second. These deflections are then projected onto the basis with mode shapes at the starting (undeformed) blade position. Therefore, the inaccuracy that exists between full-order CFD and the suggested ROM blade model deflections may be used to evaluate the influence that geometric nonlinearities have on the segments. As shown in Figure 7.12, the geometric nonlinear effects that arise as a result of substantial blade displacements result in nine times greater projection residual than the linear blade model. When substantial blade displacements are taken into consideration, this suggests that geometric nonlinearities are the primary cause of the projection residuals. Nonlinear effects, such as inertia and force, are examples of nonlinear effects that are distinct from geometric nonlinearity and can be a source of linear model residuals. The fidelity mismatch between the numerical model, which has 156 degrees of freedom for the NREL 5MW wind turbine blade, and the projection space, which has 20 modes, is another source of the linear model residuals. On the other hand, when compared to the entire deflection of the linear blade model, the total residual of all the nodes in the network is rather insignificant. The first two modes are, in order, the first flapwise mode, followed by the first edgewise mode. The eighth mode is the first mode that involves torsion, while mode 16 is the first mode that involves axial rotation.

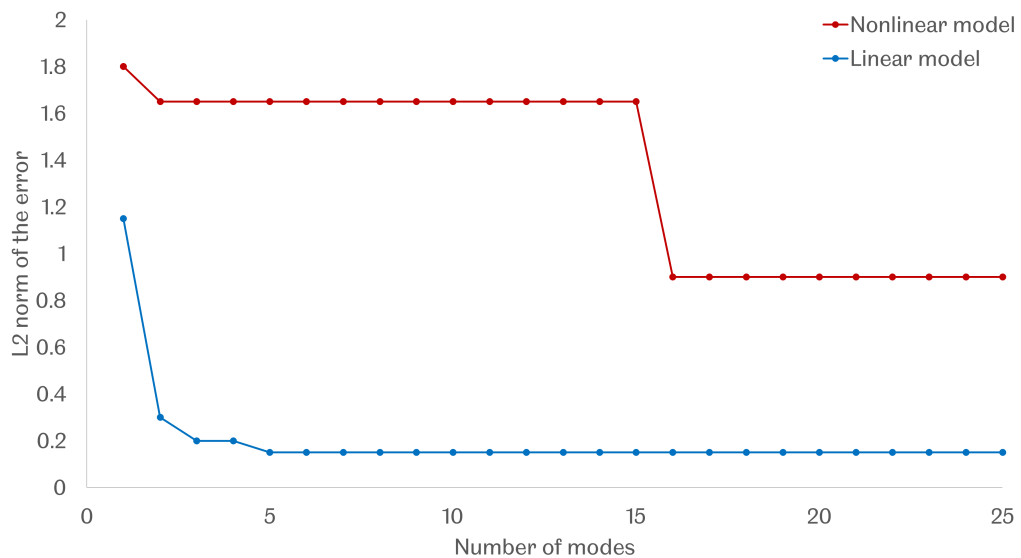


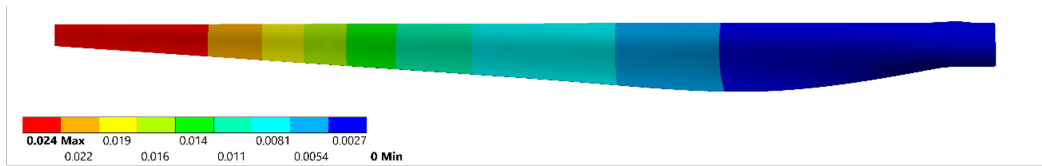
Figure 7.12: The error of the NREL 5MW wind turbine blade projection residuals with respect to the number of modes. The blade deflections are compared to the full-order CFD at 12 m/s steady wind speed and the projection basis is composed of undeflected blade mode shapes.

7.4.2 Stability analysis

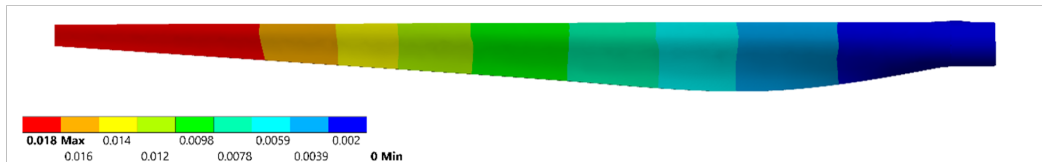
To provide a detailed overview of the overall system behaviour of the equivalent land-based version of the NREL 5-MW baseline wind turbine between the proposed ROM model using various number of segments along the wind turbine blade and the full order CFD simulation, the natural frequencies are calculated in the blade and the whole system stability analysis. During all the stability analyses, the active control, dynamic stall, or hydrodynamic radiation damping are ignored, therefore not included in the analyses.

The blade-only stability analysis is performed prior to the whole turbine simulation. The 61.5 metre NREL 5MW wind turbine blade is fixed at the base. The blade is 61.5m long, the geometric design parameters, such as the mass, flexural rigidity, flapwise and edgewise stiffness with other properties are given in Table 7.2. The wind turbine blade is treated as a cantilever beam, at the fixed end, both the deflection and slope are zero; at the tip end, the bending moment and shear force are zero.

The blade-only stability analysis is performed by the proposed ROM methodology using both 6 and 30 rigid segments for each blade. The natural frequencies are compared to the full-order baseline stability analysis done in the ANSYS. Natural frequencies are named by the governing normalised deformation along either the flap-wise, edgewise and torsion directions. Figure 7.13 shows the first six natural frequency mode shapes of the NREL 5MW wind turbine blade.



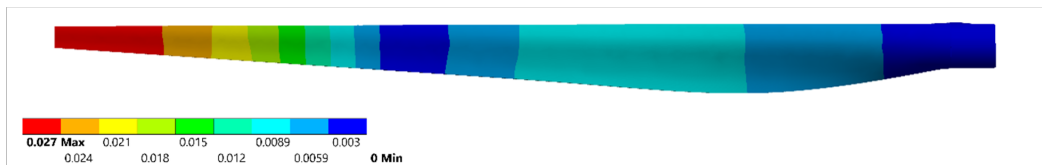
(a) Mode shape 1



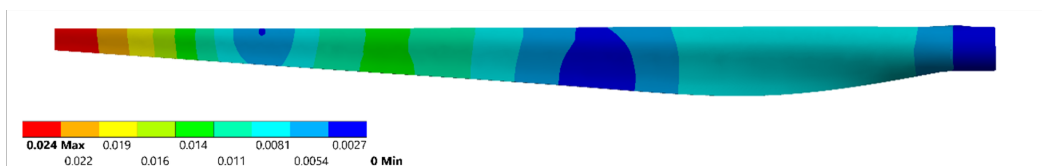
(b) Mode shape 2



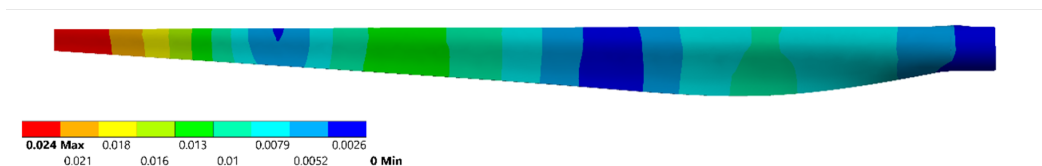
(c) Mode shape 3



(d) Mode shape 4



(e) Mode shape 5



(f) Mode shape 6

Figure 7.13: First 6 mode shapes of the NREL 5-MW wind turbine blade.

The first six natural frequencies are summarised in Table 7.4. Both ROM solutions predicts the first natural frequencies of the wind turbine blade of the blade in terms of the natural frequency and the mode shape. As the number of segments increases, the proposed ROM methodology rebuild the flexible turbine blade model more accurately. This is acceptable as the rigidity is represented by a combination of the rigid segments, fewer segments provide less information and therefore couldn't produce acceptably accurate results.

Table 7.4: First 6 mode shapes of the NREL 5-MW wind turbine blade.

	ROM solution [Hz]		ANSYS [Hz]
1st flap-wise	0.991(+53.17%)	0.767(+18.55%)	0.647
1st edge-wise	1.381(+30.16%)	0.977(-7.92%)	1.061
2nd flap-wise	2.355(+23.56%)	1.831(-3.93%)	1.906
2nd edge-wise	4.633(+14.99%)	3.991(-0.94%)	4.029
3rd flap-wise	4.992(+13.30%)	4.155(-5.70%)	4.406
1st torsion	7.992(+8.38%)	7.724(-4.75%)	7.374

During of the full-system stability analyses, the nacelle, hub, and tower are assumed to be rigid. Each HAWT blade is modelled as a chain of finite rigid segments, as shown in Figure 7.14, black and red segments indicate that they are considered rigid and flexible segments respectively.

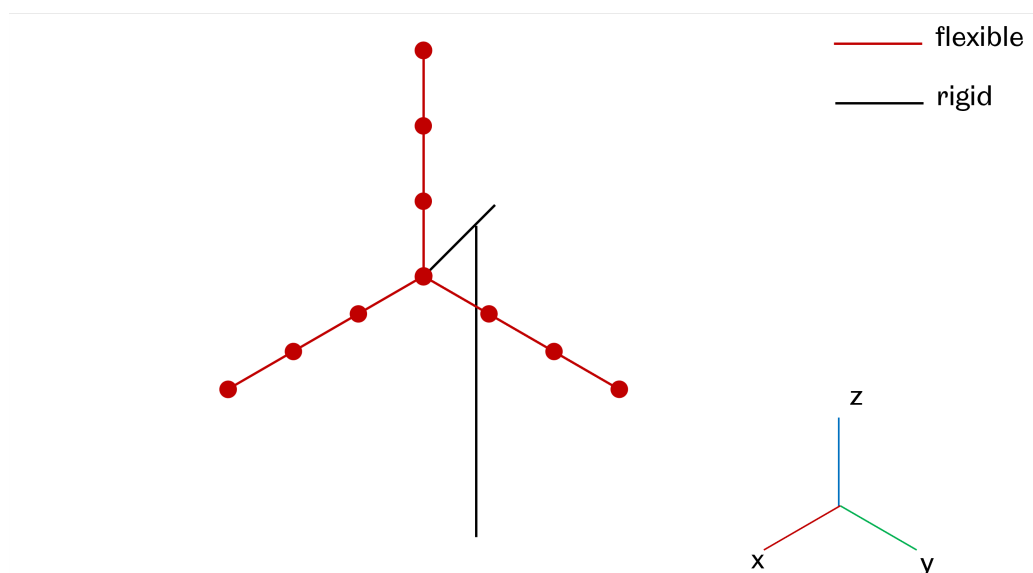


Figure 7.14: Finite element segment modelling of the NREL 5-MW wind turbine. red and black bodies represent they are modelled as flexible and rigid body respectively.

The number of finite element segments that were utilised in each model of the VAWT is summarised in Table 7.5. The number of stiff segments in the model affects the size of the issue because it changes the number of generalised coordinates and constraints in the governing equations. In every instance, the blades are the most important factor in determining the size of the problem., please refer to Chapter 5. In this simulation, each HAWT blade is modelled up to 30 rigid segments. The 30-segment blade model is the most exact and has the maximum number of restrictions, whereas the scenario in which there is only one segment is known as the linear blade case. In spite of the fact that the magnitude of the issue in the equations shifts depending on the number of entities that are described in the model, the total number of independent constraints remains unaltered for this specific turbine model.

Table 7.5: Number of rigid segments used in the wind turbine model.

Number of rigid segments of each blade	Sum of rigid segments of the NREL 5-MW wind turbine	Number of equation of constraints
1	6	36
2	9	54
3	12	72
6	21	126
9	30	180
12	39	234
15	48	288
18	57	342
21	66	396
24	75	450
27	84	504
30	93	558

Whole-system stability analysis consists of two parts: firstly, the natural frequency of this wind turbine model is computed, i.e., both the rotational speed and wind speed are set to be zero. Secondly, the stability analysis simulates the cases where the wind speed varies from the cut-in speed to cut-off speed, i.e., from 3 m/s to 25 m/s. At a given wind speed, the rotor speed is depicted in Figure 7.15. These values ensure optimum performance and power regulation as per the definition from the NREL [90].

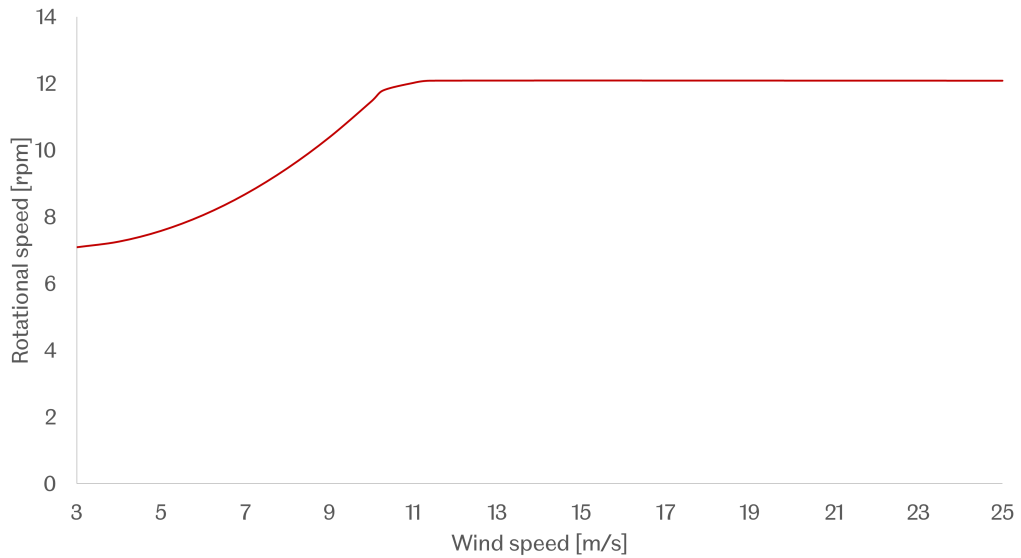


Figure 7.15: Rated rotational speed with respect to the wind speed of the NREL 5-MW wind turbine.

Table 7.6 lists the results of the first 10 natural frequencies of the NREL 5-MW wind turbine model. Natural frequencies are named by their most governing motion direction of the wind turbine model, as shown in Figure 7.5. For example, 1st tower X means during this frequency the tower oscillates forward and backward. The proposed ROM methodology provides a considerably accurate results except for several rigid-body involved mode shapes, e.g, 1st Tower X. This is due to the tower being modelled as a rigid body, the rigidity information is lost during the simulation. This error can be minimised by increasing the number of rigid segments used in the tower part.

Table 7.6: First 10 natural frequencies of the NREL 5-MW wind turbine model.

Mode	Description	30-segment ROM	Jonkman et al.,
1	1st Tower X	0.2141(-32.98%)	0.3164
2	1st Tower Y	0.3306(+3.47%)	0.3195
3	1st Nacelle torsion	0.5039(-17.31%)	0.6094
4	1st Blade flapwise	0.6276(+0.32%)	0.6296
5	2nd Blade flapwise	0.6398(-4.31%)	0.6686
6	3rd Blade flapwise	0.7347(+4.67%)	0.7019
7	1st Blade edgewise	0.9689(-9.79%)	1.0740
8	2nd Blade edgewise	1.2075(+11.01%)	1.0877
9	3rd Blade edgewise	1.4083(-14.68%)	1.6507
10	4th Blade edgewise	1.8079(-2.58%)	1.8558

In addition, in several cases, multiple coupled motions are noticed from the natu-

ral frequency analysis, and these give nearly identical results. Recalling the 4th and 5th natural frequencies, the motion of the blades are coupled by the torsion of the nacelle, and this increases the difficulty of the proposed ROM to capture accurate results. Apart from these issues, the proposed ROM methodology shows a good agreement in the referenced stability analysis, which is performed by FAST [90, 91]).

7.4.3 Deformation analysis

Similar to the stability analysis, the wind speed varies from the cut-in speed and the cut-out speed, i.e., from 3 m/s to 25 m/s. The NREL 5MW baseline wind turbine operates at the corresponding rotational speed and pitch angle illustrated in Figure 7.15. For each given wind speed, the deformation of the turbine blade is computed after the simulation reaches convergence. Figure 7.16 and 7.17 show the deformation of the HAWT working at wind speed 8 m/s and rotor speed 9 RPM. Deformation shows the same trend in each HAWT blade, the maximum deformation occurs at the tip of the each blade.

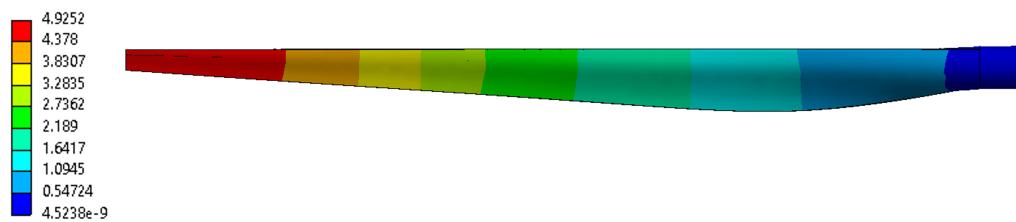


Figure 7.16: Total deformation of the NREL 5MW wind turbine blade at wind speed 8 m/s and rotor speed 9 RPM.

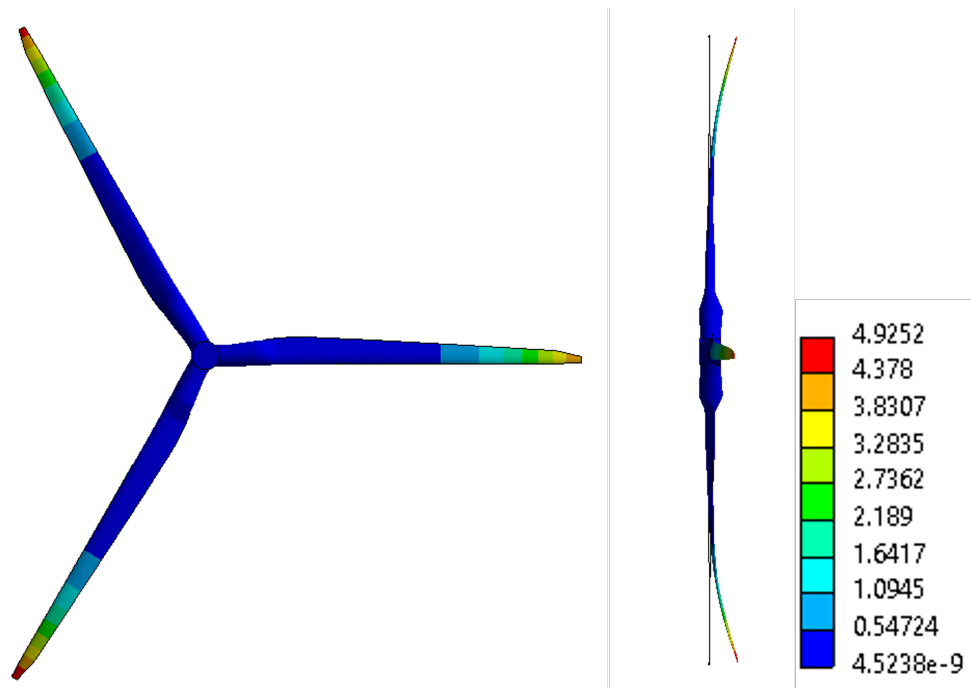


Figure 7.17: Illustrative representation of the HAWT deformation working at wind speed 8 m/s and rotor speed 9 RPM .

Table 7.7 quantitatively compares the time history of the thrust and torque once the periodic behaviour has been reached for one time step of the wind speed, namely 8 m/s . Two typical rebuilt POD-ROM solutions, which models 6 and 15 segments for each turbine blade are considered and compared to the baseline OC3 codes. Being a 3-bladed turbine, a decrease in thrust and torque occurs every $1/3$ rotation due to the presence of the tower. Using results obtained from the OC3 code as a baseline, quantitative comparisons in Table 7.7 show that the ROM approach has close predictions in different numbers of blade segments. For the thrust, the rebuilt ROM using 6 segments for each turbine blade predicts an average value of 394.74 kN , 6.02% larger than the baseline solution, while the rebuilt ROM using 30 segments predicts an average thrust of 385 kN with standard deviation of 2.6 kN , 3.4% larger than the GH Bladed. For the torque, the former one shows an average magnitude of 2096.40 kNm , while the latter case predicts an average of 2033.76 kNm with standard deviation of 27.4 kNm , 6.12% and 2.95% higher than the baseline, respectively. The proposed ROM solution predicts more accurate results as the number of segment increases. In addition, the good agreement for the averaged magnitudes, all the results exhibit similar statistics for this case, including maximum, minimum and standard deviation of the thrust and torque [111]. It should be noted that both ROM results share the same FSI simulation, and both successfully predict these aerodynamical parameters with different levels of accuracy. Since the only difference between these

rebuilt ROM cases is the number of segments on each turbine blade, even for the case with a lower number of segments of 6, it still somehow represents the flexibility of the blades. When the number decreases further, this method loses its capability of representing flexible bodies and it is unable to achieve a converged result in some running cases.

Table 7.7: Comparison between rebuilt ROM simulation with different numbers of segments on the HAWT aerodynamic parameters and OC3 codes at wind speed 8 m/s and rotor speed 9 RPM.

	Standard ROM	AdaptiveROM		OC3
Numbers of Segments	/	6	16	/
Averaged Thrust [kN]	410.2 (+9.87%)	394.74 (+6.02%)	384.97 (+3.40%)	372.32
Averaged Shaft torque [kN m]	2140.50 (+8.35%)	2096.40 (+6.12%)	2033.76 (+2.95%)	1975.54
Averaged Power [kW]	1996.88 (+7.25%)	1987.95 (+6.77%)	1975.81 (+6.12%)	1861.90
Computational Cost	432.8s	261.6s	3621.5s	/

The difference between different number of segments becomes clearer in the comparison in the deflection. Figure 7.18, 7.19 and Table 7.8 compare the predicted blade 1 tip deflections from two rebuilt ROM methods and by the OC3 code. Regarding the coned coordinate system that moves in tandem with the stiff rotor, the deflections are given. Positive out-of-plane deflection points are located downwind in the coned coordinate system. Positive in-plane deflection points are located from the leading edge to the trailing edge and are perpendicular to the rotating direction of the blade. Each and every blade's deflection will display cyclic oscillations because of the rotational and tilt effects.

Table 7.8: Comparison between rebuilt ROM simulation with different numbers of segments on the Blade 1 tip deflections at wind speed 8 m/s and rotor speed 9 RPM.

Participant	Standard ROM	Adaptive ROM		OC3
Numbers of Segments	/	6	16	/
Out-of-plane deflection [m]	3.802	3.592 (+10.73%)	3.359 (+3.55%)	3.244
In-plane deflection [m]	-0.402	-0.345 (8.49%)	(-0.340 (6.92%))	(-0.318)

The out-of-plane deflection is significant since it is connected to the structural strength and fatigue of the blade in addition to the problems associated with the tower clearance. As a result of the fact that thrust is the primary factor in out-of-plane tip deflection, the anticipated deflection follows trends that are analogous to those that were seen and described in Chapter 7.2.2 for the blade thrust. It is important to notice that the force of gravity is accounted for in every simulation that has been done. The most noticeable decreases in the curve occur approximately when the blade is at the top with the least influence from gravity, and the secondary decrease is induced by the tower shadow with a mean magnitude of about 3.5 m, as shown in Figure 7.18. The magnitude of these decreases can be seen in the figure. If the tower were not there, the deflection would keep growing until it reached its maximum value with the blade on the bottom, which is the location where the gravity effect is at its greatest because of the tilt. As a direct result of this, the tower shadow helps to enhance the blade's clearance around the tower. The rebuilt ROM using 6 segments on the turbine blade is shown to be out-of-plane by 3.592 m, those using 16 segments predicts averaged deflections of 3.359 m, 10.73% and 3.55% higher than the baseline OC3 code, respectively, as seen in Table 7.8. The rebuilt ROM using 16 segments shows a less fluctuational trend than the other rebuilt ROM results, and it is more similar to the baseline OC3 code. The maximum deflection is 3.692 m for the Rebuilt ROM using 6 segments, 3.409 m for the Rebuilt ROM using 16 segments, 9.55% and 1.16% higher than the baseline result.

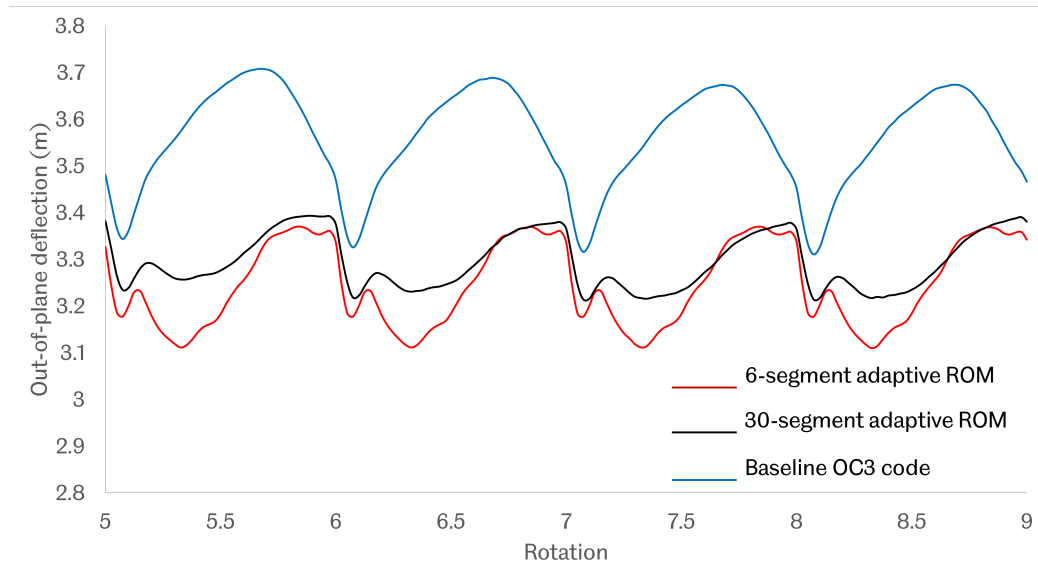


Figure 7.18: Comparison of out-of-plane deflections for blade 1 tip between rebuilt ROM solution and the baseline OC3 code for wind speed 8 m/s.

For the In-Plane deflections (shown in Figure 7.19), all of the findings of rebuilding the ROM point to roughly sinusoidal patterns. These patterns are mostly governed by the centripetal force, blade rotation, and tilt effects, although gravity is the dominant factor. As a result of the twist angle and the offset to the blade pitch axis, centripetal forces cause a negative deflection towards the leading edge, and aerodynamic forces from the wind push the curve to negative deflections. This results in asymmetric oscillations, with a smaller deflection towards the trailing edge and a larger deflection towards the leading edge. The number of segments shows less impact on the in-plane deflection. Figure 7.19 shows an average -0.345 m for the Rebuilt ROM using 6 segments, and the Rebuilt ROM using 30 segments shows an average value of -0.304 m, respectively. This is also due to the modelling strategy presented in Chapter 6, as the in-plane stiffness is not completely represented in the equivalent stiffness matrix.

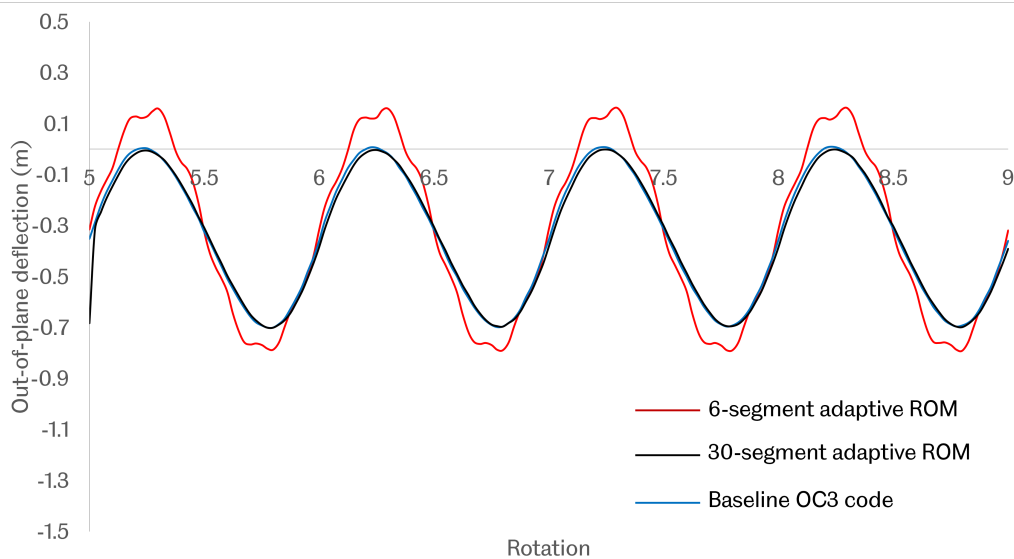


Figure 7.19: Comparison of in-plane deflections for blade 1 tip between rebuilt ROM solution and the baseline OC3 code for wind speed 8 m/s.

Extensive simulations were conducted with the conceptual NREL 5-MW offshore wind turbine in an increasing level of complexity in order to validate and analyse the aerodynamic predictions, elasticity, wind shear, and atmospheric wind turbulence. These simulations were based on the proposed coupled approach, and they were carried out with increasing levels of complexity. The ROM that had a deforming FSI interface was confirmed by comparing the predicted statistics from the rebuilt ROM results using a varied number of segments against the OC3 code that was used as a baseline. When the findings were compared with the publicly accessible simulated results from the OC3 participants, it was found that there was a good agreement for the aerodynamic loads and blade tip deflections in both the time and frequency domains.

The lift coefficient C_l and the AOA are depicted in Figure 7.20 for the 6-segment and 16-segment rebuilt ROM results, respectively, throughout the course of two rotations of the rotor. Note that in Figure 7.20, an azimuthal angle of zero corresponds to the blade being in the position where it is pointing downwards (tower passage), whereas an azimuthal angle of 180 corresponds to the blade being in the position where it is pointing upwards. Both sets of data show that there is a slight lag between C_l and AOA. As was previously said, tilt angle effects are responsible for time changes in the AOA and aerodynamic loads. As a consequence, changes in the AOA occur with an amplitude that is dictated by the tilt angle and a frequency that is determined by the rotation frequency. In addition, the existence of the tower is represented by both of the ROM solutions, which results in an extra transient in AOA and loads. An experiment was carried out by Fuglsang

et al. (Fuglsang et al., 1998) in which the dynamic AOA was controlled by a pitching motion mechanism with imposed amplitude and frequency, achieving similar effects as those caused by tilt. In this experiment, similar dynamic effects exhibiting time lag and hysteresis were observed. The drag coefficient C_d , which was not presented, exhibits trends that are comparable to those of the lift coefficient, with the exception that C_d in the section $r/R=0.16$ is approximately ten times higher than at other sections. This is because the aerofoil has a much thicker geometry in the root/aerofoil transition region. Additionally, the drag coefficient C_d exhibits significant fluctuations.

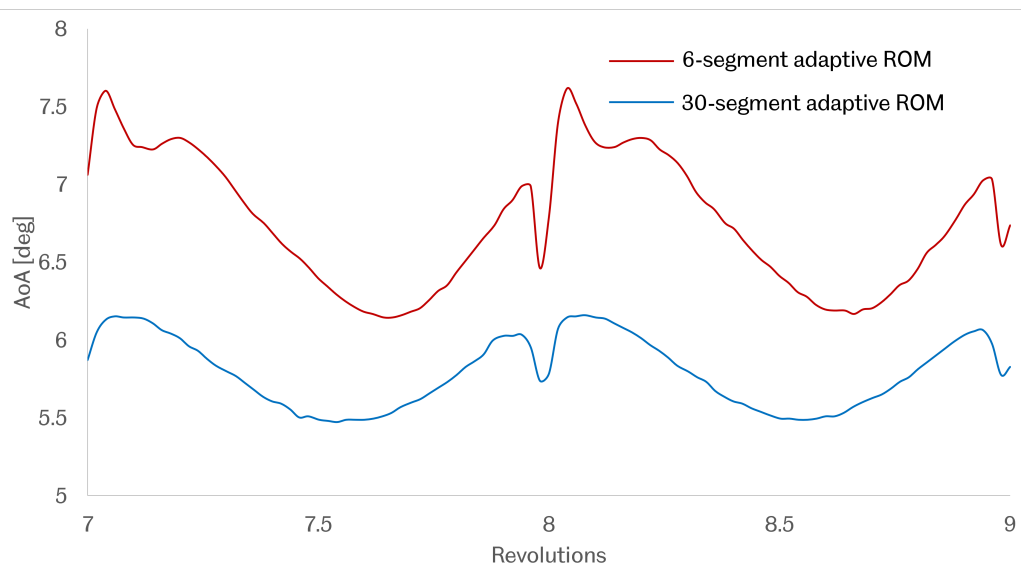


Figure 7.20: Comparison of AOA for NREL 5-MW wind turbine working at wind speed 8 m/s, $r/R=0.93$.

To further demonstrate the capability of this novel ROM method, the rated wind speed and rotor speed are increased to 11.4 m/s and 12.1 m/s, respectively. The result shows a similar trend compared to the previous case, as summarised in Table 7.9 and 7.10.

Table 7.9: Comparison between rebuilt ROM simulation with different numbers of segments on the turbine blade and OC3 codes regarding torque and computational efficiency at wind speed 11.4 m/s and rotor speed 12.1 RPM.

Participant	Standard ROM	Adaptive ROM		OC3
Number of segments	/	6	30	/
Averaged Shaft torque [kNm]	1600.5(+14.32%)	1589.4(+13.52%)	1503.5(+7.39%)	1400
Computational Cost [s]	4032	121.3	1325.2	

Table 7.10: Comparison between rebuilt ROM simulation with different numbers of segments on the turbine blade and OC3 codes regarding blade 1 tip deflections at wind speed 11.4 m/s and rotor speed 12.1 RPM.

Participant	Standard ROM	Adaptive ROM		OC3
Number of segments	/	6	30	/
Out-of-plane deflection [m]	3.72(-13.53%)	3.82(-5.67%) 4.058(+5.67%)	4.302	
In-plane deflection [m]	-0.35(-30.83%)	-0.435(-14.03%)	-0.460(-9.09%)	-0.506

The accuracy of the POD ROM results can be further improved by increasing the number of rigid body segments. Table 7.7 – 7.10 compare the full solution and the novel reduced order model when using 6 and 16 rigid bodies (for each blade) respectively. In both cases there is a visual improvement in the ROM’s predictions in comparison to the solutions provided by the standard POD ROM when the same number of basis functions are used.

7.4.4 Computational time

The results of the simulations of the blade models with varying numbers of stiff segments are compared to the results of the simulation of the blade model with 30 rigid segments, which has the maximum fidelity. The amount of time spent computing is standardised in relation to the model with the lowest level of realism, specifically the one body linear

scenario. Figure 7.21 illustrates the normalised calculation time required by the NREL 5MW reference wind turbine for the adaptive and uniform ROMs that have been suggested. Using the uniform ROM approach, the normalised calculation time is determined in comparison to the linear (one segment) scenario. The results of the CPU time calculations are presented for the 1, 2, 3, 6, 9, 12, 15, 18, 21, 24, 27, and 30 segment situations respectively. The amount of time needed to complete the computation is proportional to the number of stiff segments included in the model. As a result, it is conceivable to witness a reduction in the amount of time required for computing as the number of degrees of freedom (DOFs) and constraint equations grows. The number of time segments required reduces up to the 5-segment scenario, which also has an effect on the amount of CPU time required; after that point, the amount of CPU time required grows as the number of bodies does.

Both the proposed and uniformed ROM show a huge computationally efficiency improvement from the full-order CFD simulation. The maximum normalised solver computation time is observed for the 30-sub-body case. Uniform and adaptive ROM solvers are approximately 70% and 40% (see Figure 7.21) slower compared to the 1-segment only case. As a result of the reduction in the dimension of the matrices given by the projection grids, the adaptive reduced order model demonstrates greater computing efficiency than the uniform solution. This is due to the fact that the adaptive reduced order model uses fewer matrices. Even though there is an increase in the overall complexity of the model, the amount of time needed to complete the calculation is reduced because to a significant drop in the number of iterations that is required in the three-sub-body situation. Hence, the adaptive ROM solver computational cost owing to the growth in model complexity grows more slowly compared to the uniform ROM solution.

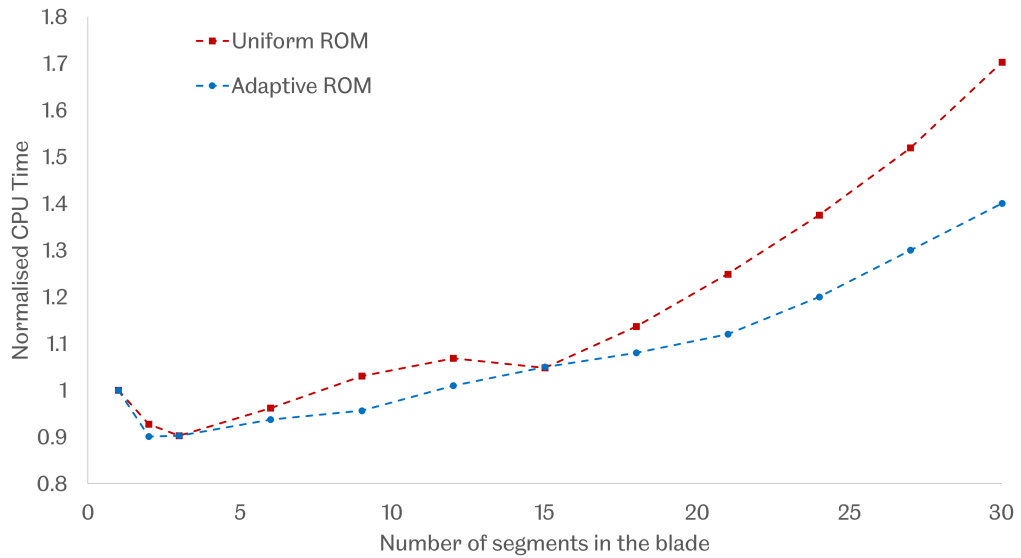


Figure 7.21: The total normalised CPU time cost of the proposed uniform and adaptive ROM.

7.5 Conclusion

In this chapter the novel ROM method is applied to the case of the 3D FSI simulation for a HAWT. The conceptual NREL 5-MW reference offshore wind turbine [90] is used as the geometry for the simulations. The proposed method solves the case of a deforming solid body by considering the deformation as a cumulation of a series of rigid segments. During the simulation, the tower, nacelle and hub are considered as rigid bodies, while the turbine blades are assumed flexible. Convergence studies are performed prior to the Reduced Order Modelling process. Multiple input parameters, including the time step and number of meshes of the full order baseline FSI simulation, and the number rigid segmentations on each turbine blade are investigated prior to the simulation. During the simulations, multiple instances are selected in the range of wind speed between 3 m/s and 25 m/s, while the NREL 5MW wind turbine is operating at the corresponding operational velocity. In this chapter, the turbine blade is modelled from one segment up to 30 uniformly distributed rigid segments. Two representable cases, 6 and 30 segments, are represented in order here to show the impact of the number of segments on the overall calculation accuracy and efficiency. Corresponding stiffness matrix and kinematics are then calculated for the ROM. The proposed method is applied on two working conditions selected between the cut-in speed and the cut-out speed, both at constant rotational speed. The simulation case with constant rotor speed of 9 RPM at

wind speed of 8 m/s to serve as the basic and simplest validation case in OC3 project. For wind speeds less than the rated wind speed of 11.4 m/s, rotor speed is selected as of 12.1 RPM. Reconstructed ROM solutions, including blade deformation and power output, via the proposed methodology are compared to the corresponding full order CFD results as well as experimental data when it is approachable. In addition, the author has performed a stability analysis of the HAWT of the topic via the proposed ROM methodology for deformable FSI interfaces. For each case, error estimations and time analyses are compared to the corresponding full-order CFD solution. Both the ROM results show a relatively good agreement with the CFD solution regarding the velocity and blade tip deformations. The 30-segment ROM solution shows an overall better computational accuracy than the 6-segment ROM solution while the computational deficiency slightly undermines the efficiency due to the increase in the governing matrices. In terms of the locally refined ROM methodology, both solutions present a better capability and accuracy compared to the traditional uniform ROM method. Although this method is slightly computationally inefficient due to its algorithm, this sacrifice in the computational cost due to the self-adaptive spatial discretisation is acceptable compared to the scale of the full order models. In addition, the capability of the local refined method, refer to Chapter 5, has been validated on a 3D complicated and time consuming simulation of a HAWT.

Chapter 8

3D ROM FSI Simulation of the 1.2kW Windspire VAWT

8.1 Introduction

In Chapters 4 - 6, the locally refined ROM approach to solve FSI problems is presented, and the validity of the resulting deformation and dynamics are reasonably confirmed in the cases of rigid and flexible bodies. In addition, the multiple locally refined ROM approaches to solve FSI problems were presented, and the validity of the resulting deformation and dynamics were confirmed in the cases of both rigid and flexible bodies. In this chapter an application of the above outlined methods is performed with a Vertical Axis Wind Turbine in various 3D simulation settings focusing on aerodynamic and aeroelastic behaviours.

8.2 Fluid-Structure Interaction of the VAWT

8.2.1 The Vertical Axis Wind Turbine employed

The computations in this section are performed for a 1.2kW Windspire design [187], as shown in Figure 8.1 and the total height of the VAWT tower is 9.0 metre and the rotor height is 6.0 metre. The rotor uses the DU06W200 aerofoil profile with the chord length of 0.127 metre (shown in Figure 8.7) and is of the Darrieus type with straight vertical blade sections attached to the main shaft with six horizontal struts.

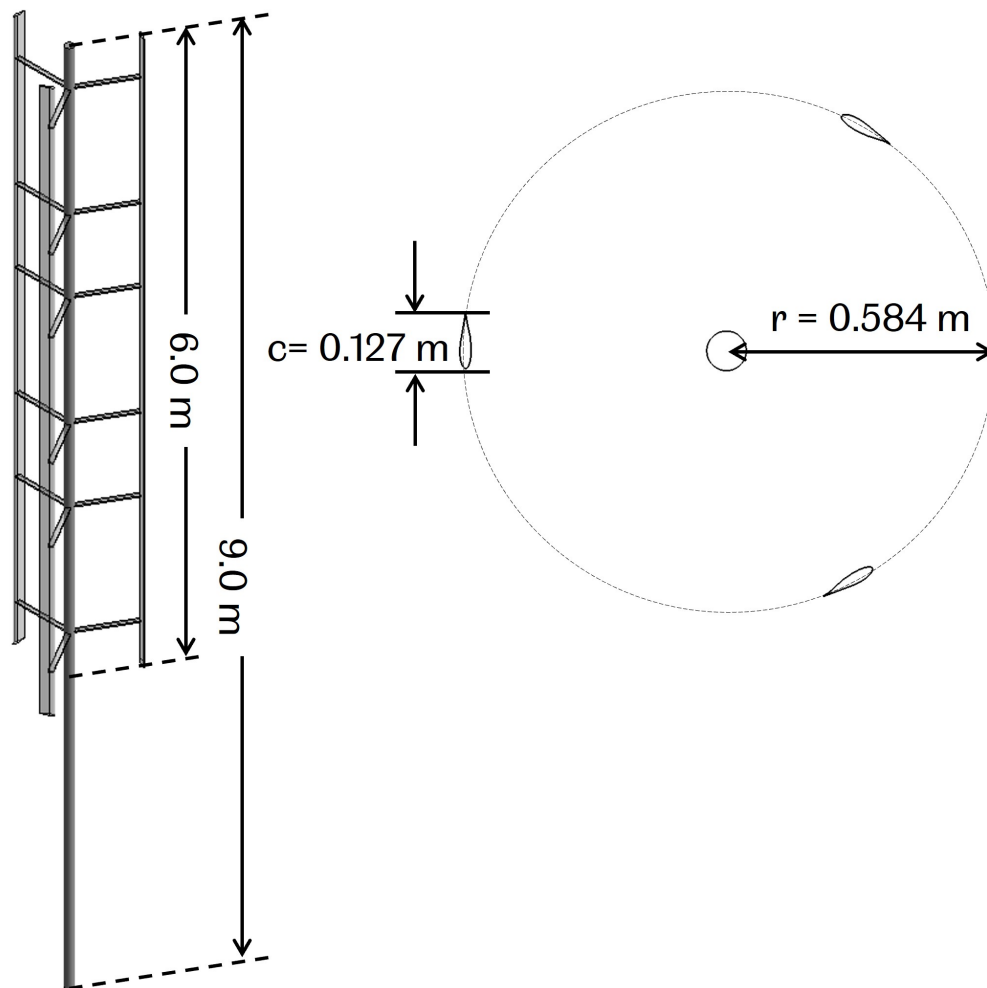


Figure 8.1: Geometry description of the 1.2 kW Windspire VAWT.

The blades and struts are made of aluminium, and the tower is made of steel. Pivotal structural properties, thickness t , radius r , Young's modulus E , Poisson's ratio ν , density ρ and mass m , are summarised in Table 8.1. In this chapter, the tower is assumed to be rigid, and the deformation of the other parts of the turbine is investigated during the FSI simulations.

Table 8.1: Geometric and material properties of the 1.2kW Windspire VAWT

Part	t [mm]	r [mm]	E [GPa]	ν	ρ [kg/m^3]	m [kg]
Blades	2	/	70	0.35	2700	26.3
Strut	12.7	/	70	0.35	2700	14.1
Tower	/	44.5	210	0.33	78	243.4

8.2.2 Computational Settings

Figure 8.2 shows the computational domain for the 3D CFD simulations. The computational domain consists of the grids defining the Windspire VAWT, including the geometrical representation of the blades, struts and tower as documented in [177, 49]. A $50m \times 20m \times 30m$ box grid is used for the present flow around the Windspire VAWT. Similar to Bazilevs' work [24], 15 metres separate the VAWT centre from the inlet and 35 m from the outlet boundaries. The rotor is contained within an inner cylindrical domain with dimensions of 1.6 metres on its radius and 7 metres on its height. At the inflow, a wind velocity profile that is uniform over its entirety is specified. No penetration boundary constraints are imposed on the top, bottom, and side surfaces of the outer domain, while zero traction boundary conditions are established at the outflow. These boundary conditions are in place. Studies of mesh and time size sensitivity are carried out in order to ascertain the suitable cell face and time step. The time-step is set at 1.0×10^{-5} s for the aerodynamics computation and 2.0×10^{-5} s for the FSI analysis.

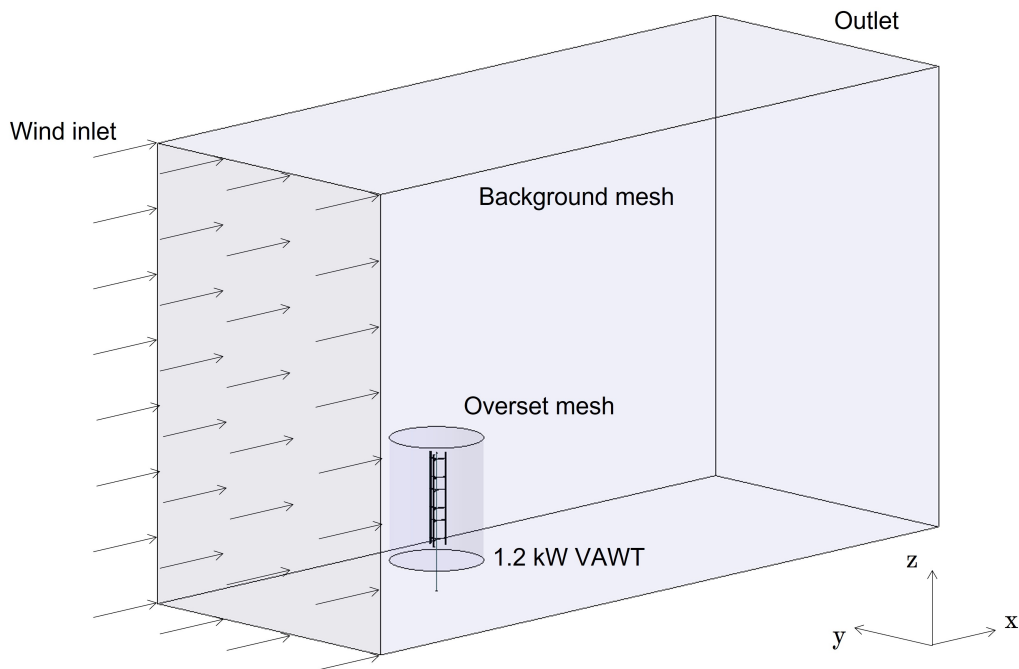


Figure 8.2: Computational domain of the Windspire 1.2kW VAWT for the 3D FSI simulations.

Apart from the moving overset meshes representing the VAWT, a stationary background grid is used to set for boundary conditions. The background grid extends $-15m \leq x \leq 35m$, $-10m \leq y \leq 10m$, and $0 \leq z \leq 30m$ with the centre of the turbine located at the origin $(0, 0, 0)$ in order to minimise the boundary effects. With this

configuration, the presence of the turbine does not significantly disturb the inlet flow. Three refinement regions are used in the vicinity of the blade to accurately capture the flow around the blades as illustrated in Figure 8.3, and one region is constructed to resolve the wake flow close to and behind the rotor. The boundary conditions on the solid surfaces are set as no-slip, with the grid spacing set so that the condition $y^+ \leq 1$ is satisfied as required by the turbulence model. Before moving on to the transient simulation, stable simulations of each instance are first calculated. It is important to note that the fixed tower and support platform are taken into consideration in this thesis. As a consequence, there is a non-slip boundary at the free surface of the backdrop grid. In this chapter, we impose the free surface as an immersed boundary using the technique that is given in [83]. There will be no roughness or wall functions applied.

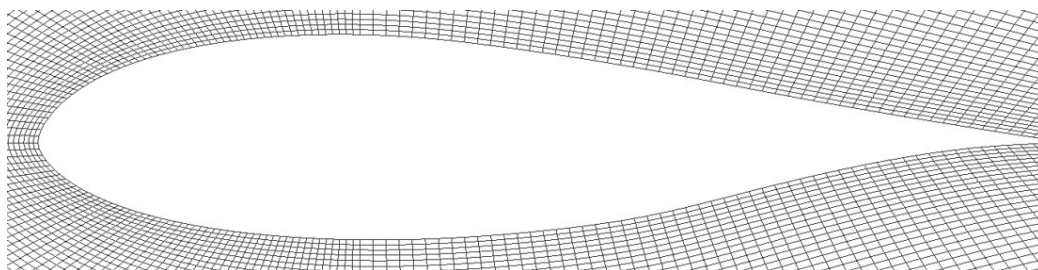


Figure 8.3: 2D cross section of the blade profile and boundary layer overset mesh.

The computational domain consists of 13 regions, organised in a parent/child hierarchy, as shown in Figure 8.4 and 8.5, has around 6 million meshes. The blades, struts and the blade refinements together form the body rotor overset mesh that rotates around the tower. Only the overset region meshes are moving during the simulations, therefore this reduces the overall computational cost. The dynamic overset technique is applied to recompute the overset meshing at the run times. With this approach, the full control or prediction of the turbine can be realised with the varying rotational speed, pitch control, and deformation of the turbine blades. A second-order implicit Euler method was utilised for all of the simulations that are discussed in this chapter in order to calculate the temporal terms. When it comes to the spatial discretization, the convective terms are handled with a scheme that has a fourth-order upwind bias, while the viscous terms are handled with a scheme that has a second-order centred base. Each simulation instance includes a total of 20 rotor spins and the time step was selected in such a way that the blades rotate 0.5 degrees every time step.

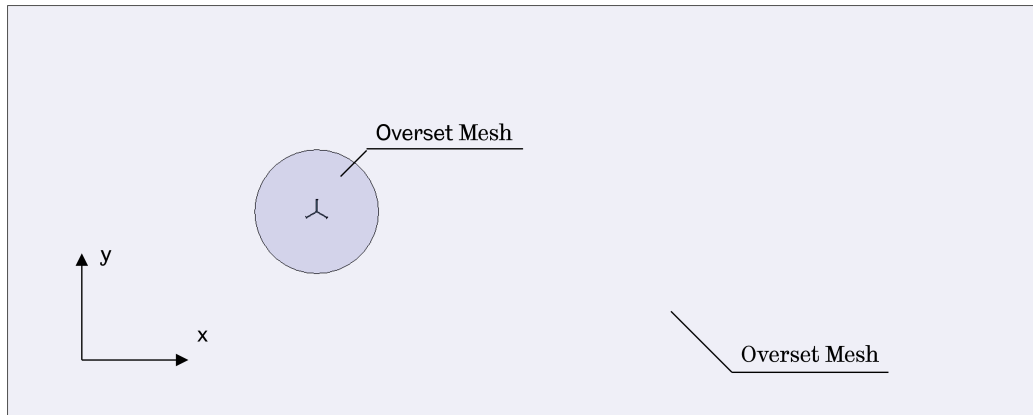


Figure 8.4: Mesh region hierarchy of the Windspire 1.2kW VAWT for the 3D FSI simulations.

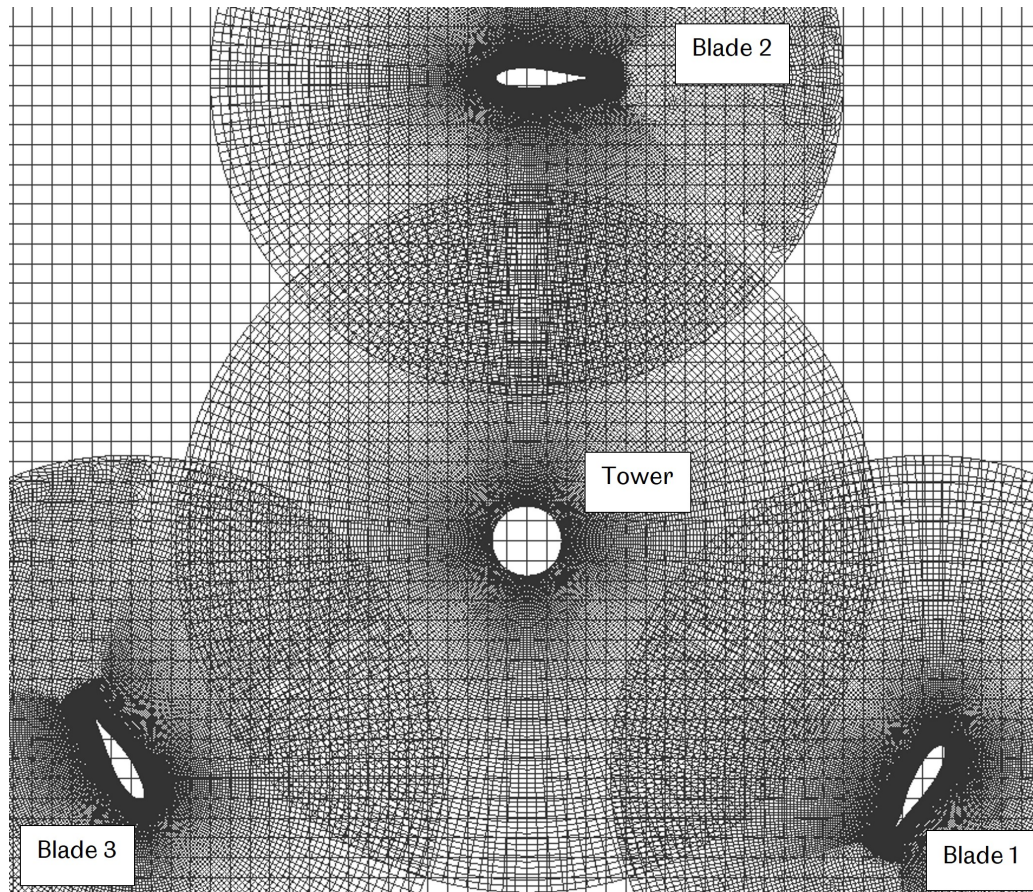


Figure 8.5: 2D cross section of the computational mesh along the rotor axis and 4 overset mesh regions have been applied on the background mesh.

Beam models are used to depict the VAWT struts and main shaft, whereas shells are used to model the VAWT blades and the portion of the tower that rotates with the rotor.

The blades, tower shell, and main shaft are all connected to the struts, which results in a reasonably straightforward structural model for the VAWT. This model is able to simulate the three-dimensional mechanics of a spinning flexible rotor that is installed on a flexible tower. The density of the tower shell is purposefully reduced to a relatively low value in order to ensure that the vast majority of the tower's mass is dispersed uniformly along the beam. The beam and shell discretisations are both accomplished with the use of quadratic NURBS.

The field-test tests that were carried out by the National Renewable Energy Laboratory and the Caltech Field Laboratory for Optimized Wind Energy revealed realistic operating conditions, which are used in the aerodynamics and FSI simulations [84]. For all the cases investigated, the air density and viscosity are set to 1.23 kg/m^3 and $17.8 \times 10^{-5} \text{ kg/ms}$, respectively.

The *k-omega* SST model is utilised as the turbulence model, and the transport equations for the SST model that are utilised to compute the turbulent kinetic energy *k* and the specific dissipation rate *omega* are those that are utilised in ANSYS FLUENT. This two-equation model is excellent for modelling the boundary layers as well as the far field flows, and as a consequence, it has been utilised widely in research involving wind turbine blades and aeroelastic issues with satisfactory results [80, 75]. The aerodynamics and FSI simulations compared to [24] are carried out at realistic operating conditions reported in the field-test experiments conducted by the NREL and Caltech Field Laboratory for Optimized Wind Energy [177, 49].

The structural properties of each component including mass, density, Poisson's ratio, and stiffness, are summarised in Table 8.2. The construction of the model follows the structural information specified in the literature [24], the structural model of the turbine consists of 6 components: 3 blades, struts, and tower. Detailed structural modelling of Windspire VAWT is represented in Figure 8.6. Because the struts are assumed to be rigid, beam force elements are used in the simulations of flexible turbines in place of links. Because of this, there are six degrees of freedom available for both the body and the tower. The following kinetic joints or restrictions are imposed so that a kinematic description of the interaction between the various components of the turbine may be provided: A bracket joint is used at each interface of the blade and strut, which limits the relative motions between the components; a revolute joint is used between the hub and nacelle along the rotational axis of the rotor to allow the rotor rotation, and this constrains the other degrees of freedom; similarly, another revolute joint is used at the interface of the nacelle and tower for the yaw motion; and finally, a bracket joint is used at each interface

of the blade We are going to make the assumption that the lay-up of the entire blade is the same for the purpose of convenience.

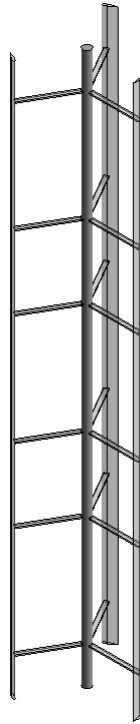


Figure 8.6: Structural modelling of the 1.2 kW Windspire VAWT.

Table 8.2: Structural properties of the 1.2kW Windspire VAWT.

Part	E [GPa]	ν	ρ [kg/m^3]	m [kg]
Blades	70	0.35	2700	26.3
Strut	70	0.35	2700	14.1
Tower	70	0.33	78	243.4

The Windspire 1.2kW wind turbine is a three-bladed vertical axis wind turbine. Each turbine blade is 6 metre long, the cross-section profile of the blade used in the turbine is illustrated in Figure 8.7. The distributed blade structural properties of each NREL 5-MW wind turbine blade, including the torsional and extensional stiffnesses, are illustrated in Table 8.1 and 8.2. The turbine blade is modelled as a flexible body using equivalent structural properties as per the definition of [67].

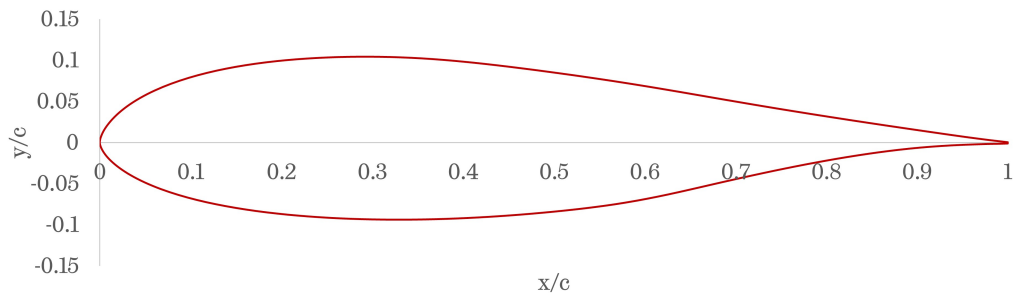


Figure 8.7: Cross sectional aerofoil profile of the 1.2kW Windspire VAWT DU06W200 blade profile.

Mesh and time size sensitivity studies are carried out to determine the appropriate cell face and time steps. Five different mesh sizes are investigated, i.e., 8 mm, 4mm, 2 mm, 1 mm, and 0.5 mm, and the associated total number of elements and calculated oscillation amplitudes are presented in Figure 8.8. It is found that the amplitude may be considered to be accurate at a mesh size of 1 mm and a further refining mesh size obtain only a 5.4% relative difference.

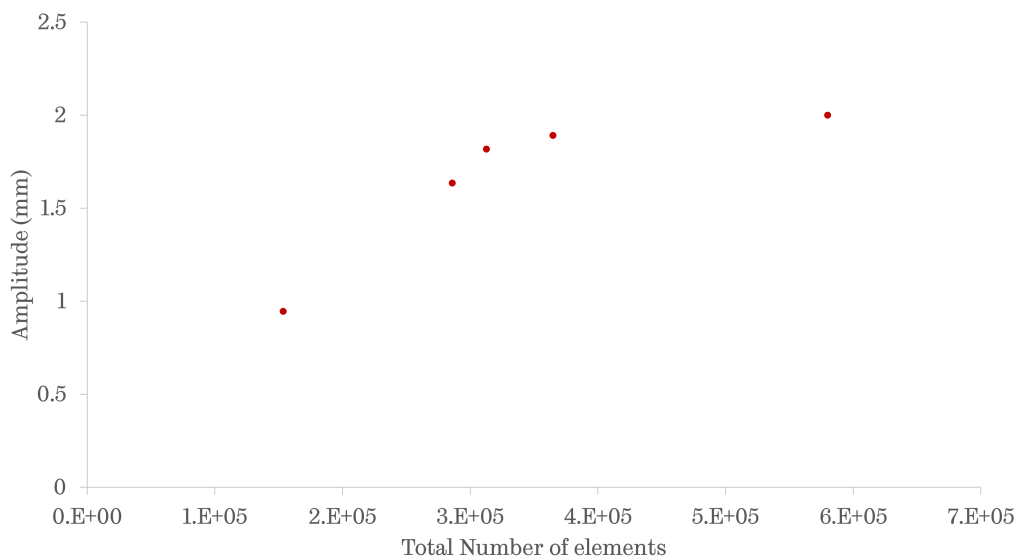


Figure 8.8: Mesh convergence study of the flow-induced vibration of an oscillating cylinder.

In the case of the time size sensitivity study, five time steps are investigated, i.e., 1×10^{-5} seconds, 1×10^{-4} seconds, 2×10^{-4} seconds, 5×10^{-4} seconds, and 1×10^{-3} seconds. The associated total number of elements and oscillation frequencies are presented in Figure 8.9 and the amplitude converges at a time size of 1×10^{-4} seconds.

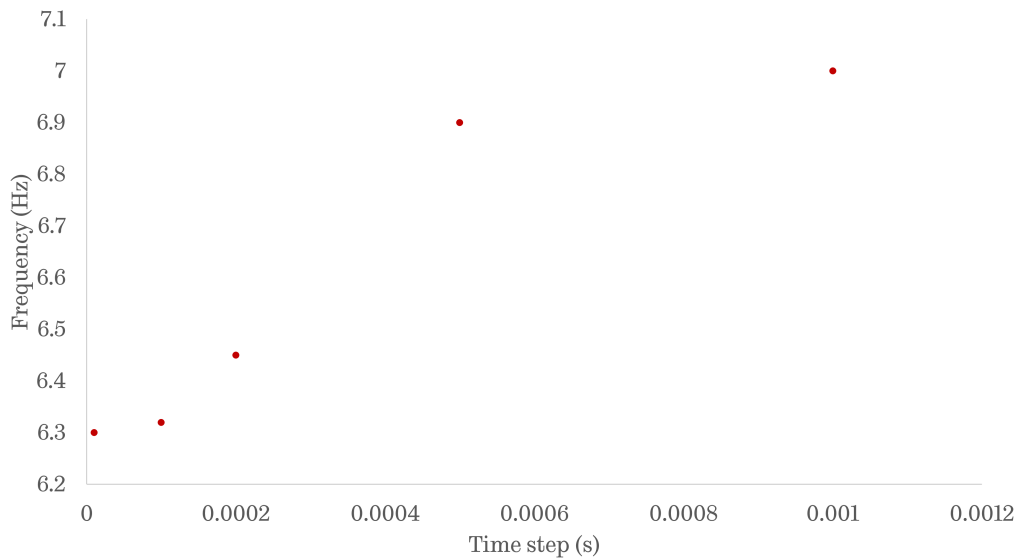


Figure 8.9: Time step convergence study of the flow-induced vibration of an oscillating cylinder.

Considering the computational time and accuracy, the mesh size of 1 mm and the time size of 1×10^{-4} seconds are deemed as the appropriate mesh size and time size for the modelling in this study. The fluidic model consists of 158,610 nodes and 579,632 elements while the structural part consists of 2595 nodes and 2422 elements. The time-step size is 1×10^{-4} seconds and the number of nonlinear iterations per time step is 500. A loose coupling strategy was applied to couple both the fluidic and structural domains. The test cases were chosen from the publicly available results. Two different test cases are performed in this chapter, both at constant rotational speed, one of constant rotor speed of 8 m/s and another at a constant rotor speed 6 m/s. The baseline full-order CFD simulations results are compared to the reference simulation prior to the reduced order modelling.

Table 8.3 summarised a comparison snapshot between the baseline CFD simulation and the results from the OC3 project. Here one typical aerodynamic parameters, averaged torque, is compared between the proposed CFD solution and the OC3 report. The difference in two case is all no larger than 6%, therefore in this project, the CFD solution is considered accurate.

Table 8.3: Comparison between the Windspire VAWT FSI simulation and the referenced codes at various speeds.

	Current Simulation	Referenced
Averaged torque [kNm] @ 6m/s	69 (+4.54%)	66
Averaged torque [kNm] @ 8m/s	95 (+5.55%)	90

8.3 Reduced Order Modelling

The refined ROM methodology (see Chapter 6) has been implemented into the simulation. The computational domain for the ROM is identical to the those for the FSI simulation with an initial uniform ROM mesh at $N_x \times N_y \times N_z = 50 \times 20 \times 30$, as shown in Figure 8.10. Mesh and time size sensitivity studies are carried out to determine the appropriate cell face and time step. 200 snapshots over 4 periods are used to build the ROM, nacelle, hub and tower that are assumed to be rigid, and therefore only the deformation of the blades is considered in this chapter. Each Windspire VAWT blade is modelled as a combination of up to 12 rigid segments. Two iterations of the ROM mesh refinement are implemented in this application, please refer to Chapter 4, as shown in Figure 8.11. The threshold is set as the difference within each sub-grid is no larger than 0.05% of the maximum velocity difference of the overall domain.

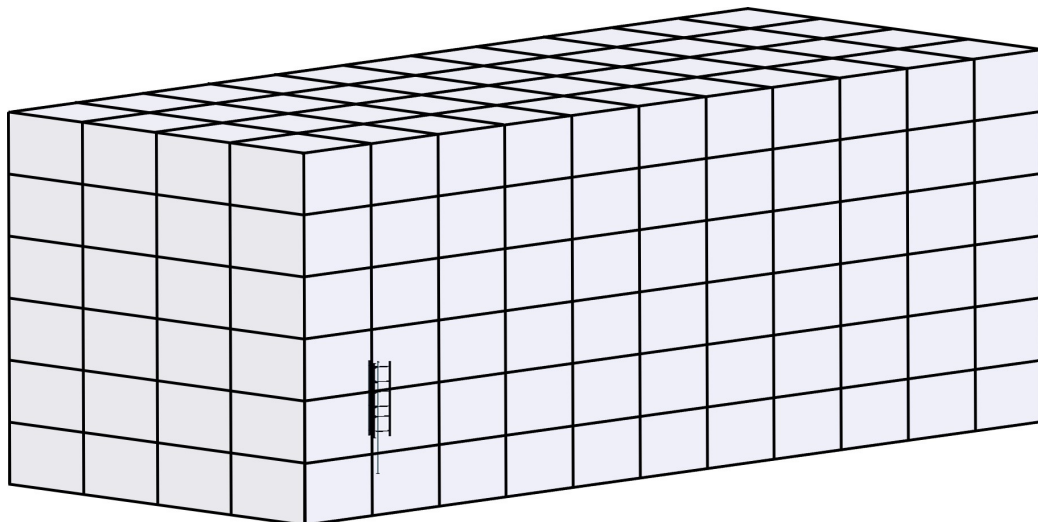


Figure 8.10: Initial uniform ROM mesh of the 3D computational domain for Windspire VAWT FSI simulation. Each grid represents a $5 \times 5 \times 5$ mesh grids in ROM calculation.

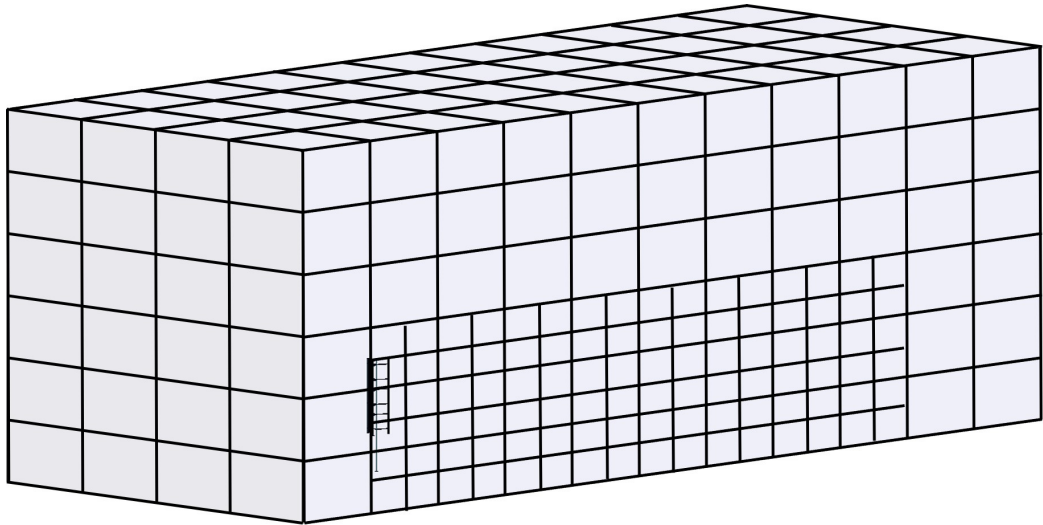


Figure 8.11: Illustrative demonstration of the ROM refined mesh of the 3D computational domain for the VAWT FSI simulation.

Recalling that the Lagrangian multipliers are introduced in the proposed reduced order modelling approach to treat the moving and/or deforming solid domain as a fluid. In addition, the introduced multiplier is compatible with the locally refinement strategy. Figure 8.12 and Figure 8.13 show the Lagrangian multiplier of two refined mesh iterations, where the blue dots represents the solid parts in the FSI simulation, please refer to Chapter 6. The POD-Galerkin ROM approach is capable to predict the moving of solid domain more accurately with 2 refinement iterations.

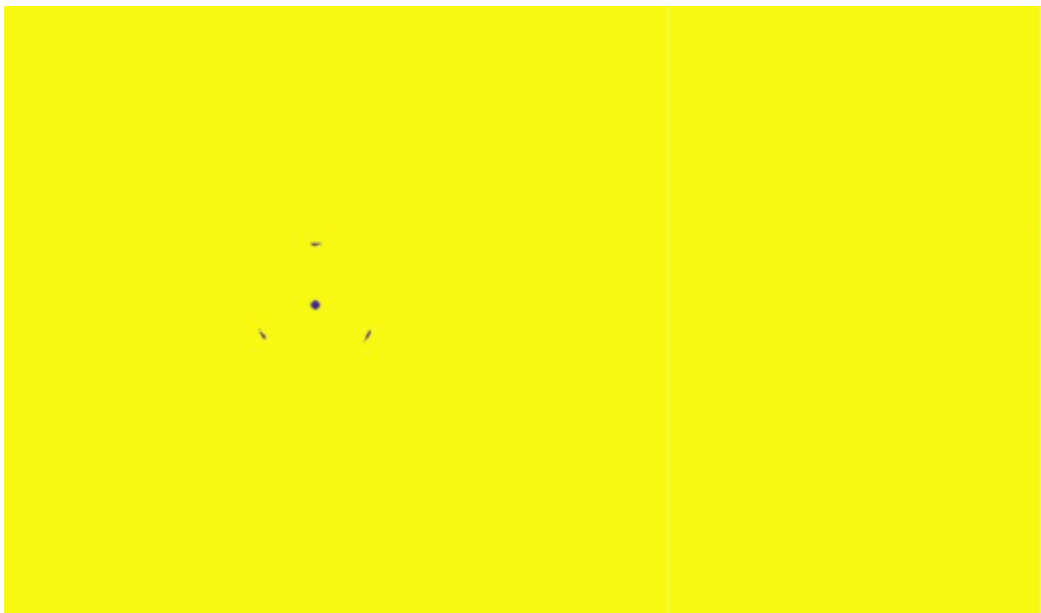


Figure 8.12: ROM grids of the initial reduced order modelling grid.

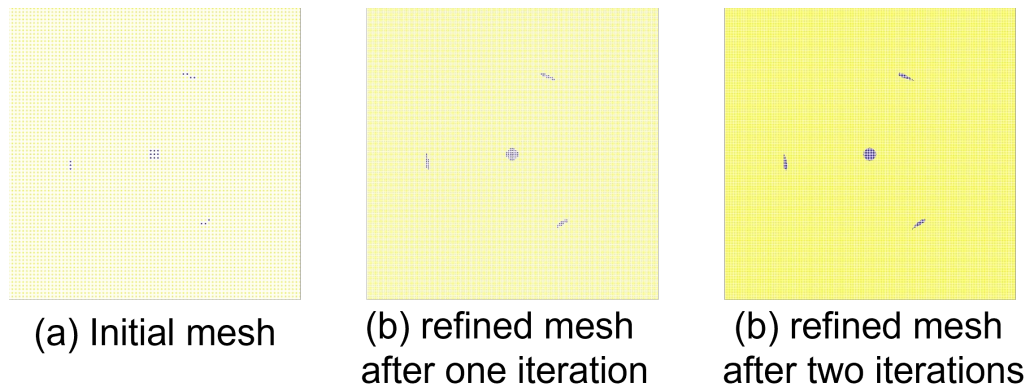


Figure 8.13: Lagrangian multiplier of two refined ROM mesh iterations on XY-plane around the rotor: (a) initial meshes, (b) refined after 1 iteration, (c) refined after 2 iterations.

In the course of the full-system stability assessments, it is assumed that the nacelle, hub, and tower all have a stiff structure. As can be seen in Figure 8.14, each HAWT blade is modelled as a series of discrete stiff segments linked together. The number of finite element segments that were utilised in the construction of the VAWT model is presented in Table 8.4. The number of rigid segments in the model affects the problem size because it changes the number of generalised coordinates and constraints in the governing equations; for more information, please refer to Chapter 5. In every instance that was looked into, the blades were the primary factor in determining the size of the problem. owing to the fact that the number of bodies included in any blade type ranges anywhere from 1 to 30. The 30-segment blade model is the most exact and has the maximum number of restrictions, whereas the scenario in which there is only one segment is known as the linear blade case. In spite of the fact that the magnitude of the issue in the equations shifts depending on the number of entities that are described in the model, the total number of independent constraints remains unaltered for this specific turbine model.

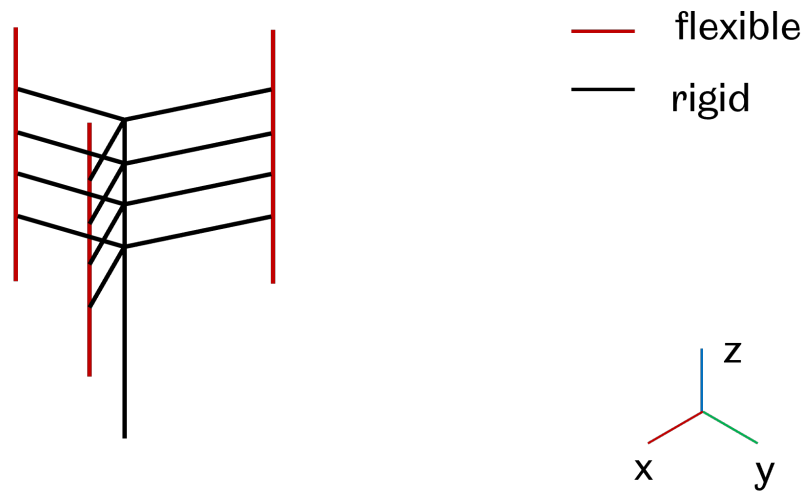


Figure 8.14: Finite element segment modelling of the WindSpire VAWT. blue and black bodies represent that they are modelled as flexible and rigid bodies, respectively.

Table 8.4: Number of rigid segments used in the wind turbine model.

Number of rigid segments of each blade	Sum of rigid segments of the NREL 5-MW wind turbine	Number of equation of constraints
1	7	42
2	10	60
3	13	78
6	22	132
9	31	186
12	40	240

Figure 8.15 shows the energy spectrum of the POD modes used for the simulation at a wind speed 8m/s. 200 snapshots over 4 periods are used to build the ROM, and the VAWT is modelled as a system of 30 rigid bodies. Figure 8.16 summarises the first six POD modes of the VAWT working at 6.0 m/s. These six dominant modes cover more than 99.9% of the total kinematic energy, and are selected to perform the following calculation. The Galerkin integration is obtained by substituting equation (3.33) onto the first six POD modes.

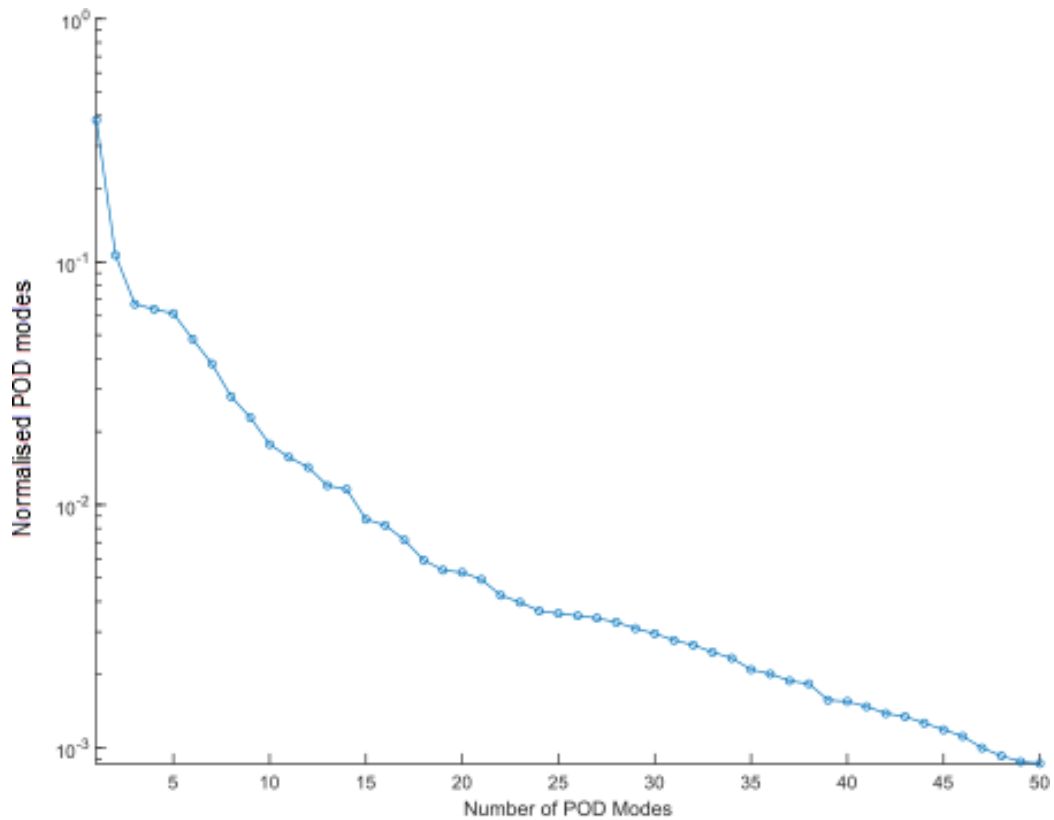


Figure 8.15: Energy spectrum of the POD modes for the Windspire VAWT working at a speed 8m/s.

400 snapshots over 4 periods are used to build the ROM, and the VAWT is modelled as a system of 40 rigid bodies, each blade consists of 12 rigid segments, and the struts and tower are assumed to be rigid, as shown in Figure 8.6. Two different aerodynamic simulations of the Windspire VAWT are performed, one using the wind speed of 8.0 m/s and rotor speed of 32.7 rad/s, and another using the wind speed of 6.0 m/s and rotor speed of 20.6 rad/s. For both cases, the time history of the torque as well as the averaged value computed from the ROM are compared to the corresponding experimental data [49] and numerical [24] results.

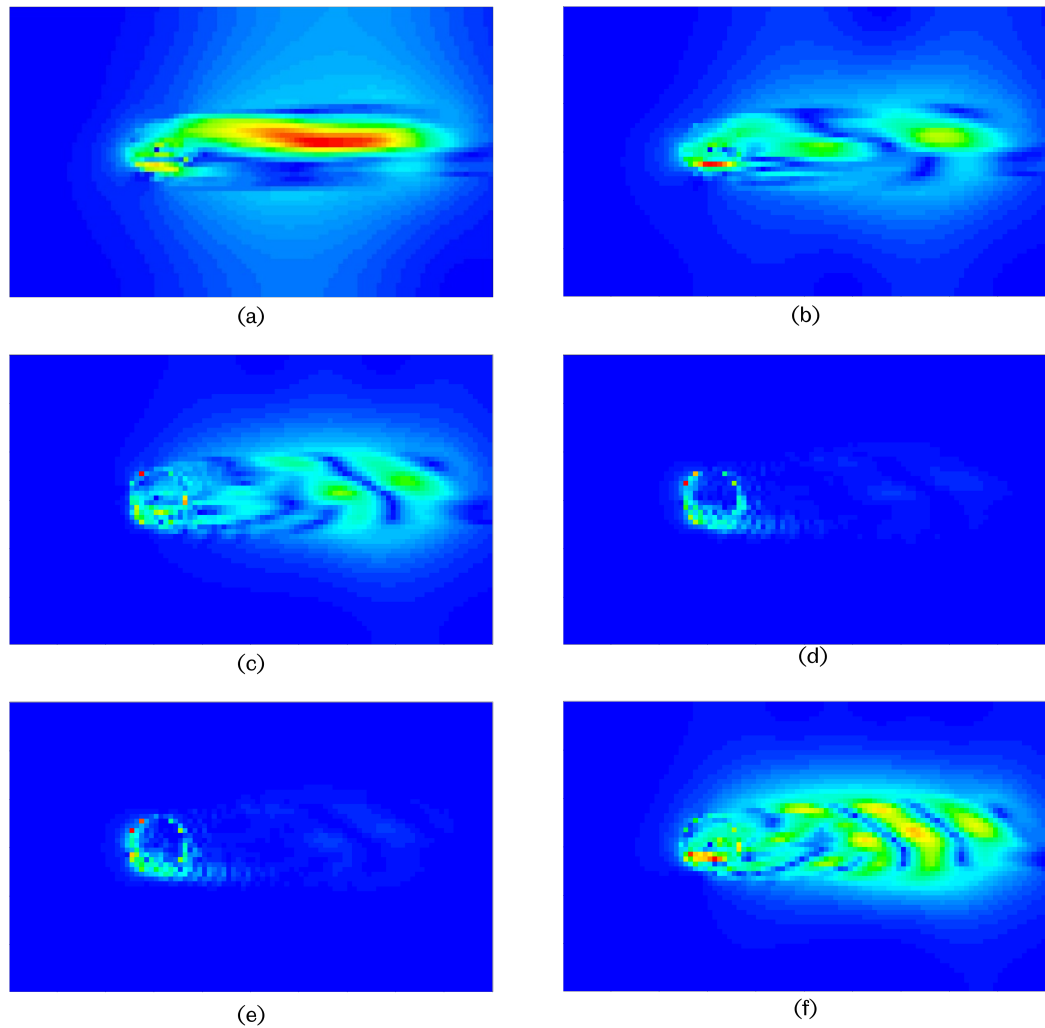


Figure 8.16: First six POD modes of the Windspire VAWT FSI Simulation at 6.0 m/s and rotor speed of 20.6 rad/s (X-Y view).

8.4 Results

8.4.1 Convergence analysis

A convergence analysis was performed with the steady wind load cases to determine the number of modes to be used in the proposed reduced order model methodology and to observe the effects of the large deflections on the projection residual. Figure 8.17 shows how the error of the Windspire VAWT blade projection residual varies with the number of finite element segments of each blade. The linear and nonlinear blade models in the solver are used to calculate the blade deflections, and then those deflections are projected onto the basis with the mode shapes at the starting (undeformed) blade

position. The steady wind load is less than 8 metres per second. Therefore, the inaccuracy in the full-order CFD and the suggested ROM blade model deflections may be used to evaluate the influence of the geometric nonlinearities on the segments. The linear blade model generates nine times higher projection residual than the geometric nonlinear effects that are caused by massive blade displacements, as seen in figure 8.17. When substantial blade displacements are taken into consideration, this suggests that geometric nonlinearities are the primary cause of the projection residuals. The linear model's origin comes from a two-fold place. In addition to the geometric nonlinearity that may be caused by things like inertia and force, the nonlinear effects can also be a source of the linear model's residuals. The fidelity mismatch between the numerical model and the reduced order model is still another source of the linear model residuals. The reduced order model has 156 degrees of freedom (DOF) for the NREL 5MW wind turbine blade and projection space with 20 modes. On the other hand, when compared to the entire deflection of the linear blade model, the total residual of all of the nodes is rather insignificant. The first two modes are, in order, the first flapwise mode, followed by the first edgewise mode. The eighth mode is the first mode that involves torsion, while mode 16 is the first mode that involves axial rotation.

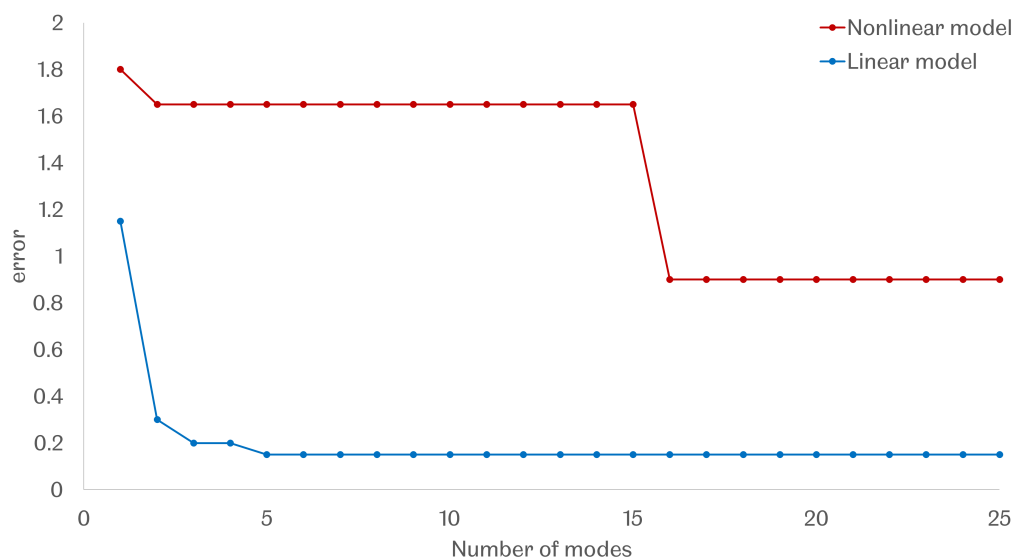


Figure 8.17: The error of the Windsprite VAWT blade projection residuals with respect to the number of modes. The blade deflections are compared to the full-order CFD at 8 m/s steady wind speed and the projection basis is composed of undeflected blade mode shapes.

8.4.2 Deformations

Figure 8.18 shows the bending displacement contour under constant inlet velocity 8.0 m/s and 6.0 m/s conditions at four evenly distributed snapshots during one cycle. It is apparent that a large deflection occurs in the vicinity of the free ends of the blade. However, the bending displacement in the middle region of the blade is around zero as there are several additional struts in this particular VAWT model. For both cases, the central part of the blade has the minimum deformation as this part of the blade is supported by struts, and this trend has been validated at all instantaneous time snapshots during one cycle. In addition, an increase in the tip speed ratio leads to an increased deformation as shown in Figure 8.18 and the ROM codes overestimate the deformation compared to the full-order numerical results. This is due to the assumption of the modelling of the flexible blades as a chain of a small number of rigid bodies. This has been validated by a further investigation on the impact of the number of rigid bodies, as the number increases, the rigidity behaviour is closer to that of the actual flexible body.

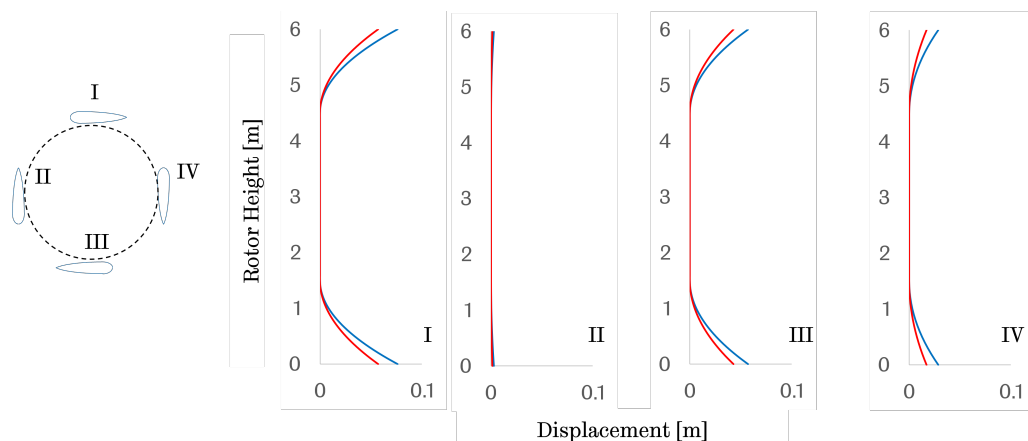


Figure 8.18: Time history of the blade bending displacement on one VAWT blade at different time snapshots during one operating period, inlet velocity 8.0 m/s (blue) and 6.0 m/s (red).

8.4.3 Aerodynamic Simulations

Figure 8.19 summarises the difference between the reconstructed ROM solution and the corresponding full-order computational results after each refined iteration. The blue region indicates the minimum difference. As shown in Figure 8.19, the pure aerodynamic ROM computation produced good agreement with the field-test data for the Windspire VAWT, despite the ROM results slightly overestimating the averaged torque. In addition,

the proposed refined strategy successfully improves the accuracy of the rebuild ROM solution. For the FSI ROM simulation (shown in Figure 8.24), the rotor naturally accelerates at a lower rotational rate for both the 0 rad/s and 4 rad/s cases. For the 4 rad/s cases, the plateau regions are accurately predicted. This is verified by the field test and the articles that focus on the FSI on VAWT. Compared to the experimental data, both the ROM and CFD simulations overestimate the torque and rotational rate on the aerodynamic and FSI simulations. In both cases, the experimental value of the aerodynamic torque is derived from the average power produced by the turbine at the target rotor speed.

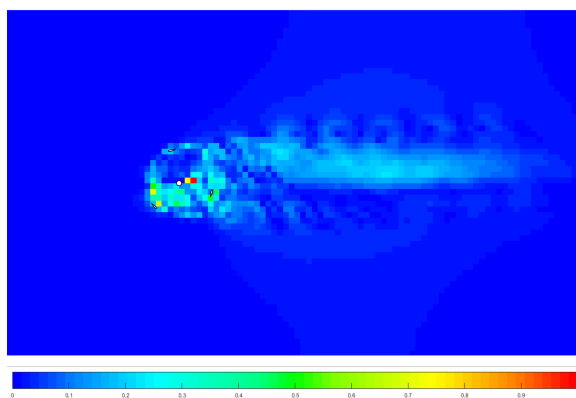


Figure 8.19: Error between the referenced CFD solution and the proposed ROM solution.

To further show the capacity of the model more clearly, the difference between the velocity flow field computed by the numerical approach and the rebuilt flow field from the ROM with a uniform grid, and the adaptive POD-Galerkin ROM models are presented. With this decomposed solid domain, the dynamics for this prescribed large solid motion problem and the corresponding adapted discretisation which have been shown in Figure 8.20. A comparison has been made between the CFD solution and the ROM solution via the initial mesh and the refined mesh after two iterations, please refer to Chapter 4. The mesh is quadrupled during each mesh refinement based on the partial differentiation of the velocity profile. The local refinement concentrates on the vicinity of the aerofoil as well as the wake region in order to minimise the velocity variance within reduced order modelling process, and it varies at different time steps. Corresponding velocity difference between the proposed reduced order model and the CFD solution is presented in Figure 8.21. The accuracy of the ROM has been improved during the adaptive refinement strategy. The accuracies of the adaptive reduced order models are preserved to be almost the same in comparison to the numerical solution after two iterations. In contrast, the reconstruct flow fields using the uniform ROM are not perfectly accurate due to the large motion of the aerofoil.

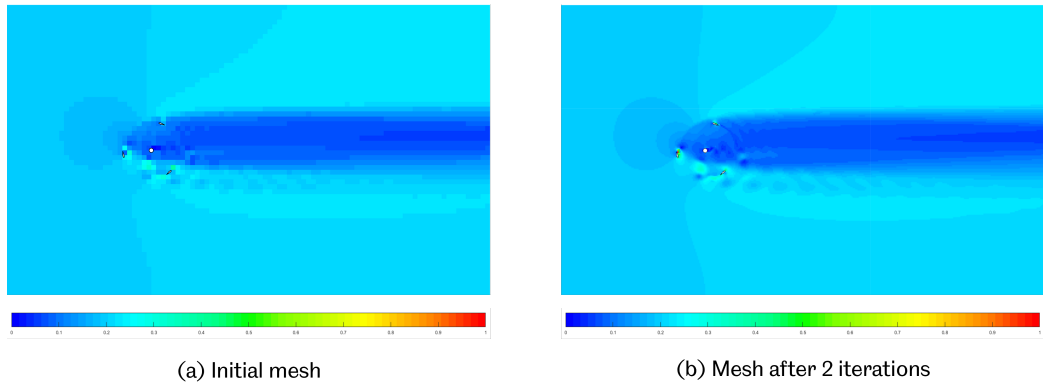


Figure 8.20: Rebuilt velocity flow field from the initial ROM mesh (a) and the mesh after two iterations (b).

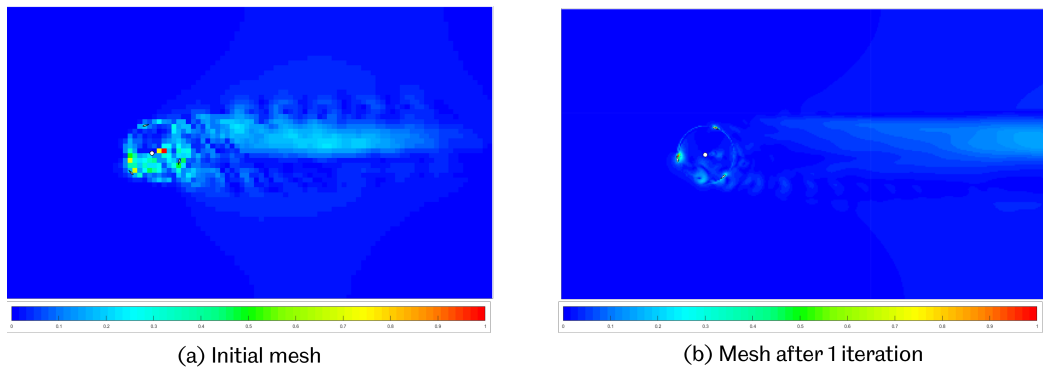
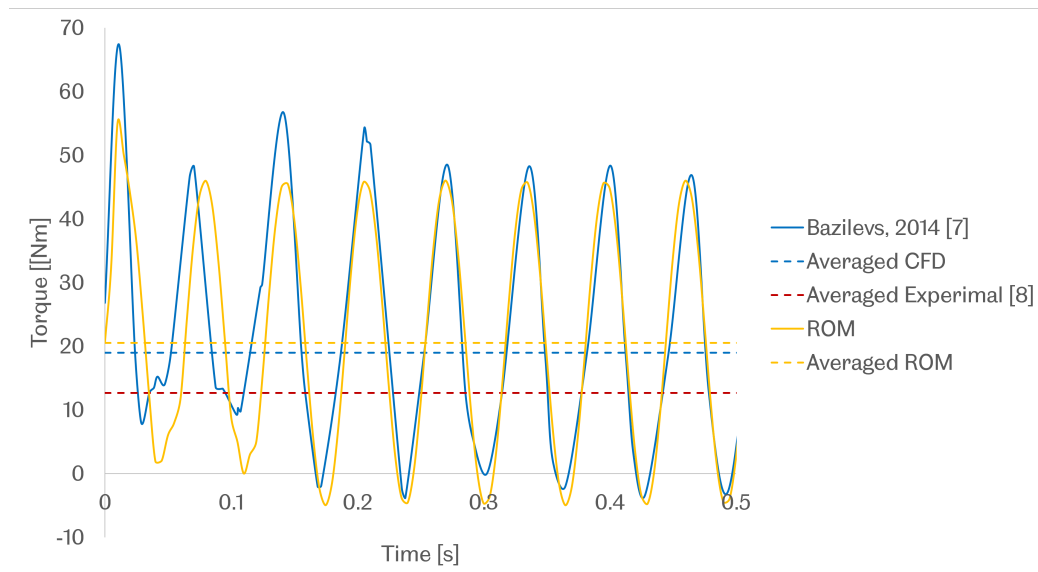
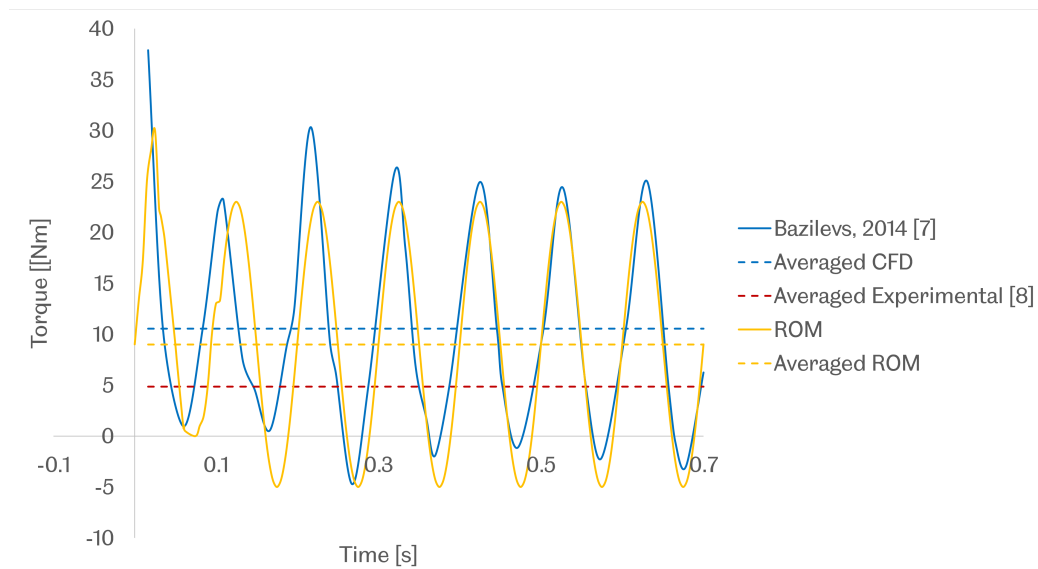


Figure 8.21: Velocity difference between the rebuilt ROM solution and FSI (a) initial ROM, (b) ROM after refined two iterations.

The first six dominating POD modes are selected to build the ROM code. These six dominant modes cover more than 99.9% of the total kinematic energy, and therefore are selected to perform the following calculations. The time history of the aerodynamics for both cases are plotted in Figure 8.22. The pure aerodynamic ROM computation shows good agreement with the CFD simulation, despite the ROM results slightly over-estimating the averaged torque. On the first few cycles, the ROM codes fail to show a consistent accuracy against the full-order solution. This may be due to it highly relying on the baseline model, and therefore cannot accurately predict the results when the full-order model is still fluctuating.



(a)



(b)

Figure 8.22: Time history of the aerodynamic torque for the aerodynamic simulations (a) 8.0 m/s; (b) 6.0 m/s.

The accuracy of the traditional ROMs can be improved by implementing the proposed locally refined strategy, please refer to Chapter 6. Figure 8.23 illustrates the time history of the reconstructed aerodynamic torque via the uniform ROM approach, and the adaptive ROM after two iterative refinements. The full-order CFD results are included as a benchmark case for comparison. The proposed methodology shows a good compatibility in the cases of the FSI problems with a deforming interface. The difference in the averaged aerodynamic torque over one cycle between the uniform ROM results and

the full order simulation is 38.39%, while those via the adaptive ROM methodology decreases to 16.48%.

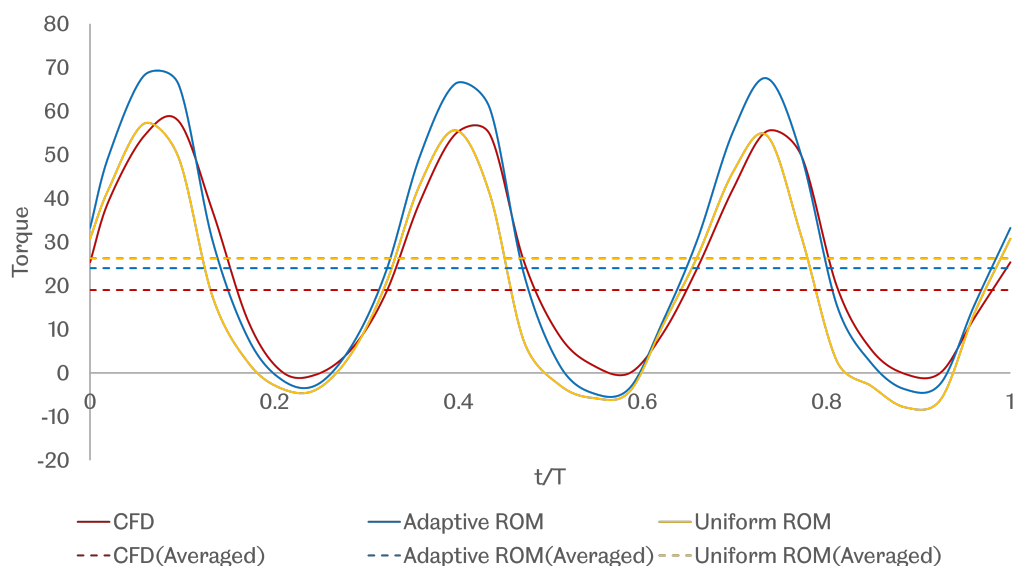
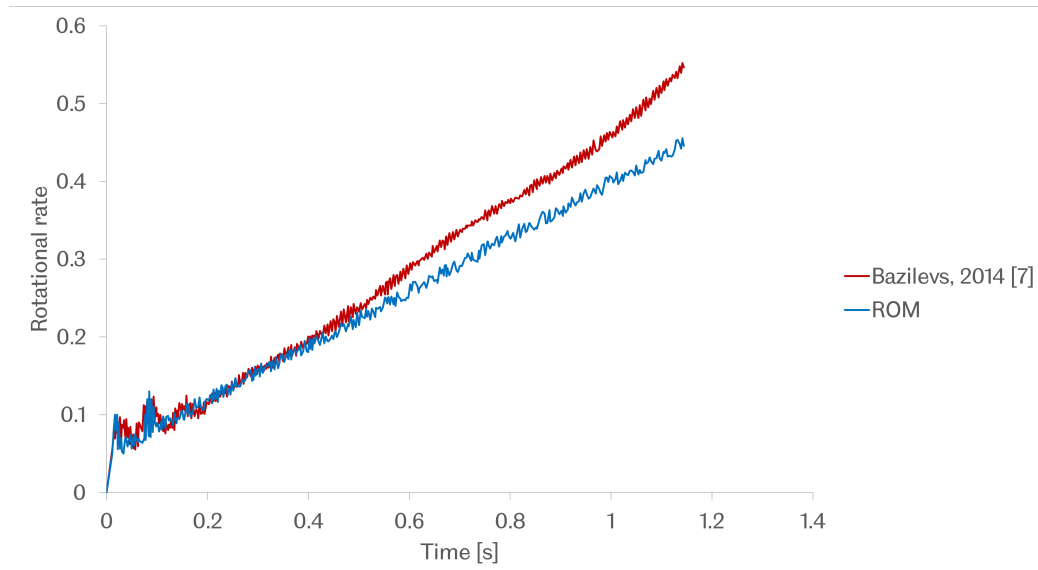


Figure 8.23: Time history of the aerodynamic torque of the Windspire VAWT working at 6.0 m/s via different reduced order modelling approaches.

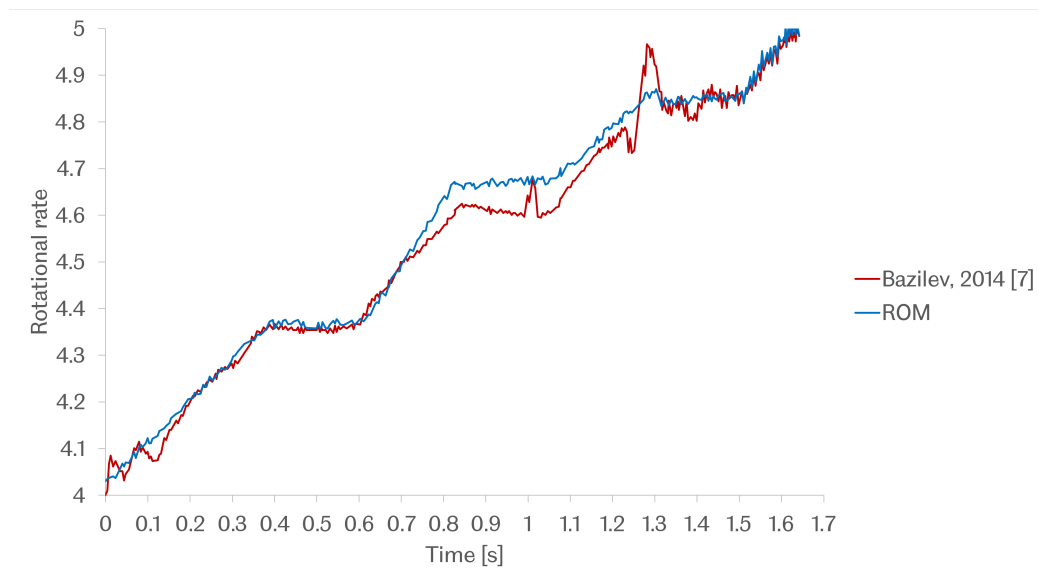
8.4.4 Self-starting behaviour simulation

An FSI investigation, particularly focused on the self-starting issues in the VAWT, is performed in this chapter. The inflow wind speed is fixed at 11.4 m/s, and we consider three initial rotor speeds: 0 rad/s and 4 rad/s. As shown in Figure 8.5, Blade 2 is placed parallel to the flow with the aerofoil leading edge facing the wind at the starting configuration of the Windspire VAWT FSI simulations. Blade 1 and 3 are placed at the the angle to the flow with the trailing edge facing the wind.

During the ROM simulation, as same as the aerodynamic modelling, the VAWT of interest is modelled as a combination of 30 rigid segments. The computational domain for the ROM is identical to the aerodynamical ROM, with an initial uniform mesh at $N_x \times N_y \times N_z = 50 \times 20 \times 30$, as shown in Figure 8.11. Two iterations of the ROM mesh refinement are implemented in this application to achieve more accurate results and to challenge the compatibility of the proposed refinement strategy (refer to Chapter 4). In the scenario when there is no radial acceleration, the rotor speed starts to grow, which suggests that this arrangement is preferable for self-starting. In the scenario with 4 rad/s, the rotor speed first goes through a zone of approximately linear acceleration, then it reaches a plateau area.



(a)



(b)

Figure 8.24: Time history of the rotor speed (a) starting from 0 rad/s; (b) starting from 4 rad/s.

Figure 8.24 shows a comparison of the rotation rate obtained from the reduced-order model to that obtained from the FSI simulations. In the scenario when there is no radial acceleration, the rotor speed starts to grow, which suggests that this arrangement is preferable for self-starting. In the scenario with 4 rad/s, the rotor speed first experiences an almost linear acceleration before reaching a plateau zone. The plateau zone is referred to as the regime in which the turbine runs at a rotational speed that is practically constant (i.e., similar to that of a steady state). It is clear, based on the angular position

of the blades, that the plateau area takes place at a frequency of around 120 degrees approximately whenever one of the blades is in a stopped state. It will continue until the blade clears the halted zone and the lift forces are sufficiently strong for the rotational speed to start growing again. This phase will persist till the end of the rotation. As the rotational speed continues to grow, the plateau area of the angular velocity is displaying signs of beginning to behave in an erratic manner locally.

The displacement of the turbine blades may be seen in Figure 8.25, which depicts the self-starting simulation. However, as a result of the rotor spinning motion, there are also observations of lateral tower displacements occurring at the same time. The majority of the movement occurs in the direction that the wind is blowing. The amplitude of the displacement is around 0.10–0.12 metres, which is likewise the case when the angular velocity is 0 rad/s. For both cases, the solution via the proposed reduced order model shows a good agreement in FSI simulations with the maximum difference of 5.24%.

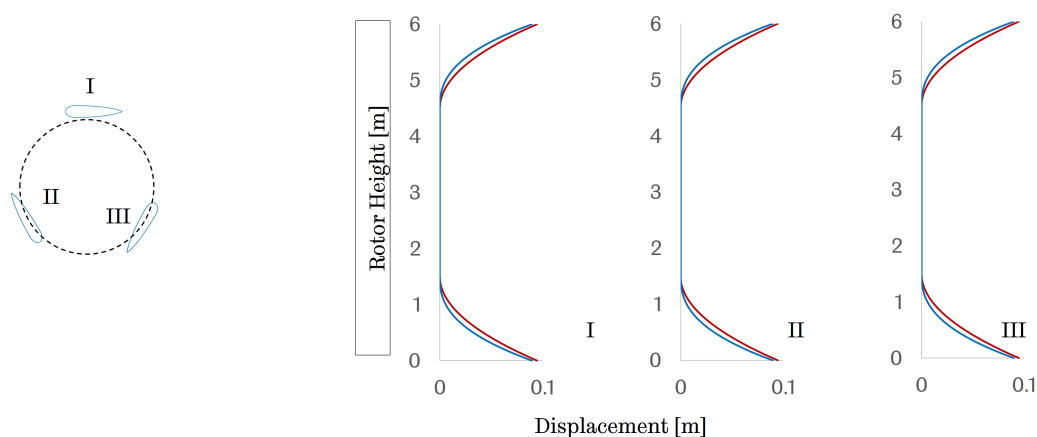


Figure 8.25: Time history of the blade maximum displacement on one VAWT blade at different time snapshots during self-starting stage at 0 m/s via FSI Simulation (blue) and ROM modelling (red).

8.5 Conclusion

In this chapter the novel ROM method is applied to various cases of 3D FSI simulations of a VAWT. The conceptual Windspire VAWT is used as the geometry for the simulations. The proposed method solves the case of a deforming solid body by considering the deformation as a cumulation of a series of rigid segments. During the validation simulation, only the turbine blades are assumed to be flexible. Various numbers of segmentation on each blade are investigated prior to the simulation. The corresponding stiffness matrix and kinematics are then calculated for the ROM. The proposed method is applied to two

working conditions, and both at constant rotational speed. Prior to the FSI simulations, several pure aerodynamic simulations are performed to validate the accuracy of the proposed model. The 8.0 m/s and rotor speed of 32.7 rad/s, and another using 1) wind speed of 8.0 m/s and rotor speed of 32.7 rad/s and 2) wind speed of 6.0 m/s and rotor speed of 20.6 rad/s, rotor speed of 12.1 RPM. The reconstructed ROM solutions are compared to the numerical results as well as the experimental data for both cases regarding the aerodynamic parameters such as torque. Error estimations and time analyses are compared to the corresponding full-order numerical solution. In addition, a typical application of the FSI simulations on a VAWT, namely the self-starting analysis, is simulated to challenge the capability of the proposed ROM model. The Windspire VAWT was set to start at 1) 0 rad/s and 2) 4 rad/s. Both the ROM results show a relatively good agreement with the CFD solution. In addition, both solutions present a better capability and accuracy compared to the traditional uniform ROM method. Specifically, the ROM results successfully capture the plateau region that occurs in the case of 4 rad/s.

Chapter 9

Conclusions and Future Work

9.1 Conclusions

In this study, a new global POD-Galerkin based ROM has been developed for the class of problems with both a fluid flow and moving solid boundaries/bodies. The goal of this PhD project is to develop a new ROM approach to the FSI problem that is applicable to moving and/or deforming solid boundaries and in particular applicable to the VAWT structure analysis. The new method can substantially improve the wind turbine fluid-structure interaction analysis method in terms of both the simulation efficiency and accuracy. A new and novel local refinement strategy on the ROM method is proposed in order to balance the increase in time cost and accuracy. Moreover, this strategy includes the elastic behaviour of solid domains, thus increasing the capability of the approach to solve FSI problems with large moving interfaces between the rigid body and the fluid.

A critical literature review on fluid-structure interaction methods and VAWT aeroelastic behaviour is presented. Various methods are presented and critically analysed to identify the resulting research gaps that exist in the literature and these are investigated in this project. In addition, a comprehensive review of the POD method, especially focused on the adaptive snapshot methods, is included in Chapter 2.

A brief overview of the Proper Orthogonal Decomposition (POD) - Galerkin method is presented in Chapter 3. An a-priori comparison of the approximation errors using different POD basis generation approaches is made. In addition, some new important aspects for an improved POD basis computation are presented. Finally, the empirical interpolation method is introduced in order to overcome the numerical complexity when evaluating the nonlinear terms in the ROM. A detailed evaluation of the ROM method is presented in a simple case, although the ROM methods can be improved by adding snapshots and/or grids. However, this hinders the performance of the ROM method. Therefore, it is necessary to propose a new multiple and adaptive snapshot method

to balance the accuracy and efficiency of the ROMs. The traditional uniform ROM predicts fluid flows that have a relatively good agreement with experimental data in the lower Reynolds number cases. However, it is not capable of predicting accurate results at high Reynolds number flows, which occur in VAWH applications, or in the cases of moving/deforming FSI problems.

In Chapter 4, a new adaptive grid discretisation approach that is based on a two-dimensional refinement strategy in which an internal node has exactly four children is presented. The strategy is implemented using a quad-tree data structure which can be implemented automatically and/or manually. To stress the necessity and importance of the adaptive grid refinement, the Stuart vortices, a special flow field with an analytical solution is selected as the application of this approach. The adaptive POD-Galerkin ROM approach shows a better accuracy compared to the base case with a uniform discretisation. The overall time cost of the adaptive discretisation strategy is longer than the uniform case but still much quicker compared to the refined case. Although the increase in the time cost may overshadow the merit of this method compared to the ROM with same level of the mesh, when compared to the benefits of improving the accuracy and the computational cost between the ROM approach and the numerical method, this sacrifice in the computational cost due to the self-adaptive spatial discretisation is therefore found to be acceptable. Therefore, the proposed ROM method is much more computationally efficient than the traditional uniform POD-Galerkin ROM.

In Chapter 5, a POD-Galerkin based ROM approach is proposed, which defines the moving solid boundaries/bodies as a continuous time-varied domain. It is straight-forward strategy, easy to apply, and can predict any kind of moving boundaries, no matter if it is rigid or flexible, flow-induced or prescribed, as long as the solid information is known. A series of flows with moving boundaries have been predicted by this method, including both two-dimensional and three-dimensional, and both translational and rotational rigid cases, e.g., oscillating aerofoil. It is found that the predictions accurately match the simulation results. The new model developed in this chapter is at least as computationally efficient and as accurate as the other models described in the literature. The concept of flexible bodies within a MBS is depicted, including beam elements and modal bodies on the basis of the order-reduced bodies. The interface between the mechanical and fluid solver is presented, which allows the exchange of forces and body kinematics. In addition, the proposed approach is compatible with the refined method proposed in the earlier chapter. However, this approach is relatively time-consuming and is not suitable for some extremely complex flexible motions, which undermines the benefit of using the ROM.

In Chapter 6, a POD-Galerkin ROM approach for flexible cases is proposed. By defining the moving solid boundaries/bodies as a characteristic function on the same combined fluid-solid domain, the POD-Galerkin projection method has also been applied to the moving solid boundaries/bodies. The concept of flexible bodies within a MBS is depicted, including beam elements and modal bodies on the basis of order-reduced bodies. The interface between the mechanical and fluid solver is modelled as joints with constraints, which represent the rigidity of the materials, thus enabling the exchange of the forces and body kinematics. This approach has been applied to both two-dimensional and three-dimensional situations with deforming boundaries, e.g., a teardrop/flat plate design is flexible in the chordwise direction only. As described in Chapter 5, the decomposed approach preserves the dynamics and keeps its capability of capturing most of the energy in the fluid flow. The fluid structures and force results show that the forcing terms perform powerfully to maintain the dynamics of the system for large solid motions, especially the prescribed velocity terms, which are presented as the energy input and make the system stable and this allows the modelling of the prescribed solid motions.

The proposed ROM approaches have also been employed to multiple problems, especially in wind turbine simulations. In Chapter 7, the novel ROM method is validated in the case of the 3D FSI simulation for a HAWT. The conceptual NREL 5-MW reference offshore wind turbine (Jonkman et al., 2009) is used as the geometry for the simulations. The proposed method solves the case of a deforming solid body by considering the deformation as a cumulation of a series of rigid segments. During the validation simulation, the tower, nacelle and hub are considered as rigid bodies, while the turbine blades are assumed to be flexible. A convergence study is performed prior to the ROM process. Multiple input parameters, including the time step and number of meshes of the full order baseline FSI simulation and the number rigid segmentations on each turbine blade are investigated prior to the simulation. The proposed ROM approach shows a good capability of the locally refinement strategy proposed in Chapter 4. Both the ROM results, i.e., the proposed ROM shows a relatively good agreement with the CFD solution regarding the velocity and blade tip deformations, while the computational deficiency slightly undermines the efficiency due to the increase in the governing matrices. In terms of the locally refined ROM methodology, both solutions present a better capability and accuracy compared to the traditional uniform ROM method. Although this method is slightly computationally inefficient due to its algorithmic structure, this sacrifice in the computational cost due to the self-adaptive spatial discretisation is acceptable compared to the scale of the full order models.

In order to improve the accuracy of the proposed model, the dynamic behaviour of a VAWT was examined. The turbine was loaded with a varying inflow and the resulting self-starting behaviour and fluctuations in the rotational velocity were observed and discussed in Chapter 8. The fluctuations were in good agreement with the referenced experimental data. Reconstructed ROM solutions are compared to numerical results as well as experimental solution when it is approachable. Error estimation and time analysis are compared to the corresponding full-order numerical solution. In addition, a typical application of FSI simulations on VAWT, self-starting analysis, is simulated to challenge the capacity of the proposed ROM model. In order to challenge the capability of the FSI problem, the VAWT is set to start at various speeds of rotation. The proposed ROM solutions show a good capability and accuracy compared to the traditional uniform ROM method. In addition, the proposed method successfully capture the plateau region occurs in the case which the uniform ROM is no capable. Similar to the previous chapter, the computational efficiency and accuracy is investigated. The proposed adaptive ROM is more computationally efficient compared to the uniform ROM with the same level of mesh. In addition, the proposed POD-Galerkin ROM shows a good compatibility in other FSI fields, e.g., multi-phase simulation.

9.2 Future Work

The novel self-adaptive Reduced Order Modelling and the POD-Galerkin based Reduced Order Modelling approaches have been proposed, implemented and demonstrated in this work, and there are several possible further extensions.

It would be interesting to apply the proposed methodology to more problems as well as optimisation where many cases of the models are required. We have applied the proposed ROM to oscillating solid body problems, such as a rigid oscillating aerofoil and a flexible teardrop/flat shape, as well as fluid-structure interaction problems in Chapters 5, 6, 7 and 8. In particular, the proposed ROMs have been implemented on fluid-structure interaction problems of wind turbines. In the future, it would be very interesting to apply the adaptive POD-Galerkin based ROM to even more complicated problems, such as multiphase, multibody FSI problems. In the future, the optimisation of the proposed adaptive refinement strategy can be optimised by introducing optimisation methodologies, such as neural network optimization and deep learning methods.

The proposed self-adaptive Reduced Order Modelling for Fluid-Structure Interaction problem is based on the assumption that the flexible rigid domain is a slender body. The

proposed methodology behaves very well in various cases, including oscillating aerofoils and wind turbines. In conclusion, it would be very interesting to develop a novel method based on the propose POD-Galerkin based ROM for slender deforming FSI problem.

List of Publications

1. Dong J, Ingham D, Ma L, Pourkashanian M (2021) POD-Galerkin Based Reduced Order Modelling for Flow-Structure Interactions. *Int J Astronaut Aeronautical Eng* 6:057
2. Dong J, Ingham D, Ma L, Pourkashanian M (2021) Towards an adaptive Reduced-Order modelling of the VAWT aeroelasticity behaviour. *Online Symposium on Aeroelasticity, Fluid-Structure Interaction, and Vibrations*.

References

- [1] Ali M. AbdelSalam and Velraj Ramalingam. Wake prediction of horizontal-axis wind turbine using full-rotor modeling. *Journal of Wind Engineering and Industrial Aerodynamics*, 124:7–19, 1 2014.
- [2] D. Abouri, A. Parry, and A. Hamdouni. A stable fluid rigid body interaction algorithm: Application to industrial problems. pages 107–114. ASMEDC, 1 2004.
- [3] P. Acar and M. Nikbay. Reduced order modelling of high-fidelity computational fluid-structure interaction analysis for aeroelastic systems. pages 149–171. Institute of Structural Analysis and Antiseismic Research School of Civil Engineering National Technical University of Athens (NTUA) Greece, 2014.
- [4] Iwona Adamiec-Wójcik, Lucyna Brzozowska, and Łukasz Drąg. An analysis of dynamics of risers during vessel motion by means of the rigid finite element method. *Ocean Engineering*, 106:102–114, 9 2015.
- [5] Frederico Afonso, José Vale, Éder Oliveira, Fernando Lau, and Afzal Suleman. A review on non-linear aeroelasticity of high aspect-ratio wings. *Progress in Aerospace Sciences*, 89:40–57, 2 2017.
- [6] Mesfin Belayneh Ageze, Yefa Hu, and Huachun Wu. Wind turbine aeroelastic modeling: Basics and cutting edge trends, 2017.
- [7] Mazen Ali, Kristina Steih, and Karsten Urban. Reduced basis methods based upon adaptive snapshot computations. pages 1–30, 7 2014.
- [8] Mazen Ali and Karsten Urban. *Reduced Basis Exact Error Estimates with Wavelets*, pages 359–367. 2016.
- [9] A. Alla, C. Gräßle, and M. Hinze. A residual based snapshot location strategy for pod in distributed optimal control of linear parabolic equations. *IFAC-PapersOnLine*, 49:13–18, 2016.

- [10] David Amsallem, Matthew J. Zahr, and Charbel Farhat. Nonlinear model order reduction based on local reduced-order bases. *International Journal for Numerical Methods in Engineering*, 92:891–916, 12 2012.
- [11] Kari Appa, Michael Yankulich, and David L. Cowan. The determination of load and slope transformation matrices for aeroelastic analysis. *Journal of Aircraft*, 22:734–736, 8 1985.
- [12] Nadine Aubry. On the hidden beauty of the proper orthogonal decomposition. *Theoretical and Computational Fluid Dynamics*, 2:339–352, 8 1991.
- [13] Nadine Aubry, Philip Holmes, John L. Lumley, Emily Stone, Philip Holmestil, and Emily Stone. The dynamics of coherent structures in the wall region of a turbulent boundary layer. *Journal of Fluid Mechanics*, 192:115–173, 7 1988.
- [14] Myles Baker, D. Mingori, and Patrick Goggin. Approximate subspace iteration for constructing internally balanced reduced order models of unsteady aerodynamic systems. pages 1070–1085. American Institute of Aeronautics and Astronautics, 4 1996.
- [15] Timothy J. Baker. Mesh deformation and reconstruction for time evolving domains. American Institute of Aeronautics and Astronautics, 6 2001.
- [16] Francesco Ballarin and Gianluigi Rozza. Pod–galerkin monolithic reduced order models for parametrized fluid-structure interaction problems. *International Journal for Numerical Methods in Fluids*, 82:1010–1034, 12 2016.
- [17] P. Z. Bar-Yoseph, S. Mereu, S. Chippada, and V. J. Kalro. Automatic monitoring of element shape quality in 2-d and 3-d computational mesh dynamics. *Computational Mechanics*, 27:378–395, 5 2001.
- [18] Matthew F. Barone, Irina Kalashnikova, Matthew R. Brake, and Daniel J. Segalman. Reduced order modeling of fluid/structure interaction. *Sandia National Laboratories*, page 124, 2009.
- [19] Matthew F Barone and Jeffrey L Payne. Methods for simulation-based analysis of fluid-structure interaction. *Sandia Report*, 6573:10, 2005.

- [20] Maxime Barrault, Yvon Maday, Ngoc Cuong Nguyen, and Anthony T. Patera. An ‘empirical interpolation’ method: application to efficient reduced-basis discretization of partial differential equations. *Comptes Rendus Mathematique*, 339:667–672, 2004.
- [21] Robert E. Bartels. Mesh strategies for accurate computation of unsteady spoiler and aeroelastic problems. *Journal of Aircraft*, 37:521–525, 5 2000.
- [22] John T. Batina, David A. Seidel, Samuel R. Bland, and Robert M. Bennett. Unsteady transonic flow calculations for realistic aircraft configurations. *Journal of Aircraft*, 26:21–28, 1 1989.
- [23] Ulrike Baur and Peter Benner. Cross-gramian based model reduction for data-sparse systems. *Electronic Transactions on Numerical Analysis*, 31:27, 2008.
- [24] Y. Bazilevs, A. Korobenko, X. Deng, J. Yan, M. Kinzel, and J. O. Dabiri. Fluid-structure interaction modeling of vertical-axis wind turbines. *Journal of Applied Mechanics*, 81:081006, 5 2014.
- [25] Yuri Bazilevs, Kenji Takizawa, and Tayfun E. Tezduyar. *Computational Fluid-Structure Interaction: Methods and Applications*. John Wiley & Sons, Ltd, 1 2012.
- [26] Oddvar Bendiksen. A new approach to computational aeroelasticity. American Institute of Aeronautics and Astronautics, 4 1991.
- [27] Gal Berkooz, Philip Holmes, and John L. Lumley. The proper orthogonal decomposition in the analysis of turbulent flows. *Annual Review of Fluid Mechanics*, 25:539–575, 1 1993.
- [28] Tomáš Bodnár, Giovanni P Galdi, and Šárka Nečasová. *Fluid-structure interaction and biomedical applications*. Springer, 2014.
- [29] Bradley N. Bond and Luca Daniel. Guaranteed stable projection-based model reduction for indefinite and unstable linear systems. *IEEE/ACM International Conference on Computer-Aided Design, Digest of Technical Papers, ICCAD*, pages 728–735, 2008.
- [30] Rémi Bourguet, Marianna Braza, and Alain Dervieux. Reduced-order modeling of transonic flows around an airfoil submitted to small deformations. *Journal of Computational Physics*, 230:159–184, 2011.

- [31] S. Brown and S. Brown. Displacement extrapolations for cfd+csm aeroelastic analysis. American Institute of Aeronautics and Astronautics, 4 1997.
- [32] Annalisa Buffa, Yvon Maday, Anthony T. Patera, Christophe Prud’Homme, and Gabriel Turinici. A priori convergence of the greedy algorithm for the parametrized reduced basis method. *ESAIM: Mathematical Modelling and Numerical Analysis*, 46:595–603, 2012.
- [33] Marshall Buhl and Andreas Manjock. A comparison of wind turbine aeroelastic codes used for certification. volume 13, pages 1–14. American Institute of Aeronautics and Astronautics, 1 2006.
- [34] Hans-Joachim Bungartz and Michael Schäfer. *Fluid-structure interaction: modelling, simulation, optimisation*, volume 53. Springer Science & Business Media, 2006.
- [35] Kevin Carlberg, Charbel Bou-Mosleh, and Charbel Farhat. Efficient non-linear model reduction via a least-squares petrov-galerkin projection and compressive tensor approximations. *International Journal for Numerical Methods in Engineering*, 86:155–181, 4 2011.
- [36] Volker Carstens, Ralf Kemme, and Stefan Schmitt. Coupled simulation of flow-structure interaction in turbomachinery. *Aerospace Science and Technology*, 7:298–306, 2003.
- [37] Ryan James Caverly, Chenyang Li, Eun Jung Chae, James Richard Forbes, and Yin Lu Young. Modeling and control of flow-induced vibrations of a flexible hydrofoil in viscous flow. *Smart Materials and Structures*, 25:065007, 6 2016.
- [38] Juan Cebral and Rainald Lohner. On the loose coupling of implicit time-marching codes. pages 10079–10093. American Institute of Aeronautics and Astronautics, 1 2005.
- [39] Juan Raul Cebral and Rainald Lohner. Conservative load projection and tracking for fluid-structure problems. *AIAA Journal*, 35:687–692, 4 1997.
- [40] Jean Jacques Chattot. Helicoidal vortex model for wind turbine aeroelastic simulation. *Computers and Structures*, 85:1072–1079, 6 2007.

- [41] Saifon Chaturantabut and Danny C. Sorensen. Nonlinear model reduction via discrete empirical interpolation. *SIAM Journal on Scientific Computing*, 32:2737–2764, 1 2010.
- [42] P. K. Chaviaropoulos and M. O. L. Hansen. Investigating three-dimensional and rotational effects on wind turbine blades by means of a quasi-3d navier-stokes solver. *Journal of Fluids Engineering*, 122:330, 2000.
- [43] P. Chen and L. Hill. A three-dimensional boundary element method for cfd/csd grid interfacing. American Institute of Aeronautics and Astronautics, 4 1999.
- [44] Dominique Paul Chevallier and Jean Lerbet. *Multi-body kinematics and dynamics with lie groups*. Elsevier, 2017.
- [45] Tai-Yih Chiu. Model reduction by the low-frequency approximation balancing method for unstable systems. *IEEE Transactions on Automatic Control*, 41:995–997, 7 1996.
- [46] Said Chkir. Unsteady loads evaluation for a wind turbine rotor using free wake method. volume 6, pages 777–785, 2011.
- [47] Yunfei Chu, Mitchell Serpas, and Juergen Hahn. State-preserving nonlinear model reduction procedure. *Chemical Engineering Science*, 66:3907–3913, 2011.
- [48] Matthew Churchfield, Scott Schreck, Luis A Martínez-Tossas, Charles Meneveau, Philippe R Spalart, Matthew J Churchfield, and Luis A Martínez-Tossas. An advanced actuator line method for wind energy applications and beyond preprint an advanced actuator line method for wind energy applications and beyond, 2017.
- [49] John O. Dabiri. Potential order-of-magnitude enhancement of wind farm power density via counter-rotating vertical-axis wind turbine arrays. *Journal of Renewable and Sustainable Energy*, 3, 2011.
- [50] I. Dobrev, F. Massouh, and M. Rapin. Actuator surface hybrid model. *Journal of Physics: Conference Series*, 75:012019, 7 2007.
- [51] J. Donea, S. Giuliani, and J.P. Halleux. An arbitrary lagrangian-eulerian finite element method for transient dynamic fluid-structure interactions. *Computer Methods in Applied Mechanics and Engineering*, 33:689–723, 9 1982.

- [52] J. Du, F. Fang, C. C. Pain, I. M. Navon, J. Zhu, and D. A. Ham. Pod reduced-order unstructured mesh modeling applied to 2d and 3d fluid flow. *Computers and Mathematics with Applications*, 65:362–379, 2013.
- [53] Zhaohui Du and Michael Selig. A 3-d stall-delay model for horizontal axis wind turbine performance prediction. pages 9–19. American Institute of Aeronautics and Astronautics, 1 1998.
- [54] V. Esfahanian, A. Salavati Pour, I. Harsini, A. Haghani, R. Pasandeh, A. Shahbazi, and G. Ahmadi. Numerical analysis of flow field around nrel phase ii wind turbine by a hybrid cfd/bem method. *Journal of Wind Engineering and Industrial Aerodynamics*, 120:29–36, 9 2013.
- [55] F. Fang, C. C. Pain, I. M. Navon, A. H. Elsheikh, J. Du, and D. Xiao. Non-linear petrov-galerkin methods for reduced order hyperbolic equations and discontinuous finite element methods. *Journal of Computational Physics*, 234:540–559, 2013.
- [56] F. Fang, T. Zhang, D. Pavlidis, C. C. Pain, A. G. Buchan, and I. M. Navon. Reduced order modelling of an unstructured mesh air pollution model and application in 2d/3d urban street canyons. *Atmospheric Environment*, 96:96–106, 2014.
- [57] C. Farhat, C. Degand, B. Koobus, and M. Lesoinne. Torsional springs for two-dimensional dynamic unstructured fluid meshes. *Computer Methods in Applied Mechanics and Engineering*, 163:231–245, 9 1998.
- [58] C. Farhat and M. Lesoinne. Two efficient staggered algorithms for the serial and parallel solution of three-dimensional nonlinear transient aeroelastic problems. *Computer Methods in Applied Mechanics and Engineering*, 182:499–515, 2000.
- [59] R. A. Finkel and J. L. Bentley. Quad trees a data structure for retrieval on composite keys. *Acta Informatica*, 4:1–9, 1974.
- [60] Davide Forti and Gianluigi Rozza. Efficient geometrical parametrisation techniques of interfaces for reduced-order modelling: application to fluid–structure interaction coupling problems. *International Journal of Computational Fluid Dynamics*, 28:158–169, 2014.
- [61] Leopoldo P. Franca and Sérgio L. Frey. Stabilized finite element methods: li. the incompressible navier-stokes equations. *Computer Methods in Applied Mechanics and Engineering*, 99:209–233, 9 1992.

- [62] M. Frangos, Y. Marzouk, K. Willcox, and B. van Bloemen Waanders. Surrogate and reduced-order modeling: A comparison of approaches for large-scale statistical inverse problems. *Large-Scale Inverse Problems and Quantification of Uncertainty*, pages 123–149, 2010.
- [63] Peretz P. Friedmann. Aeroelastic modeling of large wind turbines. *Journal of the American Helicopter Society*, 21:17–27, 10 1976.
- [64] Daniele Gallardo, Riccardo Bevilacqua, and Onkar Sahni. Data-based hybrid reduced order modeling for vortex-induced nonlinear fluid–structure interaction at low reynolds numbers. *Journal of Fluids and Structures*, 44:115–128, 1 2014.
- [65] Xiao-Wei Gao, Ping-Chih Chen, and Lei Tang. Deforming mesh for computational aeroelasticity using a nonlinear elastic boundary element method. *AIAA Journal*, 40:1512–1517, 8 2002.
- [66] C. G. Giannopapa and G. Papadakis. Linear stability analysis and application of a new solution method of the elastodynamic equations suitable for a unified fluid-structure-interaction approach. *Journal of Pressure Vessel Technology*, 130:031303, 8 2008.
- [67] Simone Giorgetti, Giulio Pellegrini, and Stefania Zanforlin. Cfd investigation on the aerodynamic interferences between medium-solidity darrieus vertical axis wind turbines. *Energy Procedia*, 81:227–239, 12 2015.
- [68] H. Glauert. *Airplane Propellers*, pages 169–360. Springer Berlin Heidelberg, 1935.
- [69] Roland Glowinski, Tsorng-Whay Whay Pan, Todd I. Hesla, Daniel D. Joseph, Jacques Périaux, and Jacques Pé Riaux. A distributed lagrange multiplier/fictitious domain method for flows around moving rigid bodies: Application to particulate flow. *International Journal for Numerical Methods in Fluids*, 30:1043–1066, 8 1999.
- [70] W. R. Graham, J. Peraire, and K. Y. Tang. Optimal control of vortex shedding using low-order models. part i - open-loop model development. *International Journal for Numerical Methods in Engineering*, 44:945–972, 1999.
- [71] Serkan Gugercin and Athanasios C. Antoulas. A survey of model reduction by balanced truncation and some new results. *International Journal of Control*, 77:748–766, 2004.

- [72] Guru P. Guruswamy. A review of numerical fluids/structures interface methods for computations using high-fidelity equations. *Computers & Structures*, 80:31–41, 1 2002.
- [73] Guru P. Guruswamy and Chansup Byun. Fluid-structural interactions using navier-stokes flow equations coupled with shell finite element structures. American Institute of Aeronautics and Astronautics, 7 1993.
- [74] Bernard Haasdonk and Mario Ohlberger. Reduced basis method for finite volume approximations of parametrized linear evolution equations. *ESAIM: Mathematical Modelling and Numerical Analysis*, 42:277–302, 3 2008.
- [75] Amr M Halawa, Basman Elhadidi, and Shigeo Yoshida. Pod & mlsm application on du96-w180 wind turbine airfoil. *Evergreen*, 4:36–43, 3 2017.
- [76] Kenneth C. Hall, Jeffrey P. Thomas, and Earl H. Dowell. Reduced-order modelling of unsteady small-disturbance flows using a frequency-domain proper orthogonal decomposition technique. volume 0300, pages 96–0528. American Institute of Aeronautics and Astronautics, 1 1999.
- [77] M. O.L. Hansen, J. N. Sørensen, S. Voutsinas, N. Sørensen, and H. Aa Madsen. State of the art in wind turbine aerodynamics and aeroelasticity. *Progress in Aerospace Sciences*, 42:285–330, 2006.
- [78] Martin O. L. Hansen and Helge Aagaard Madsen. Review paper on wind turbine aerodynamics. *Journal of Fluids Engineering*, 133:114001, 11 2011.
- [79] Alexander Hay, Jeffrey T Borggaard, and Dominique Pelletier. Local improvements to reduced-order models using sensitivity analysis of the proper orthogonal decomposition. *Journal of Fluid Mechanics*, 629:41, 6 2009.
- [80] Joachim C. Heinz, Niels N. Sørensen, and Frederik Zahle. Fluid-structure interaction computations for geometrically resolved rotor simulations using cfd. *Wind Energy*, 19:2205–2221, 12 2016.
- [81] Christian Himpe and Mario Ohlberger. Cross-gramian-based combined state and parameter reduction for large-scale control systems. *Mathematical Problems in Engineering*, 2014:1–13, 2014.
- [82] Philip Holmes, John L. Lumley, and Gal Berkooz. *Turbulence, Coherent Structures, Dynamical Systems and Symmetry*. Cambridge University Press, 1996.

- [83] Juntao Huang, Pablo M. Carrica, and Frederick Stern. Semi-coupled air/water immersed boundary approach for curvilinear dynamic overset grids with application to ship hydrodynamics. *International Journal for Numerical Methods in Fluids*, 58:591–624, 10 2008.
- [84] A Huskey, Amy Bowen, and David Jager. Wind turbine generator system power performance test report for the mariah windspire 1-kw wind turbine, 2009.
- [85] Angelo Iollo and Alain Dervieux. Computing and visualization in science regular article two stable pod-based approximations to the navier – stokes equations. *Computing and Visualization in Science*, 66:61–66, 2000.
- [86] K. Ito and S. S. Ravindran. *A Reduced Basis Method for Control Problems Governed by PDEs*, volume 8205, pages 153–168. Birkhäuser Basel, 1998.
- [87] F.M. Jensen, B.G. Falzon, J. Ankersen, and H. Stang. Structural testing and numerical simulation of a 34m composite wind turbine blade. *Composite Structures*, 76:52–61, 10 2006.
- [88] Rui Jiang and Louis J. Durlofsky. Implementation and detailed assessment of a gnat reduced-order model for subsurface flow simulation. *Journal of Computational Physics*, 379:192–213, 2019.
- [89] A. A. Johnson and T. E. Tezduyar. Mesh update strategies in parallel finite element computations of flow problems with moving boundaries and interfaces. *Computer Methods in Applied Mechanics and Engineering*, 119:73–94, 11 1994.
- [90] J. Jonkman, S. Butterfield, W. Musial, and G. Scott. Definition of a 5-mw reference wind turbine for offshore system development. 2009.
- [91] J Jonkman and W Musial. Offshore code comparison collaboration (oc3) for iea task 23 offshore wind technology and deployment offshore code comparison collaboration (oc3) for iea task 23 offshore wind technology and deployment. 2010.
- [92] Jason Jonkman. Definition of the floating system for phase iv of oc3, 2010.
- [93] Jason Jonkman and Walter Musial. Offshore code comparison collaboration (oc3) for iea wind task 23 offshore wind technology and deployment, 2010.

- [94] Jason Jonkman, A N Robertson, Wojciech Popko, Fabian Vorpahl, Adam Zuga, Martin Kohlmeier, Torben J Larsen, A Yde, K Saeterro, Knut M Okstad, James Nichols, Tor A Nygaard, Zhen Gao, Dimitris Manolas, Kunho Kim, Qing Yu, Wei Shi, Hyunchul Park, A Vasquez-Rojas, J Dubois, D Kaufer, P Thomassen, M J de Ruyter, JM Peeringa, Huang Zhiwen, and H von Waaden. Offshore code comparison collaboration continuation (oc4), phase i – results of coupled simulations of an offshore wind turbine with jacket support structure. *Isopre 2012*, 4:880653, 2012.
- [95] Jason M Jonkman and Marshall L Buhl Jr. Fast user’s guide. *Golden, CO: National Renewable Energy Laboratory*, 365:366, 2005.
- [96] I. Kalashnikova and M. F. Barone. On the stability and convergence of a galerkin reduced order model (rom) of compressible flow with solid wall and far-field boundary treatment. *International Journal for Numerical Methods in Engineering*, 83:1345–1375, 9 2010.
- [97] I. Kalashnikova, M.F. Barone, and M.R. Brake. A stable galerkin reduced order model for coupled fluid-structure interaction problems. *International Journal for Numerical Methods in Engineering*, 95:121–144, 7 2013.
- [98] Siri Kalvig, Eirik Manger, and Bjørn Hjertager. Comparing different cfd wind turbine modelling approaches with wind tunnel measurements. volume 555, page 012056, 12 2014.
- [99] Ramji Kamakoti and Wei Shyy. Fluid–structure interaction for aeroelastic applications. *Progress in Aerospace Sciences*, 40:535–558, 11 2004.
- [100] A. Kapahi, S. Sambasivan, and H.S. Udaykumar. A three-dimensional sharp interface cartesian grid method for solving high speed multi-material impact, penetration and fragmentation problems. *Journal of Computational Physics*, 241:308–332, 5 2013.
- [101] Taehyoun Kim. Frequency-domain karhunen-loeve method and its application to linear dynamic systems. *AIAA Journal*, 36:2117–2123, 11 1998.
- [102] Taewoo Kim, Sejong Oh, and Kwanjung Yee. Improved actuator surface method for wind turbine application. *Renewable Energy*, 76:16–26, 4 2015.
- [103] T. Kinsey and G. Dumas. Optimal operating parameters for an oscillating foil turbine at reynolds number 500, 000. *AIAA Journal*, 52:1885–1895, 2014.

- [104] Bruno Koobus and Charbel Farhat. Second-order time-accurate and geometrically conservative implicit schemes for flow computations on unstructured dynamic meshes. *Computer Methods in Applied Mechanics and Engineering*, 170:103–129, 2 1999.
- [105] A. Korobenko, M. C. Hsu, I. Akkerman, and Y. Bazilevs. Aerodynamic simulation of vertical-axis wind turbines. *Journal of Applied Mechanics, Transactions ASME*, 81, 2 2014.
- [106] Karl Kunisch and Stefan Volkwein. Optimal snapshot location for computing pod basis functions. *ESAIM: Mathematical Modelling and Numerical Analysis-Modélisation Mathématique et Analyse Numérique*, 44:509–529, 2010.
- [107] David J. Laino, A. Craig Hansen, and Jeff E. Minnema. Validation of the aerodyn subroutines using nrel unsteady aerodynamics experiment data. *Wind Energy*, 5:227–244, 4 2002.
- [108] Oliver. Lass. Reduced order modeling and parameter identification for coupled nonlinear pde systems. 2014.
- [109] Ya Jung Lee, Yu Ti Jhan, and Cheng Hsien Chung. Fluid-structure interaction of frp wind turbine blades under aerodynamic effect. *Composites Part B: Engineering*, 43:2180–2191, 2012.
- [110] M. Lesoinne and C. Farhat. Higher-order subiteration-free staggered algorithm for nonlinear transient aeroelastic problems. *AIAA Journal*, 36:1754–1757, 9 1998.
- [111] Y. Li, A. M. Castro, T. Sinokrot, W. Prescott, and P. M. Carrica. Coupled multi-body dynamics and cfd for wind turbine simulation including explicit wind turbulence. *Renewable Energy*, 76:338–361, 2015.
- [112] E. Liberge and A. Hamdouni. Reduced order modelling method via proper orthogonal decomposition (pod) for flow around an oscillating cylinder. *Journal of Fluids and Structures*, 26:292–311, 2 2010.
- [113] T. Lieu, C. Farhat, and M. Lesoinne. Reduced-order fluid/structure modeling of a complete aircraft configuration. *Computer Methods in Applied Mechanics and Engineering*, 195:5730–5742, 8 2006.
- [114] Thuan Lieu and Charbel Farhat. Adaptation of aeroelastic reduced-order models and application to an f-16 configuration. *AIAA Journal*, 45:1244–1257, 6 2007.

- [115] Kai Liu, Daochun Li, and Jinwu Xiang. Reduced-order modeling of unsteady aerodynamics of a flapping wing based on the volterra theory. *Results in Physics*, 7:2451–2457, 2017.
- [116] Wendi Liu and Qing Xiao. Investigation on darrieus type straight blade vertical axis wind turbine with flexible blade. *Ocean Engineering*, 110:339–356, 2015.
- [117] M. Loeve. *Probability Theory: Third Edition*. Dover Books on Mathematics. Dover Publications, 2017.
- [118] David J. Lucia, Philip S. Beran, and Walter A. Silva. Reduced-order modeling: New approaches for computational physics, 2 2004.
- [119] J L Lumley. The structure of inhomogeneous turbulence. atmospheric turbulence and wave propagation. *AM Yaglom, VI Tatarski*, pages 166–178, 1967.
- [120] Rainald Löhner and Chi Yang. Improved ale mesh velocities for moving bodies. *Communications in Numerical Methods in Engineering*, 12:599–608, 10 1996.
- [121] David W. MacPhee and Asfaw Beyene. Experimental and fluid structure interaction analysis of a morphing wind turbine rotor. *Energy*, 90:1055–1065, 10 2015.
- [122] N. Maman and C. Farhat. Matching fluid and structure meshes for aeroelastic computations: A parallel approach. *Computers and Structures*, 54:779–785, 2 1995.
- [123] D. G. Martineau and J. M. Georgala. A mesh movement algorithm for high quality generalised meshes. pages 5983–5996. American Institute of Aeronautics and Astronautics, 1 2004.
- [124] Pierangelo Masarati, Marco Morandini, and Paolo Mantegazza. An efficient formulation for general-purpose multibody/multiphysics analysis. *Journal of Computational and Nonlinear Dynamics*, 9, 10 2014.
- [125] Volker Mehrmann and Tatjana Stykel. *Balanced Truncation Model Reduction for Large-Scale Systems in Descriptor Form*, pages 83–115. Springer-Verlag, 2005.
- [126] Reid Melville. Nonlinear mechanisms of transonic aeroelastic instability for the f-16. American Institute of Aeronautics and Astronautics, 1 2002.
- [127] Reid B. Melville, Scott A. Morton, and Donald P. Rizzetta. Implementation of a fully-implicit, aeroelastic navier-stokes solver. American Institute of Aeronautics and Astronautics, 6 1997.

- [128] Satsuki Minami, Hiroshi Kawai, and Shinobu Yoshimura. Parallel bdd-based monolithic approach for acoustic fluid-structure interaction. *Computational Mechanics*, 50:707–718, 12 2012.
- [129] Scott A. Morton, Reid B. Melville, and Miguel R. Visbal. Accuracy and coupling issues of aeroelastic navier-stokes solutions on deforming meshes. *Journal of Aircraft*, 35:798–805, 9 1998.
- [130] Mitsuhiro Murayama, Kazuhiro Nakahashi, and Kisa Matsushima. Unstructured dynamic mesh for large movement and deformation. American Institute of Aeronautics and Astronautics, 1 2002.
- [131] N. C. Nguyen, A. T. Patera, and J. Peraire. A ‘best points’ interpolation method for efficient approximation of parametrized functions. *International Journal for Numerical Methods in Engineering*, 73:521–543, 1 2008.
- [132] Eric J. Nielsen and W. Kyle Anderson. Recent improvements in aerodynamic design optimization on unstructured meshes. *AIAA Journal*, 40:1155–1163, 6 2002.
- [133] BERND R. Noack, KONSTANTIN AFANASIEV, MAREK MORZYŃSKI, GILEAD TADMOR, and FRANK THIELE. A hierarchy of low-dimensional models for the transient and post-transient cylinder wake. *Journal of Fluid Mechanics*, 497:S0022112003006694, 12 2003.
- [134] J.M. O’Brien, T.M. Young, D.C. O’Mahoney, and P.C. Griffin. Horizontal axis wind turbine research: A review of commercial cfd, fe codes and experimental practices. *Progress in Aerospace Sciences*, 92:1–24, 7 2017.
- [135] B. C. Owens and D. T. Griffith. Aeroelastic stability investigations for large-scale vertical axis wind turbines. *Journal of Physics: Conference Series*, 524:012092, 6 2014.
- [136] R. Parameshwaran, Sai Jathin Dhulipalla, and Daseswara Rao Yendluri. Fluid-structure interactions and flow induced vibrations: A review. *Procedia Engineering*, 144:1286–1293, 2016.
- [137] N.A. Patankar, P. Singh, D.D. Joseph, R. Glowinski, and T.-W. Pan. A new formulation of the distributed lagrange multiplier/fictitious domain method for particulate flows. *International Journal of Multiphase Flow*, 26:1509–1524, 9 2000.

- [138] Charles S Peskin. Flow patterns around heart valves: A numerical method. *Journal of Computational Physics*, 10:252–271, 10 1972.
- [139] Janet S Peterson. The reduced basis method for incompressible viscous flow calculations. *SIAM Journal on Scientific and Statistical Computing*, 10:777–786, 1989.
- [140] Serge Piperno and Charbel Farhat. Partitioned procedures for the transient solution of coupled aeroelastic problems – part ii: energy transfer analysis and three-dimensional applications. *Computer Methods in Applied Mechanics and Engineering*, 190:3147–3170, 3 2001.
- [141] Serge Piperno, Charbel Farhat, and Bernard Larrouturou. Partitioned procedures for the transient solution of coupled aroelastic problems part i: Model problem, theory and two-dimensional application. *Computer Methods in Applied Mechanics and Engineering*, 124:79–112, 6 1995.
- [142] Flemming Rasmussen, Morten Hartvig Hansen, Kenneth Thomsen, Torben Juul Larsen, Franck Bertagnolio, Jeppe Johansen, Helge Aagaard Madsen, Christian Bak, and Anders Melchior Hansen. Present status of aeroelasticity of wind turbines, 7 2003.
- [143] M.J. Rewiński. A trajectory piecewise-linear approach to model order reduction of nonlinear dynamical systems. page 126, 2003.
- [144] Mohammad M. Rezaei, Mehdi Behzad, Hassan Haddadpour, and Hamed Moradi. Development of a reduced order model for nonlinear analysis of the wind turbine blade dynamics. *Renewable Energy*, 76:264–282, 4 2015.
- [145] Michael C. Romanowski and Earl H. Dowell. Reduced order euler equations for unsteady aerodynamic flows: Numerical techniques. American Institute of Aeronautics and Astronautics, 1 1996.
- [146] John A. Rule, David E. Cox, and Robert L. Clark. Aerodynamic model reduction through balanced realization. *AIAA Journal*, 42:1045–1048, 5 2004.
- [147] Feriedoun Sabetghadam and Alireza Jafarpour. regularization of the pod-galerkin dynamical systems of the kuramoto–sivashinsky equation. *Applied Mathematics and Computation*, 218:6012–6026, 2012.
- [148] M Schetzen. *The Volterra and Wiener Theories of Nonlinear Systems*. Krieger Pub., 2006.

- [149] Michael Schlegel and Bernd R. Noack. On long-term boundedness of galerkin models. *Journal of Fluid Mechanics*, 765:325–352, 2015.
- [150] Wen Zhong Shen, Martin O.L. Hansen, and Jens Nørkær Sørensen. Determination of the angle of attack on rotor blades. *Wind Energy*, 12:91–98, 2009.
- [151] Kiran Singh, Sebastien Michelin, and Emmanuel de Langre. The effect of non-uniform damping on flutter in axial flow and energy harvesting strategies. *Proceedings of the Royal Society A: Mathematical, Physical and Engineering Sciences*, 468:3620–3635, 7 2012.
- [152] S. Sirisup and G. E. Karniadakis. A spectral viscosity method for correcting the long-term behavior of pod models. *Journal of Computational Physics*, 194:92–116, 2004.
- [153] S. Sirisup and G. E. Karniadakis. Stability and accuracy of periodic flow solutions obtained by a pod-penalty method. *Physica D: Nonlinear Phenomena*, 202:218–237, 2005.
- [154] Lawrence Sirovich. Turbulence and the dynamics of coherent structures. iii. dynamics and scaling. *Quarterly of Applied Mathematics*, 45:583–590, 10 1987.
- [155] Marilyn J. Smith, Dewey H. Hodges, and Carlos E.S. Cesnik. Evaluation of computational algorithms suitable for fluid-structure interactions. *Journal of Aircraft*, 37:282–294, 3 2000.
- [156] H Snel, R. Houwink, J. Bosschers, W. J. Piers, G. J. W. van Bussel, and A. Bruining. Sectional prediction of 3d effects for stalled flow on rotating blades and comparison with measurements. pages 395–399. Netherlands Energy Research Foundation ECN, 1993.
- [157] G. W. Stewart. On the early history of the singular value decomposition. *SIAM Review*, 35:551–566, 12 1993.
- [158] J. T. Stuart. On finite amplitude oscillations in laminar mixing layers. *Journal of Fluid Mechanics*, 29:417–440, 1967.
- [159] D. Sturge, D. Sobotta, R. Howell, A. While, and J. Lou. A hybrid actuator disc – full rotor cfd methodology for modelling the effects of wind turbine wake interactions on performance. *Renewable Energy*, 80:525–537, 8 2015.

- [160] Kensuke Suzuki, Sven Schmitz, Hua Ouyang, and Jean Jacques Chattot. Extension of an unsteady hybrid navier-stokes/vortex-panel solver to wind turbine aerodynamic simulations at higher yaw angles. volume 3B, page V03BT46A011. ASME, 6 2014.
- [161] Jens N. Sørensen, Robert F Mikkelsen, Dan S. Henningson, Stefan Ivanell, Sasan Sarmast, and Søren J Andersen. Simulation of wind turbine wakes using the actuator line technique. *Philosophical Transactions of the Royal Society A: Mathematical, Physical and Engineering Sciences*, 373:20140071, 2 2015.
- [162] Jens Nørkærkær Sørensen. Aerodynamic aspects of wind energy conversion. *Annual Review of Fluid Mechanics*, 43:427–448, 1 2011.
- [163] Kunihiro Taira, Steven L Brunton, Scott T M Dawson, Clarence W Rowley, Tim Colonius, Beverley J McKeon, Oliver T Schmidt, Stanislav Gordeyev, Vassilios Theofilis, and Lawrence S Ukeiley. Modal analysis of fluid flows: An overview. *Aiaa Journal*, 55:4013–4041, 2017.
- [164] Kenji Takizawa, Yuri Bazilevs, Tayfun E. Tezduyar, Ming-Chen Hsu, Ole Øiseth, Kjell M. Mathisen, Nikolay Kostov, and Spenser McIntyre. Engineering analysis and design with ale-vms and space-time methods. *Archives of Computational Methods in Engineering*, 21:481–508, 12 2014.
- [165] Andrew A Tchieu. The development of low-order models for the study of fluid-structure interactions. 2010, 2010.
- [166] Jeffrey Thomas, Earl Dowell, Kenneth Hall, and Charles Denegri. Further investigation of modeling limit cycle oscillation behavior of the f-16 fighter using a harmonic balance approach. volume 3, pages 1457–1466. American Institute of Aeronautics and Astronautics, 4 2005.
- [167] Jeffrey P Thomas, Kenneth C Hall, and Earl H Dowell. Reduced-order aeroelastic modeling using proper-orthogonal decompositions. 1999.
- [168] S.P. Timoshenko. X. on the transverse vibrations of bars of uniform cross-section. *The London, Edinburgh, and Dublin Philosophical Magazine and Journal of Science*, 43:125–131, 1 1922.
- [169] Sumeet Trehan and Louis J. Durlofsky. Trajectory piecewise quadratic reduced-order model for subsurface flow, with application to pde-constrained optimization. *Journal of Computational Physics*, 326:446–473, 2016.

- [170] Paul S. Veers, Thomas D. Ashwill, Herbert J. Sutherland, Daniel L. Laird, Donald W. Lobitz, Dayton A. Griffin, John F. Mandell, Walter D. Musial, Kevin Jackson, Michael Zuteck, Antonio Miravete, Stephen W. Tsai, and James L. Richmond. Trends in the design, manufacture and evaluation of wind turbine blades. *Wind Energy*, 6:245–259, 7 2003.
- [171] Larry A. Viterna. Fixed pitch rotor performance of large horizontal axis wind turbines. *R. Thresher (Ed.), Large Horizontal-Axis Wind Turbines*, 1982.
- [172] V Volterra, G C Evans, and E T Whittaker. *Theory of Functionals and of Integral and Integro-differential Equations*. Dover Publications, 1959.
- [173] S. Walton, O. Hassan, and K. Morgan. Reduced order modelling for unsteady fluid flow using proper orthogonal decomposition and radial basis functions. *Applied Mathematical Modelling*, 37:8930–8945, 2013.
- [174] Lin Wang, Xiongwei Liu, and Athanasios Kolios. State of the art in the aeroelasticity of wind turbine blades: Aeroelastic modelling. *Renewable and Sustainable Energy Reviews*, 64:195–210, 10 2016.
- [175] David S Watkins. *Fundamentals of matrix computations*, volume 64. John Wiley & Sons, 2004.
- [176] Sisira Weeratunga and Eddy Pramono. Direct coupled aeroelastic analysis through concurrent implicit time integration on a parallel computer. volume 4, pages 1814–1825. American Institute of Aeronautics and Astronautics, 4 1994.
- [177] National Wind, National Renewable, Jeroen Van Dam, and Mark Meadors. Wind turbine generator system power performance test report for the mariah windspire 1-kw wind turbine. 2:1–44, 2003.
- [178] B A Winther, P J Goggin, and J R Dykman. Reduced-order dynamic aeroelastic model development and integration with nonlinear simulation. *Journal of Aircraft*, 37:833–839, 9 2000.
- [179] Teng Wu and Ahsan Kareem. Vortex-induced vibration of bridge decks: Volterra series-based model. *Journal of Engineering Mechanics*, 139:1831–1843, 12 2013.
- [180] D. Xiao, F. Fang, A. G. Buchan, C. C. Pain, I. M. Navon, J. Du, and G. Hu. Non-linear model reduction for the navier-stokes equations using residual deim method. *Journal of Computational Physics*, 263:1–18, 2014.

- [181] D. Xiao, F. Fang, J. Du, C.C. Pain, I.M. Navon, A.G. Buchan, A.H. ElSheikh, and G. Hu. Non-linear petrov–galerkin methods for reduced order modelling of the navier–stokes equations using a mixed finite element pair. *Computer Methods in Applied Mechanics and Engineering*, 255:147–157, 3 2013.
- [182] D. Xiao, P. Yang, F. Fang, J. Xiang, C.C. Pain, and I.M. Navon. Non-intrusive reduced order modelling of fluid–structure interactions. *Computer Methods in Applied Mechanics and Engineering*, 303:35–54, 5 2016.
- [183] Chun Yang, Dalin Tang, and Shu Q. Liu. A multi-physics growth model with fluid–structure interactions for blood flow and re-stenosis in rat vein grafts: A growth model for blood flow and re-stenosis in grafts. *Computers and Structures*, 81:1041–1058, 2003.
- [184] Guo Wei Yang, Guan Nan Zheng, and Gui Bo Li. Computational methods and engineering applications of static/dynamic aeroelasticity based on cfd/csd coupling solution. *Science China Technological Sciences*, 55:2453–2461, 9 2012.
- [185] Masayuki Yano. A minimum-residual mixed reduced basis method: Exact residual certification and simultaneous finite-element reduced-basis refinement. *ESAIM: Mathematical Modelling and Numerical Analysis*, 50:163–185, 1 2016.
- [186] Dong Ok Yu and Oh Joon Kwon. Predicting wind turbine blade loads and aeroelastic response using a coupled cfd-csd method. *Renewable Energy*, 70:184–196, 2014.
- [187] S. Zanforlin and S. Letizia. Improving the performance of wind turbines in urban environment by integrating the action of a diffuser with the aerodynamics of the rooftops. *Energy Procedia*, 82:774–781, 12 2015.
- [188] H.F. Zhou, H.Y. Dou, L.Z. Qin, Y. Chen, Y.Q. Ni, and J.M. Ko. A review of full-scale structural testing of wind turbine blades. *Renewable and Sustainable Energy Reviews*, 33:177–187, 5 2014.
- [189] Jan Östh, Bernd R. Noack, Siniša Krajnović, Diogo Barros, and Jacques Borée. On the need for a nonlinear subscale turbulence term in pod models as exemplified for a high-reynolds-number flow over an ahmed body. *Journal of Fluid Mechanics*, 747:518–544, 2014.

- [190] R. Ștefănescu, A. Sandu, and I. M. Navon. Pod/deim reduced-order strategies for efficient four dimensional variational data assimilation. *Journal of Computational Physics*, 295:569–595, 2015.
- [191] Petr Šidlof, Václav Vlček, and Martin Štěpán. Experimental investigation of flow-induced vibration of a pitch–plunge naca 0015 airfoil under deep dynamic stall. *Journal of Fluids and Structures*, 67:48–59, 11 2016.